Max-Planck-Institut für Polymerforschung
Max Planck Institute for Polymer Research

Selective surface functionalization and cell uptake of reproducibly synthesized biocompatible nanocapsules

Dissertation

zur Erlangung des Grades
„Doktor der Naturwissenschaften“
im Promotionsfach Chemie

des Fachbereiches Chemie, Pharmazie und Geowissenschaften (FB 09)
der Johannes Gutenberg-Universität Mainz

Marie-Luise Frey

geboren in Tuttlingen

Mainz, 2021

Dekan:
Erste Gutachterin:
Zweiter Gutachter:

Tag der mündlichen Prüfung: 21.06.2021

Die vorliegende Arbeit wurde im Zeitraum von Mai 2017 bis Mai 2021 am Max-Planck-Institut für Polymerforschung in Mainz angefertigt. Ich versichere die vorliegende Arbeit selbstständig angefertigt zu haben. Alle verwendeten Hilfsmittel und Quellen habe ich eindeutig als solche kenntlich gemacht. Weder die vorliegende Arbeit noch Teile davon wurden bei einer anderen Fakultät bzw. einem anderen Fachbereich als Dissertation eingereicht.

Mainz, den 11.05.2021

Marie-Luise Frey

Abstract

Recent developments in vaccine research demonstrate that engineered nanomaterials such as nanocarriers play an increasingly important role in modern medicine. The use of nanocarriers is an elaborate strategy that originally launched its involvement in cancer therapy. Next to the decrease of side-effects due to packaging of the drug, therapeutic efficacy is not limited to the sole delivery of the drug to its destination, but the carrier itself can also participate in the therapeutic approach using targeting moieties and smart materials.

Liposomal formulations are so far the most successful ones, representing the largest group of nanocarriers in clinical applications and trials, while other nanoparticulate materials have not shown a similar therapeutic scope yet. Reproducibility of nanocarrier syntheses is essential for successful translation to the clinic, however, this is difficult because nanoparticulate materials are, from a chemical point of view, extraordinarily complex. Furthermore, distinct physicochemical properties of the carriers are associated to biological characteristics, which are not fully understood yet.

This work aims to elucidate in detail the synthesis and surface functionalization of biocompatible nanocapsules, as potential drug delivery vehicles and the effects induced on a cellular level. In the first part it is shown that hydroxylethyl starch (HES) nanocapsules were reproducibly synthesized and biomolecules relevant for the targeting and selective proliferation of specific immune cells are attached to the surface, thus accomplishing the desired cell response. It is confirmed that also protein nanocapsules can be synthesized in the same manner and thermodynamic details for the binding constitutions are analyzed using a model system. In the third part it is shown that protein nanocapsules were synthesized using a bioorthogonal crosslinking approach, while revealing different uptake properties due to alteration of the surface constitution. In the fourth part, unambiguous localization of the protein nanocapsules inside cells is demonstrated, enabling elucidation of trafficking pathways.

In summary, an overall relationship of size, surface charge, and binding constitutions of different biocompatible nanocapsules, consisting of hydroxylethyl starch and proteins is given and their cellular uptake is illustrated. The findings are therefore an example for the analysis of structure-effect relationships for nanocarriers and are presenting further advances for nanocarrier characterizations and novel insights in order to improve clinical feasibility.

Zusammenfassung

Aktuelle Entwicklungen in der Impfstoff-Forschung zeigen, dass ausgearbeitete Nanomaterialien, wie beispielsweise Nanocarrier, eine immer wichtigere Rolle in der modernen Medizin spielen. Der Einsatz von Nanocarriern ist eine ausgeklügelte Strategie, die ursprünglich in der Krebstherapie ihren Anfang nahm. Neben der Verringerung von Nebenwirkungen durch die Verpackung des Medikaments beschränkt sich die therapeutische Wirksamkeit nicht nur auf die reine Lieferung des Arzneistoffs an seinen Bestimmungsort, sondern auch der Carrier selbst kann durch die Verwendung von zielgerichteten Bausteinen und intelligenter Materialien, am therapeutischen Ansatz teilnehmen.
Liposomale Formulierungen sind bisher am erfolgreichsten und stellen die größte Gruppe von Nanocarriern in klinischen Anwendungen und Studien dar, während andere nanopartikuläre Materialien noch keine ähnliche therapeutische Reichweite gezeigt haben. Die Reproduzierbarkeit der Nanocarrier-Synthese ist essenziell für eine erfolgreiche Umsetzung in die Klinik, jedoch ist diese schwierig, da nanopartikuläre Materialien aus chemischer Sicht, außerordentlich komplex sind. Des Weiteren sind bestimmte physikochemische Eigenschaften der Carrier mit Biologischen verknüpft, die noch nicht vollständig verstanden sind.

Diese Arbeit zeigt die Synthese und Oberflächenfunktionalisierung von verschiedenen biokompatiblen Nanokapseln, welche potenzielle Arzneistoff-Vehikel darstellen, und ihre auf zellulärer Ebene induzierten Effekte. Im ersten Teil wird gezeigt, dass Hydroxyethylstärke (HES)- Nanokapseln reproduzierbar synthetisiert werden können und Biomoleküle, welche relevant für das Targeting und die selektive Proliferation spezifischer Immunzellen sind, angebracht werden können, womit die gewünschte Zellantwort erreicht wird.
Es kann bestätigt werden, dass Protein-Nanokapseln auf die gleiche Weise synthetisiert werden können und es werden thermodynamische Details für die Bindungskonstitutionen anhand eines Modellsystems analysiert. Im dritten Teil wird gezeigt, dass Protein-Nanokapseln mit Hilfe eines bioorthogonalen Vernetzungsansatzes synthetisiert werden können und damit andere Aufnahme-Eigenschaften aufgrund von Veränderungen in der Oberflächenbeschaffenheit aufweisen.
Im vierten Teil kann eine eindeutige Lokalisierung der Protein Nanokapseln in Zellen demonstriert werden, welche die Aufklärung von Transportwegen ermöglicht.
Zusammenfassend wird ein Gesamtverhältnis von Größe, Oberflächenladung und Bindungskonstitution von verschiedenen biokompatiblen Nanokapseln, bestehend aus Hydroxyethylstärke und Proteinen, gezeigt und ihre zelluläre Aufnahme erläutert. Die Ergebnisse sind daher ein Beispiel für die Analyse einer Struktur-Wirkungsbeziehung von Nanocarriern und sollen Weiterentwicklungen für Nanocarrier-Charakterisierungen sowie neue Erkenntnisse für eine Verbesserung der klinischen Umsetzbarkeit darlegen.

Table of Contents

I. Introduction and Motivation

The most common causes of death depend strongly on the standard of living in the respective country.[1] Non communicable diseases (NCDs) which basically include all chronic diseases, are the leading cause for deaths in middle- and high income countries, first and foremost, cardiovascular diseases and cancer.[2] However, over the last thirty years, a change in mortality rates have been observed, especially for cancer-related causes of death.[3] Cancer mortality is constantly declining and performed an overall drop of around 29% from 1991 until 2017 as reported for the US.[4] This achievement in the combat of cancer is undoubted a success story written by many. It is owed to better understanding and the detection of new markers. It is owed to increased screening of patients and a better standard of preventive care. It is also owed to a rediscovered approach, which will be presented in the following, representing the basis of this work.

The elaborate strategy of using the mechanisms and elements of the patients' immune system for the treatment of cancer, is addressed in the concept of cancer immunotherapy and has been increasingly expanded and refined in recent years. Exploiting the ability of the immune system to eliminate degenerated cells has a clear advantage over the utilization of classical cancer therapies. Elimination can be performed well-targeted with the absence of usually associated dramatic side-effects of conventional cytotoxic cancer therapies.

Edward Jenner was one of the early pioneers of immunotherapy, as he was the first who recognized that by introducing antigens into the body, an immunity can be achieved.[5] With his findings he created the fundaments of vaccination, which was and is life-saving for millions of people each year. William Bradley Coley already described in 1891 tumor regression after an acute bacterial infection of a patient and was the first who successfully exploited his findings to treat cancer.[6,7] Coley's important achievements were long forgotten and are more popular and important today than ever before.

Over time, more discoveries regarding different parts and tasks of the immune system were made, which resulted in novel, ingenious therapeutical approaches. The ability of vertebrates to produce antibodies against any target with high specificity was addressed in the monoclonal antibody approach.[8] The administration of monoclonal antibodies, such as anti-HER-2 (Trastuzumab) or anti-CD20 (Rituximab), which is the first monoclonal antibody developed against cancer, was one of the earliest immunotherapy concepts, setting a milestone in modern cancer therapy.[9,10] Other antibody-based therapeutics followed quickly, leading to about 64 clinically approved monoclonal antibodies in the year 2018 for various treatments, most of them against cancer.[11] Even earlier than the successful monoclonal antibodies was the administration of immunostimulating cytokines and interferons. The cytokine interleukin-2 (IL-2, commercially available as Proleukin, or Aldesleukin, which is a recombinant high-dose IL-2) and Interferon-α (IFN- α), which are naturally secreted by cells of the immune system, are both approved for the treatment of melanoma and renal cell cancer, though having rather low response rates (~ 15%) and bear high risks of systemic inflammation and high-dose toxicity respectively.[12] Nevertheless in combination with other therapeutics, like monoclonal antibodies, different molecular inhibitors, or with T cell receptor targeting, IL-2 for instance, takes part in various ongoing clinical trials.[13] Furthermore, the possibility to produce recombinant IL-2 opened the door to effectively grow effector lymphocytes, having the ability to kill tumor cells (i.e. tumor-infiltrating lymphocytes (TILs)).

These lymphocytes in combination with IL-2 can be administered to patients, leading to several reported cases of significantly reduced tumor mass.[14,15] Studies and also the progress in clinical trials show that when IL-2 or related cytokines are administered, there is a greater benefit for cancer patients, if such combinatorial therapies are applied.[14] Until today there is an increasing significance of cancer immunotherapy (Figure 1).

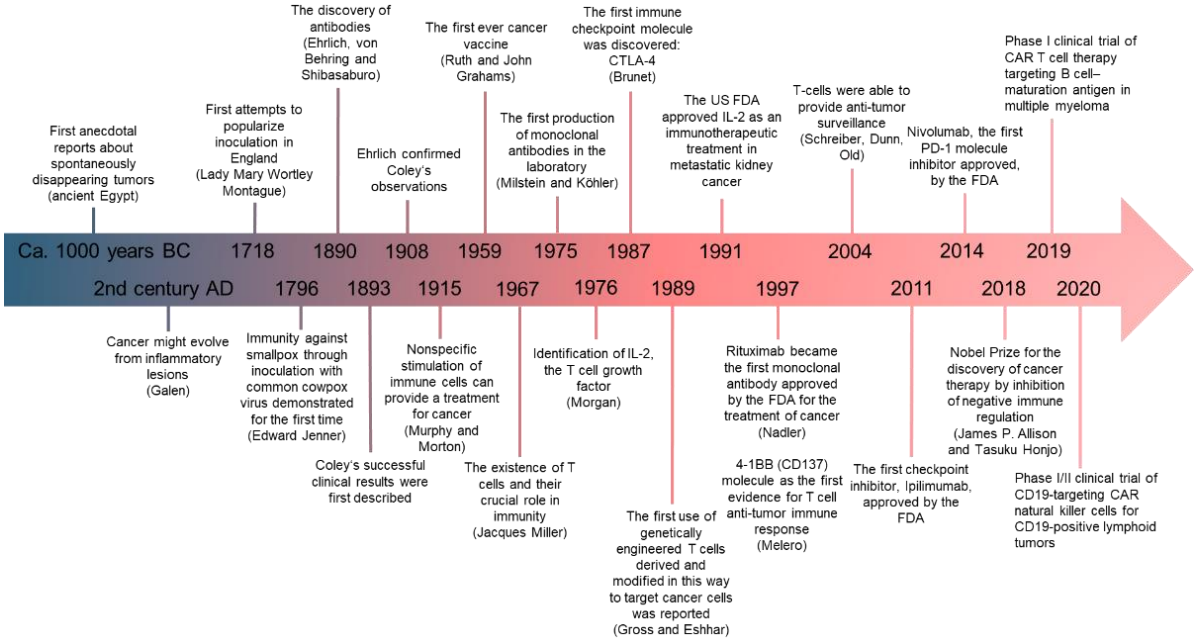

Figure 1: Timeline of milestones and important achievements in cancer immunotherapy. Adapted from reference[7] Copyright © 2019 Dobosz and Dzieciątkowski and https://www.nature.com/immersive/d42859-020-00083-8/index.html, 13.01.2021.[16]

The use of combinatorial approaches for cancer immunotherapy rises the better the understanding of the immune system is, since more and more complex relationships are found.[17,18]

The use of suitable nanocarriers is therefore of great importance for modernizing cancer therapy, since the nanocarrier can be engineered specifically combining multiple purposes. Nanocarriers represent an elaborate and further refined strategy compared to conventional systemic drug administrations into the human body, and with the approval of Doxil® in 1995 actively exists for 26 years now.[19] However, the concept of nanocarriers, is much older. The group around Watkins discovered liposomes as early as the 1960s.[20] However, there is not a high variety of different nanocarrier formulations that have made it successfully into clinical trials yet, although nanocarriers for drug delivery have been investigated for over 30 years now.

On the one hand, this is probably related to the high complexity of the nanosystems, in which different materials, morphologies, possibilities for surface functionalizations, encapsulated or linked cargoes, represent endless combinations of different systems, all exhibiting different properties. On the other hand, it is often not clear how the physicochemical properties are related to the biological ones.

Usually, a certain nanomaterial does not consist of one type of nanocarrier with the same structure. Here, too, there is a high variability of different material densities, morphologies, degrees of functionalizations, adsorbed surfactants, all combined to a heterogenous mixture of all kinds of nanocarriers exhibiting differences in all the mentioned characteristics, coexisting just in one single batch.

For these reasons, there is a particular need for a higher standard of nanocarrier characterization and reproducibility. Elucidating every single step of the nanocarrier synthesis, compare different materials and exploit several analytical techniques are a first step towards a better understanding of the relationship between the structure of the nanomaterial and the biological outcome.

In this work, the construction of biocompatible nanocapsules (NCs), considered as potential drug delivery vehicles, regarding immune cell targeting and specific uptake, is elucidated. The NCs were endowed with particular surface modifications and were prepared using different materials, inducing specific biological and immunological responses.
In Chapter A, NCs made of hydroxylethyl starch are presented and their synthesis, via inverse miniemulsion, is described in detail. It is shown that the cytokine IL-2 was attached to the capsules' surface in dependency of added concentrations, leading to a specific proliferation stimulation of IL-2 receptor bearing murine cells. In a similar approach, using different carbohydrates, the DC-SIGN receptor, which is specific for dendritic cells, was targeted in dependency of the structure of the corresponding carbohydrates displayed on the capsules' surface. Next to the goal of stimulation of specific immune cells, it is shown that the NCs were reproducibly synthesized and functionalized leading to an adjusted and selective surface.
In Chapter B special attention is paid to protein-NCs. Here different proteins are compared regarding their surface properties and the resulting NCs were functionalized to enable copper-free click reaction on the capsules' surface. Moreover, polystyrene nanoparticles (PS-NPs) with different degrees of functionalization are used as a model system in order to evaluate covalent reaction on the particle surface.
Next to exploiting the bioorthogonal copper-free click reaction on the different particle surfaces, another bioorthogonal approach is used for capsule crosslinking. This is especially useful when sensitive cargo has to be encapsulated. Chapter C demonstrates the synthesis of protein-NCs by using triazolinedione (TAD). The comparison of the uptake behaviour of conventional non-bioorthogonally crosslinked protein-NCs and TAD crosslinked protein-NCs reveals a surprising difference in the uptake behavior of the two different capsule systems, indicating a fundamentally different surface structure of the respective protein-NCs. In Chapter D, it is shown that protein-NCs encapsulating water-dispersible nanoplatelets (NPLs) can be tracked inside cells using correlative light and electron microscopy (CLEM), revealing different processing mechanisms of protein-NCs inside macrophages.

II. Theoretical background

II. 1. The human immune system

The immune system is one of the most complex networks in the human body and is subject to a dynamic learning and evolution process. The cellular part of the immune system includes a wide range of cells, all of which have been originally formed from bone marrow stem cells and which, after differentiation, have various tasks. Many of these cells produce a variety of signaling molecules, such as cytokines, which are responsible for the signal transduction among different parts of the immune system or are responsible for the production and release of antibodies (humoral immune response). Antibodies can bind specifically to any target and mark it readily for elimination by e.g., phagocytes. Furthermore, the immune system is divided into innate immunity, which provides the first undirected protection against antigens and adapted immunity, which is activated by antigen presentation of the innate immunity, acting specifically against the presented fragments. Typically, immune cells such as macrophages, dendritic cells and natural killer cells belong to the innate immune response, with T and B lymphocytes belonging to the adaptive one. There is a close synergy between the innate and adaptive immune response, though their mechanisms are completely different (Figure 2).

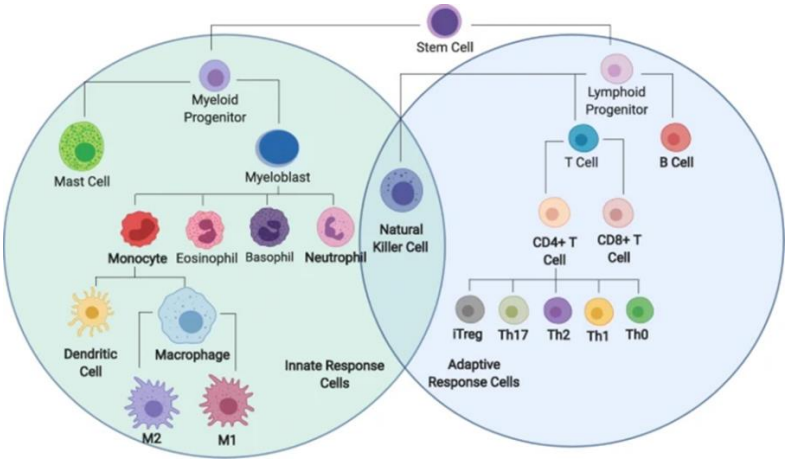

Figure 2: Cells of the human immune system, divided in cells of the innate immune response and in cells of the adapted immune response. Image reprinted with permission from reference [21]. Published by Springer Nature. Copyright © 2019, The Author(s).

In the early stages of development, the immune system must learn which molecular structures belong to the body's own products and which belong to foreign ones to optimally protect the organism from pathogens.[22] Not only pathogens entering the body are recognized by the immune system, but the immune system is fundamentally well equipped to eliminate degenerated and malignant cells, such as cancer cells. In the next section, the defense mechanisms of specific cells of the immune system will be elucidated.

II. 1.1 T lymphocyte mediated mechanisms of the immune system

T lymphocytes are the main regulators of the adaptive immune system and act as main effectors for cell-mediated immunity. The T cell receptor (TCR), which is located on their surface, forms antigen-specific bonds with the major histocompatibility complex (MHC), exhibiting fragmented antigens on the surface of antigen-presenting cells (APCs).

Recognition of the MHC-antigen complex results in activation of naïve T lymphocytes.[23] At this stage, the T lymphocytes already passed through various maturation processes, bearing different cell surface proteins, so called, clusters of differentiation (CD). These CDs enable the determination of cell phenotypes and interact with diverse cell receptors, such as the MHC complexes.[24] MHC-I proteins interact with cytotoxic T cells ($CD8^+$) while MHC-II proteins interact with $CD4^+$ T helper cells (T_h cells). After binding of the respective MHC protein with the TCR, activation of the T cells is enabled which leads to further effector processes. These effector processes include the initiation of apoptosis of infected or malignant cells by cytotoxic T cells, activation of B cells for antibody production and the secretion of inflammatory molecules by T- helper cell subsets (T_h cells). In addition, another T cell subtype, so called regulatory T cells (Tregs), regulate anti-inflammatory processes and are responsible for the downregulation of the immune system, which in principle represents a protective mechanism against autoimmune reactions.[25] However, the differentiation into distinct effector T cells, is dependent on the cytokines and stimulations which naïve $CD4^+$ or $CD8^+$ T cells receive and therefore also the regulation of inflammatory processes are subject to the complex mixture of cytokines and interferons.[26] Furthermore, there are T cell subpopulations, so called γδ T cells, which have unconventional T cell receptors (non-MHC restricted) and thus are not involved in classical antigen presentation and therefore cannot be clearly assigned to the adaptive immune response.[27,28]

Taking control over the differentiation processes of T lymphocytes is exceedingly desirable in cancer immunotherapy. However, achieving this targeted control over specific and defined differentiation processes is particularly difficult and thus complicate immunotherapies.

The cytokine Interleukin-2 (IL-2), which is secreted by naive and activated T cells, is a messenger molecule that can control the differentiation of T lymphocytes and will be discussed in the next section.

II. 1.1.1 Interleukin-2 (IL-2) – the main regulatory cytokine of T cells

The cytokine IL-2 is the key signaling protein in the regulation of differentiation and proliferation processes of T lymphocytes.[29] Furthermore, it is important for the induction of proliferation of natural killer (NK) cells and stimulates antibody production of B lymphocytes.[30,31] IL-2 is a α-helical protein with a molecular weight of approximately 15 kDa and promptly produced upon TCR signaling by $CD4^+$ T cells and sometimes also by $CD8^+$ T cells.[30] The protein structure is explained in detail in Chapter A IV. 4.1. The regulation of the IL-2 production is underlying a complex mechanism, in which the differentiation of the effector T cell plays a crucial role. The highest IL-2 production is enabled by memory $CD4^+$ T cells, while naïve $CD4^+$ T cells produce lower amounts, whereby $CD4^+$ regulatory T cells do not produce IL-2 at all.[32] IL-2 producing naïve $CD4^+$ T cells can even lose their ability to produce IL-2 after differentiation into Tregs.[32] Next to the own production of IL-2, the different T cell subsets are sensitive to the secreted amounts of IL-2 in dependency on the composition of the IL-2 receptor (IL-2R) presented on their surface. IL-2R can consist of up to three different subunits, which in dependency of their composition, endows the receptor with different affinities to IL-2. Subunit α (CD25) shows to have the lowest affinity to IL-2 and is expressed by Tregs at a higher level than other T cell subpopulations.[33] Furthermore IL-2R can consist of subunit β (CD122) and γ (CD132). IL-2R has the highest affinity for IL-2 if all three subunits appear on the cell surface of a T cell.

IL-2Rβ is also expressed by Tregs, but also memory $CD8^+$ T cells, NK cells and at some level by monocytes and neutrophils.[33–35] The IL-2Rγ subunit is exclusively deposited intracellularly and expressed only upon activation of CD4 T lymphocytes.[36]

Interestingly, Tregs contain all the subunits which are necessary to express the high affinity IL-2R, but they are dependent on paracrine IL-2 expression, since they are not able to produce IL-2 by themselves.[29] This means, that expression of IL-2 by other $CD4^+$ T cells can lead ultimately to the binding on CD25 of Tregs, which in turn start to express the other subunits of the IL-2R resulting in the binding of IL-2 with high affinity and therefore activation of Treg effector processes might take place in a preferential way to the other processes not involving high affinity receptors.

As already mentioned in the Introduction, the discovery that IL-2 triggers the proliferation of T cells and NK cells, led to the early use of IL-2 in combinatorial strategies for cancer therapy. However, the possibility to address different subpopulations of effector T cells by IL-2 and, above all, to specifically reach Tregs, offers new possibilities for immunotherapy. This is especially true if cancer cells are able to escape the usual immune reactions.

II. 1.1.2 T cell tolerance induced tumor escape mechanisms

There are basically two possibilities which tumors can use to evade elimination by the immune system. One possibility is based on the mutation of tumor antigens, to avoid recognition by antigen-presenting cells (APCs), leading to a preferential expansion of mutated tumor cells. In addition, a change in antigen presentation, due to defects in e.g. the MHC complex, can be enforced, which also prevents tumor detection.[37]

In a second scenario, the tumor can keep its antigenicity, but still escape elimination by diminishing its immunogenicity, by inducing an immunosuppressive microenvironment.[37] Suppression mechanisms in which Tregs are involved, contribute substantially in the preservation of this decrease in immunogenicity.[38] Classical $CD4^+CD25^+$ Tregs (expressing FOXP3 – an important transcription factor), can modulate the anti-tumor response by releasing different cytokines and other soluble factors and by direct cell-cell contact.[38,39] The main mechanisms for Treg immune suppression include the suppression of DCs by blocking the interaction of important surface markers which are abundant on DCs (mainly CD80 and CD86) which leads to a loss of activation of naïve T cells, and the induction of apoptosis to T cells and DCs, by IL-2 deprivation, leading to inhibition of T cell activation and by release of IL-10 and IL-35, as well as granzyme B and perforin (Figure 3).[38]

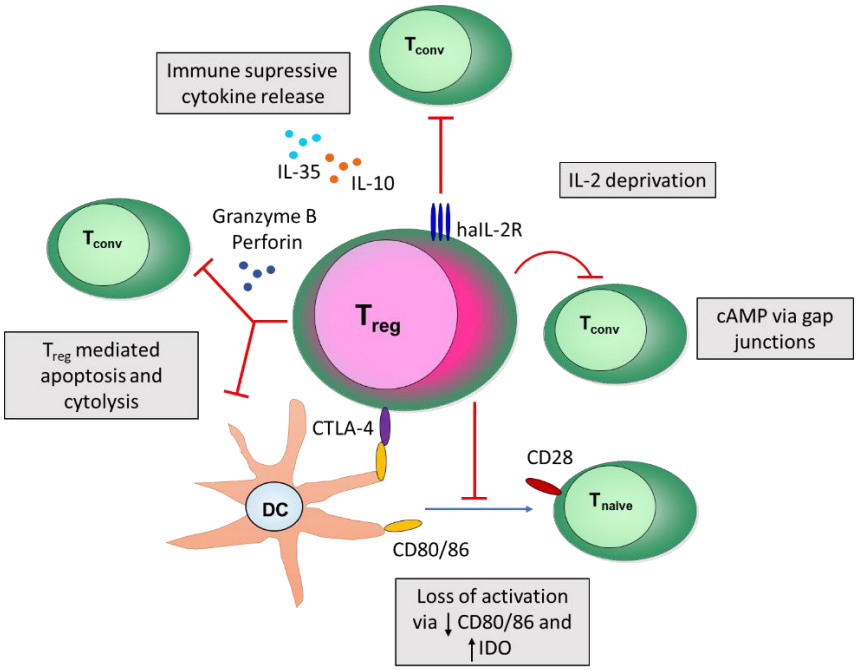

Figure 3: Tumor escape mechanisms induced by regulatory T cells (Tregs). Adapted with permission from reference[38] © 2012 British Society for Immunology.

There are several suggestions how tumors exploit Tregs immunosuppressive properties in their microenvironment. One possibility is the chemokine driven accumulation of Tregs in tumor tissue[39] or the direct expansion of Tregs in the tumor by using IL-2 as an important growth and surviving factor for Tregs.[40]

Furthermore, the STAT proteins, which are involved in signal transduction in the JAK STAT pathway, are believed to play an important role in cancer immunity. STAT3 in particular is believed to be involved in proliferation, survival, angiogenesis and metastasis and to prevent anti-tumor immunity.[41] Several studies show that STAT3 is significantly contributing to Tregs expansion in tumor microenvironment.[42,43] Cytokine receptors, such as IL-2R, activate STAT3 and STAT3 vice versa mediates the expression of cytokines, which as a consequence lead to a persistent activation of STAT3 and therefore an induction of cancer-inflammation and anti-tumor immunity.[41,44]

Targeting STAT3 for cancer therapy was already discussed almost 20 years ago and it has been shown that inhibitors of JAK family kinases can effectively block STAT3 activation, which had dramatic consequences for the survival of for example breast cancer cells.[45] More recently, direct STAT3 inhibitors were discussed, which were able to bind to the SH2 domain of STAT3, inhibiting dimerization of the protein.[46] Interestingly, blocking STAT3 leads to a lower overall toxicity than expected, as tumor cells may be dependent on STAT signaling to survive.[47]

II. 1.2 Dendritic cells (DCs) – gate keepers of the immune system

The main task of DCs, which are found in skin, mucosa, and lymphoid tissues, is to essentially catch antigens, fragment them and present them on their surface for T cell activation and therefore the induction of an adaptive immune response. Before activation, DCs are found in an immature state with a reduced metabolic activity and a low surface expression.

Their maturation is induced by recognition of so called PAMPs (pathogen-associated molecular patterns) and DAMPs (damage-associated molecular patterns), which leads to a fundamental structural change of the cells.[48] Upon maturation, DCs increase their motility and therefore migrate into secondary lymphoid organs, where mainly T cells are found.[49] Maturation leads to increased MHC expression and secretion of inflammatory cytokines.[48,50] All these steps lead to an optimal T cell activation and results in differentiation into $CD4^+$ T helper cell subsets and also into Tregs by different stimulatory factors.[48] These interactions of DCs with T cells (and also with other cells) are essential for the whole functioning of the adaptive immune response. The most important task of DCs, the cell-cell interactions, must therefore be subject to precise regulation. Therefore, the different surface markers on DCs are of crucial importance and it turns out that there are also markers which are exclusively, with few exceptions, restricted to DCs. The most prominent example is DC SIGN, which will be presented in the next section.

II. 1.2.1 DC-SIGN

On the surface of DCs, two different types of receptors are usually responsible for pathogen recognition. On the one hand, the large group of Toll-like receptors (TLRs) and on the other hand the C-type lectin receptors such as Dendritic Cell-Specific ICAM-3 Grabbing Nonintegrin (DC-SIGN), which is mostly found on immature DCs. While TLRs bind to lipopolysaccharides (LPS), lipoproteins and bacterial DNA,[51,52] C-type lectins detect various carbohydrate structures, which often serve as recognition sequences on cellular membranes, such as of bacteria, viruses, yeast and parasites.[53] DC-SIGN's specific structure, in which due to oligomerization,[54] four carbohydrate recognition domains (CRDs) can be found, allows the binding of multiple ligands, leading to an amplification of signaling and an increase of binding probability. This signaling concept can be continually encountered in biological systems and proves to be advantageous over monomeric binding strategies in several biological interactions.[55] Common ligands for DC-SIGN are mannose and fucose containing carbohydrates, which are often targets derived from pathogens.[54] However, Holla and Skerra demonstrate in their extensive study, plenty of different saccharidic structures which are supposed to be potential DC-SIGN binders, elucidating the high complexity of affinity and avidity of DC-SIGN to target structures.[56]

II. 1.3 Cancer therapies based on different mechanisms of the immune system

The overall goal of immunotherapy is the expansion of activated T-cell subsets, which are able to 1) detect and kill malignant cells,[57,58] 2) generate a durable memory effect,[59,60] 3) prevent the overexpression of immunosuppressive cells (Tregs).[61] In the next section, common strategies based on these goals are presented and recent therapies are elucidated.

II. 1.3.1 T cell-based therapies

The findings that tumors can abolish immune responses and use escape mechanisms to prevent the attack of the immune system, resulted in the development of checkpoint inhibitors.[62,63] As a result, T cell targeted immunomodulators such as immune checkpoint inhibitors CTLA4 or PD1 reformed the field of immunotherapy a decade ago.[64]

CTLA4 (cytotoxic T lymphocyte-associated antigen-4) and PD1 (programmed cell death protein 1), which gained the most attention, are expressed on activated T cells and regulatory T cells (Tregs). Binding of the ligand B7 on the CTLA4 receptor results in inhibition of proliferation and IL-2 secretion by T cells.[65] Therefore, the blocking of CTLA4 and PD1 prevents the hampering of T cells from initiating further response mechanisms.

The approach to enhance immune responses by influencing immunosurveillance is extremely successful. Monoclonal antibodies that target immune checkpoints, such as Ipilimumab, an antibody against CTLA4, are currently the greatest accomplishments of this approach, showing plenty of phase I/II and phase III/IV clinical trials carried out against various cancer types, exploiting the efficacy of these therapeutics.[66]

Another approach using the capabilities of T cells, is the CAR-T cell method, in which T cells are harvested from a patient and modified genetically *ex vivo* to express chimeric antigen receptors (CARs). After modification, the T cells bear engineered T cell receptors (TCRs) which are specific against known tumor antigens and can be transferred back to the patients' blood system.[67] This technique recently showed encouraging effects for instance in the treatment of patients with multiple myeloma and synovial cell sarcoma.[67–69]

Furthermore, more and more voices are being raised to include the identification and evaluation of more biomarkers in T cell-based cancer therapy. The effective evaluation of T cell bioactivity in cancer patients, requires a basic understanding of the biomarkers relevant for the proper functioning of T cells.[70]

II. 1.3.2 Therapies via dendritic cells (DCs)

Certain cells of the immune system, such as DCs, macrophages and B cells, can present antigens by incorporating the antigen and presenting fragments of it on their surface. This presentation enables an immune response, usually by the activation of T cells. In healthy human beings, this antigen-presentation leads naturally to the elimination of malignant cells. Different models suggest, that a presentation of tumor-antigens by DCs leads to a protective anti-tumor immunity.[71,72] For this reason, DC vaccination was developed, which is intended to mediate antigen-specific immunity by activation of tumor-specific effector T cells.[71]

Palucka *et al.* describe three main DC-based vaccination strategies: 1) vaccines composed of non-targeted peptide, protein, or nucleic acids, which are captured by DCs *in vivo*. 2) vaccines consisting of antigens linked to DC antibodies. 3) vaccines made of DCs which are cultured *ex vivo*, loaded with antigens and transferred back to the patient.[73] However, using vaccines made of synthetic peptides have not yet shown the desired comprehensive clinical response.[73,74] Nonetheless, several studies showed that the combination of peptide or protein vaccines with adjuvants such as different TLR agonists (i.e. TLR 7: Imiquimod or TLR7-TLR8: Resiquimod), improve anti-tumoral effects inside the patients.[75,76]

Also, in the targeted vaccine approach, in which antibodies are used, the addition of adjuvants plays a major role to establish a consequent immunity. Prominent examples are antigens linked to antibodies, which are specific against certain DC surface receptors like DEC205 or DC SIGN.[73,77,78]

The first therapeutic DC-based vaccine against cancer is Sipuleucel-T, which was FDA approved in the year 2010.[79] Sipuleucel-T, which is a drug against late-stage prostate cancer, utilizes the DC expansion *ex vivo* approach. In this process, cells are collected from the patients' blood and cultured *ex vivo* together with a recombinant fusion protein (in the case of Sipuleucel-T: prostatic acid phosphatase), representing the antigen, linked to granulocyte-macrophage colony-stimulating factor (GM-CSF) resulting in the activation of antigen-presenting cells (APCs) which are transferred back to the patient.[80]

Next to the approach of cancer vaccines and adoptive T cell therapies, several studies have shown that combinatorial therapies have the most promising effects to achieve an effective immune response against malignant cells, since with this approach several events inside the cells can be addressed. Nanomaterials, such as nanocarriers, offer another possibility to unite these combinatorial therapies in one material, since they are multifunctional and can be specifically designed for the patients' needs. Nanocarriers for drug delivery represent the third cornerstone of modern cancer therapy (Figure 4, highlighted in green) and will be explained in more detail in the next Section.

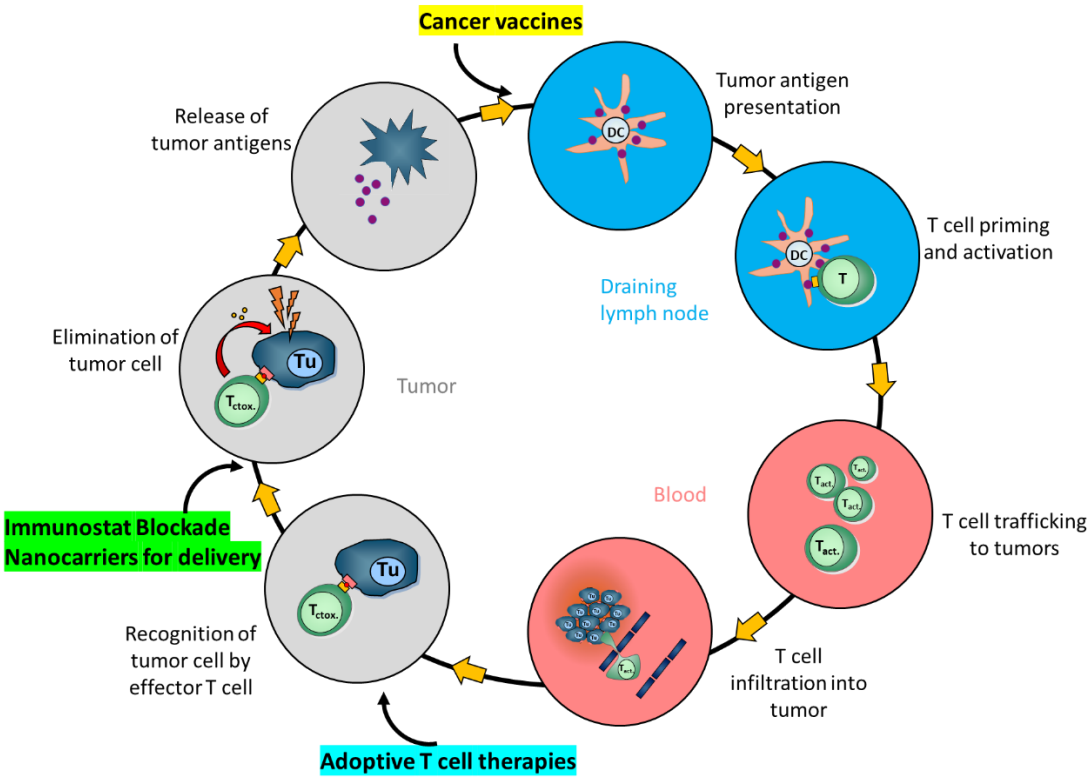

Figure 4: Cancer-immunity cycle with the three cornerstones of modern therapy: Cancer vaccination (yellow), adoptive T cell therapies (cyan) and immunostat blockade, e.g., by nanocarriers (green). Adapted with permission from reference[81] Copyright © 2015 Elsevier Ltd. all rights reserved, and with permission from reference[82] Copyright © 2013 Elsevier Inc. all rights reserved.

II. 2. Nanocarriers for drug delivery – design and concept

Drug delivery comprises all techniques and synthesis steps required to deliver a drug safely packaged in a nanosized carrier into the human body for the purpose of protecting the drug from degradation and vice versa also for protecting the organism from possible side effects caused by the drug.

Higher protection due to the packaging leads to a minimization of the drug dosage and an improved accumulation at the target site. The vehicle should exhibit biocompatibility and degradability to avoid being harmful to the organism and to release the drug at the desired location. The high surface to volume ratio furthermore provides improved biodistribution and pharmacokinetics.[83,84] In the next section an overview of the known systems and colloidal nanomaterials which are currently in clinical trials are presented.

II. 2.1 Common nanocarriers and current examples used in cancer therapy

The most prominent examples which are investigated as nanocarriers for drug delivery are polymeric or inorganic nanoparticles, dendrimers and core-shell structures such as polymeric nanocapsules, micelles and liposomes. (Figure 5).

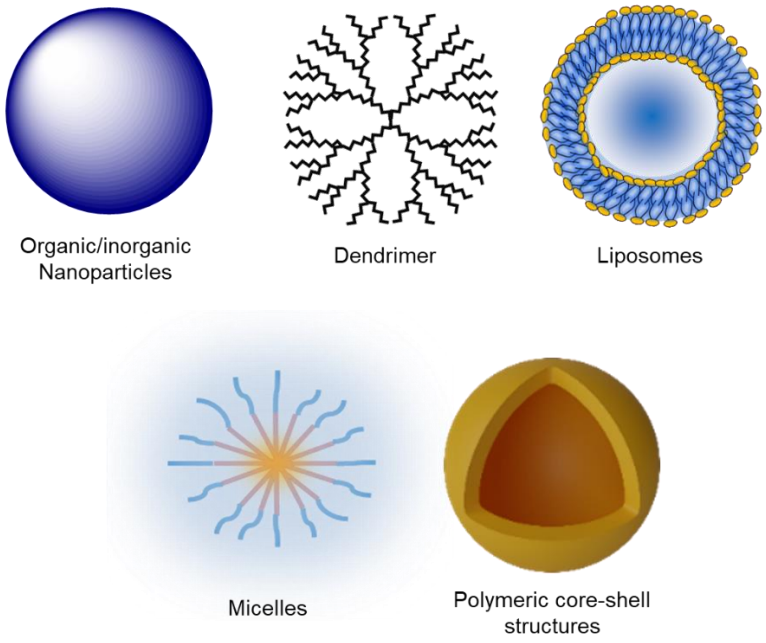

Figure 5: Overview of common nanocarriers.[85] https://polymerdatabase.com/polymer%20chemistry/Dendrimers.html, 13.01.2021.

All of them have different advantages regarding synthesis and characteristics. For example, micelles and dendrimers are usually the smallest nanocarriers and thus provide high permeability. In addition, the latter offers precise adjustment of the molecular weight and polyvalency, which is beneficial for the signaling of specific pathways as mentioned before.[86,87] However, especially high-generation dendrimers showed considerable cytotoxicity.[88] Nanoparticles in the narrower sense of nanospheres are very universal and can be made from various materials. Synthetic polymers offer the advantages that they can be produced precisely and can be equipped with any functional group. The advantage of using natural monomers and polymers for the nanoparticles is the high biocompatibility of the resulting nanomaterial. Furthermore, they can be synthesized by a variety of methods like emulsion techniques,[89] nanoprecipitation,[90] ionic gelation[91] and microfluidics.[92,93] Inorganic nanoparticles are often used for imaging purposes, however due to their unique physical properties, they are also used for theranostic applications.[94]

The self-assembly of liposomes is a major advantage in their production. Thus, they can be synthesized with high reproducibility in just a few steps. This is probably one of the reasons why most nanocarriers found on the market are mostly liposomal formulations and predominate current clinical trials in which nanocarriers are involved.

There are a few liposomal formulations for cancer therapy in various clinical trial phases. A selection is shown in Table 1. Not only liposomes, but also polymeric micelles and nanoparticles made it into clinical trials (Table 1).

Table 1: Selection of nanocarriers currently in clinical trials. Highlighted in green: liposomal formulations, red: micellar formulations, blue: nanoparticulate formulations. Adapted from reference[95] © 2019 The Authors. Bioengineering & Translational Medicine published by Wiley Periodicals, Inc. on behalf of The American Institute of Chemical Engineers.

Name	Nanocarrier type	Application	Clinical Trial/ National Clinical Trial Number
JVRS-100	Cationic liposome incorporating plasmid DNA complex	Leukemia	Phase I NCT00860522
PROMITIL (Lipomedix Pharmaceuticals)	PEGylated liposomal mitomycin-C	Solid tumors	Phase I NCT01705002
Oncoprex (Genprex)	FUS1 (TUSC2) encapsulated liposome	Lung cancer	Phase I/II NCT01455389
TKM-080301 (Arbutus Biopharma)	Lipid particle targeting polo-like kinase 1 (PLK1) for delivery of siRNA	Hepatocellular carcinoma	Phase I/II NCT02191878
NC-6004 Nanoplatin	Micellar cisplatin formulation	Advanced solid tumors, lung, biliary, bladder, or pancreatic cancers	Phase III NCT02043288
NK105 (Nippon Kayaku)	Paclitaxel micelle	Breast cancer	Phase III NCT01644890
CRLX101 (Cerulean)	Cyclodextrin based nanoparticle-camptothecin conjugate	Ovarian, renal cell, small cell lung, or rectal cancers	Phase II NCT02187302
ABI-009 (Aadi with Celgene)	Albumin bound rapamycin	Bladder cancer	Phase II NCT02494570
Magnablate	Iron nanoparticles	Thermal ablation for prostate cancer	Early Phase I NCT02033447

It is remarkable, that especially in the case of nanoparticles, often conjugates or physically adsorbed drugs are found to make the next steps to clinical trials. Abraxane®, a formulation of the drug paclitaxel bound to albumin nanoparticles, is one of the most famous examples for such a nanocarrier. It was approved by the FDA in 2005.[95] In Table 1 another example of a similar nanocarrier is shown, using the drug rapamycin (ABI-009). Furthermore, paclitaxel is again found and is currently competing in clinical trial phase III in form of a micellar formulation (NK105).

Many nanocarrier candidates shown in Table 1, represent formulations of known cytostatic drugs, which are already in use for cancer therapy, such as paclitaxel, camptothecin, mitomycin-C and cisplatin.

The formulation of these compounds as nanocarrier is in particular advantageous to improve solubility and to decrease toxicity to healthy cells. Especially the clinical use of camptothecin and paclitaxel was limited due to their poor bioavailability.[96] The formulation of a drug as a nanocarrier can influence the physicochemical properties of the molecule and thus improve therapeutic efficacy.[97,98] However, the list in Table 1 also reveals that traditional cytostatic drugs are often still used, which have strong side effects and act in an undirected manner against both tumor cells and healthy cells.

The increasing significance of nanocarrier systems as drug delivery vehicles emphasizes the potential of such formulations for future applications. The next Section elucidates the concept and design of nanocarriers and demonstrates the broad advantages which are addressed by them.

II. 2.2 Design and materials of drug delivery vehicles

Both, the nanocarrier material used and the reactions for ligation of the carrier, as well as for functionalization, are crucial for the nature of the nanocarrier. However, choosing the right polymer as drug delivery vehicle is already a difficult task, because not only is it necessary to be able to easily produce a nanomaterial from the polymer, but the resulting new surface properties must match the intended biological properties, and accessibility for subsequent functionalization of the nanocarrier must be ensured.[99]

Using biopolymers for nanocarrier synthesis is a popular approach because of their low toxicity and high biodegradability. The most popular natural polymers are proteins, like albumin, collagen and polysaccharides or cellulose-derivatives like hyaluronic acid, heparin, dextran, chitosan and more.[100] Hydroxylethyl starch (HES, Figure 6) which is a glucose polymer exhibiting mainly *α*-1,4 glycosidic bonds, represents another example of a suitable biopolymeric material, since it can readily be delivered in a sterile isotonic solution, as it was FDA-approved for the use as blood plasma expander for a long time.[101] In the literature HES can be found as material for nanocarriers and hydrogels.[102–104]

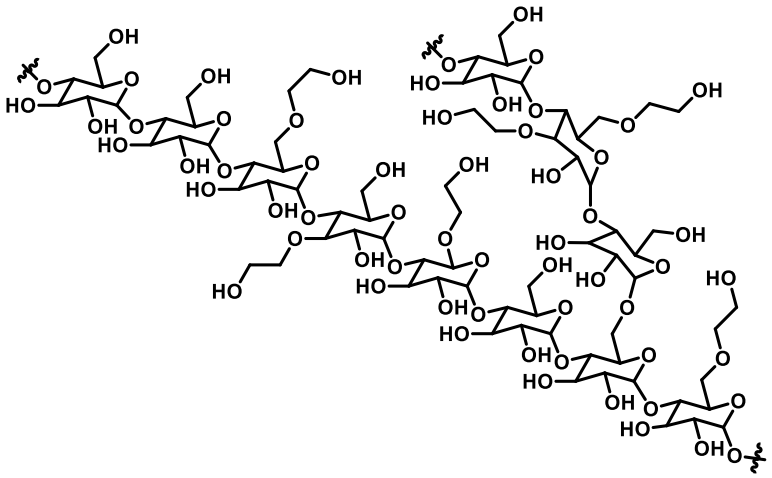

Figure 6: Structure of hydroxylethyl starch (HES).

Proteins and peptides are interesting materials for drug vehicles since they offer various possibilities for further functionalization due to the exposition of different functional groups.[105]

In addition, they exhibit functions for instance enzymatic ones[106] or boosting the immune system[107] which can be preserved after processing into a nanocarrier. Morphology-wise there are numerous possibilities to use proteins as nanocarriers.

Solid nanoparticles can be synthesized using desolvation,[105] protein nanocapsules can be prepared using miniemulsion,[108] a layer-by-layer template-assisted approach leads to nanotubes[109] and by self-assembly nanosheets can be obtained.[110] Moreover, by means of protein engineering, proteins can be customized as multifunctional nanomaterials.[111]

Nicolas *et al*. summarize in their review the most important points for a successful design strategy of nanocarriers (Figure 7).

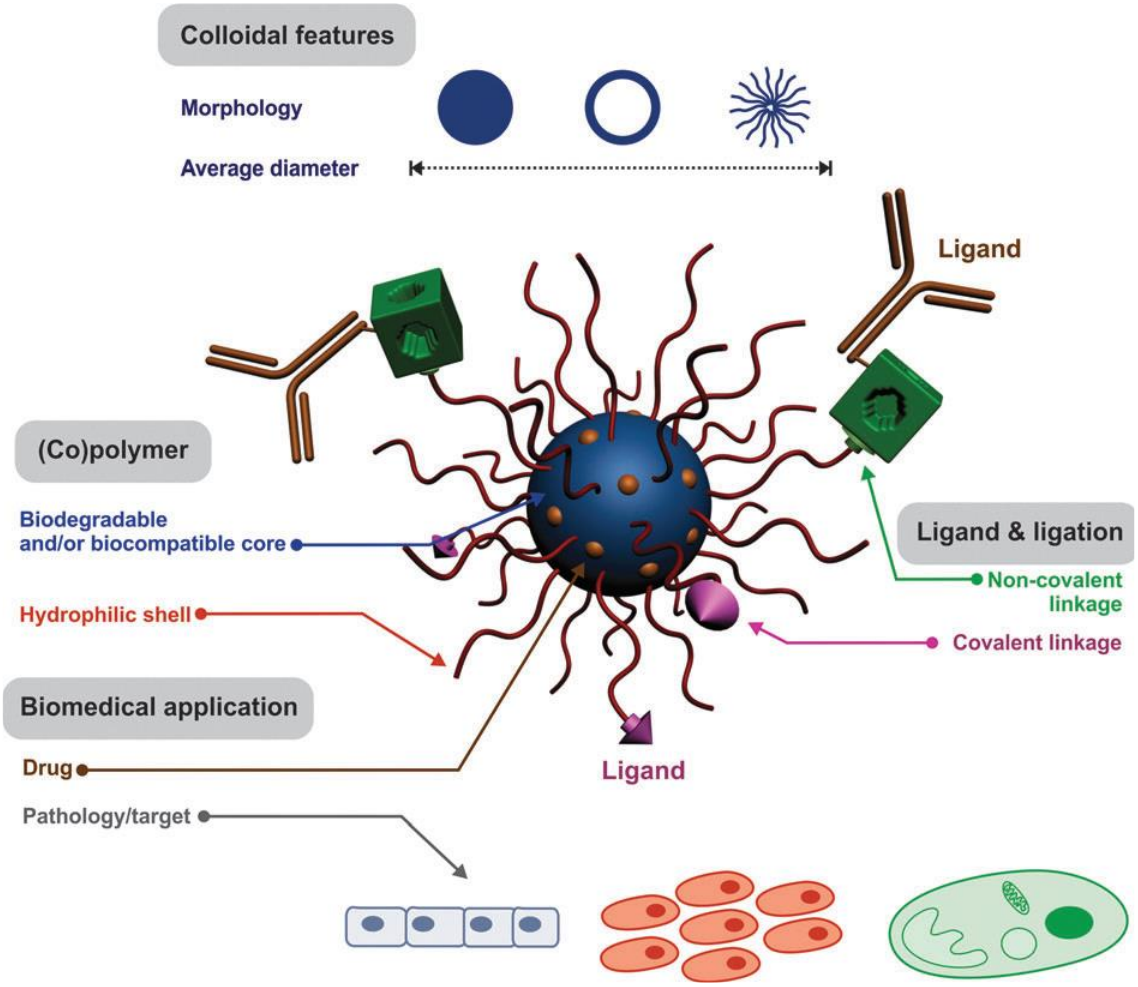

Figure 7: Different building blocks for the design of a nanocarrier for drug delivery. The therapeutical success of a nanocarrier is dependent on functional features such as the material, the ligand and the ligation strategy, the colloidal constitution and the morphology and the biomedical application. Reproduced from reference[112] with permission from The Royal Society of Chemistry.

They illustrate that next to the colloidal morphology and the used polymer which plays a crucial role, and which has been discussed in the Section before (II. 2.1), the attachment of a hydrophilic shell is necessary. A hydrophilic shell ensures a low and specific protein binding, the protein corona, when the nanocarrier is in contact with biological fluids such as blood. It was shown that this low protein binding with an increased abundance of clusterin to nanocarriers with hydrophilic polymer shells, leads to the so called stealth effect.[113] The stealth effect is responsible for a prolonged blood circulation of the carrier caused by reduced elimination by phagocytosis. Exploiting the stealth effect represents one of the most important design strategies for nanocarriers as the increased blood circulation time can increase the likelihood of enhanced accumulation of the nanocarrier at the tumor site of a patient by passive targeting (EPR effect).[114] This passive targeting is facilitated due to altered physiological properties of tumors such as enhanced vascular permeability.[115]

The most common polymer leading to stealth properties, is polyethylene glycol (PEG), however, PEG has recently fallen into disrepute because of reported immunogenicity in the context of the formation of anti-PEG antibodies.[116,117] For this reason, in the last few years more and more polymeric materials have been described which have similar properties and can also be used as coatings for nanomaterials, such as polyphosphoesters,[118,119] poly(2-oxazolines)[120] and polysaccharides[121,122].

Endowing stealth properties comprises one of many functionalization strategies which proved to be important steps towards reaching the goal of understanding targeting. However, it is important to actively influence targeting by an elaborate nanocarrier design.

Active targeting can be accomplished if molecules with high specificity such as antibodies, are bound to the nanomaterial (compare Figure 7). Previous studies have shown that adsorptive binding of antibodies can induce beneficial effects in contrast to directed covalent binding.[123] Nevertheless, it is exceedingly desirable to achieve a directed orientation on the nanocarrier since the success of the targeting is depending on the correct revelation of specific binding motifs.[124] To achieve directed binding, bioorthogonal reactions are necessary which will be discussed in the next Section.

II. 2.3 Functionalization and ligation strategies using bioorthogonal reactions

Bioorthogonal reactions have gained wide popularity among functionalization techniques in which biomolecules or even living organisms are engaged. This is in particular interesting when nanomaterials such as drug delivery vehicles, are intended to be functionalized with proteins and peptides. The term bioorthogonal reaction or ligation was coined by Bertozzi who defined the following principles facilitating bioorthogonal reactions: A bioorthogonal reaction do “neiter interact with nor interfere with a biological system.” The groups “selectively react with each other under biocompatible conditions, and, for *in vivo* applications, must be nontoxic to cells and organisms.”[125]

The classical comprehension of bioorthogonality is related with the concept of bioconjugation in which mainly binding strategies for the side chains of amino acids were explored.[125] Nucleophilic groups in side chains such as amino, or thiol groups from lysines or cysteins, respectively, are especially interesting because of their responsiveness. The use of active esters, such as *N*-hydroxy succinimide (NHS) ester for the reaction with amino groups are widely spread (Scheme 1). Furthermore, several other reagents for the formation of active esters which allow for a smooth and direct reaction with amines are known. Many of them are particularly interesting for peptide syntheses, such as dicyclohexyl carbodiimide (DCC) and 1-ethyl-3-(3-dimethylaminopropyl) carbodiimide (EDC), or the next generation coupling reagents derived from benzotriazoles hydroxy benzotriazole (HOBt), *N*,*N*,*N*′,*N*′-tetramethyl-*O*-(benzotriazol-1-yl)uronium tetrafluoroborate (TBTU) and (2-(1*H*-benzotriazol-1-yl)-1,1,3,3-tetramethyluronium hexafluorophosphate (HBTU).

For the conjugation of thiol groups, Michael-additions are suitable. The most popular among these are the thiol maleimide conjugation or the thiol-ene reaction, which works via a radical mechanism.

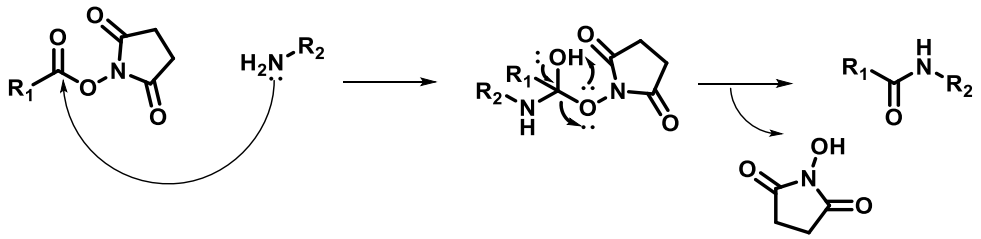

Scheme 1: Reaction of an NHS ester with an amine generating an amide.

Next to lysines and cysteins, tyrosines can be addressed due to their positive mesomeric (+M) effect, allowing for electrophilic aromatic substitutions on the aromatic ring. Thus, azo-containing groups are particularly suitable for the reaction with phenolic residues, such as diazonium salts or the rediscovered triazolinedione (TAD).

II. 2.3.1 Triazolinedione (TAD) as bioconjugation reagent to aromatic amino acids

TAD is a true allrounder when it comes to reactions with conjugated double bonds and with aromats. TADs reactivity was first described in detail by Cookson in 1962 who recognized its potential as dienophile and enophile as “Diels-Alder adduct”.[126] At that time, the Diels-Alder reaction had only been known for about 30 years.[127] Today more reactions regarding TAD are known and utilized in different contexts (Scheme 2).

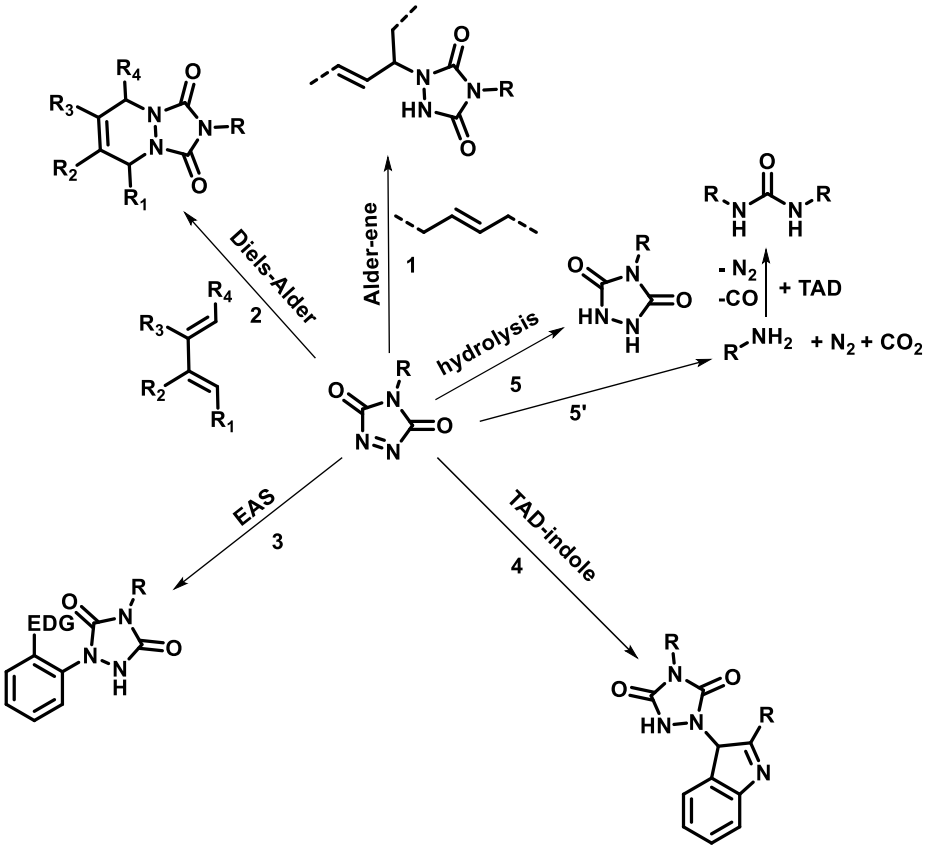

Scheme 2: Reactions of triazolinedione described in the review of De Bruycker *et al*.[128] 1: Alder-ene reaction with alkenes, 2: Diels-Alder reaction with dienes, 3: Electrophilic aromatic substitutions with aromats with electron donating groups (EDG), 4: TAD-indole reaction with indoles and tryptophan, 5: hydrolysis to corresponding urazole derivative and further hydrolysis to amines (5’) with possible side reaction of amines and TAD to urea derivatives.

Especially in the field of polymer modifications, crosslinking and surface modification TAD-chemistry is experiencing a revival. Particularly scientists around Du Prez and Barner-Kowollik describe current and modern applications for TAD. The most popular reactions are those with dienes and alkenes with which TAD is known to react exceptionally fast by Diels-Alder and Alder-ene reactions (Scheme 2, 1 and 2) even at low temperatures and without further auxiliaries.[128] Biosustainable materials such as unsaturated plant-oils can be easily converted to polymeric materials employing TAD in water as cosolvent in an Alder-ene reaction, making TAD in consideration of green chemistry applications very attractive.[129,130]

Du Prez and coworkers described that the TAD-ene reaction (Scheme 2, 2) is not yet fully understood and that there are several suggestions which draw conclusions of a zwitterionic intermediate.[128,131] Based on this, Du Prez and coworker explained that the electrophilic aromatic substitution of TAD on electron-rich aromats such as phenols (Scheme 2, 3), can also be understood as ene-reaction, in a broader sense, with subsequent rearomatization. They demonstrated a reaction mechanism for the EAS (Scheme 3).

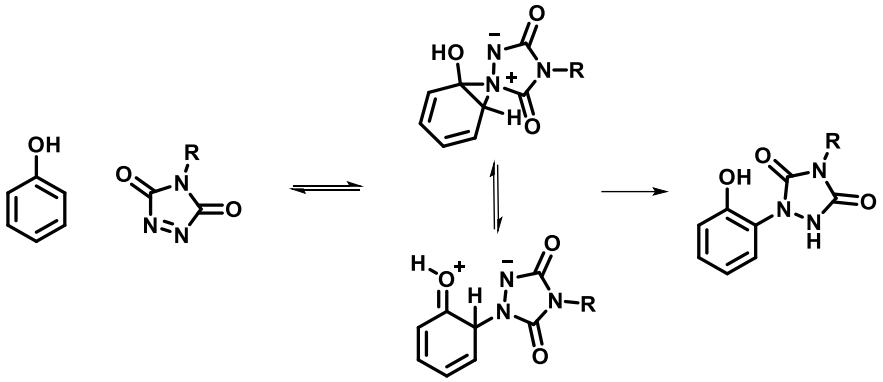

Scheme 3: Reaction mechanism of an electrophilic aromatic substitution of phenol using TAD.[128]

An interesting reaction type is the TAD-indole reaction (Scheme 2, 4) in which TAD can bind to the 3-position of an indole in a reversible manner. Thus, in the original application TAD was used as a protective group for indoles for instance in enantioselective syntheses.[132] The TAD-indole adduct is formed at room temperature and lower, while deprotection can be achieved by heating. In the context of protection and deprotection, the use of TAD is unpractical since the TAD-indole adduct again forms quantitatively upon cooling. However, when an alternative TAD reactant is offered, for example a diene, the TAD-indole adduct can be irreversibly converted to a new TAD adduct and a TAD-indole product is not formed (Scheme 4). This process has been introduced as “transclick” reaction by Du Prez and his coworkers.[133] TAD can be used to achieve exceedingly fast “click-like” conjugation to dienes, enes, aromats and indoles, which within the transclick approach, nevertheless reveal dynamic potentials.

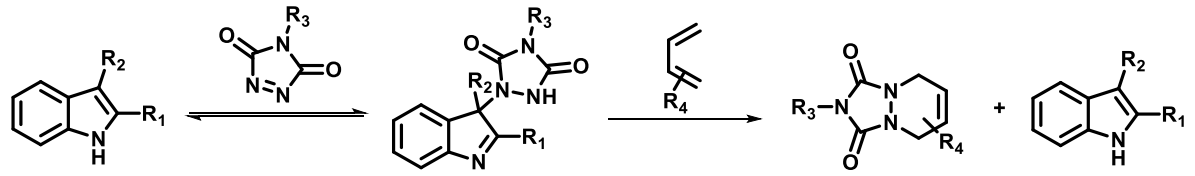

Scheme 4: TAD-indole reaction with subsequent transclick reaction with a diene.[128]

However, TAD is prone to hydrolysis and reduction by certain reagents, such as alcohols forming the corresponding urazole derivative (Scheme 2, 5).[134,135]

It has been shown that TAD-derivatives might even degrade to the corresponding amine species under thermal stress.[136] The fact that TAD might undergo a reaction with primary, secondary and tertiary amines resulting in urea derivatives indicate the rather poor bioorthogonal properties.[128] However, the excellent reaction rates support TAD as a suitable reagent for bioconjugation on biomolecules such as proteins bearing tyrosines and tryptophans. This bioconjugation strategy is impressively demonstrated in several applications such as the conjugation of a RGD peptide to the therapeutic antibody Herceptin,[137] covalent protein PEGylation by a phenyl-TAD reagent[138] or the formation of DNA-protein conjugates.[139] Regarding the attachment of TAD derivatives to proteins, it has been shown that solvents play a crucial role in the binding efficiency pointing reduced conjugation efficiencies with different solvent combinations (acetonitrile and DMSO) and with increased water concentrations due to TAD hydrolysis.[140]

Facilitating the transclick approach, Du Prez and coworkers reported a polyurethane material which was polymerized with a TAD-indole crosslinker revealing self-healing processes after thermo-treatment.[141] These possibilities point that exciting material properties are to be uncovered and new possibilities for future applications are still to be explored.

Again, TAD can be used to specifically modify olefinic compounds or proteins in order to attach them to the nanomaterial. This is particularly attractive in the case of proteins, since the proportion of tyrosines and tryptophans in proteins is usually significantly lower than that of lysines. This then leads to the attachment of significantly fewer linker molecules and thus to a better control of the modification. However, since aromatic amino groups are often located buried inside a protein, unlike the charged amino groups which often project outward from the protein, this could lead to more difficult binding conditions and increase the risk of a possible change in the tertiary structure of the protein.

II. 2.3.2 Alkyne-azide cycloadditions

The introduction of the 1,3-dipolar [3+2] cycloaddition by Huisgen in 1960 was not only from a chemical point of view an eminent breakthrough but revolutionized the world of bioconjugation and biolabeling in the same way.[142] The cycloaddition between azides and alkynes was discovered much earlier in 1893 by Michael, however, it was Huisgen who assigned them to the 1,3-dipolar cycloadditions and who reported about the reaction in detail recognizing the great potential.[143] Nowadays, alkyne-azide cycloaddition offer great application possibilities over many other bioconjugation reactions, since azides are absent in nature and therefore a high bioorthogonality can be achieved. The high reactivity combined with low demanding reaction conditions, such as room temperature and quantitative yields in aqueous solutions, also prompted Sharpless and coworkers to lead the [3+2] Huisgen cycloaddition of alkynes and azides under the prominent term “click chemistry”.[144] In the further process, Sharpless discovered that the alkyne azide cycloaddition could be efficiently catalyzed by copper (I) ions resulting in regioselective triazoles (Scheme 5).[145]

In the following years, a lot of time was invested to exploit the full potential of the Huisgen reaction and to further optimize reactants. Leading the way, Bertozzi and coworkers opened up new paths for the development and optimization of bioorthogonal click reactions and pioneered the synthesis and characterization of new reactants for, among others, the Huisgen reaction.

Thus, they developed cyclooctynes for strain-promoted azide-alkyne cycloadditions (SpAAC), which operate efficiently without the need of copper ions at room temperature (Scheme 5).[146] The avoidance of copper ions paved the way for bioorthogonal reactions also in organisms and cells, as the cytotoxic effect of copper is bypassed.

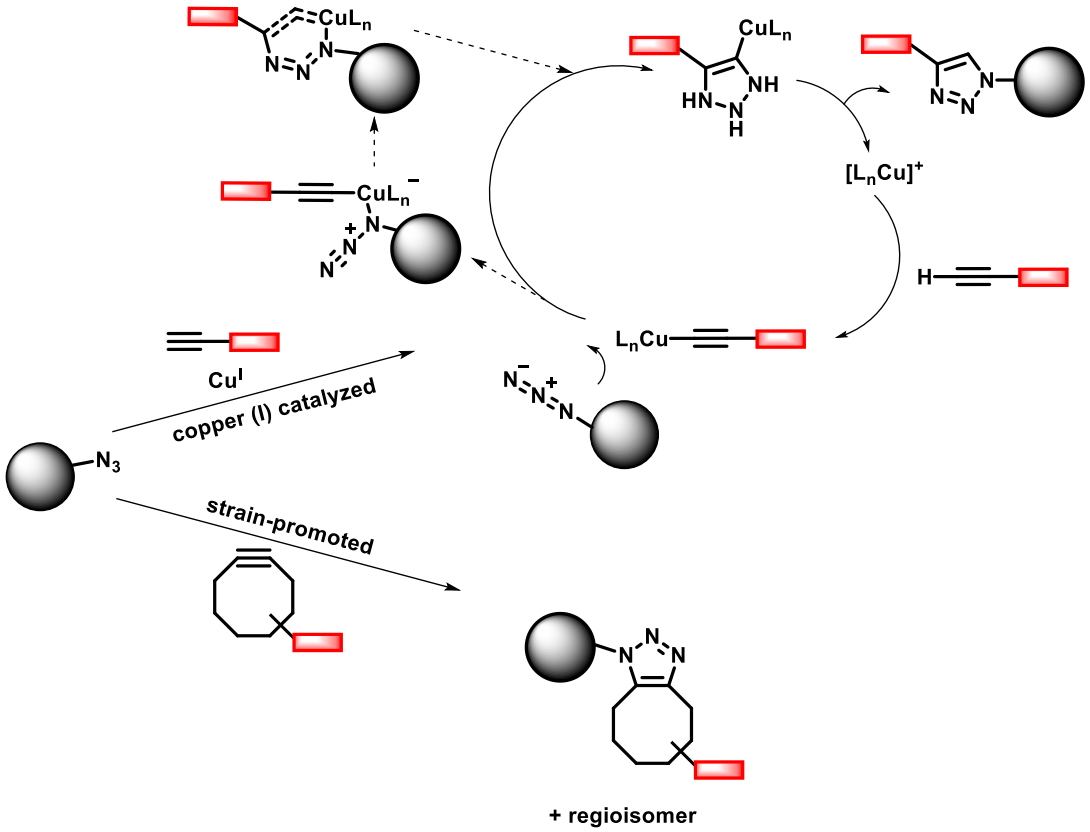

Scheme 5: 1,3 dipolar alkyne-azide cycloaddition as copper (I) catalyzed reaction with proposed catalytic cycle by Rostovtsev *et al.*[145] and strain-promoted cycloaddition reported by Agard *et al*.[146]

A number of strained cyclooctynes are now available, some of which differ in their reaction rate. Among these DIFO (difluorocyclooctyne) and BCN (bicyclononyne) are popular (Figure 8). The electron-withdrawing fluorines on DIFO are supposed to increase further sensitivity of the SpAAC.[147] Further variations on the alkynes by addition of biaryl groups next to the strained cyclooctyne lead to enhanced strain-energy and therefore accelerate reaction kinetics. Moreover, dibenzocyclooctynol (DIBO) which displayed excellent reaction kinetics and was applied for live-cell imaging[148] and aza-dibenzocyclooctynes were developed.[149,150] There are numerous variations of the latter and they are readily available commercially today as DBCO (dibenzoazacyclooctyne), BARAC (biarylazacyclooctynone) etc. (Figure 8).

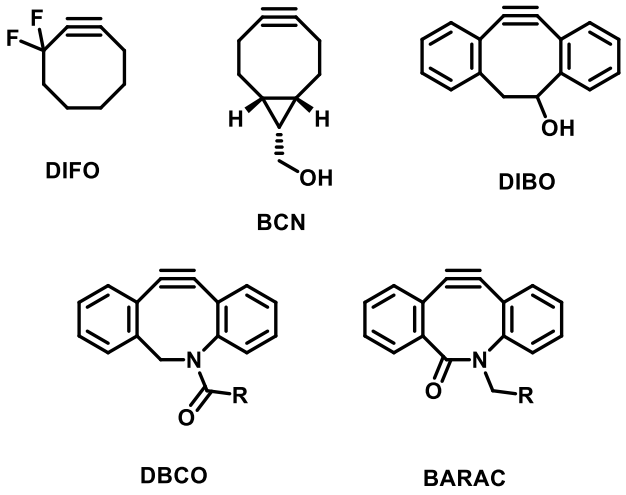

Figure 8: Structures of common strained cycloocytnes for strain-promoted alkyne-azide cycloaddition (SpAAC).

A wide range of specific strained alkynes has been designed which provide accelerated reaction towards cycloadditions in a bioorthogonal manner. However, reaction kinetics of SpAAC remain comparably poor (10^{-2} – 1 M^{-1} s^{-1}).[151] For this reason, it was suggested to also consider the role of the azide in the cycloaddition regarding efficient design for improved bioorthognal labeling. It was found that there are differences in reactivity regarding aliphatic and aromatic azides when they are reacted with the same alkyne.[152] In view of these results, SpAAC could be even further developed to SpANC (strain-promoted alkyne nitrone cycloadditon) which show even better reaction kinetics than the former (k < 30 $M^{-1}s^{-1}$)[151] and showed promising results in protein modification.[153]

II. 2.4 Cellular uptake and trafficking of nanocarriers

Already in 1970 it was observed how particles made out of lipids and synthetic polymers, concentrated inside cells.[154] These observations thus sealed the fate of the nanocarriers for one of their most important use, namely as drug delivery vehicles. Hillaireau *et al.* describe that in dependency on the physicochemical properties and the chemical constitution of the nanocarrier, the internalization happens either in a phagocytic or non-phagocytic pathway.[154] However, phagocytosis is mainly utilized by specific cells such as macrophages, dendritic cells etc. and is preceded by prior opsonization by e.g., the adsorption of blood proteins. Additionally to the chemical composition of the particle surface also size, surface charge and shape play a major role for the uptake by phagocytosis.[155,156] Especially larger particles (250 nm – 3 µm)[156] are mainly taken up *via* phagocytosis and also more negatively charged particles show a higher interaction with the cell surface than uncharged carriers.[154,157]

Non-phagocytic pathways, which include clathrin- and calveolae-mediated endocytosis, are not restricted to certain cell types but can basically occur in every cell. It is, regarding targeted drug delivery, the favorable cellular uptake mechanism since it is not necessarily resulting in elimination of the nanocarriers. Clathrin and caveolin are both proteins and make up the most important components for the respective cell uptake mechanism. Clathrin forms a polyhedron, stabilizing vesicles by coating them. Caveolin is the main structural element of the so called caveolae, which are invaginations of the cell membrane.

Once again, it was shown that the size of the particles is essential for the respective non-phagocytic uptake mechanism, for example with polystyrene particles (40 nm) which were found to be internalized via a clathrin- and a caveolin-endocytic pathway.[158] Also polymeric micelles are found to be usually internalized by clathrin-mediated or caveolae-mediated endocytosis.[159]

Although many examples demonstrate that nanocarrier sizes, shapes and charges determine the nature of cellular uptake, most of the carriers are found to follow the lysosomal pathway as soon as they are internalized, leading to the endolysosomal pathway being the most studied one. First the particles arrive in early/late endosomes and are trafficking to the acidic lysosomes at the end in which they usually undergo degradation. Nevertheless, there are examples which revealed that lysosomal escape mechanisms are possible and favorable to prevent degradation.[160,161] It was shown in the case of RNA delivery that the efficiency was often dictated by the occurrence of endosomal escape.[162,163]

These observations are important in understanding the success or failure of nanocarrier efficacy. Further analysis, such as unambiguous localization of the nanocarriers in specific compartments or the discovery of proteins involved in certain pathways can then provide guidance for more promising nanocarrier syntheses. In the latter, significant steps towards an elucidation of important proteins could already been made by using mass spectrometry approaches.[164]

II. 2.5 Nanocapsules for drug delivery and medical applications prepared by miniemulsion

Polymeric core-shell nanocapsules are elaborate drug delivery vehicles which can be used to transport hydrophilic as well as hydrophobic cargoes. They can be synthesized in a miniemulsion procedure, in which the components to be encapsulated and a polymer or a monomer are dissolved in the corresponding phase. In a direct miniemulsion, the dispersed phase consists of an organic solvent, while an aqueous phase represents the continuous one. Therefore, direct miniemulsions are suitable for the encapsulation of hydrophobic compounds, while hydrophilic materials can be encapsulated in an inverse miniemulsion, in which water is the dispersed phase (Figure 9).The utilization of shear stress by ultrasonication or high-pressure homogenizers enables the generation of stable nano-sized droplets.[165] The droplets are stabilized using a surfactant, which prevents coalescence, meaning the formation of bigger droplets by agglomeration of smaller droplets. By ionic surfactants the stabilization is facilitated by electrostatic repulsion, while by non-ionic surfactants the droplets are sterically stabilized.[166] Due to the increased Laplace pressure of small droplets in comparison to bigger droplets, material from the small droplets tend to flow to the bigger ones, leading to an overall increase of the average droplet size. This process is known as Ostwald ripening and can be avoided when an osmotic agent is added to the dispersed phase, keeping osmotic pressure inside droplets constant.[166,167] To be effective, the osmotic agent must be highly soluble in the dispersed phase.[168]

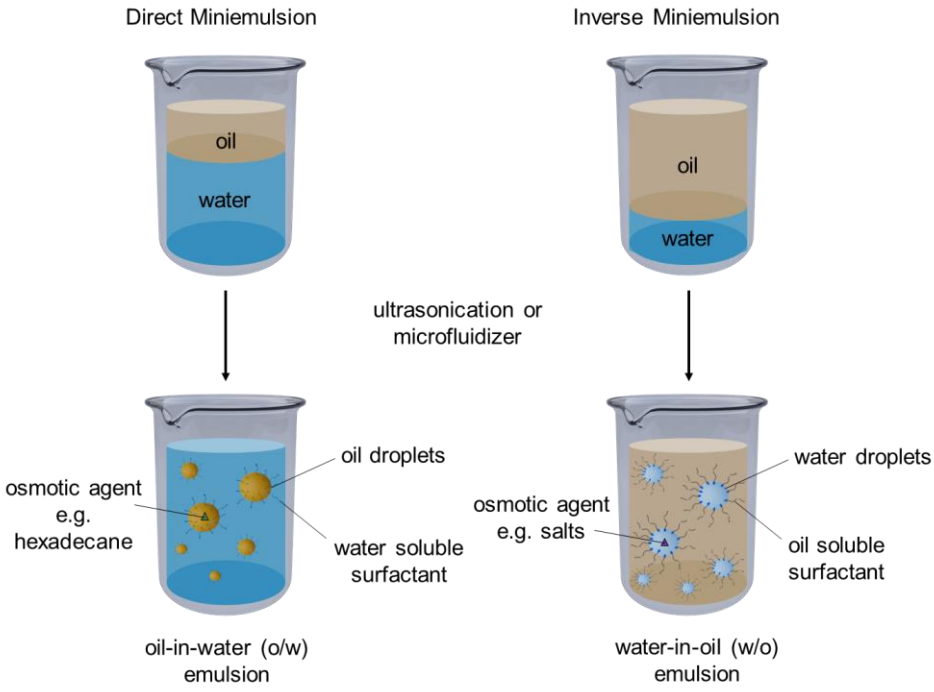

Figure 9: Preparation of oil-in water (direct) miniemulsion and water-in-oil (inverse) miniemulsion.

After generating stable droplets, a dense polymeric shell can be formed by initiating a reaction at the droplet interface. Therefore, depending on which type of miniemulsion is performed and which material is processed, different reactions can be chosen to form nanocapsules (Table 2).

Table 2: Selection of nanocapsules prepared by different materials and reactions in direct miniemulsion (yellow) and inverse miniemulsion (blue) and examples for their applications.

Reaction type	Crosslinker, resp. Initiator/ Polymer or Monomer	Generated material	Examples for applications
Radical (Free radical polymerization)	V59/Styrene	Polystyrene	Triplet–triplet annihilation upconversion under protective conditions[169]
	Potassium peroxodisulfate (KPS)/ Methyacrylates	Poly(methyl methacrylate)	Encapsulation of *α*-pinene[170]
Polycondensation /Polyaddition	Isophorone diisocyanate (IPDI)/ 1,6 Hexanediol	Polyurethane	Nanocapsules with oily core[171]
	Isophorone diisocyanate (IPDI)/ diethylene triamine or dipropylene triamine	Polyurea	Encapsulation of *α*-tocopherol[172]
	Sebacoyl chloride/ Diethylene triamine or Dipropylene triamine	Polyamide	
Bioorthogonal	bis(propargyloxy)butane/6,6′-diazido-6,6′-dideoxysucrose/ Cu (I)	Glycopolytriazoles	Biocompatible nanocapsules with oily core[173]

Reaction type		Crosslinker, resp. Initiator/ Polymer or Monomer	Generated capsule material	Examples for applications
Radical	Reversible-addition-fragmentation chain-transfer polymerization (RAFT)	AIBN/Methacrylates, Methacrylamide	Poly(*N*-(2-hydroxypropyl) methacrylamide)	Encapsulation of gemcitabine[174]
	Free radical polymerization (FRP)	Ammonium persulfate (APS) & AIBN/ *N*-isopropyl acrylamide & *N*, *N*′-methylene bis(acrylamide)	Poly(*N*-isopropylacrylamide)	Thermosensitive nanocapsules[175]
Polyaddition		Toluene diisocyanate (TDI)/ HES or Protein	Polyurethane/ Polyurea	Surface functionalized nanocapsules[176]/ Encapsulation of adjuvants[107]
Polycondensation		KF/ Silanes (TMS & APTMS) and Tetraethyl orthosilicate (TEOS)	Silica	Encapsulation of enzymes[177]
Bio-orthogonal	Electrophilic aromatic substitution (EAS)	Triazolinedione (TAD)/Protein	Protein-TAD adduct	Biodegradable capsules with specific protein surface[178]
	1,3 dipolar cyclo-addition	Dialkyne/hyaluronic acid (azide-modified)	Hyaluronic acid-triazole adduct	Glutathione responsive nanocapsules[179]
Ionic (anionic)		Alkyl cyanoacrylates	Poly(n-butyl cyanoacrylate)	Encapsulation of oligonucleotides[180]

As already pointed out in Table 2, nanocapsules can be utilized in a variety of applications and their synthesis can be easily adapted using the versatile miniemulsion technique. Not only cargo and shell material can be varied during nanocapsule synthesis, but also individual features such as shell thickness, permeability and surface functionalities can be manipulated, providing the nanocarriers with new properties. Thus, it could be shown that permeability of polyurethane nanocapsules is not only dependent on the thickness of the nanocapsule shell and therefore on the amount of monomers used, but furthermore on the crystallinity of the involved polymers.[181]

Drugs, especially cytostatic ones, should only be able to be released at their destination otherwise the special advantage of packaging is useless. Thus, the shell of nanocapsules should be dense and not release even small molecules. Model molecules, preferably dyes, can be used to determine whether molecules of a certain molecular weight can diffuse out of the capsule and therefore in this way it can be determined if the synthesis needs further improvements and optimizations. Nevertheless, it is sometimes desirable to design a nanocapsule shell that is porous and allows substances of certain size to diffuse out. Thus, an exchange of water molecules can be advantageous for nanocapsules encapsulating MRI contrast agents.[182]

II. 2.6 First steps towards improved clinical translation of nanomaterials – a short overview and suggestions

As already mentioned in the Motivation, there is an urgency to improve the translation of nanomaterials into the clinic. The number of publications on novel nanomaterials exhibiting specific properties demonstrates that there is no lack of ideas, but rather a lack of feasibility to bring the nanomaterials into their field of use. There are mainly three approaches discussed in the literature to be implemented in order to overcome the current obstacles:

1. A smarter characterization of nanocarriers and standardization of measurements as well as data evaluation. A standardized characterization is common practice for small molecules, however, the same characterization methods cannot always be applied to the same extent for nanomaterials, since from a physicochemical point of view they are considerably more complex. For this reason, other unified methods need to be developed to enable a more precise characterization and to make nanomaterials more comparable with each other.

2. The structure-effect relationship between biological, chemical and physical properties, as well as immunocompatibility. There is still too little knowledge about how physicochemical parameters such as size, charge, morphology, hydrophilicity, binding constitution and more affect biological responses regardless of the effects intended by targeting or stealth coating.

3. Specific regulations and toxicological assessments adjusted to nanomaterials. In the field of small molecules and pharmaceutical drugs, toxicological terminology such as LD_{50} (median lethal dose), NOEL (no observed effect level) etc. are established terms. However, the question arises if toxicological data determined for a substance are valid if the substance is associated to a nanomaterial. Moreover, there is still much to be learned about how the intrinsic nature of a nanomaterial alone should be evaluated from a toxicological perspective.

Khorasani *et al.* suggested standard sets for nanocarrier characterization. These include detailed characterization of starting materials and synthesized polymers, prior to nanocarrier synthesis, and the use of the same material batches.[183] Furthermore, the use of the same equipment for the same synthesis steps and the same measurement settings. For instance, nanocarrier size distributions can be averaged in several ways. Based on the recommendations of the US National Characterization Laboratory, Khorasani *et al*. suggest considering an intensity-weighted distribution for light scattering measurements instead of number- or volume-weighted distribution.[183] Dependent on the distribution type, the results can vary significantly. In a number-weighted distribution the signals obtain equal weighting, independently of the size of the particles. This in turn leads to a highlighting of smaller particles, compared to the analysis using the other distributions. In a volume-weighted distribution, the relative signal is proportional to the size of the particle, while in an intensity-weighted distribution, the contribution is proportional to the scattered light.

All types of distributions are useful in different contexts, however, for the same characterizations of different samples, the same distribution should be considered. A unification is therefore important, since it is widely reported, that the particle size and dispersity seem to play a crucial role in translation.[184,185]
The analysis of the nanocarrier's surface displays a specific challenge. Since there is a large variety of different nanocarriers composed of different materials, shapes and sizes, there is consequently a large variety of surface compositions and chemical identities. Hence, there is no universal technique for the detection of surface groups and their distribution. Well-established and sophisticated methods, such as NMR are reaching their limits here, since they are just suitable for the detection of flexible terminating groups attached to the nanocarrier. Therefore, more elaborate and combinatorial approaches have to be used in order to give a higher significance to the chemical identity of the carriers. Again, Khorasani *et al.* suggest the use of more complex methods such as the use of specific microscopy techniques that should elucidate more about the three-dimensional structure of the nanocarrier.[183] Fregnaux *et al.* propose a combinatorial approach such as the use of mass spectrometry combined with TEM analysis, exemplarily demonstrated on CdSe quantum dots, to elucidate the relationship between size and chemical composition for inorganic particles.[186]
Assay-based approaches are often used to determine molecules such as fluorescent labels attached to the surface. However, the ways how the assay is evaluated significantly influences the result. Here, too, it is advisable to analyze the results using standardized procedures or at least to include the type of evaluation performed.
Surface modifications on nanocarriers for drug delivery are usually designed to increase blood circulation time and enable specific targeting.[187] PEGylation of nanocarriers in order to reduce clearance, has been proven to be a successful strategy, however recent studies reveal that the stealth effect induced by PEG is influenced by the conformation and grafting density of the polymer.[188,189] Thus, a simple quantification of PEG chains is no longer sufficient to precisely predict elimination of the nanocarriers, but complex NMR analyses must be performed to illuminate such conformations. The analysis of the protein corona is a field that has grown rapidly in recent years and has shown the importance of combinatorial analysis of chemical, physical and biological properties in colloidal- and nanoscience. For example, it is now known that a dynamic protein corona forms around a nanoparticle, depending on what material the particle is made of.[190–192] The corona can undo previous efforts to design the particle as efficient as possible, for example by masking covalently attached ligands with proteins of the protein corona.[193] These findings demonstrate that we are just at the beginning of understanding the interaction of designed material properties and biological results.

For regulatory purposes, more than for scientific ones, specific definitions for a particular material are essential. However, nanomaterials are until today still very poorly defined and classified.[194] For instance, Boverhof *et al.* found that there are inconsistencies of the definition of "nanomaterial" e.g., for size limitations at different national organizations.[195] Such fundamental incoherencies make reliable standardization of nanomaterials impossible and thus impair translation.

For this reason, the mentioned concerns of poor characterization seem to reach a much greater significance than first suspected, because a precise classification and thus a precise definition can only be given when the material is properly characterized. Therefore, it can be said, that proper characterizations precede uniform definitions which precede regulations.

Another emerging field of nanomaterial regulation is the assessment of risks associated to the use of nanomaterials. So far, just a few researchers have investigated risk perceptions of engineered nanomaterials.[196] However, the growing field of nanotoxicology shows the need for a specific evaluation of nanomaterials apart from small molecule toxicology.[197,198] This is especially in the interest of companies that produce the materials. Hofmann-Amtenbrink *et al.* therefore propose to introduce a special “standardized nanosafety research strategy” for pharmaceutical companies in order to simplify discovery of promising nanoparticulate formulations and for a faster elimination of candidates which show toxicity in the course of evaluation.[199] Looking at the regulations so far, it once again gets clear, that there is still a lot of room for improvement

III. Characterization methods

III. 1. Dynamic light scattering (DLS)

The principles described in this section are adapted from reference[200].

Dynamic light scattering (DLS) is the most common technique for the determination of the size and the dispersity of colloidal systems. It is based on the principle that an electromagnetic wave is creating an oscillating dipole when reaching a molecule, emitting the wave back in the same wavelength (elastic scattering). However, for nanoparticulate systems, exhibiting particles $d > \lambda/20$, there are several of oscillating dipoles per particle, resulting in interference of the scattered wave and therefore leading to angle-dependency of the intensity of the scattered light. For particles $d < \lambda/20$, the resulting interference is inconsiderable and is therefore independent on the scattering angle.

However, it must be considered, that particles are moving within their dispersant (Brownian motion). This leads to fluctuations in interparticle positions and correspondingly to changes in temporal concentrations within the dispersion, resulting in changes of the scattering intensity within time. By using an autocorrelation function, the fluctuations can be converted leading to a time-dependent intermediate scattering function. Since the Brownian motion of particles is furthermore dependent on the dispersant, such as viscosity, and on the temperature, these specific parameters are crucial for the determination and must be specified individually. The obtained diffusion coefficient is associated to the hydrodynamic radius by the Stokes-Einstein equation (Eq. 1):

$$D_S = \frac{k_B T}{6\pi\eta R_h} \qquad \text{(Eq. 1)}$$

With D_s = the self diffusion coefficient

k_B = Boltzmann constant

T = temperature

η = viscosity

R_h = hydrodynamic radius

Light scattering can be used to obtain the hydrodynamic radius of a particle (Eq. 1) and to obtain information about the dispersity of the sample. However, the method can also be used to obtain information about the concentration of the sample, as the intensity of the scattered light correlates linearly with the concentration of the particles in the sample. This approach is presented in Chapter A IV. 2.3. Figure 10 displays a schematic dynamic light scattering setup.

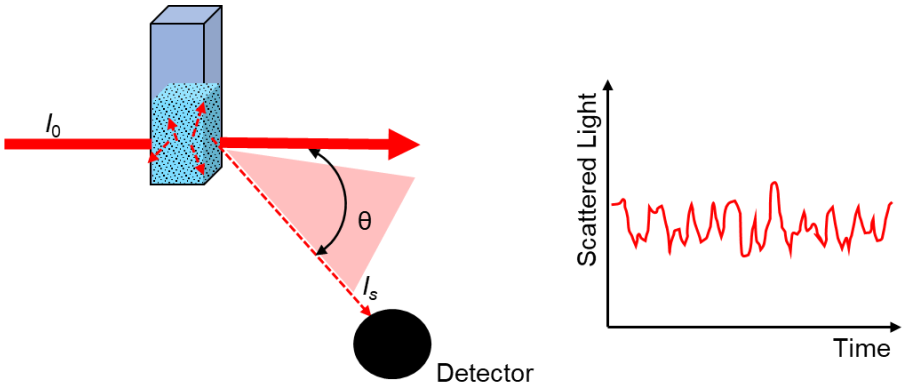

Figure 10: Dynamic light scattering setup at an angle θ, with I_0 as the intensity of the initial light beam, I_s as the intensity of the scattered light beam. Fluctuations of the intensity of the scattered light are recorded as function of time. Adapted from reference[200] with permission from Springer Link © 2007.

III. 2. Zeta potential

The zeta potential (ζ potential) is used to determine the electrophoretic mobility of particles in suspensions. If two phases, such as a solid interphase of a particle and the liquid interface of the dispersant, are in direct contact, the charges directly associated with the interphases separate and an electrostatic potential occurs.[201] According to the theory of Otto Stern, there is one layer of ions which is rigidly associated at the interface and a second layer which consist of oppositely charged ions attracted by the ions of the first layer binding diffusely (Stern double layer).[202] Since the potential which is directly associated to the interface (Nernst layer) cannot be determined, the Stern layer is the basis of particle charge analysis. During the zeta potential measurement, an external potential is applied across which the particles migrate (electrophoresis). During movement of the particles only rigidly associated ions will move, too, while loosely bound ions will not move with the particle. The potential caused by the displacement, is the so-called zeta potential. For the determination, the velocity of the particles is measured during their migration to the oppositely charged electrode and by applying the Smoluchowski fit, the zeta potential can be obtained. This technique is called laser Doppler velocimetry. As charge determines the properties of the material, the measurement of the zeta potential is particularly interesting for the characterization of particles. Adsorbed molecules, such as surfactants as well as charged surface groups can influence the zeta potential and their presence can therefore be analyzed qualitatively. Moreover, the stability of the dispersion can be analyzed since electrostatic repulsion is necessary for the stability of particles towards coagulation.

III. 3. Basics of analyte quantification by colorimetric assays

Colorimetric assays are widely applied for quantitative and qualitative analysis in all kinds of scientific disciplines. They are based on the detection of a functional group, a biomolecule such as metabolites, proteins, carbohydrates, DNA/RNA, reactive species (e.g., ROS), antigens or antibodies by means of a secondary reagent. The reaction of the corresponding species with the reagent leads to a specific signal, such as the absorbance of light at a specific wavelength, the emission of fluorescence, luminescence at a certain wavelength or radioactivity. In the case of living organisms such as cells, assays can also be used to indicate the viability state of the cells and indicate proliferation or apoptosis.

Absorbance- and fluorescence-based assays are usually easy to handle and offer a high sensitivity depending on the analyte, leading to extremely low amounts of analytes necessary for the detection. In addition, these forms of assays can be easily standardized, as they can often be read out in microplate readers. Especially in biological and pharmaceutical fields such assays are applied very frequently, as many of them are commercially available fully equipped as kits. Nevertheless, the result of the assay-based analysis strongly depends on the proper detection of the analyte. For this reason, the terms limit of detection (LoD) and limit of blank (LoB) were introduced, which are important to define the lowest concentration of the analyte which can reliably be detected by the used procedure.[203]
Therefore, the LoD and the LoB serve as detection threshold to differ obtained signals from the distribution of instrument noise and to avoid false positives.[204]
The LoB is defined as "the highest apparent analyte concentration expected to be found when replicates of a sample containing no analyte are tested:"[203,205]

$$LoB = mean_{blank} + 1.645(\text{standard deviation}_{blank}) \quad \text{(Eq. 2)}$$

The LoD is defined as "the lowest analyte concentration likely to be reliably distinguished from the LoB and at which detection is feasible:"[203]

$$LoD = LoB + 1.645(\text{standard deviation}_{\text{low concentration sample}}) \quad \text{(Eq. 3)}$$

With the assumption of a Gaussian distribution, the represented LoB shown in Eq. 2 include 95% of the measured values. With the same assumption, the LoD represented by Eq. 3 will result in a threshold exceeding the previously determined LoB by 95%.[203]
However, Armbruster *et al*. suggested using at least 20 replicates to verify the parameters.

III. 3.1 The principle of immuno assays - ELISA

In immuno assays the analyte is usually detected using an antibody or an antigen, which is labeled by a dye[206], an enzyme which converts a substrate triggering the signaling[207] or a radiolabel[208]. More recently also immuno assays based on label-free techniques such as SPR[209], Raman spectroscopy[210] and others are found.
Nowadays the enzyme-linked immunosorbent assay (ELISA), which was presented for the first time in 1971[211], is a popular technique and is widely applied in several variants (direct/ indirect – sandwich).
In this work, a sandwich ELISA is applied for the detection of IL-2 on the capsule surface.
Therefore, an anti-IL-2 antibody is fixed on the bottom of a well plate and unspecific binding sites are blocked by a specific blocking buffer. Upon addition of the sample, the analyte will be captured by the fixed antibodies and another antibody exhibiting a different epitope, which is labeled with the enzyme horseradish peroxidase is added. After addition of the horseradish peroxidase substrate tetramethylbenzidine and hydrogen peroxide, the enzyme converts the substrate, and a detectable dye can be read out.

III. 4. Nuclear magnetic resonance (NMR) spectroscopy

NMR spectroscopy is one of the most important analytical methods to gather the structural information and gain insights into the dynamics of molecules. It is based on the principle that the magnetic moments of atom nuclei align when a strong external magnetic field is applied. A short radio frequency (RF) pulse is applied to disturb this ordered state and during the following decay the emitted frequencies are detected. With the help of Fourier transformation, the detected time-dependent signal can be converted into the frequency domain. Comparison of the frequencies to a standard reference gives the chemical shifts which are generally known as the NMR spectrum. The energy necessary for the spin resonance is dependent on the electronic surrounding of the nuclei and is apparent from the chemical shift in the spectrum. Even more information about the molecule can be obtained when 2D NMR spectroscopy is performed. Here, multiple complex RF pulses are applied to transfer magnetization to adjacent nuclei. The resulting spectra are plotted as a plane with two axes which either depict the frequency of the same nuclei, such as ^{1}H (COSY, TOCSY etc.) or two different nuclei (e.g., HSQC or HMBC for ^{1}H and ^{13}C). HSQC identifies correlations of nuclei which are connected by one bond, while HMBC identifies correlations connected by multiple bonds (up to 4). Since not every nucleus has the same sensitivity towards spin resonance (high or low Boltzmann population), the signal can be enhanced in a special procedure in which magnetization is transferred from the first nucleus to the second and then reverse. This magnetization transfer (INEPT pulse) is used during HSQC measurements in which a series of magnetization transfers is recorded resulting in the 2D spectrum.

III. 5. Mass spectrometry

Next to NMR spectroscopy, mass spectrometry is equally relevant as tool for modern structure analysis. In this technique a mass-to-charge ratio of fragmented analyte can be determined. Depending on the molecular weight, structure and morphology of the analyte, different kinds of mass spectrometry techniques can be applied.

III. 5.1 Matrix assisted laser desorption ionization – Time of flight (MALDI-ToF)

In MALDI-ToF the analyte is embedded in a crystalline matrix, such as *α*-cyano-4-hydroxycinnamic acid and is afterwards ionized by a laser, leading to vaporization of the sample (desorption process).
By applying a high voltage, the ions are accelerated and are afterwards detected by a ToF (time of flight) analyzer. The linear ToF analyzed can be combined with a reflectron, diverting the ions which impinge at a second detector, leading to a higher resolution than in the linear mode. Lighter-mass molecules arrive earlier at the detector than higher-weight molecules, leading to a direct correlation of observed peaks to the corresponding masses. MALDI-ToF can be widely applied and is also suitable for the detection of higher molecular weight molecules such as proteins.

III. 5.2 Time of flight – Secondary ion mass spectrometry (ToF-SIMS)

In ToF-SIMS, the surface of a sample is bombarded with primary ions, i.e., a pulsed Bi_3^+ ion beam, leading to the desorption of secondary ions from the first atom layers of the sample.

These secondary ions, which can be neutral, positively or negatively charged, are extracted and detected by a ToF analyzer. The obtained information can be used to analyze molecular conformations and distributions of the sample. Data analysis is complex, since in every pixel a full mass spectrum is incorporated from which successive ion images can be obtained. Due to the high resolution and the high specificity for the first layers of the sample, the technique provides an accurate mapping of the surface (Figure 11).

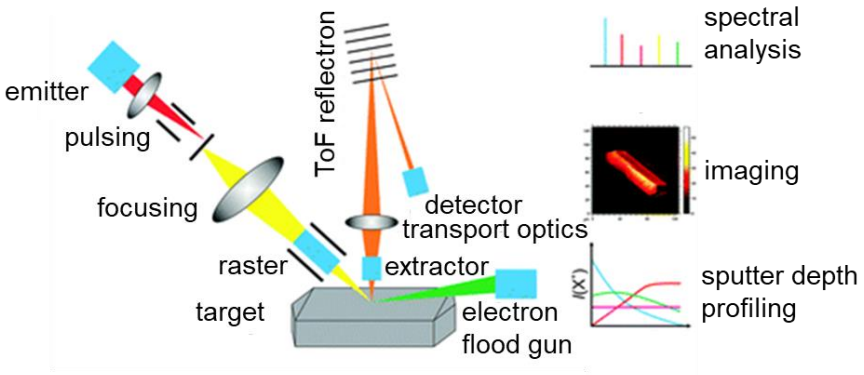

Figure 11: Basic principle of the ToF-SIMS device with subsequent surface and bulk analysis. Reproduced from reference[212] - Published by The Royal Society of Chemistry.

III. 6. Nano differential scanning fluorimetry (nanoDSF)

NanoDSF is a technique to determine protein stability and alterations in protein conformation. It is based on the fluorescence measurement of tyrosines and tryptophans at 330 nm and 350 nm in the respective proteins. During the measurement, the sample is continuously heated in a uniform slope, leading to the unfolding of the protein. This unfolding leads to a transformation of the protein structure, exposing amino acids which are usually buried in the interior of the protein, and hence leading to a temperature-dependent change in fluorescence intensity of the sample. By plotting the first derivative of the fluorescence intensity against the temperature, a melting point T_m, which demonstrates the maximum intensity, can be determined. Such protein stability measurements are important, when chemical modifications on proteins are performed or detergents such as surfactants are used which have been shown to influence protein structures.

The particular advantages over CD spectroscopy are the small sample volume (ca. 10 µL of diluted protein solution) and the high throughput by simultaneous measurement of up to 48 samples at once independent on their protein concentrations.

III. 7. Flow cytometry

Flow cytometry is often used in the context of FACS (fluorescence-activated cell sorting) however, this technique does not necessarily have to be applied to cells, but it can also be applied to particles of a certain size. In flow cytometry, the fluorescently labeled particles (or cells) are focused using a constant liquid flow, which allows them to pass through a channel one by one. During the single passing, they cross a laser beam, emitting light at a particular wavelength.

The fluorescence signal is sensed by detectors using suitable filters and to which usually a photomultiplier for signal amplification is connected. Next to a fluorescent signal also scattered light is detected by forward (FSC) and side scatter (SSC). The forward scatter detector is located in a small angle distance to the sample, providing results about the size and the volume of the detected object. The side scatter detector is placed perpendicular to the laser and is therefore detecting orthogonal light scatter. With the side scatter, information about the complexity of the sample (such as granularity of the cells) is obtained. By plotting the detected events of the forwards scatter on the x-axis and the events of the side scatter on the y-axis, a comprehensive impression of the sample composition can be obtained. The possibility to select certain subpopulations and exclude others (gating), enables analysis of the fluorescence intensity of the objects of interest.

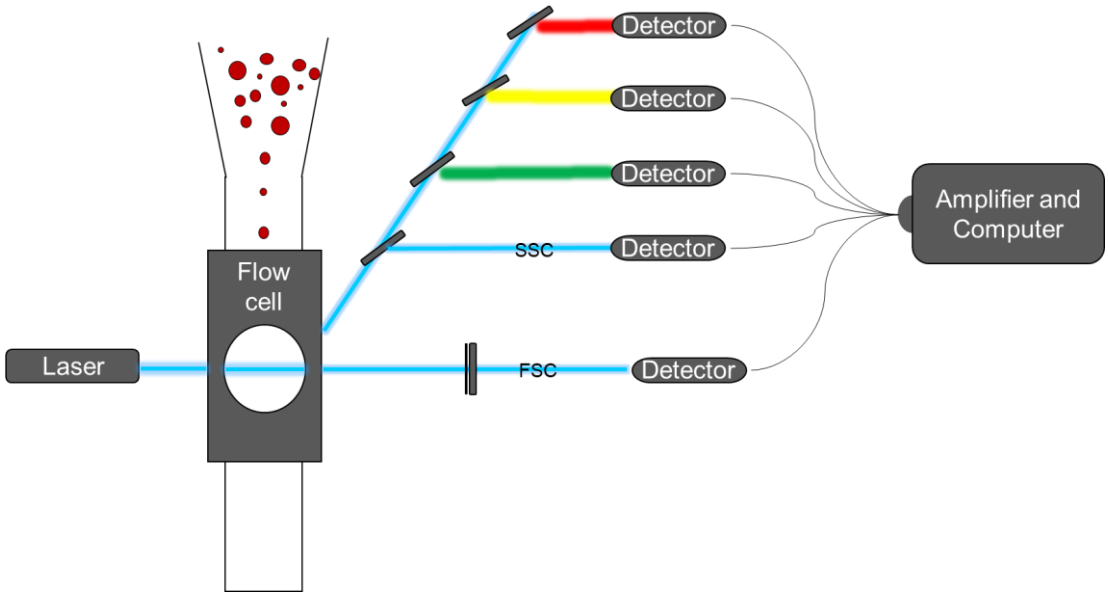

Figure 12: Schematic representation of the flow cytometry setup.

III. 8. Fluorescence correlation spectroscopy (FCS)

In FCS, time-dependent fluctuations of the fluorescence intensities of molecules or particles are measured. Since the components of the sample have to pass through a specific observation volume in which the detection takes place, temporal changes in fluorescence can be detected. This means that the fluorescence of the object can be detected according to the diffusion time, which gives information about the size, concentration as well as specific fluorescence characteristics of the sample. The most important parts of the experimental setup are a very sensitive confocal microscope, a laser, exciting the molecules in the sample and a single photon sensitive detector. The intensity changes are converted into an autocorrelation function and similar as for DLS, the diffusion times and also the hydrodynamic radii using equation (Eq. 1) can be obtained. FCS is a very sensitive method since it detects a small number of molecules in a small observation volume.

A modification of the classical FCS is FCCS (fluorescence cross correlation spectroscopy).

With the help of FCCS, information about the interaction of two fluorescence signals can be obtained, enabling analysis of i.e., binding kinetics of a system. For employing FCCS, two lasers and two single-photon detectors need to be utilized.

III. 9. Isothermal titration calorimetry (ITC)

ITC enables analysis of different biomolecular interactions, i.e., ligand-receptor binding, by measuring the heat transfer during binding. The device is constructed of two cells, from which one is a reference cell and filled with water, while the other cell is the measuring cell, which contains one of the binding components. Both cells are kept at a constant temperature, regulated by the instrument. With a stirring syringe, the first component placed in the measurement cell is constantly stirred, while the second binding component is automatically added into small steps by the syringe into the measurement cell, in order to react with the first component. Upon binding of the two components, temperature sensors detect temperature differences between the two cells since the binding occurring in the measurement cell will either produce heat (exothermic reaction) or withdraw heat from the system (endothermic reaction). The instrument compensates for the temperature differences keeping the same temperature conditions at all times. While adjusting for the temperature change, the instrument records the heat or cooling rate which is necessary to return to the initial temperature. The raw data are depicted as time-dependent heat rate. Usually, the heat rate produced upon dilution of the second component, which is placed in the syringe, in the solvent located in the measurement cell needs to be considered. For this reason, the stepwise titration of component 2 into the measurement cell will be measured as reference and subtracted from the data obtained for the initial measurement or neglected if the heat rate is considerably low.

For data analysis different fit models can be applied. In this work, all data was analyzed using the fit of an independent model[213,214] (Eq. 4), assuming that a ligand L is binding independently to one site of a macromolecule or particle M without interference with other binding sites (cooperativity):

$$\Delta \mathrm{q} = \left(\frac{(n[M]K_a + [L]K_a + 1) - \sqrt{(n[M]K_a + [L]K_a + 1)^2 - 4n{K_a}^2[M][L]}}{2K_a} \right) - [ML]_{n-1}\Delta \mathrm{H}\Delta V_{cell} \qquad \text{(Eq. 4)}$$

A great advantage of this technique is the simultaneous determination of parameters such as binding constant (K_a), enthalpy (ΔH), entropy (ΔS) and stoichiometry (n). [M] represents the concentration of the macromolecule or particle, [L] represents the concentration of the ligand and [ML] is the concentration of the complex. ΔV_{cell} represents the volume change upon ligand addition. To obtain the entropy change ΔS, the Gibbs-Helmholtz equation (Eq. 5.2) has to be solved using the binding constant obtained from equation (Eq. 4):

$$\Delta G = -\mathrm{RT} \cdot \ln K_a \qquad \text{(Eq. 5.1)}$$

$$\Delta G = \Delta H - T \cdot \Delta S \qquad \text{(Eq. 5.2)}$$

$$\Delta S = R \cdot \ln K_a + \frac{\Delta H}{T} \qquad \text{(Eq. 5.3)}$$

IV. Results and Discussion

Chapter A - Multi-step surface functionalization of hydroxylethyl starch (HES) nanocapsules: awarding of targeting structures by controlled binding

Section 3.2 (page 98-106) are based on the paper “Multivalency Beats Complexity: A Study on the Cell Uptake of Carbohydrate Functionalized Nanocarriers to Dendritic Cells” published in Cells, 2020, 9, 2087. Reproduced from Ref[215]

[redacted] synthesized and characterized all carbohydrate structures. I, Marie-Luise Frey, synthesized and characterized the HES-NCs, surface-modified and quantified the DBCO groups by means of an anthracene azide assay, evaluated together with [redacted] the HPLC analysis and evaluated together with [redacted] the cell uptake experiments.

Sections 2, 3 and 4.1 presented in this chapter are part of the manuscript:

[redacted]

manuscript in preparation.

I, Marie-Luise Frey, synthesized the HES-NCs, performed the surface functionalization, performed all the characterization experiments on the HES-NCs and performed quantification of the DBCO groups. Furthermore, I performed bioconjugation and protein stability experiments on IL-2. [redacted] performed ELISA and the CTLL-2 proliferation assay. [redacted] performed ELISA experiments. [redacted] performed FCS and FCCS measurements.

IV. 1. Introduction

Reproducibility of the desired biological effect is decisive for the therapeutic success of a drug and therefore a constant quality of the product is essential.[216]

Constant quality of a compound is achieved by meticulously complying with every single step of the synthesis process and through accurate reporting of every single change in the procedure.[217] In standard operating procedures (SOPs), synthesis processes are described in great detail and guidelines for implementation and exact documentation are established, which leads to a high degree of consistency of product batches.[218] However, the application of standardized protocols for the production of nanocarriers for drug delivery is not common.[183,219,220] This seems surprising, considering that nanocarrier syntheses require many steps, each of which is highly process dependent, demanding detailed documentation.[221]

From a chemical point of view, a defined biomodification of the surface of a nanocarrier is very challenging, as it depends on many factors that have been determined in earlier synthesis steps, such as size, surface charge, functional groups, or properties of the material itself.[222–224] Hence, from a biological point of view, maintaining a constant biological response of biomodified nanocarriers must consequently depend on the previously performed synthesis steps.

To understand the parameters of the synthesis that are essential for a defined biological effect, we modified in our model system the surface of hydroxylethyl starch (HES) nanocapsules (NCs) with Interleukin-2 (IL-2) and in another approach with specific carbohydrate structures to achieve defined immunological effects. We therefore split the synthesis into many small steps, by taking the SOP as a benchmark. We synthesized the NCs in inverse miniemulsion and transferred them into aqueous medium. Afterwards, we surface-functionalized the NCs with dibenzocyclooctyne (DBCO) groups, enabling copper-free alkyne-azide click reaction with azide-modified biomolecules (Figure 13). We analyzed the size of the NCs under different conditions and tested the use of different surfactants for the water transfer. Next to the analysis of the size, FTIR spectroscopy demonstrated chemical stability of the NCs. Analysis of the surface of the capsules by means of fluorescence intensity and mass spectrometry confirmed the hypothesis that nucleophilic amino groups are present on the surface. We revealed the detectability of DBCO groups in many different HES-NC samples and compared them.[225] Thus, we were able to get an overview of the determined averaged groups which are most likely to be found in the different dispersions.

In further experiments we confirmed adjustability of these groups in dispersion and biofunctionalized the HES-NCs according to the calculated DBCO functionalization. All the differently modified capsules showed specific biological functions.

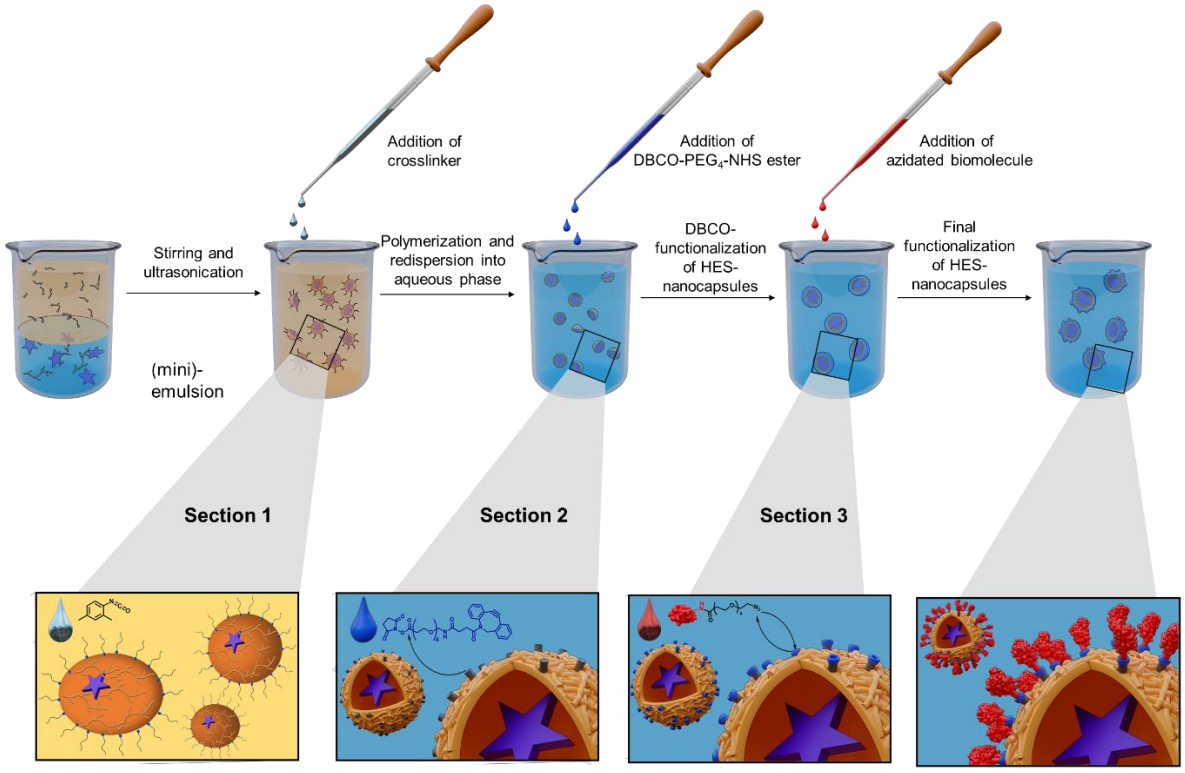

Figure 13: Overview of the stepwise synthesis and surface-functionalization of HES-NCs with biomolecules.

IV. 2. Reproducibility studies of the hydroxylethyl starch nanocapsule (HES-NCs) synthesis by inverse miniemulsion

Hydroxylethyl starch (HES) nanocapsules (NCs) were synthesized by an interfacial polymerization reaction in an inverse miniemulsion. Therefore, HES was added into the aqueous dispersed phase and reacted with toluene diisocyanate (TDI) in a polyaddition at the droplet interphase, generating NCs with hydrophilic core.[103] The stepwise synthesis procedure is depicted in Figure 14.

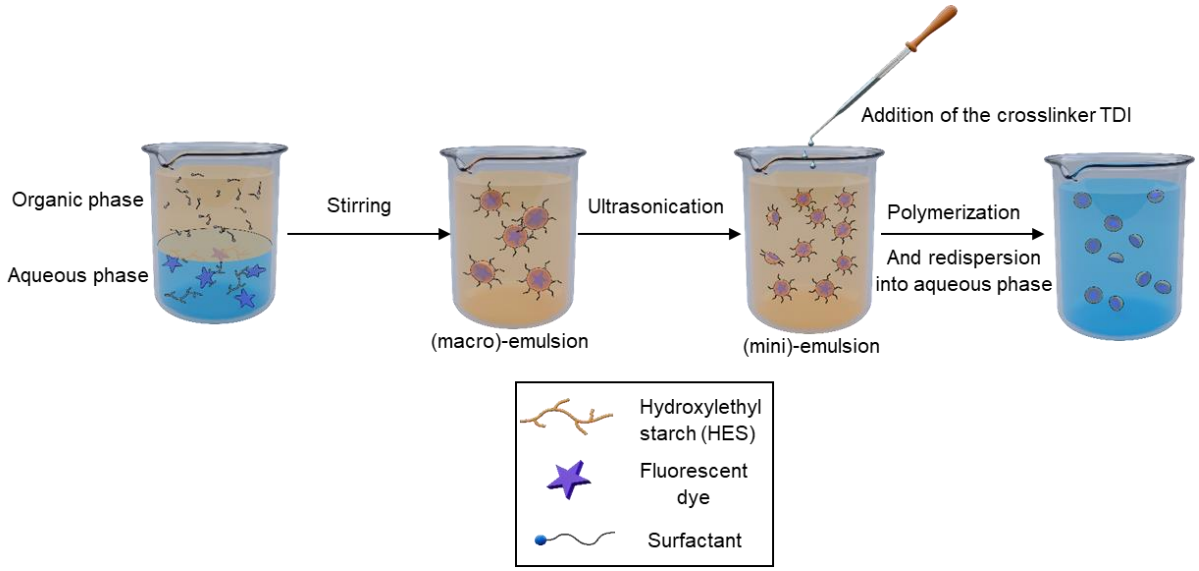

Figure 14: Stepwise synthesis procedure of HES-nanocapsule (NCs) synthesis by inverse miniemulsion.

Since each step influences the subsequent step, it was determined which parameters in the synthesis are crucial for reproducibility studies and which measurements need to be performed to determine reproducibility (Table 3).

Table 3: Synthesis steps and parameters determining reproducibility and performed measurements.

Synthesis step	Parameter	Measurement		
nanocapsule formation in cyclohexane	Long-term stability of the formed NCs, conversion of TDI	FTIR		
	Homogenization method, purification by centrifugation	Size distribution		
		Multi-angle LS	90° LS	
redispersion to water	Capsule size after transfer	LS		
	Amount of surfactant	Colorimetric Assay	Zeta Potential	
	Stability at different pH	LS		
	Solid content and concentration of the NCs	Gravimetric/ LS		
	Encapsulation efficiency of dyes	Fluorescence intensity measurements	cLSM	FCS

IV. 2.1 Nanocapsule formation in cyclohexane

An important requirement for reproducibility is the use of the same chemicals to achieve the same reaction conditions. Therefore, the chemicals used are given in Table 4 and the necessary specifications are listed.

Table 4: Used chemicals and specifications for the synthesis of HES-NCs.

Chemical	Specifications
HES solution (3%)	Sterile from infusion bag
NaCl	Osmotic agent
SR101 or Cy5 Oligo	Fluorescent marker: Cy5 Oligo in RNAse-free water
Cyclohexane	Dried (molecular sieve 5 Å)
poly((ethylene-*co*-butylene)-*b*-(ethylene oxide) P(E/B)-*b*-EO)	Synthesized with a molecular weight of (M_w = 8500 g/mol, with approx. 6800 g/mol of the poly(ethylene-co-butylene) block and approx. 1700 g/mol PEO) determined with GPC
Toluene diisocyanate (TDI)	Stored in freezer and freshly dissolved in cyclohexane

Figure 15 shows the reaction scheme of the polyaddition at the droplet interface during the miniemulsion.

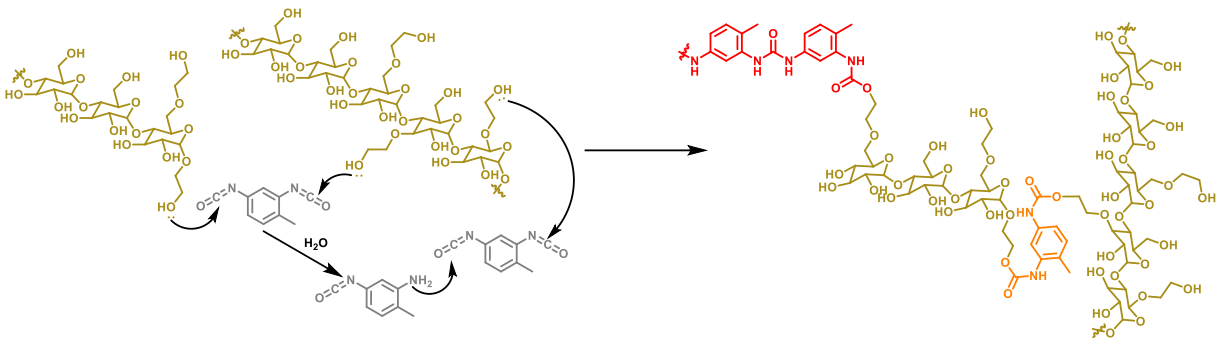

Figure 15: Synthesis of hydroxylethyl starch (HES) nanocapsules (NCs) by inverse miniemulsion. Reaction scheme of HES (yellow ocher) reacting with TDI (grey) forming a polyurethane polymer (orange), or in a side reaction, hydrolyzed TDI reacts with HES forming urea groups (red).

In a polyaddition reaction, the isocyanate groups of the TDI (Figure 15, grey) react with nucleophiles such as the hydroxyl groups of HES (Figure 15, yellow ocher). As a side reaction, TDI also reacts with amino groups which are generated by hydrolysis of TDI in the aqueous emulsion forming polyurethane (Figure 15 orange) and polyurea (Figure 15, red). Polyurethanes, which are typically produced by a polyaddition using TDI, are known for their good stability and toughness.[226] However, colloidal materials such as HES-NCs can have other properties, since during the miniemulsion also urea groups are formed. For this reason, it is important to assess the conversion of TDI during the reaction and therefore evaluate the chemical stability of the NCs in order to determine the time of further processing.

In the continuous organic phase, the capsule surface cannot be chemically altered without the presence of potential nucleophiles. To evaluate the chemical stability of the generated HES-NCs, three different HES-NC dispersions in cyclohexane of different ages were dried and measured with FTIR spectroscopy (Figure 16).

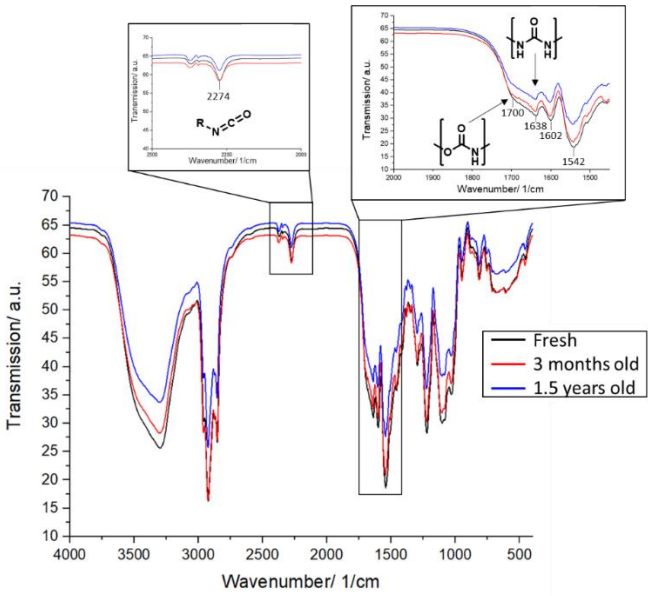

Figure 16: FTIR spectra of dried NC dispersions after storage in cyclohexane for different time periods.

In all the spectra the characteristic vibration for carbonyl containing compounds can be found. The band at 1638 cm^{-1} (C=O stretching, secondary amide, see inlet) is resulting from the polyurea vibration while the band at 1700 cm^{-1} (C=O stretching, see inlet) results from the polyurethane vibration.[227] In all spectra the characteristic isocyanate band is visible (ν = 2274 cm^{-1} , N=C=O stretching). The apprearence of the isocyanate stretch in all dispersions, illustrates that TDI was not fully converted to urethane and urea groups during the polyaddition and was not further converted in cyclohexane phase during the storage time.

By means of FTIR measurements, we show that the dispersions remain chemically stable in organic solvent over 1.5 years, which is fundamental for the further processing of the NCs, since they can be stored over this period of time without chemical alterations such as further hydrolysis of TDI.

However, in aqueous environment a change is detected. As soon as the NCs are transferred to water, an exchange between the inside of the capsule and the external environment occurs. For example, diffusion processes can lead to the release of small encapsulated water-soluble molecules, leading to different concentrations of the cargo or different salt concentration changing the osmotic pressure inside the capsules. Furthermore, in water, biopolymers, such as HES, are able to incorporate water molecules leading to swelling and therefore to size alterations.[228] For this reason, HES-NCs should always be stored in the organic phase before further processing. Next to the chemical stability during storage, especially for nanocarriers, it is also important to assess the colloidal stability.

In the following, DLS measurements are used to analyze the average size distribution of different HES-NC samples and thus shed light on the reproducibility of the synthesis.

IV. 2.1.1 Determination of the capsule size as an indicator for reproducibility

A stable size distribution from batch to batch is an important indication that capsule synthesis is reproducible, because this means that droplet formation in miniemulsion is underlying a repeatable mechanism exhibiting optimal droplet stabilization. An important point to reduce batch-to-batch variance is the use of the same equipment for each synthesis. Especially ultrasonic baths often have strong frequency fluctuations and ultrasonic tips must not show any damages like scratches, which can lead to a change of the surface due to an unequal distribution of sonic waves.

For homogenization of the emulsion, the ultrasonic (US) tip and high-pressure microfluidics can be used, which could lead to different results in the size distribution of the HES-NCs. In addition, the attachment of different dyes either inside the capsule or outside can influence capsule formation.

This section therefore considers the size distribution of NCs according to different parameters and steps performed in the capsule formation of HES-NCs in cyclohexane (Table 5).

Table 5: Different parameters influencing the size distribution of HES-NCs synthesis in cyclohexane and measurements to determine possible alterations.

	Parameter	**Measurement**
Size distribution in cyclohexane	Homogenization using the ultrasonic (US) tip	Multi-angle LS
		LS measurements at 90°
	Homogenization using high-pressure microfluidics	Multi-angle LS
	Encapsulation of different dyes	Multi-angle LS

After synthesis, the HES-NCs were diluted 1:10 with cyclohexane and subjected to light scattering measurements. It is important that the samples are always diluted in the same way, as the concentration of the capsules affects the scattering intensity. Moreover, a too concentrated sample favors the aggregation of the capsules

A precise way to determine the distribution of capsule diameters is to measure light scattering as a function of angle which is shown for HES-NCs prepared using the US tip with SR101 as a marker (Figure 17).

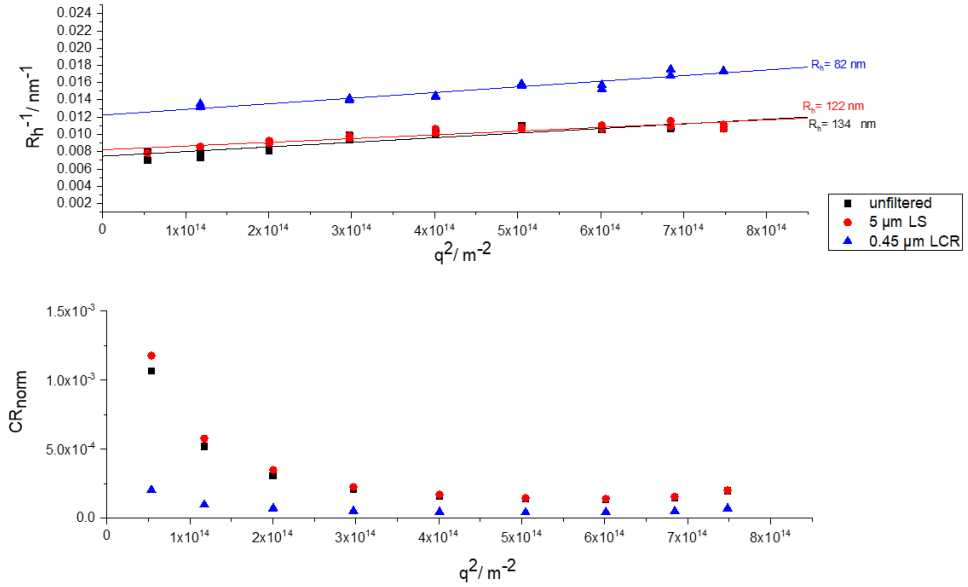

Figure 17: Dynamic light scattering measurement of a HES-NC sample prepared using the ultrasonic tip (MF-020-2) measured at 20°C in cyclohexane. Different filters prior to measurements were used to remove potential agglomerates. Experimental error is 10%. **A:** Angular dependency of the hydrodynamic radius R_h. **B:** Normalized count rate plotted against the scattering angle.

With the reciprocal value of the hydrodynamic radius plotted against the scattering angle, the intersection of the y-axis indicates the average hydrodynamic radius of the sample in an angle-dependent manner (Figure 17). The obtained average hydrodynamic radius of the HES-NC sample is 134 nm (268 nm in diameter respectively) in an unfiltered state. Filtration decreases obtained radii as expected, since bigger capsules and agglomerates are filtered off the dispersion. The normalized count rate (CR_{norm}) plotted against the scattering angle demonstrates potential material loss caused by filtration (Figure 17 lower graph). Hardly any material is separated by filtering through the 5 µm filter, since the plot is similar to that of the unfiltered sample. This also shows that there is no object inside the dispersion with a radius larger than 5 µm. However, filtration through a 0.45 µm filter causes sample separation as depicted in the decrease in normalized count rate. In further light scattering experiments another three independently synthesized HES-NC dispersions with SR101 could be measured in an unfiltered state without showing agglomerates, making measurements impossible.

The average hydrodynamic radius of all the HES-NC dispersions, which did not need filtration prior to measurement and therefore represent optimal HES-NC dispersions is 158 nm (d = 317 nm, n = 4, unfiltered).

In the field of user-friendly instruments for the measurement of particle size by light scattering, measurements at 90° are well suited as a quality check of nanocarriers. Measurements with orthogonal scattering setup are considered to be less prone to errors, since at this angle usually large objects such as dust are excluded from the measurements. In addition, the measurement at one angle saves time. We show the size distribution of 21 HES-NC batches in cyclohexane, which were synthesized independently in time by the same procedure determined at a scattering angle of 90°. The intensities found in the samples were averaged and were depicted as one averaged size distribution (Figure 18, black curve).

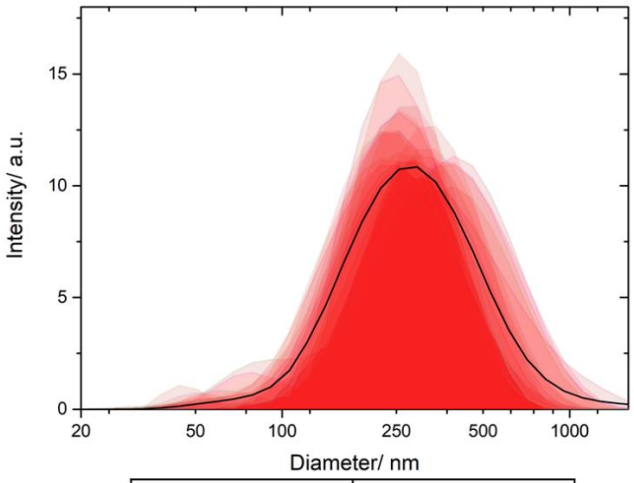

Average NC diameter	Standard deviation
292 nm	± 67 nm

Figure 18: Size distribution of 21 different HES-NC samples prepared using the US tip and labeled with sulforhodamine (SR101). Measured with DLS at a scattering angle of 90°. The averaged size distribution of the 21 size distributions is displayed as black curve.

Figure 18 reveals that similar size distributions for the 21 different HES-NCs batches were obtained. For data analysis, the intensity-weighted size distributions of the individual NCs samples were averaged (Figure 18, black curve), and the standard deviation of the obtained intensity maxima was determined. In this way an averaged diameter of 292 nm ± 67 nm was obtained for 21 individual HES-NCs samples (compare Table Figure 18). The result obtained demonstrates that a simple 90° scattering setup can be used to obtain information if the synthesized NCs reveal comparable results and if the NCs synthesis was conducted in a reproducible manner.

The comparison of both light scattering measurements points, that the simplified 90° light scattering measurement revealed a similar capsule diameter within the specified standard deviation as the advanced multi-angle measurement. Therefore, it was shown that the averaged 90° light scattering measurement is sufficient as a quality check of different HES-NCs batches prepared using the same procedure. However, for a more precise result, the multi-angle measurement should be preferred.

Next to the preparation of the NCs by using the ultrasonic tip, synthesis can be conducted using microfluidic systems.[229] These systems have the advantage that larger synthesis scales can be run at once. In Figure 19 dynamic light scattering of a HES-NC sample, which was again labeled with SR101 and was prepared by high-pressure microfluidics is shown.

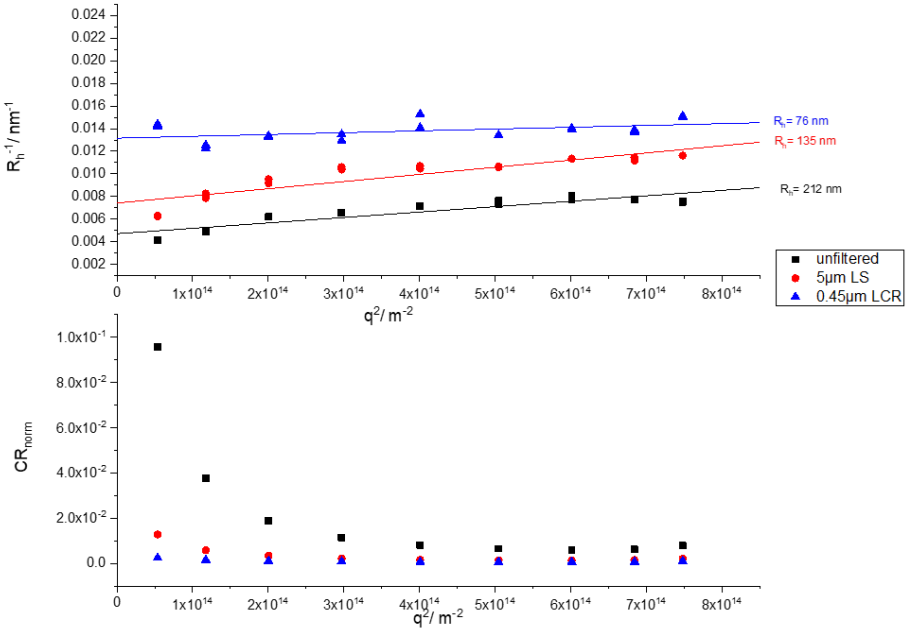

Figure 19: Dynamic light scattering measurement of a HES-NC sample prepared using the microfluidizer (MF-021) measured at 20 °C in cyclohexane. Different filters prior to measurements were used to remove potential agglomerates. Experimental error is 10%. **A:** Angular dependency of the hydrodynamic radius R_h. **B:** Normalized count rate plotted against the scattering angle.

As in Figure 17, the reciprocal hydrodynamic radius is plotted against the scattering angle and reveal a similar decrease of hydrodynamic radii caused by filtration as the sample measured in Figure 17. The average hydrodynamic radius of the HES-NC synthesized by the microfluidizer and without filtration is 212 nm (424 nm in diameter respectively). In comparison to the HES-NC dispersion prepared by using the ultrasonic tip, the obtained sizes are larger. In this case a stronger separation of the material due to filtration was observed (Figure 19, lower graph), since the filtration through the 5 µm filter indicates a more significant decrease in count rate in comparison to the non-filtered sample as this was the case for the HES-NC dispersion depicted in Figure 17. These results support the findings of an overall larger radius for the unfiltered sample in comparison to the radius of the HES-NC dispersion prepared by the ultrasonic tip.

However, the number of emulsification cycles plays a crucial role in the preparation of NCs by the microfluidizer. The sample was homogenized using three emulsification cycles. With increasing the number of cycles, a better homogenization and higher dispersity can be achieved, with an equilibrium being reached after a certain number of cycles. The curve progression after filtration through the 0.45 µm filter again shows a similar result as for the dispersion shown in Figure 17, revealing a comparable size distribution of the HES-NCs to NCs prepared by the US tip after removal of agglomerates.

As described above, the synthesis method and the use of the same equipment is important for the reproducibility of the capsule size. However, sometimes it is necessary to vary the NCs synthesis such as by labeling the NCs with different dyes.

For the measurements described above, all samples were labeled with the dye sulforhodamine (SR101, Figure 20, **1**), a stable, inexpensive dye with a high fluorescence intensity.

SR101 is a derivative of the hydrophobic rhodamine dye which is modified with two sulfonyl groups resulting in an amphiphilic dye, which is highly soluble in water but at the same time also slightly soluble in organic solvents. Due to its low molecular weight, it can leak out of the capsule by diffusion if the pore sizes are sufficiently large in water phase. For this reason, encapsulation and labeling of larger and more hydrophilic dyes is preferred. The dye Cy5 Oligo (Figure 20, **2**) was chosen, since it has a high molecular weight of around 5 kDa, bearing an oligonucleotide sequence. Furthermore, the dye Cy5 was additionally covalently attached onto HES by using an NHS (*N*-hydroxysuccinimid) modified Cy5 derivative (Figure 20, **3**). Afterwards NCs were prepared with the modified HES as well as with the encapsulated dyes and obtained sizes are compared by multi-angle light scattering.

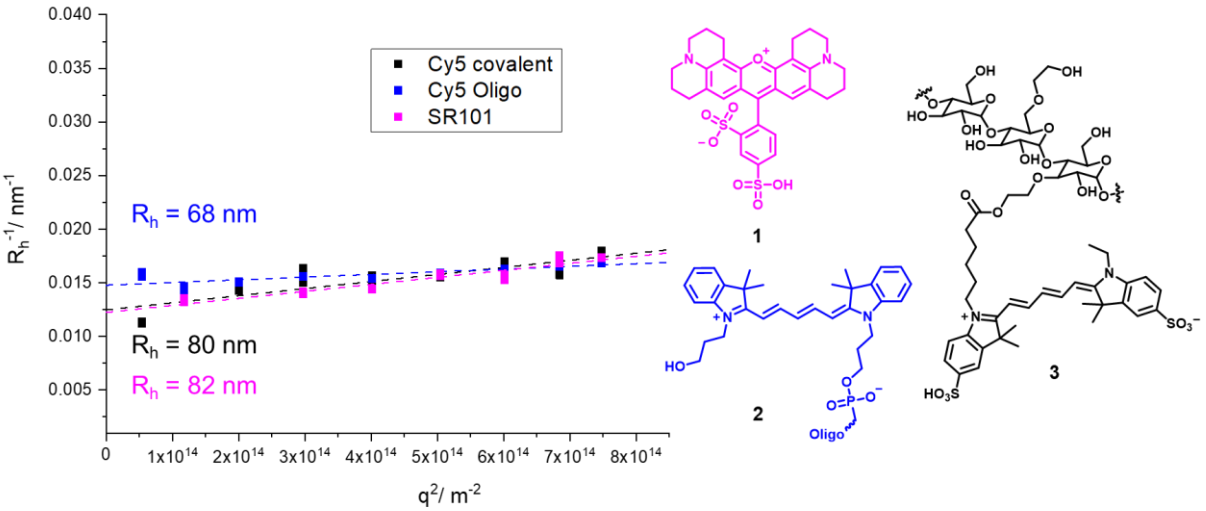

Figure 20: Dynamic light scattering of HES-NC with encapsulated SR101 (**1**) Cy5 Oligo (**2**) and covalently attached Cy5 (**3**), filtered 0.45 µm LCR. Experimental error is 10%.

With the dye Cy5, HES-NCs with hydrodynamic radii between 68 nm (Cy5 Oligo) and 80 nm (Cy5 covalent) after filtration through a 0.45 µm LCR filter were obtained and therefore capsule sizes are similar to NCs with encapsulated SR101 (Figure 20).

The DLS results for the covalently bound Cy5 show a stronger angle dependency for this sample than the simultaneously performed HES-NC synthesis with encapsulated Cy5 oligo. This is observed by the stronger slope of the fit through the plotted data points for the measurement of the covalently modified sample in comparison to the Cy5 Oligo sample. These results suggest that the covalent modification on the HES polymer may lead to variations in the emulsion process leading to a more polydisperse dispersion. In addition, the capsule surface is altered due to the chemical labeling of the surface and can therefore lead to an inhomogeneous surface modification. For this reason, labeling of HES-NCs with fluorescent dyes is usually performed by physical entrapment of the dye inside the NCs.

After successful synthesis of the HES-NCs by inverse miniemulsion, with reproducible size distributions, the NCs are transferred into aqueous phase. The capsules are purified by centrifugation, so that residual surfactant is washed off and redispersed into aqueous SDS solution (0.1 wt%). Since this step leads to a change in the size distribution of the NCs within the new continuous phase and a transformation of the surface and the properties of the NCs is likely to occur, the capsules are analyzed in detail.

IV. 2.2 Redispersion of HES-NCs in water – stabilization and size distribution

After synthesis via inverse miniemulsion, HES-NCs are redispersed in water containing a water-soluble surfactant. Then a functionalization with biomolecules and an application in biological media is possible. Redispersion is a critical point for the reproducibility, since the formed NCs are transferred to water exhibiting a different density. Especially biopolymers show a different behavior in organic solvent than in water causing them to incorporate water molecules which leads to swelling of the material.[230] Keeping reaction conditions constant is therefore essential to obtain reproducible results for each redispersion. This section considers the size distribution of redispersed NCs according to different parameters shown in Table 6.

Table 6: Different parameters influencing the size distribution of HES-NCs synthesis after water transfer and measurements to determine possible alterations.

	Parameter	**Measurement**
Size distribution in water	different surfactants	LS at 90°
	different pH	LS at 90°

For an adequate stabilization of the formed NCs in water, a surfactant needs to be added. It was reported that sodium dodecyl sulfate (SDS, Figure 21, **4**) is a suitable surfactant for HES-NC redispersion.[103,225,231] In addition, the stabilizing properties towards HES-NCs of the ionic surfactant SDS is compared with the non-ionic surfactant Lutensol AT50 (Figure 21, **5**).

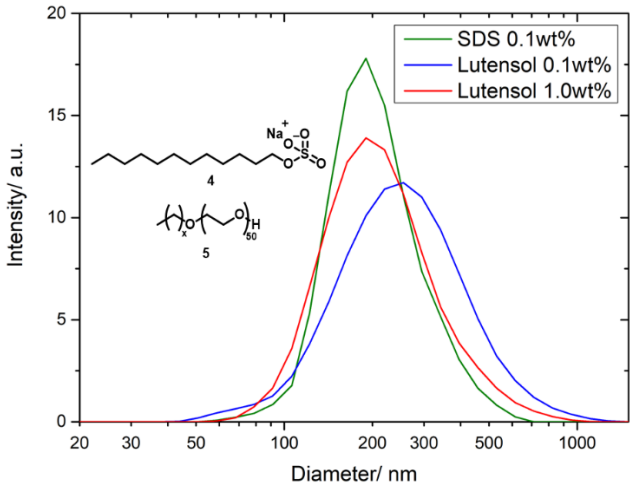

Figure 21: Size distribution of redispersed HES-NCs in water using either SDS (**4**) or Lutensol AT50 (**5**).

The ionic SDS (**4**) as well as the non-ionic Lutensol AT50 (**5**) are able to stabilize redispersed HES-NCs in aqueous continuous phase (Figure 21). Both surfactants show comparable size distributions as after synthesis in cyclohexane (compare Figure 18). For SDS it is sufficient to use 0.1 wt% for a proper stabilization, while the same stabilization effect can be achieved using 1.0 wt% Lutensol AT50 (Figure 21, red curve). If a Lutensol concentration of only 0.1 wt% is used, it results in a broader size distribution and higher average size (Figure 21, blue curve).

Based on this result, it can be concluded that ionic stabilization of the NCs in water has a more advantageous effect than steric stabilization during water transfer. This is in contrast to the stabilization of the NCs in cyclohexane, where steric stabilization by the surfactant P(E/B)-*b*-EO) is achieved. Further information about an adequate stabilization can be obtained by the critical micelle concentration (CMC) of the surfactant. The CMC of SDS at 25°C is 8.2 mM (0.24 wt%), while the CMC of Lutensol AT50 is 2 x 10^{-3} mM (4.92 x 10^{-4} wt%).[232,233] It was reported, that SDS is a very efficient colloidal stabilizer, while non-ionic surfactants have a different stabilizing mechanism, resulting in poorer nucleating capacities.[234,235] For this reason, in the case of non-ionic surfactants stabilizing effects improve even using concentrations above the CMC.[234]

Since the efficient stabilizing effect of SDS was demonstrated, the reproducibility of the redispersion process was studied using 0.1 wt% of SDS as surfactant.

Figure 22 shows the size distribution of 28 HES-NC samples in aqueous SDS solution. These aqueous dispersions are redispersed samples originating from different HES-NC batches in cyclohexane. In the previous section it was shown that light scattering measurements at 90° are a sufficient method to obtain comparable size distributions as with multi-angle light scattering and therefore can be used to determine reproducibility within redispersed samples. For this reason, all redispersed samples were analyzed by DLS measurements at 90° (Figure 22).

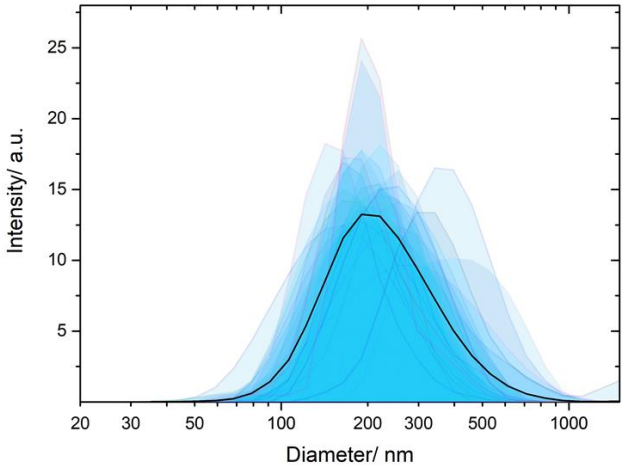

Average NC diameter	Standard deviation
222 nm	± 69 nm

Figure 22: Size distribution of 28 different HES-NC samples redispersed in 0.1 wt% SDS solution. Measured with DLS at a scattering angle of 90°. The averaged size distribution of the 28 size distributions is displayed as black curve.

In Figure 22 the size distributions of 28 independently redispersed HES-NCs samples are depicted. Again, for data analysis, the intensity-weighted size distributions of the individual NCs samples were averaged (Figure 22, black curve) to obtain an averaged size distribution of all samples. From this curve the averaged NC diameter (222 nm) was obtained revealing a slightly smaller capsule diameter than in cyclohexane. From the low average NC diameter and the comparable standard deviation as in the step before, a high reproducibility of the redispersion process can be concluded. The standard deviation of 69 nm, which was calculated as in the section above comparing the maximum intensity of the 28 distribution curves, reveals just a slightly higher value than for NCs in the cyclohexane phase.

The slightly increased standard deviation can be explained by a higher variance of the individual size distributions of the water samples. These results indicate that the redispersion process causes a higher variation of sample size distributions than right after synthesis. However, this was expected as the samples originated from different cyclohexane batches exhibiting differences in size distributions among themselves.

IV. 2.2.1 Influence of salt concentrations and washing on the redispersed HES-NCs – the role of the zeta potential

SDS (**4**) was used to guarantee colloidal stabilization of redispersed HES-NCs in aqueous phase. For biological testing, SDS needs to be minimized as it is toxic to cells, since it was reported to induce significant conformational alterations to proteins such as lysozyme at concentrations of 0.2 mM.[236]
Not only because of SDS' cytotoxicity the removal is useful, but also to ensure continuous stability of the NCs in buffers, since salts and protons might influence the stabilization behavior of ionic surfactants leading to destabilization effects of the dispersion. HES-NCs were redispersed using demineralized water and the resulting pH values of the dispersions were 6-7, depending on the day performance of the desalination system. To evaluate the stability of HES-NCs at different pH values, HES-NCs were redispersed in 0.1 wt% SDS solution and afterwards the pH was adjusted before and after centrifugal washing of the capsules. Figure 23 demonstrates the resulting size distributions of the corresponding HES-NC dispersions.

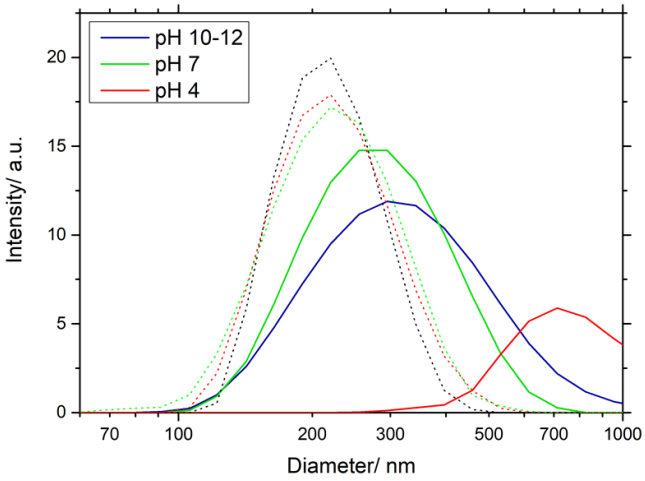

Figure 23: Size distributions of HES-NC dispersions at different pH values at 90°. Solid lines represent size distributions of a non-washed dispersion, dotted lines represent size distributions of a washed dispersion at the different pH values.

HES-NCs exhibit different size distributions in dependency of washing and of the pH value of the dispersion. If the dispersions were not washed and therefore contain the entirely added SDS (Figure 23, solid lines), the pH value significantly influences the size distribution of the HES-NCs. At basic pH (blue solid curve) the size distribution is slightly shifted to larger diameters in comparison to the distribution at neutral pH (green solid curve), while at acidic pH (red solid curve) the size distribution is significantly broadened, revealing aggregates of more than 1 µm in diameter. When the dispersion was purified by centrifugation before pH adjustment, variations in the size distributions are not observed (Figure 23, dotted curves).

These observations point that the pH value and especially an excess of protons can influence the stabilization of redispersed HES-NCs, which is furthermore dependent on SDS. concentrations in the dispersion. For this reason, it is important to remove SDS in order to maintain colloidal stability when a transfer to buffers or solutions exhibiting different pH values is pursued.

A precise quantification of SDS in a NC dispersion and simultaneously checking for possible size alterations e.g., due to changes in aggregation behavior are important parameters in quality control.
SDS concentrations should be kept as low and as constant as possible to ensure the reproducibility and biocompatibility of the NC samples. SDS concentrations as low as approx. 0.1 mM can be easily assessed using a colorimetric assay for SDS detection.
In the assay described by Rusconi *et al*, it is shown how the carbocyanine dye stains-all (**5**) can be used to quantify SDS levels in the microgram range, for example in protein samples, since proteins are usually sensitive to denaturation by SDS.[237] Svenja Winzen showed that this protocol can also be applied to HES-NC dispersions to determine their SDS content. The absorption spectrum of the stains all dye shows an absorption maximum at 453 nm when 10 mM SDS is added (Figure 24, yellow molecule **6**), whereby the curve shifts to an absorption maximum to 510 nm at increasingly lower SDS concentrations up to no SDS (Figure 24, pink molecule, **5**).

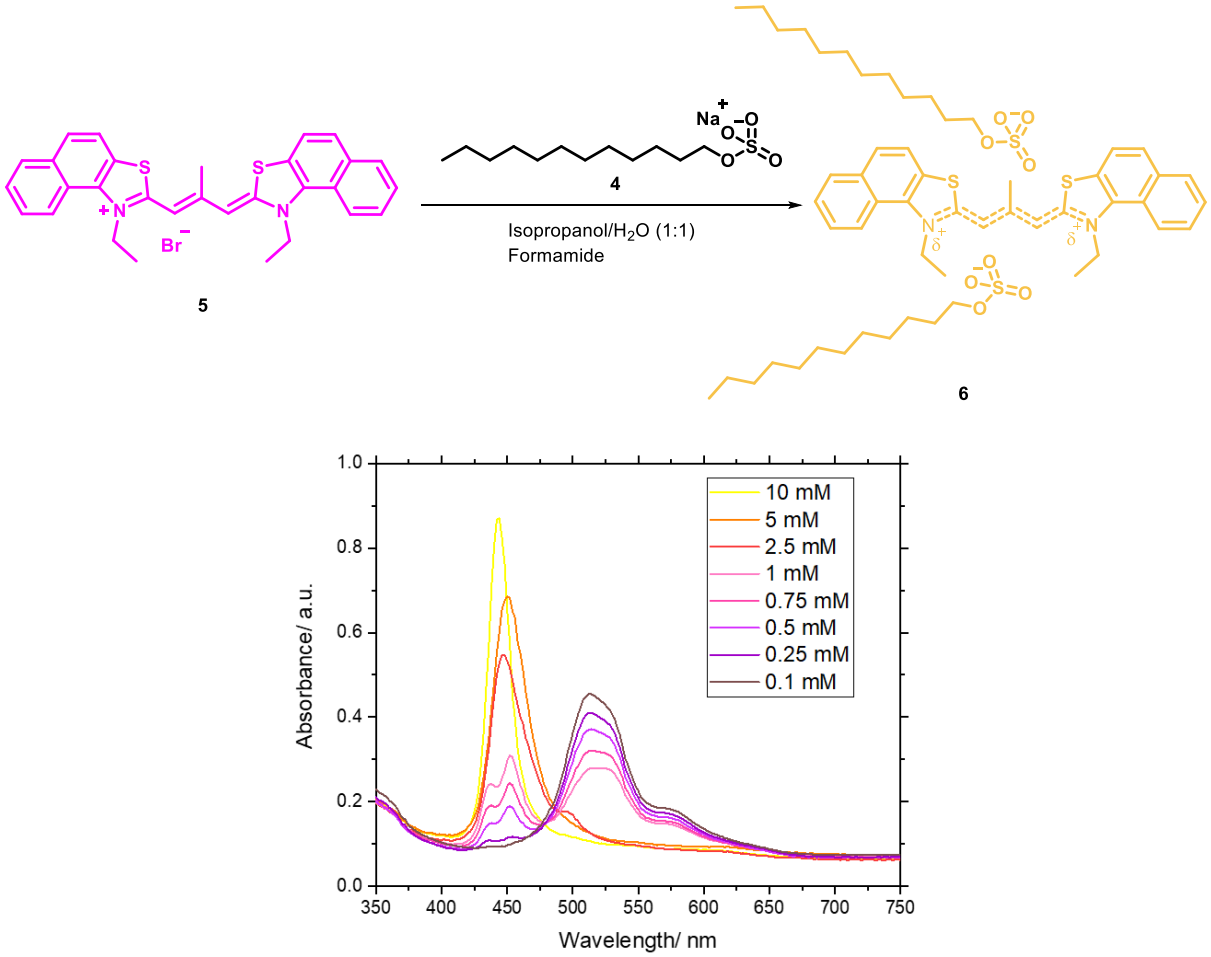

Figure 24: Absorbance scan of the dye stains-all after incubation with different SDS concentrations (reproduced from S. Winzen, Dissertation, Johannes Gutenberg-University, Mainz, 2015, p.95).

In our studies we showed that the SDS on the NCs was effectively removed by means of centrifugal washing steps. Since the SDS concentration is proportional to the measured absorbance of the dye, an external calibration was performed. After each washing step, the amount of SDS present in dispersion was determined (Figure 25 A) and the resulting capsule sizes were analyzed (Figure 25 B).

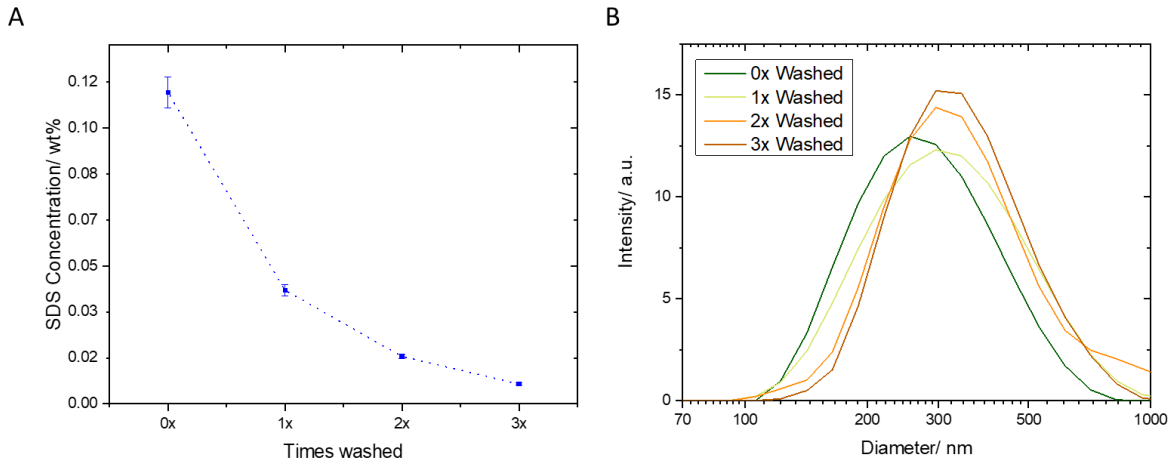

Figure 25: SDS concentration in a HES-NC dispersion decreases with amount of washing (solid content 0.1 wt%, encapsulated SR101). **B**: Size distribution at an angle of 90° of a HES-NC dispersion after washing cycles.

The SDS concentration decreased rapidly by centrifugal washing steps and was reduced up to tenfold of the originally added amount by three washing steps (Figure 25 A). After these steps SDS does not play a significant role for cytotoxicity anymore since the detected SDS amounts are very low and in addition, more centrifugal washing steps increase the risk for aggregation of the capsules. The size distribution of the washed dispersions changed marginally during this procedure. To obtain these results washing was performed carefully which means rather slower centrifugation speed but longer spinning time (Figure 25 B).

The absorbance scans of the successively washed HES-NCs and the obtained supernatants, show the expected shifts from 453 nm to 510 nm (Figure 26, black arrows).

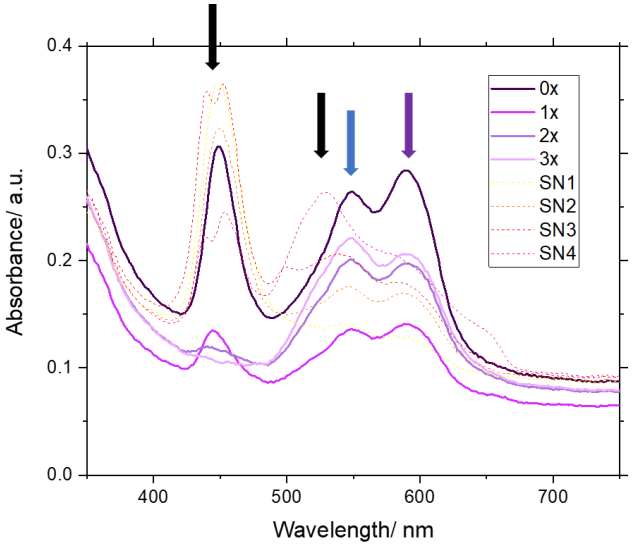

Figure 26: Absorbance scan of HES-NCs during successive washing steps. Dispersions are depicted with solid lines, while corresponding supernatants are depicted with dotted lines. Numbers represent washing steps. SN = supernatant. Arrows depict corresponding absorbance maxima.

As depicted in Figure 26, the purple curve and the yellow dotted curve at an absorbance maximum at 453 nm represent samples with high SDS amount, as expected for the non-washed dispersion (0x) and the first supernatant (Figure 26, SN 1). During washing cycles these maxima decreased and another increasing maximum at approx. 510 nm appeared (compare black arrows of yellow dotted curve, Figure 26). The same maximum at 510 nm did not occur for the capsule dispersion (purple curves), however, the absorbance maxima were slightly shifted and a second absorbance maximum was visible which can be attributed to SR101 as it was encapsulated into the NCs (blue and purple arrows, Figure 26). By means of absorbance scans the dynamics of the SDS removal were followed and it was demonstrated that SDS can efficiently be removed by centrifugal washing.

Since the zeta potential provides information about the surface charge of the NCs, it was further evaluated whether zeta potential measurements can be used to analyze the SDS loadings in HES-NC dispersions. Therefore, the gradually washed NCs were diluted in 1 mM KCl solution and were subjected to zeta potential measurements (Figure 27).

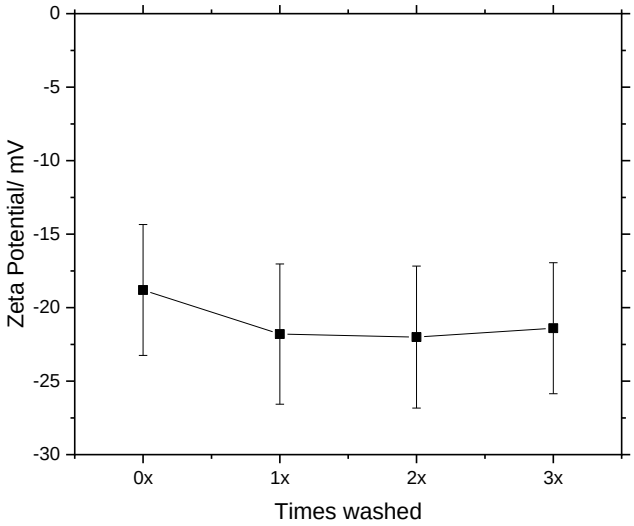

Figure 27: Zeta potential measurement of HES-NCs after successive washing steps.

The zeta potential of the HES-NC dispersion after 3 washing steps is -20 mV ± 7 mV. Gradually washing of the HES-NCs did not change the zeta potential significantly, but the determined potentials remained at a constant level. Surfactants, stabilizing particles for example by ionic interaction such as SDS, are located on the surface, influencing the surface charge. For this reason, it was expected that removing SDS increases the zeta potential. For high concentrations of surfactant this might be true, nevertheless for HES-NC dispersions with the usually applied amount of 0.1 wt% this was not observed. From these observations it was concluded that zeta potential cannot provide reliable information about how much surfactant may still be present on the NCs if the surfactant concentration is comparably low at 0.1 wt%. After the capsules have been transferred to the aqueous phase and were purified, the concentration of the capsules in dispersion must be analyzed. For this purpose, the solid content of the dispersion was determined.

IV. 2.3 Yield of the NC dispersion – the solid content

In contrast to molecules, for which there are numerous methods for the determination of their concentration, such as various chromatography techniques, UV-Vis or NMR methods, there is only a limited number of possibilities for colloids. If the NCs are completely insoluble in different kind of solvents, only a gravimetric determination of the concentration is possible. The exact gravimetric determination of the solid content of the dispersion is difficult to perform, as possible surfactant residues and salts are also measured during weighing. Furthermore, it also leads to a high loss of material, since NCs cannot be recovered after drying. Dynamic light scattering does not only allow one to determine the size of NCs but can also be used to analyze the solid content of the sample. In principle, this is possible as the intensity of scattered light depends linearly on the concentration of scattering objects. This means, that in monodisperse dispersions the scattering intensity is proportional to the solid content. Prior to the analysis of the solid content of a NC sample by DLS, a calibration was gravimetrically determined from a dilution series from 2 wt% to up to 0.125 wt%. Then, dynamic light scattering was performed with these differently diluted HES NC dispersions and besides the hydrodynamic radius, the diode current and the count rate was obtained (Figure 28, Table).

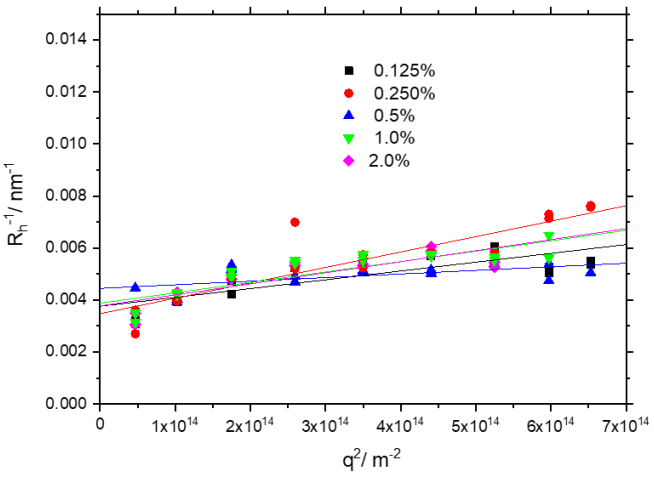

Sample	Solvent	Concentration/ wt%	Diode current	Count rate/ kHz	Count rate normalized	R_h 90°/nm
MF-020-2-8	Water	0.125	635420	290	4.6	185
		0.25	204550	200	9.8	183
		0.50	204470	396	19.4	196
		1.0	90460	332	36.7	178
		2.0	33520	251	74.9	187

Figure 28: Dynamic light scattering measurements of a HES NC dispersion of different concentrations.

Since the diode current, which basically represents the laser intensity, cannot be kept constant during measurement, the count rate is normalized to the respective diode current (count rate normalized).

The measured hydrodynamic radii of the samples differ from 178 to 196 nm, revealing reproducible capsule sizes within the dilution series. The values obtained in the table of Figure 28, were used as standard calibration, whereby the scattering intensity of the samples were determined by DLS and plotted against the gravimetrically determined solid content (Figure 29, black data points). Then the solid content of another HES-NC sample was first determined gravimetrically and afterwards light scattering measurements were performed, using the standard calibration to determine the solid content by the new method (Figure 29, red data points). The results of both methods are showing high consistencies in the determination, especially at low solid contents (Figure 29).

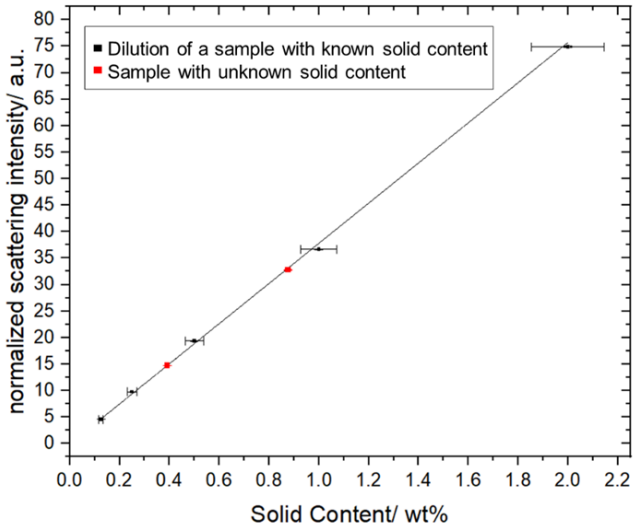

DLS	Gravimetric	Deviation
0.887 wt%	0.750 wt%	15%
0.391 wt%	0.375 wt%	4.1%

Figure 29: Relation between the solid content of a NC dispersion with the normalized scattering intensity during LS measurements (black data points, calibration with known concentrations) and test of a second independent sample (red data points) for comparison with the gravimetrically determined solid content.

In Figure 29 a linear correlation between the normalized scattering intensities of the dilution series and the solid content was obtained, indicating that light scattering can be used for the determination of the concentration of HES-NCs dispersions (black data points). The solid contents of two dilutions of a second sample revealed that the obtained results from both methods are not identical, but very similar with regard to both measurement inaccuracies (Figure 29 table). This means that the LS method of concentration determination via a calibration curve can be very useful to perform fast quality controls of the same batch, e.g., during upscaling or when only very limited sample amounts are available. It needs to be pointed out that for a meaningful determination of the solid content the hydrodynamic radius and the polydispersity of the sample must be constant as the size and the size distribution influence the scattering intensity even more than the concentration.

IV. 2.4 Detectability of encapsulated markers

To detect the NCs in a biological surrounding such as a cell, a fluorescent dye is encapsulated. Therefore, it is important that the dye to be detected remains colocalized with the NCs to ensure reliable and reproducible visualization of the NCs.

IV. 2.4.1 Encapsulation of SR101

We used the dye sulforhodamine SR101 (Figure 20 structure **1**) for HES-NC synthesis since it is soluble in water, stable and highly fluorescent. Therefore, SR101 was added to the aqueous dispersed phase and was encapsulated during the miniemulsion procedure.

As mentioned in Section 2.1.1, SR101 exhibits an amphiphilic character, which means that despite its high water solubility the dye can also be found at the interface with organic solvents.[238] To evaluate the reproducibility of SR101 colocalization in HES-NCs, the fluorescence intensity of HES-NCs prepared from covalently labeled HES with fluorescein was correlated with HES-NCs prepared using the same material with encapsulated SR101 by cLSM measurements.

Scheme 6 shows the reaction of 5-carboxyfluorescein with HES using DCC as coupling agent.

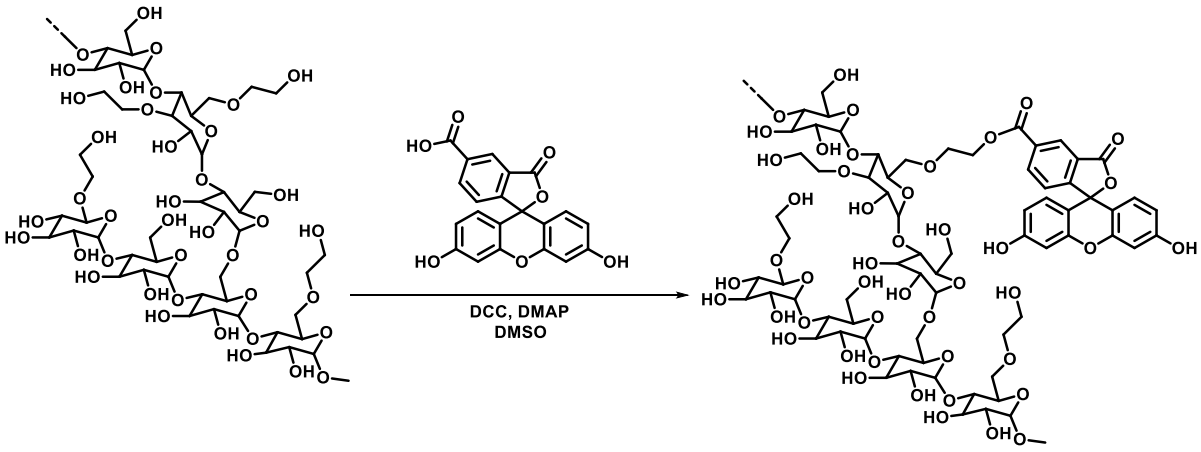

Scheme 6: Labeling of HES (130 kDa) with 5-Carboxyfluorescein by DCC coupling.

After reaction, the labeled HES was purified by dialysis and freeze-dried. Successful labeling was verified by visible illumination of the dried HES under UV light (Figure 30 A). HES-fluorescein NCs with encapsulated SR101 were prepared by placing the labeled HES and SR101 into the dispersed phase of an inverse miniemulsion. After reaction, the capsules were transferred to an aqueous SDS solution. Fluorescein- and SR101 fluorescence was confirmed in the resulting aqueous dispersion.

The aqueous dispersion was subjected to cLSM measurements and the fluorescence overlay of the objects were analyzed (Figure 30 B). The experiment and correlation analysis were performed by [redacted].

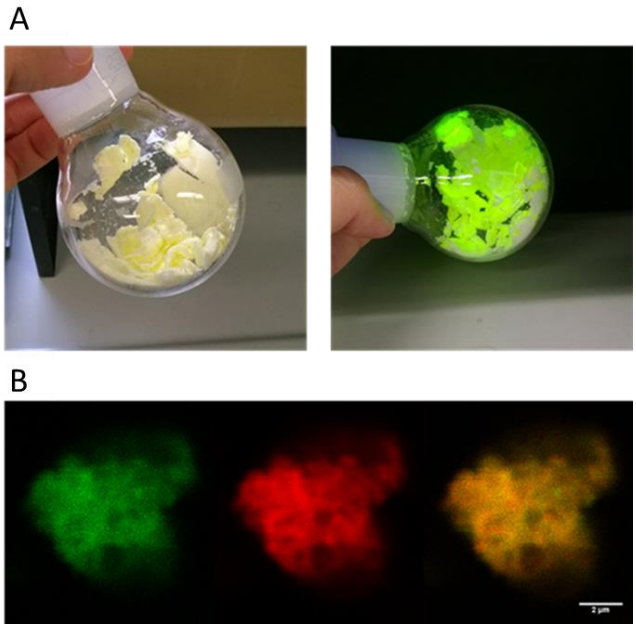

Figure 30: A: Fluorescein modified HES fluorescent under daylight (left) and UV light (right). **B:** Confocal laser scanning microscopy (cLSM) overlay of an aqueous HES-NC dispersion synthesized with fluorescein-modified HES and encapsulated SR101. Scale bar corresponds to 2 µm. CLSM imaging was performed by [redacted].

By cLSM, the fluorescence intensity of attached fluorescein (green) and of encapsulated SR101 (red) was detected in the aqueous HES-NC dispersion (Figure 30 B). The overlay of the green with the red fluorescence resulted in the yellow superposition, shown in Figure 30 B. By analysis of 6 images, an averaged Pearson correlation coefficient of 0.93 ± 0.035, revealing a high correlation of both dyes in the visualized dispersion (Pearson correlation coefficient = 1 complete correlation, Pearson correlation coefficient = 0, no correlation). Since fluorescein is directly correlated with the NC shell, these observations confirm SR101 correlation with the HES-NCs, detected by cLSM. However, objects in the nanometer range cannot be resolved in cLSM; only larger objects are adequately visualized. For this reason, the correlation cannot be determined for a single capsule.

IV. 2.4.2 Encapsulation of Cy5 Oligo

The encapsulation of large hydrophilic dyes is a great advantage and gives greater reliability that the dye is effectively colocalized with the capsules since diffusion is prevented. For this reason, fluorescence correlation spectroscopy (FCS) is used to investigate whether the oligonucleotide dye Cy5 Oligo (Figure 20 structure **2**) is encapsulated in HES-NCs or whether it is adsorbed to the outer surface of the capsule. The oligonucleotide dye Cy5 Oligo exhibits a size of 5 kDa, which is sufficient to prevent it from diffusing out of the NCs. Under these conditions, FCS was first performed with the pure dye (data points in cyan) and then with HES-NCs without dye to which Cy5 Oligo was added (blue data points). The data points in red show HES-NCs where Cy5 oligo was added to the dispersed phase of the emulsion and where it was expected that the dye would be encapsulated after polymerization (Figure 31). The measurements and data evaluation were performed by [redacted].

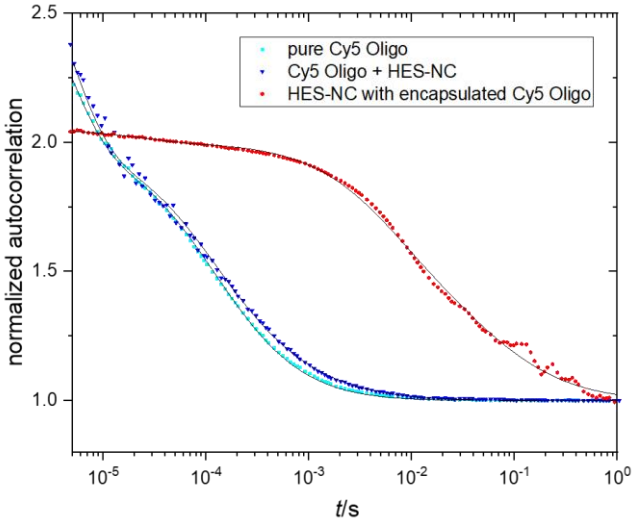

Figure 31: Fluorescence correlation spectroscopy of HES-NCs with Cy5 Oligo encapsulated (red) or with free Cy5 Oligo (cyan and blue) measured in water by [redacted].

FCS reveals that the oligonucleotide dye Cy5 Oligo remains encapsulated in HES-NCs and that there is no interaction between the capsule surface and freely diffusing Cy5 Oligo in case it is not encapsulated (blue curve). The measured fluctuations of fluorescence of free Cy5 Oligo dye (cyan) and unlabeled NCs with additionally added Cy5 Oligo (blue) show a similar behavior, while HES NCs with encapsulated Cy5 Oligo reveal a different correlation function (red) (Figure 31).

These findings demonstrate that there is no adsorption of free Cy5 Oligo dye to the capsule surface and additionally a clear colocalization of dye and NC, if the dye is encapsulated. Since the oligo dye is allocated inside the NCs when it is added during the emulsion (red curve), a free diffusion of the dye is prevented, and the detected diffusion coefficient correlates with the diffusion coefficient and thus the size of the nanocarriers. Due to the high water solubility and the large molecular size of the Cy5 Oligo dye, an encapsulation and therefore a colocalization of dye and NCs is observed. This property is important if the presence of nanocarriers in biological environments has to be verified, as this is often done by fluorescence measurements. Additionally, the concentration of free dye (i.e., resulting from insufficient washing or leaking) can be quantified by FCS measurements and was approximately 3%, allowing for a reliable detection of the HES-NCs.

Both dyes, SR101 and Cy5 Oligo, can be used as a marker for reliable detection of HES-NCs, since both dyes revealed reliable colocalization with the HES-NCs when encapsulated.

IV. 3. Surface functionalization of HES-NCs – Detectability of different groups and binding to HES-NCs

A reproducible surface-functionalization of nanocarriers is crucial for the therapeutic success of a drug delivery vehicle. However, achieving a reproducible surface functionalization is difficult and needs to be studied in detail. Literature often only addresses plane surfaces as the surface analysis of spherical objects is very challenging.

In this chapter, the surface-functionalization of HES-NCs was studied in order to attach targeting moieties to the capsules in a reproducible manner.

For this purpose, combinatorial approaches were used to first detect surface groups at all and second, to quantify them in many samples to evaluate reproducibility of the functionalization.
The first step was therefore to understand the surface of the nanocarrier since it was essential to assess further chemical reactivity towards added linker molecules and to understand material properties. Afterwards, HES-NCs were functionalized, and the attached groups were detected and quantified.
In this thesis two approaches were followed to analyze the surface of HES-NCs just right after water transfer, which confirmed the presence of the suspected groups.
The crosslinker toluene diisocyanate (TDI) is sensitive to aqueous media hydrolyzing to amino groups. The FTIR spectra in Figure 16 provide evidence by showing typical polyurea vibrations, confirming the reaction of isocyanates with amines.[239] To detect residual amino groups on the capsule surface, two methods were performed. A classical method for the detection of amino groups is the fluorescamine assay which is often used for biomolecules like proteins. Furthermore, ToF-SIMS which is a sensitive mass spectrometry technique applied to films, was performed. The appearance of amino groups and their quantification is important to assess further functionalization of the NCs with biomolecules. To control this binding of biomolecules, DBCO-PEG-NHS ester was attached to the capsule surface to exploit a copper-free click reaction on the capsule surface. This reaction is known to be very efficient, as it provides high yields at room temperature and in aqueous solutions.[240] The absence of copper results in a better biocompatibility of the functionalized NCs as traces of the metal are toxic and complete removal is difficult. Adjusting the concentration of the surface groups, allows a specific binding of following azide-terminated biomolecules and therefore the awarding of biological functions to these HES-DBCO-NCs. In Table 7 the synthesis steps, parameters determining them and the used method are shown.

Table 7: Synthesis step and analysis of HES-NCs for the functionalization with DBCO-PEG$_4$-NHS ester.

Step	Changed parameter	Method
Surface-modification of HES-NCs with DBCO-PEG$_4$-NHS ester	Reaction time of the NHS ester to the HES-NC	Anthracene azide assay
	Reaction time of the click reaction	
	Binding of different amounts of the NHS ester to the HES-NCs	
	pH dependency	
	Washing of excess NHS ester	
	Stability of attached DBCO groups	

IV. 3.1 Exploring the surface of HES-NCs

In this section the detection and quantification of amino groups on HES-NCs are discussed.

The presence of amino groups is decisive for the subsequent attachment of linker molecules to the HES-NCs. Therefore, it should be investigated in the following which methods are suitable to determine amino groups on the HES-NC surface.

IV. 3.1.1 Time of flight secondary ion mass spectrometry (ToF-SIMS) of the nanocapsule surface

ToF-SIMS analysis was applied to verify the presence of amino groups on the capsule surface, which occur due to TDI hydrolysis. When dealing with particle characterization, literature often addresses planar surfaces, as the molecules attached to the surface are easier to analyze, than on spherical objects in dispersion. For the ToF-SIMS measurements, NC dispersions were applied as a multi-layered film on a glass substrate and the upper surfaces of these films were then analyzed detecting secondary ions desorbed from the films as a result of primary ion bombardment.

To investigate possible differences in the surface composition after the redispersion process, different samples were prepared, and the dispersions were purified by centrifugation. Spin coating of the capsule dispersions on the glass substrate resulted in a colloidal film. Due to hydrolysis of residual TDI during the redispersion of HES-NC to water, it was expected that a significant increase of amino groups on HES-NCs in water (Figure 32, sample 1) compared to HES-NCs in cyclohexane (Figure 32, sample 2) occurs and will be detected in the films. Furthermore, two additional samples were prepared in which an aqueous HES solution and TDI were emulsified in cyclohexane without surfactant and reacted overnight. The resulting polymer was dissolved in a mixture of DMSO and THF and applied to the substrate (Figure 32, sample 3). In the fourth sample, HES was dissolved in DMSO and applied to a glass substrate. Subsequently TDI, dissolved in DMSO, was added to the HES solution and reacted in situ on the glass substrate with HES (Figure 32, sample 4). Using the prepared films 3 and 4 (sample 3 and 4), the reaction of HES and TDI in bulk should be compared with the reaction in emulsion. For the film processing, the dispersions were spin coated with a speed of 500 rpm on the glass substrate and the polymer solutions were drop casted and dried overnight. Afterwards the obtained films were analyzed under the microscope and the film thickness was determined by a profilometer (Figure 32).

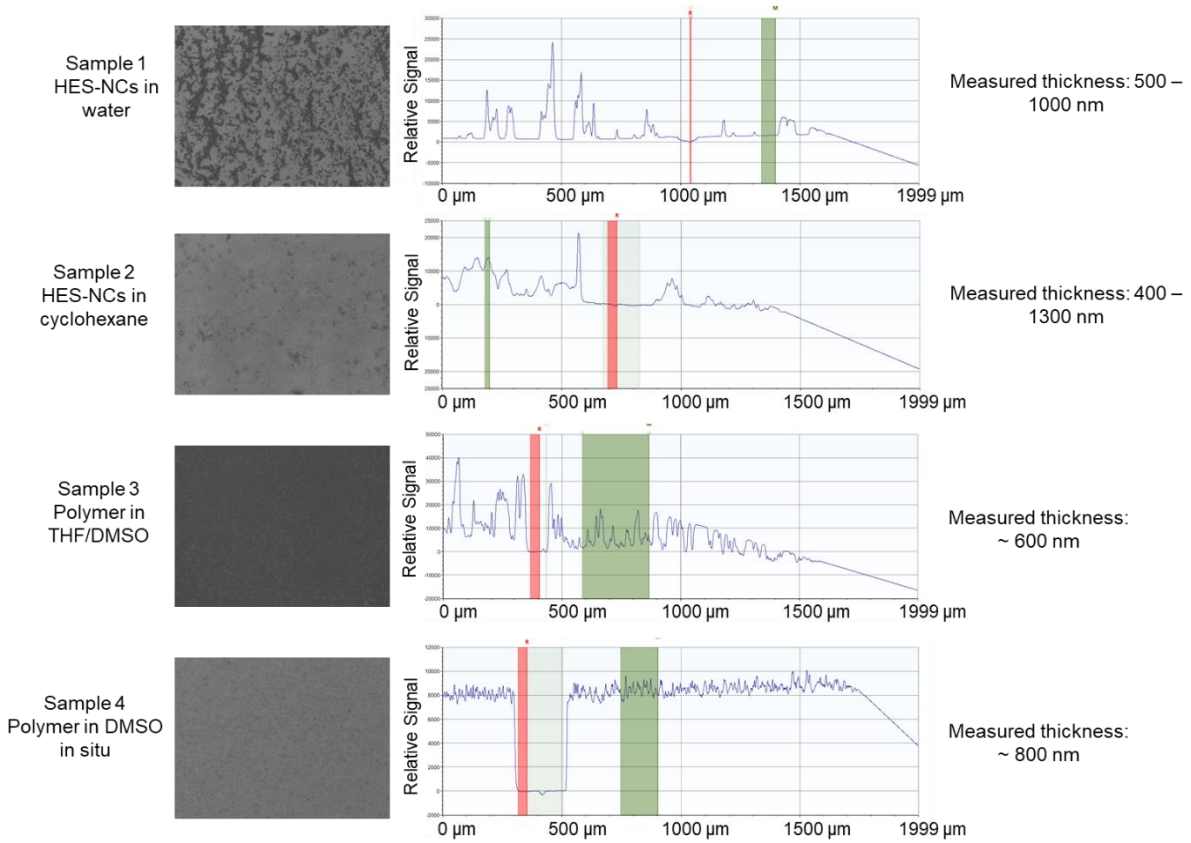

Figure 32: Microscopy images and profilometry results of spin coated and drop casted films prepared of NCs and HES and TDI, measured by [redacted]. Microscopy images display a 5x magnification. Red boxes display parts of the substrates that were scratched with a needle to determine tip location. Green boxes display areas in which averaged film thickness was determined.

Microscopy and profilometry confirmed film thicknesses of several hundred nanometers, achieved by spin coating the dispersions several times onto the substrate. Since the information depth of ToF-SIMS is in the single nanometer range, the film thicknesses were sufficient to completely cover the glass substrates. Comparing the microscope images of samples 1 and 2, uneven distributions of material on the substrate were observed, which could result from a certain polydispersity of the NCs. However, since the covered areas were visible to the naked eye, the navigation and selection of covered areas for analysis in the ToF-SIMS was straightforward. Figure 33 shows the results of the ToF-SIMS analyses in positive ion mode which was measured and evaluated by [redacted].

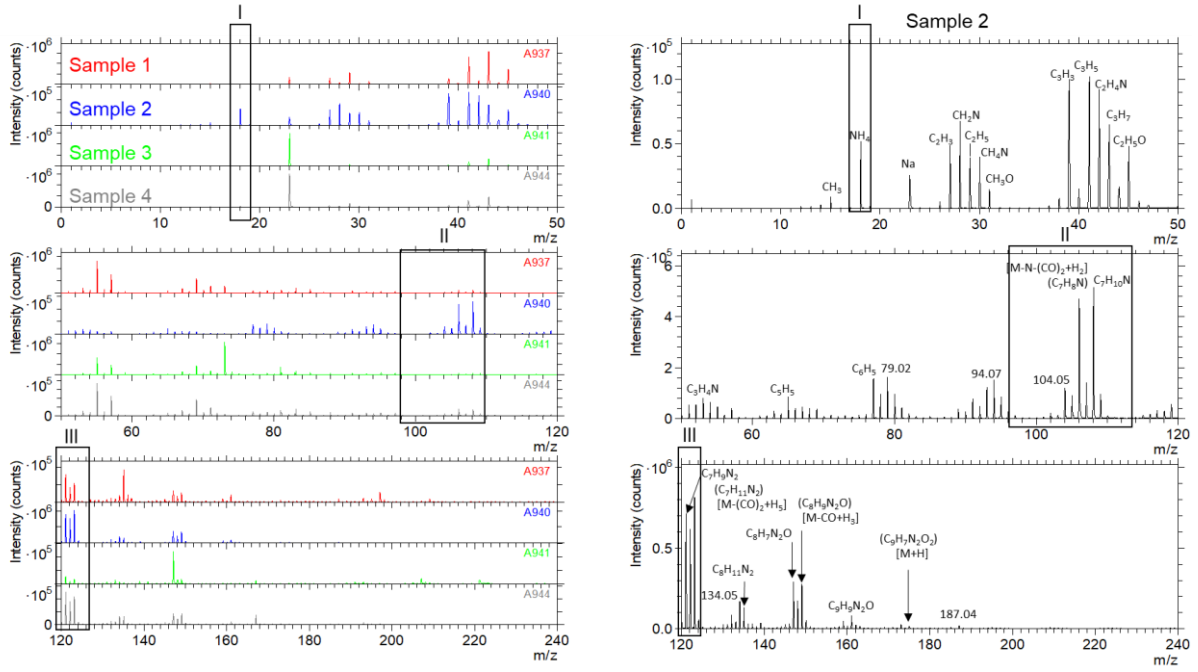

Figure 33: ToF-SIMS surface spectra of the prepared samples 1-4 in positive ion mode, measured and evaluated by [redacted]. Black boxes (I-III) mark prominent signals. On the right side prominent patterns of sample 2 are exemplarily shown which are also found in the other samples.

ToF-SIMS analyses of the different films reveal several signals, found in all four samples. In addition to a number of very prominent signals for the typically encountered hydrocarbon species (in the range of m/z 25-80), a signal for the ammonium ion NH_4 (I) was found which revealed the strongest intensity in sample 2 and weakly in sample 1. Signals at m/z 106.07 and 108.07 (II) demonstrate a notable pattern in sample 2 which are associated to the fragments C_7H_8N and $C_7H_{10}N$ and can be attributed to hydrolysis products of TDI. Furthermore, intense signals at 121 to 123 m/z (III) were found in all samples which are attributed to the fragments $C_7H_9N_2$ and $C_7H_{11}N_2$. (Figure 33). The finding of these amino-containing fragments suggests successive hydrolysis of the isocyanate TDI. This was confirmed in separate experiments in which a diisocyanate species (methylene diphenyl diisocyanate, $C_{15}H_{10}N_2O_2$) revealed the same signals. These signals show the strongest intensity in sample 2. The samples were complementarily analyzed in negative ion mode (Figure 34).

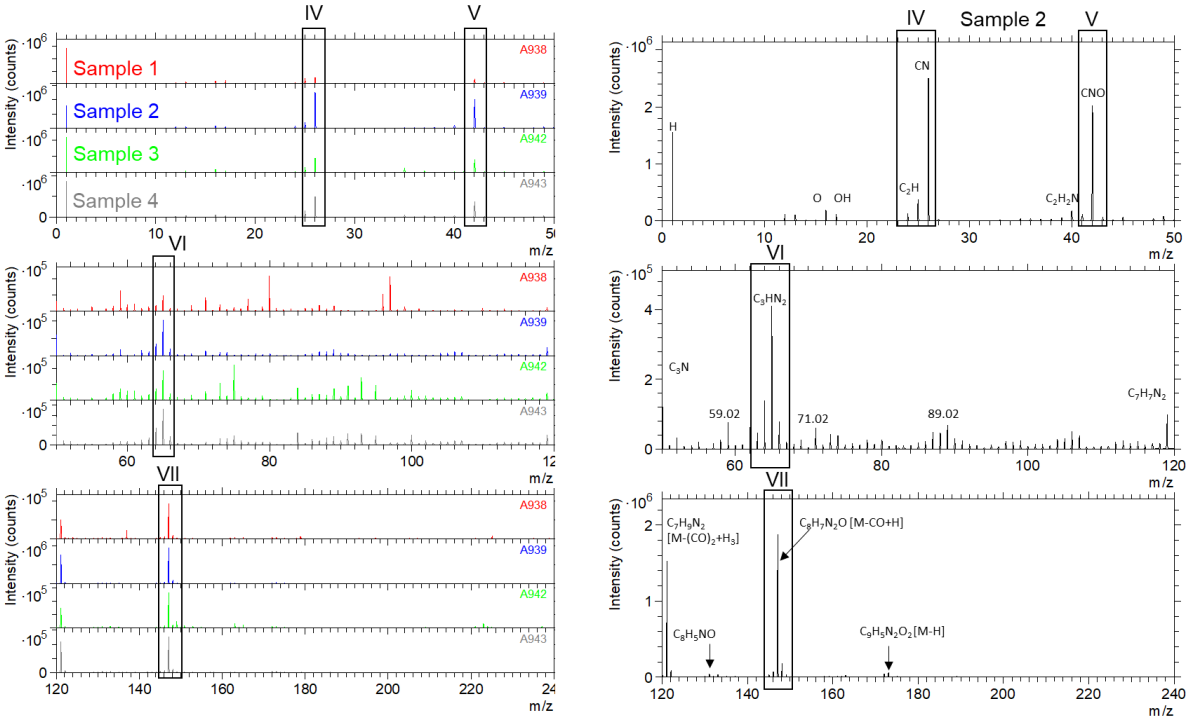

Figure 34: ToF-SIMS surface spectra of the prepared samples 1-4 in negative ion mode from 0 - 240 m/z, measured and evaluated by [redacted]. Black boxes (IV-VII) mark prominent signals. On the right side prominent patterns of sample 2 are exemplarily shown, which are also found in the other samples.

In all the samples the typical signal for N-containing hydrocarbons CN^- (IV) were detected, while in sample 1 (HES-NC in water) the signal has the lowest intensity (Figure 34). This observation was expected, since the detected cyanide ion most likely originates from residual TDI which further reacted in water phase. These findings are further supported by the isocyanate signal (CNO, V) which was found especially in sample 2, 3 and 4 while sample 1 revealed just a weak signal. Prominent patterns are found at m/z 65.02 (VI), m/z 119.06 ($C_7H_7N_2$), m/z 121.09 ($C_7H_9N_2$) and 147.08 (VII) for all samples.

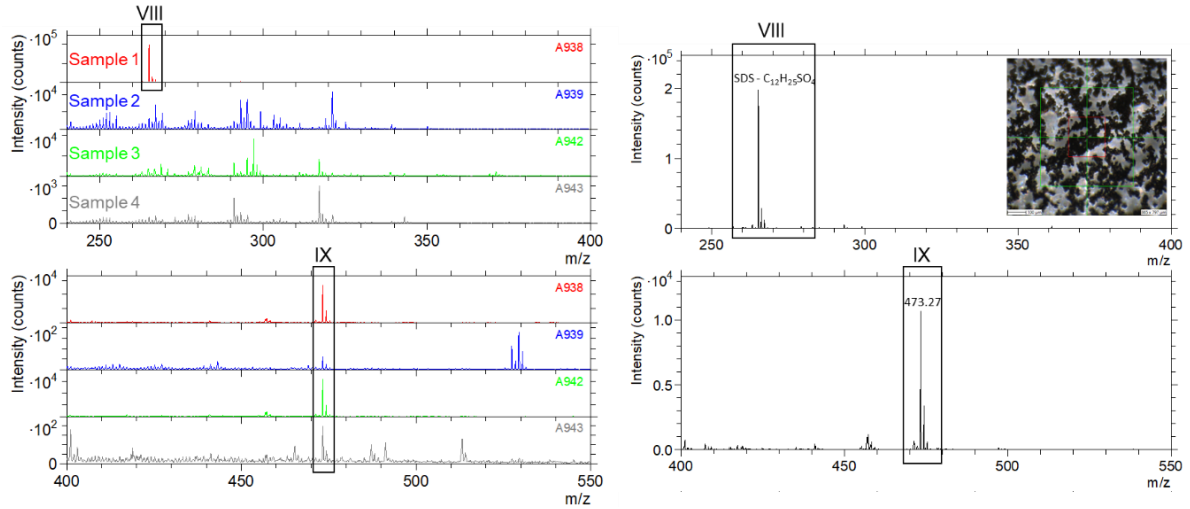

Figure 35: ToF-SIMS analyses of the prepared films 1-4 in negative ion mode, from 240 – 550 m/z, measured and evaluated by [redacted]. Black boxes (VIII-IX) mark prominent signals. On the right sight signals from sample 1 are exemplarily shown.

Furthermore, a prominent signal for all the films was found at m/z 473.24 (IX) and is shown exemplarily for sample 1 in the magnifications on the right side (Figure 35). However, no molecular formula could be assigned to this signal. Sample 1 also reveals SDS residues (VIII) (Figure 35, upper right panel).

The results from Figure 33, 34 and 35 reveal different signals, which were present in all samples, indicating that there is a similarity between the bulk material and the capsules. In positive ion mode the ammonium ion (NH_4^+) was detected most intense for the capsule dispersions in cyclohexane and water. However, in negative ion mode the cyanide (CN^-) and cyanate ion (CNO^-) are very strongly represented in all samples except for the aqueous capsule dispersion (sample 1) since it is expected that both ions resulting from TDI, fully react in aqueous conditions. The hydrolysis was confirmed by the presence of prominent patterns (Signals II, III and VII) revealing successive hydrolysis steps (M-CO+Hx). Furthermore, other specific signals were found, which mainly represent larger carbon containing fragments. The signal strength varied from sample to sample, since different amounts of material were applied to the film and the substrates had different surface coverages.

As a next step, the part of the substrate is shown on which the ion beam hit the material and the respective surface coverage for the ammonium ion NH_4^+ and cyanide CN^- is demonstrated (Figure 36). Furthermore, signal distributions for silicon and aluminum reveal areas, which are not covered by material and show complementary results to the covered areas (not shown in this chapter, but complete data set is included in the Appendix).

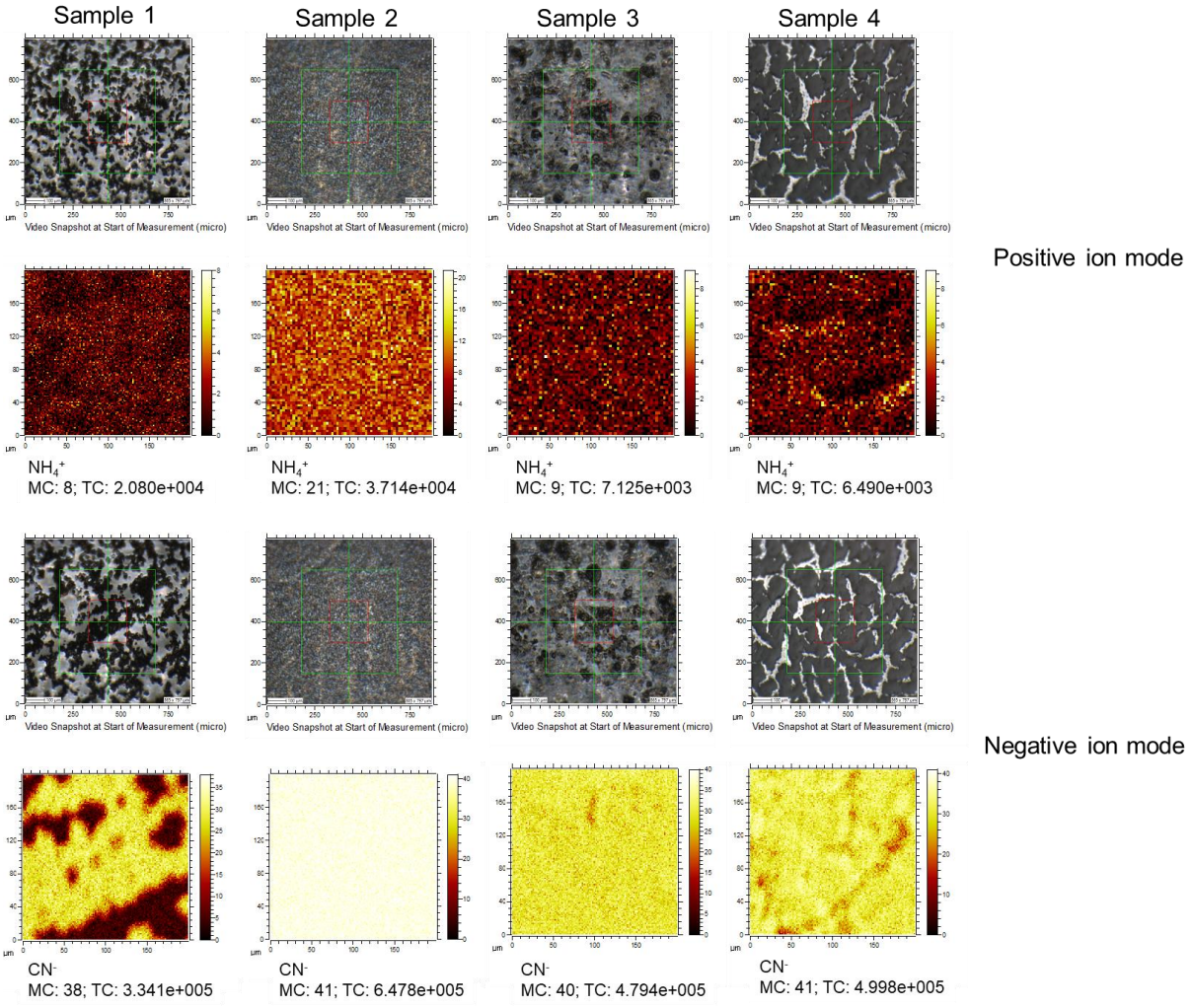

Figure 36: Optical images ("Video Snapshots") of the glass substrates with the samples 1-4 and the corresponding chemical surface images revealing the signal distributions for NH_4^+ ions (positive ion mode) and CN^- (negative ion mode) measured by [redacted]. Red squares in the optical images indicate the position of the ToF-SIMS imaging analyses. TC: total counts in image, MC: Maximum counts in pixel.

The lateral signal intensity distributions for the ammonium ion in positive ion mode and for the cyanide in negative ion mode are shown in heat maps (i.e. chemical maps) revealing strong/intense signals in bright color and weak signal in dark colors (Figure 36). The upper panel shows the corresponding image of the part of the glass substrate, on which parts of the film are identified.

With the heat map for each sample in two different modes, the abundance of the corresponding ions was visualized. It is clearly seen that film 2 (sample 2 – HES-NC in cyclohexane) has the highest intensities for both NH_4^+ and CN^-. As there are strong differences in the homogeneity of samples 1, 3 and 4 observed for NH_4^+ (also visible in optical images), a surface coverage compensation needs to be performed to allow a semi-quantitative comparison between the samples. This correction of the measured intensities has been performed by identifying the fraction of covered area in the substrate signal distributions (compare appendix) in the field-of-view and multiplying by a factor to obtain the signal for 100% covered field-of-view. Afterwards intensities for the different ions were compared (Figure 37).

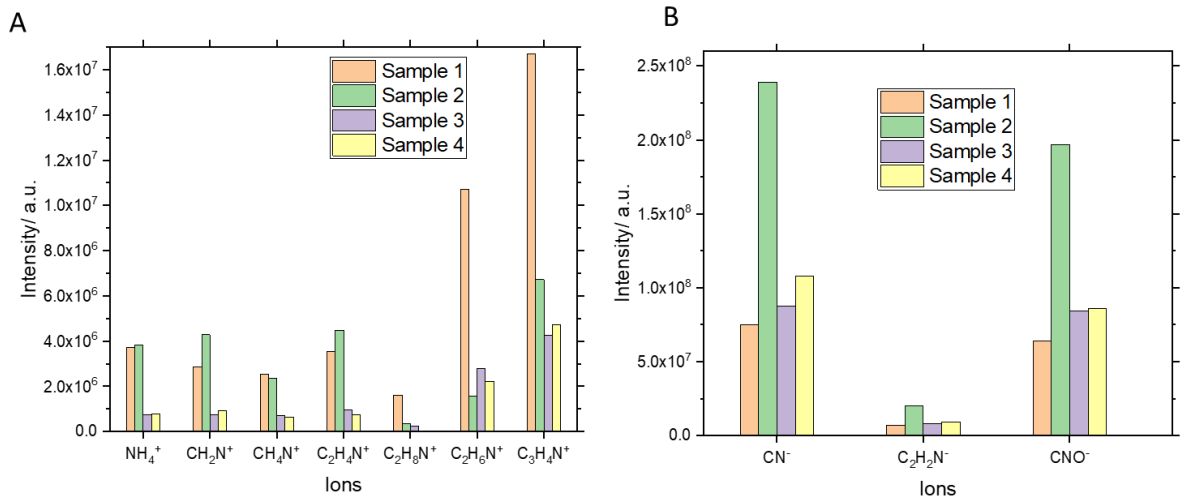

Figure 37: Evaluation of different secondary ion intensities on the films in positive ion mode **A** and negative ion mode **B** after surface compensation.

ToF-SIMS analyses yield plenty of different N-containing species in the samples for the measurement in positive ion mode (Figure 37 A). Before surface compensation, the ammonium ion NH_4^+ is found with a lower intensity than N-containing species with higher molecular weight like $C_3H_4N^+$ or $C_2H_6N^+$. Interestingly, after surface compensation, the high molecular weight species are found to a higher extent in sample 1 (HES-NC in water), while for the lower molecular weight species (NH_4^+, CH_2N^+, CH_4N^+ and $C_2H_4N^+$) measured intensities for sample 1 and sample 2 are very similar. Sample 3 and sample 4 both show rather low intensities for all the species illustrated in positive ion mode, which was expected due to the lack of hydrolyzing conditions. The results obtained for positive ion mode (Figure 37 A) confirm an increased number of amino-containing groups in the aqueous HES dispersion. In negative ion mode, especially cyanide (CN^-) and isocyanate (CNO^-) were found in sample 2 (HES-NC in cyclohexane) as expected but not to a higher extent for the samples 3 and 4 (Figure 37 B). This is aligned with the fact that in sample 3 and 4 less TDI was used, while for the HES-NCs dispersion in cyclohexane applied as sample 2, excess TDI was used. Sample 1 shows the lowest intensity for these ions, as TDI is hydrolyzed in the aqueous environment. By means of ToF-SIMS measurements of HES-NC dispersions before and after water transfer as well as analyses of the bulk material, it was demonstrated that HES-NCs in water and in cyclohexane exhibit amino-containing species.

HES-NCs in cyclohexane contain excess TDI which hydrolyzes upon water transfer. The presence of amino groups is important for the subsequent surface functionalization of the HES-NCs.

IV. 3.1.2 The use of the fluorescamine assay for the detection of amino groups on HES-NCs

Fluorescamine (**7**, see Scheme 7) is a spiro compound which undergoes a ring opening after attack by nucleophiles such as amines, emitting fluorescence (**8**).

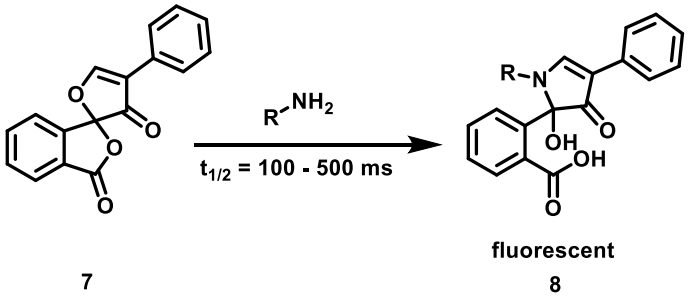

Scheme 7: Fluorescamine (**7**) reacting to a fluorescent species (**8**) upon reaction with amines.[241]

Udenfriend *et al*. showed that fluorescamine reacts with amine-containing compounds in a few milliseconds on a picogram scale, making it very popular for the detection of peptides and proteins.[241] A calibration can be performed using simple, water-soluble amines like e.g. hexylamine. In addition, the order in which all the components are added to the well for fluorescence intensity measurements, is decisive for the success of the measurement. Borate buffer (pH 8.3) was used to dilute the analyte, since amino groups were deprotonated. Since fluorescamine reacts very fast (compare scheme 7) and is prone to hydrolysis at a pH above 9[241], the fluorescamine solution was added to the analyte and the standard as a last component and fluorescence intensity measurements were performed directly after fluorescamine addition.

The assay was performed using HES-NC dispersions with solid contents between 0.1 wt% and 1 wt%, but the measured values were under the detection limit. These findings support, that there is a small number of amino groups on the HES-NCs. For this reasons, different HES-NC dispersions were highly concentrated to up to 7.2 wt%. In Figure 38 fluorescence intensity measurements of different samples exhibiting different solid contents are shown. External calibration was performed using hexylamine dilution series. In order to compare batch-to-batch variability of detected amino groups on redispersed samples, two samples originated from the same cyclohexane batch, redispersed separately (sample F3-A/-B, orange data points and F3-A-2/-B-2, green data points) were performed. In addition, a sample in which a higher HES concentration was used in the miniemulsion procedure was prepared (sample F1). Fluorescamine assay was performed on four different days measuring different samples, and therefore four different calibration curves were applied and are depicted as dotted lines (Figure 38).

Sample	Original HES-NC Dispersion	HES solution (wt%)	Solid content
F1	KK160	6%	7.2 – 1.8 wt%
F2	KK100	3%	7.2 – 1.8 wt%
F3-A-2	MF-215-A	3%	4.2 wt%
F3-B-2	MF-215-B	3%	4.2 wt%
F3-A	MF-215-A	3%	3.6 – 1.8 wt%
F3-B	MF-215-B	3%	7.2 – 3.6 wt%

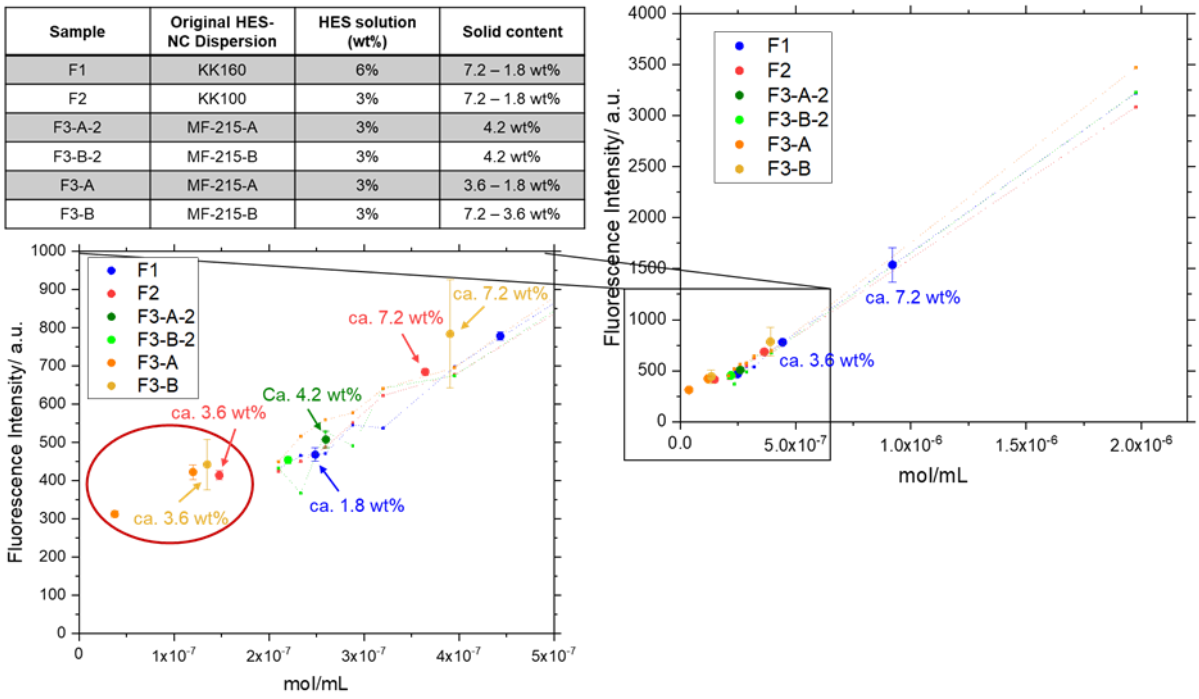

Figure 38: Reaction of fluorescamine with different aqueous HES-NC dispersions, concentrated to final solid contents of between 7.2 wt% to 1.8 wt%. Dotted lines represent respective calibration curves prepared for each sample, using hexylamine as a standard. Data points inside the red circle represent samples which are not within the used standards and are therefore under the detection limit.

For the fluorescence intensity measurements shown in Figure 38, in total six different samples, with up to three different concentrations, originating from four different HES-NC dispersions were measured. The four calibration curves demonstrate a reproducible linear correlation between hexylamine concentration and signal intensity, as each of the curves were measured on different days using fresh buffer and fresh hexylamine. It was observed that samples with a similar solid content are in a similar detection range and thus it is shown that different samples as well as samples originated from the same cyclohexane batch, reveal a reproducible fluorescence intensity in fluorescamine assay.

As seen from the inlet (0 mol/mL to 5 x 10^{-7} mol/mL), most of the samples are in a range, in which quantification can not reliably performed anymore, since the samples reach the detection limits of the standard (see data points within the red circle, Figure 38). The results in Figure 38 reveal, that HES-NCs need to be concentrated to up to 7 wt% to appear within the calibration, while at a solid content of around 4 wt% and lower, the samples are under the detection limit.

For sample F1 (Figure 38, blue data points) fluorescence intensities within the calibration for all the measured solid contents were obtained. This sample was prepared by an upscaling procedure, processing seven times more material as in a usual batch. Furthermore, a more concentrated HES solution (6%) was used (compare Table 8, F1 in comparison to standard reaction conditions).

Table 8: Reaction conditions resulting in an increased shell thickness of sample F1 in comparison to the standard procotol.

Procedure	Dispersed phase	Continuous phase	Parameter changed
Standard	1.4 g HES (3 wt%)	130 mg surfactant/ 12.5 g cyclohexane	-
Upscaled (Sample F1)	16.3 g (6 wt%)	910 mg surfactant/ 87.5 g cyclohexane	Shell thickness

This procedure led to an increase of the shell thickness of the generated HES-NC, which could favor the detectability of groups on the NCs. Fluorescence intensity spectra for sample F1 are compared at different capsule concentrations, revealing linearity of measured fluorescence intensity in dependency of the solid content (Figure 39).

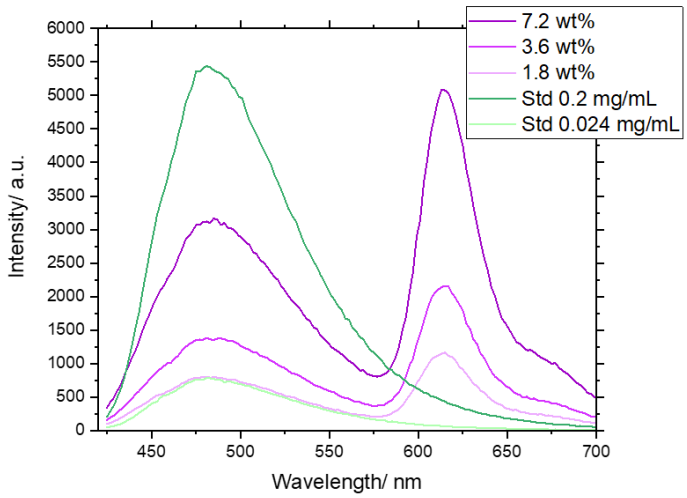

Figure 39: Fluorescence intensity scan of three different concentrations of the HES-NC dispersion F1 (purple curves, compare table of Figure 38), compared with 0.2 mg/mL and 0.024 mg/mL of hexylamine standard (Std, green curves) used in the fluorescamine assay.

Sharp fluorescence emission spectra can be obtained for sample F1 (Figure 39). The purple curves show maxima at around 475 nm which coincide with the maximum of the hexylamine standard (Std, green curves) and a second one at 620 nm which can be attributed to the encapsulated SR101 inside the NCs. The fluorescence intensity increases linearly to the measured solid content as it is seen in Table 9. Furthermore, using the solid content of the dispersion and the measured diameters of the NCs, the concentration of NCs per mL dispersion was calculated as well as the number of amino groups per NCs. Eq. 6 shows how the number of groups per NC can be calculated, at the respective solid content and an assumption that the density of the HES-NCs is approximately 1 g/cm^3:

$$\frac{\text{groups per mL Dispersion}}{\left(\frac{\frac{4}{3}\pi(r \times 0.000000001)^3}{\text{solid content in m}^3}\right)} = \text{groups per NC} \qquad \text{(Eq. 6)}$$

By solving Eq. 6 for each sample involving the measured capsule diameter, the detected groups per NC can be compared (see Table 9).

Table 9: Calculation of amino content on the aqueous HES-NC dispersion (F1).

Sample	Intensity/ a.u.	Standard deviation	Calculated mol/mL	Amount of NH_2/mL	NC/ mL	NH_2/NC
7.2 wt%	1537	171.1	9.202×10^{-07}	5.542×10^{17}	4.208×10^{12}	~ 132 000
3.6 wt%	778.5	10.60	4.435×10^{-07}	2.671×10^{17}	2.104×10^{12}	~ 127 000
1.8 wt%	468.5	17.68	2.487×10^{-07}	1.498×10^{17}	1.052×10^{12}	~ 142 000

In Table 9 the calculated amino groups per mL and per NCs are displayed for sample F1. As expected, the concentration of the groups per mL decreases linearly according to the solid content of the dispersion, as less NCs are present in dispersions at lower solid content. Since the amount of NC/mL is decreasing as solid content decreases, the calculated amino groups per NC (NH_2/NC) stay at a constant level of around 134 000 ± 7900 groups. As sample F1 has been prepared using a HES concentration which is approx. three times higher as in the standard procedure, the amino content was high enough to detect. Sample F3-A-2 shows a number of 1.57×10^{17} amino groups per mL. With a measured capsule diameter of 307 nm and a solid content of 4.2 wt%, approximately 56 000 NH_2/NC could be obtained. This means that in sample F3-A-2 about 45% of the amino groups were detected which were reliably found on sample F1.

The results of the fluorescamine assay show that the capsule dispersions have to be strongly concentrated to give a reliable result in the assay. Moreover, it could be shown that with decreasing solid content also decreasing amino groups are observable and that the content of amino groups depends on the HES amount used. By means of fluorescence emission scans performed by the reaction of fluorescamine with HES-NCs dispersions and ToF-SIMS analysis of different capsule films, the presence of amino-containing species was verified. Therefore, in the next step, covalent attachment to the amino groups on the HES-NC surface was evaluated.

IV. 3.2 Binding of dibenzocyclooctyne (DBCO) onto HES-NCs – evaluation of DBCO as copper-free click reagent for the surface modification of nanocapsules

HES-NCs were surface functionalized using DBCO-PEG_4-NHS ester (Figure 40, **9**) for a subsequent copper-free click reaction on the HES-NC surface using an azidated biomolecule. As the presence of amino groups on the HES-NC surface was verified (see Section 3.1), an NHS ester was used to covalently attach DBCO to the HES-NCs. **9** is a sticky orange oil which readily dissolves in DMSO and was added to the HES-NCs and stirred at room temperature. After reaction, the modified capsules were purified by centrifugation.

To confirm the binding of the NHS ester and to confirm the reproducibility of the DBCO attachment to the capsule surface, a detection reaction was used. The bound DBCO was reacted in a copper-free click reaction with anthracene azide (**10**) to a fluorescent species (Figure 40).

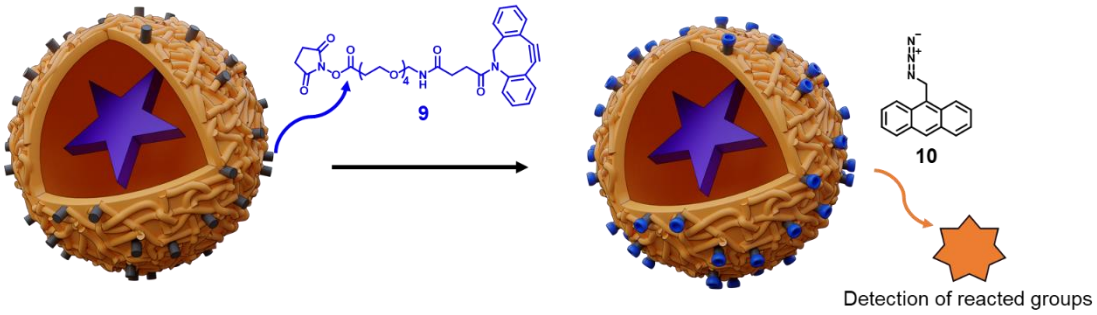

Figure 40: Covalent binding of DBCO-PEG$_4$-NHS ester (**9**) to HES-NCs and detection by reaction of anthracene azide (**10**) to a fluorescent species.

Anthracene azide (**10**) is particularly suitable for the reaction with DBCO, as **10** itself exhibits just a low fluorescence intensity, while the coupling product is a triazole derivative (**11**) with high fluorescence intensity, which allows the reaction to be followed over time (Figure 41). The amount of **9** converted in the reaction shown in Figure 41 corresponded to a concentration of 0.4 mg/mL DBCO. Equimolar amounts of azide **10** were added. For the fluorescence measurements, the reaction mixture was further diluted in DMSO (1:100). The generated fluorophore can be excited at 370 nm and emission maxima can be observed at 395 nm, 418 nm and 444 nm. The reaction of the pure reactants without NCs is shown in Figure 41.

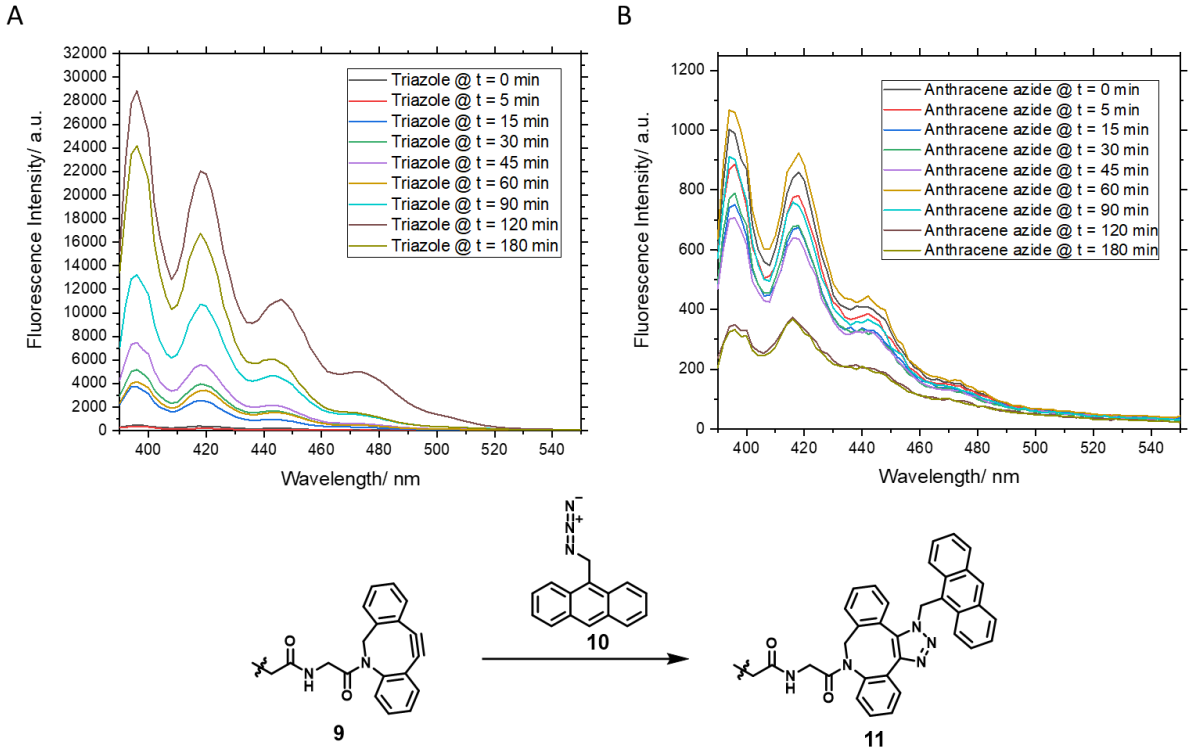

Figure 41: Time-dependent fluorescence intensity spectra of the reaction of anthracene azide (**10)** with DBCO-PEG-NHS Ester in DMSO (**A**) and pure anthracene azide (**B**). The fluorescence intensity of anthracene azide was subtracted from the fluorescence intensity from the generated triazole (**11)** in every time period in spectrum A.

After 15 min, the fluorescence intensity of the reaction mixture increased rapidly and therefore indicated that the reaction just took a few minutes until triazole **11** is generated (Figure 41 A). In every fluorescence intensity measurement, the intensity of the pure anthracene azide **10** was subtracted from the fluorescence intensity of the reaction mixture after each time period and therefore the spectra in Figure 41 A illustrate the pure intensity of the generated click product.

A photoinduced electron transfer (PET) process between the azide group and the anthryl backbone lowers the quantum yield of **10**. The generation of a triazole abolishes this process, increasing the fluorescence of the complex significantly.[242] For this reason, **10** is just weakly fluorescent while **11** is highly fluorescent. Comparing the fluorescence spectra of both (Figure 41 A and B) this is particularly visible, since the fluorescence intensity of pure **10** is multiple orders lower than that of **11**. Furthermore, the fluorescence intensity of **10** decreases significantly after two hours (compare Figure 41 B, curves in brown and ochre), which is not the case for the generated triazole **11**.

According to Sharpless' definition, a click reaction also implies high regioselectivity.[144] However, NMR studies of the reaction of a dibenzocyclooctyne amine derivative with **10** in DMSO point that strain promoted alkyne azide click reaction for the given reactants provides poor regioselectivity and no quantitative yields, as several species were found in the reaction mixture as determined in HSQC and ^{1}H-NMR spectra after a reaction time of one hour at room temperature (Figure 42).

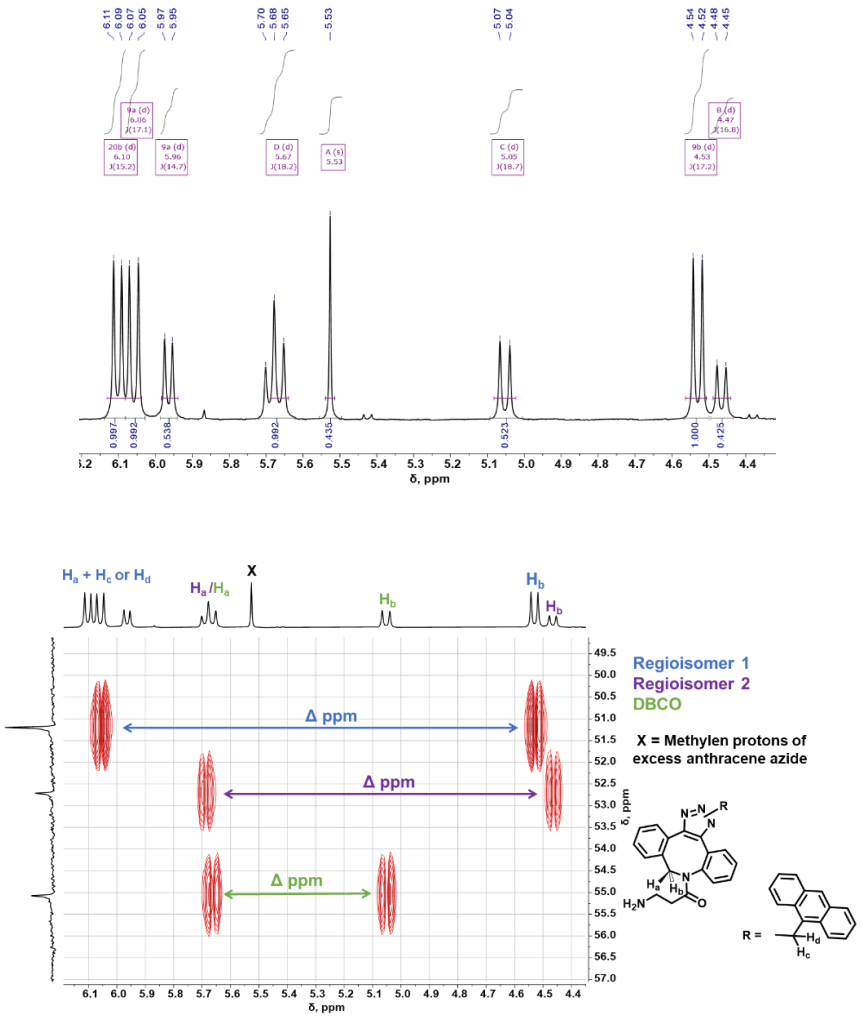

Figure 42: ^{1}H-NMR and HSQC spectra of the reaction of dibenzocyclooctyne amine with anthracene azide **10** for one hour at room temperature measured at 700 MHz in DMSO-d6.

The HSQC spectrum shown in Figure 42 illustrates the signals of the aliphatic diastereotopic protons on the eight-membered ring system. Three distinct pairs (-CH_2) are detected which are well resolved in the ^{13}C dimension. It is obvious that the difference in chemical shifts of geminal proton signals (blue and purple) are comparable whereas the third signal pair has a much lower Δppm (green).

Next to the similar difference in chemical shifts of the protons marked in blue and purple, almost identical coupling constants (~ 17 Hz, see ^{1}H-NMR) of these geminal protons' signals were identified, while the third species reveals a slightly higher coupling constant (~ 18 Hz).
These differences between geminal proton shifts could be explained by a similar geometry in the underlying cyclic system. The findings support the generation of two regioisomers next to another compound with a fundamentally different molecular geometry, which is presumably the non-reacted DBCO ester, since the cyclooctyne has a very high ring tension. The latter is significantly reduced after generation of the triazole by the click reaction with the azide derivative. Additionally, this hypothesis is supported by the occurrence of the singlet X (5.53 ppm), which corresponds to the methylene protons of anthracene azide (protons H_c and H_d of the starting material).
The ^{1}H-NMR spectrum provides information on the proportions between the respective species. Thus, it becomes clear that one of the regioisomers is preferred, because the integrals are higher than the integrals of the remaining species. The signals of the second regioisomer and the DBCO species share approximately equal ratios. This results in an approximate ratio of 50:25:25 (regioisomer 1: regioisomer 2: non-reacted species). It is difficult to say which of the respective regioisomers is preferred since the chemical shifts of the respective isomers are very similar and there is no significant signal to distinguish one from another. Moreover, it is unclear if the different species produce different fluorescent emission spectra which might be invisible due to overlapping of the most abundant species in solution.

The fluorescent properties of **11** lead to the possibility to use **10** for the quantification of DBCO groups on the HES-NC surface. Significant increase of fluorescence intensity of the reaction of **9** and **10** occurs after 15 min indicating that after that time a low signal-to-noise-ratio of fluorescence intensities can be reached. It must be noted that the conversion to **11** is not regioselective, forming at least two species, while the generation of one isomer is preferred. Since 25% of unreacted DBCO species was found after reaction of equimolar amounts of **9** and **10**, it has to be considered, that when no excess of **10** is used for DBCO quantification, this may result in the quantification of less groups than actually present.
In the next section, the binding of **9** to HES-NCs is elucidated using the so-called anthracene azide assay, which was developed in our group.

IV. 3.2.1 Reaction of DBCO-PEG$_4$-NHS ester to HES-NCs and detection using anthracene azide

DBCO-NHS ester (**9**) was added to a HES-NC dispersion (1 wt%), the mixture reacted overnight, was purified and equimolar amounts of **10** were added to the HES-NC dispersion. After addition of azide **10** to DBCO functionalized HES-NCs the fluorescence intensity increases in the same time-dependent manner as after addition of pure **10** to **9**, while pristine HES-NCs do not show an increased fluorescence intensity (Figure 43).

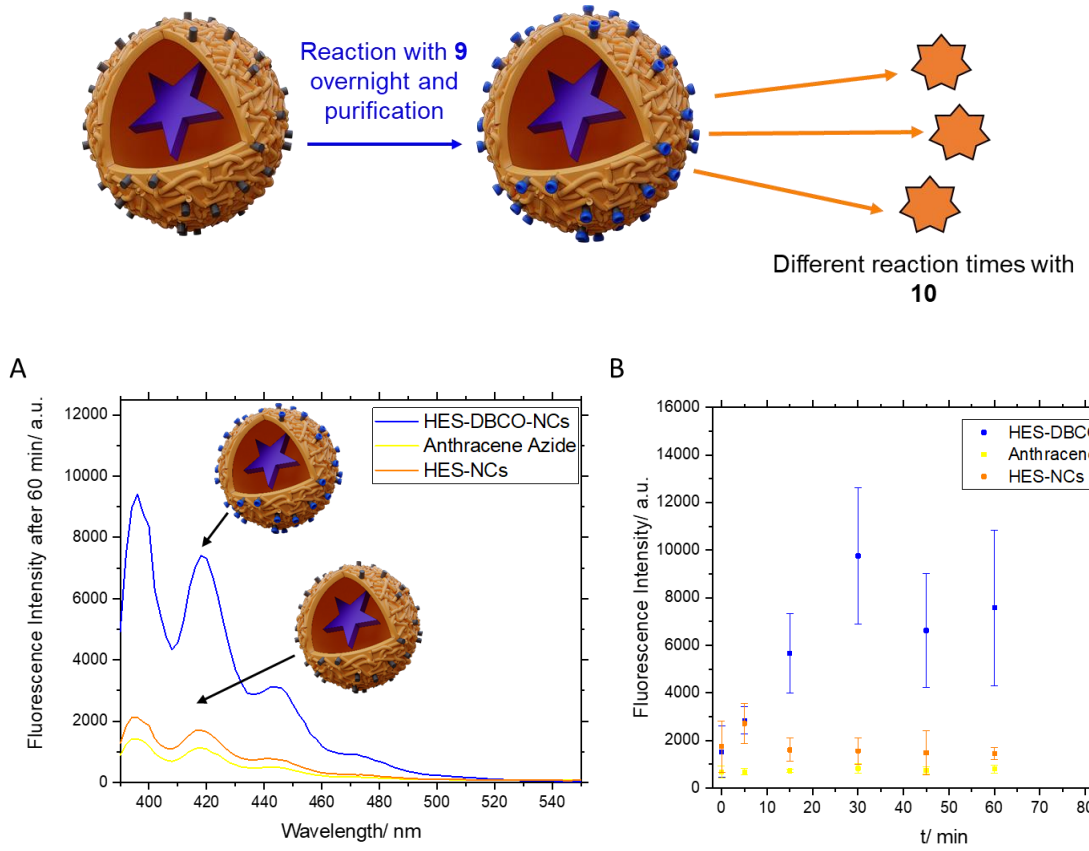

Figure 43: Time-dependent fluorescence intensity spectra of the reaction of anthracene azide (**10**) with DBCO functionalized HES-NCs (addition of 3.3 mg DBCO-PEG-NHS ester per mL NC dispersion). **A:** Fluorescence intensity spectra after a reaction time of 60 min. Blue curve: DBCO-functionalized HES NCs, orange curve: pristine HES-NCs to which azide **10** was added. Yellow curve: the same concentration of pure anthracene azide **10**. **B:** Time-dependent fluorescence intensity measurements of the same samples depicted in **A**.

The fluorescence intensity measurements indicate, that just as with pure DBCO ester (Figure 41 A), the fluorescence intensity of DBCO modified NCs increases significantly in presence of azide **10** and show the same curve progression of the fluorescence emission as with pure reactants. The fluorescence intensity of pure **10** was subtracted from the fluorescence intensity of DBCO modified NCs so that the absolute fluorescence of the complex can be compared. When a time-dependent measurement was performed, it was observed that after 30 min the reaction reached a maximum and stayed at a constant level after the mentioned time (Figure 43 B data points in blue). An overnight incubation does not lead to a significant increase in fluorescence intensity anymore, indicating that the conversion is complete. Fluorescence intensity measurements of pure **10** (Figure 43 B, data points in yellow) and HES-NCs without DBCO functionalization (but with added **10**) (Figure 43 B, data points in orange) reveal a similar emission spectra as observed for the DBCO-functionalized sample, however the intensity is significantly lower than after DBCO functionalization, indicating that there is no click reaction taking place for non-functionalized capsules which prove the functionalization of the NCs with DBCO in a qualitative manner. In addition, the results demonstrate that for a quantitative analysis, a reaction time for at least 30 min should be considered, since after this time period the fluorescence intensity of the formed triazole is significant enough to distinguish from non-functionalized samples.

To evaluate the reaction time of the NHS ester **9** to the capsule surface, equal amounts of **9** in DMSO were added to HES-NCs (1 wt%) and reacted for different time periods.

Afterwards the NCs were purified by centrifugation and equimolar amounts of **10** were added to the modified HES-NCs, reacted for 1 h and fluorescence intensity of the different samples were compared. In each data point the fluorescence intensity of the pure solution of **10** was subtracted from the fluorescence intensity exhibited by the modified HES-NC samples (Figure 44).

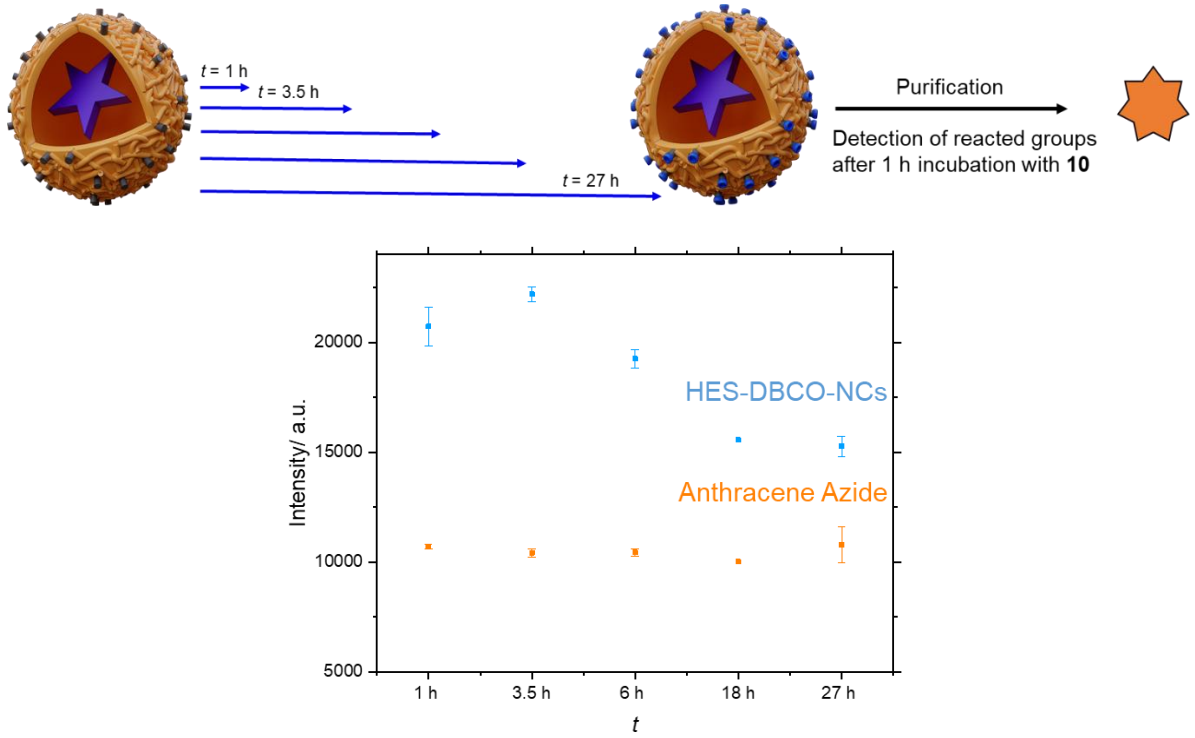

Figure 44: Fluorescence intensity measurements of HES-NCs subjected to **9** for different reaction times. The modified capsules were purified and reacted with **10** for one hour. Measured in DMSO for two dilutions.

As already observed in Figure 43, the DBCO-modified HES-NCs revealed a significant increase in fluorescence intensity in comparison to pure anthracene azide solution. This increase in intensity is already visible after one hour of reaction time of **9** to the capsule surface and increases in the course of 3.5 h, indicating an ongoing reaction of **9** to HES-NCs. After 6 h a decrease of fluorescence intensity was observed and remained at a constant fluorescence intensity level after 18 h (Figure 44).

The observations of Figure 44 point that DBCO **9** reacts at the NC surface in the course of 3.5 h. However, the decrease of fluorescence intensity after a longer reaction time (beginning from 6 h) does not necessarily mean that groups no longer bind to the capsule, but it may indicate a reduction in detectability. For this reason, it is important that reaction times of **9** to the capsule and assay execution are performed in a reproducible manner. The reproducibility of the surface functionalization of HES-NCs with **9** using **10** is discussed in the next section.

IV. 3.2.2 Influences of DBCO binding to HES-NCs

As shown in the previous chapters, DBCO is attached to NCs using an NHS ester. It is well known from literature that successful conjugation using NHS esters are dependent on the pH value.[243] Therefore, it was investigated whether the DBCO-NHS ester attachment to HES-NCs is also subject to pH value dependency. For this reason, HES-NCs of the same dispersion were split up and the pH value was adjusted either directly or after washing up to two times by centrifugation. Two different DBCO concentrations were added to the NCs (1 wt%) in order to compare concentration dependent effects.

After functionalization, the NCs were washed by centrifugation and the fluorescence intensity was checked by adding azide **10** in equimolar ratios. The result of the DBCO quantification for the different conditions and for two different added DBCO concentrations (3.3 mg/mL – high (**A**) and 0.055 mg/mL – low (**B**)) are shown (Figure 45).

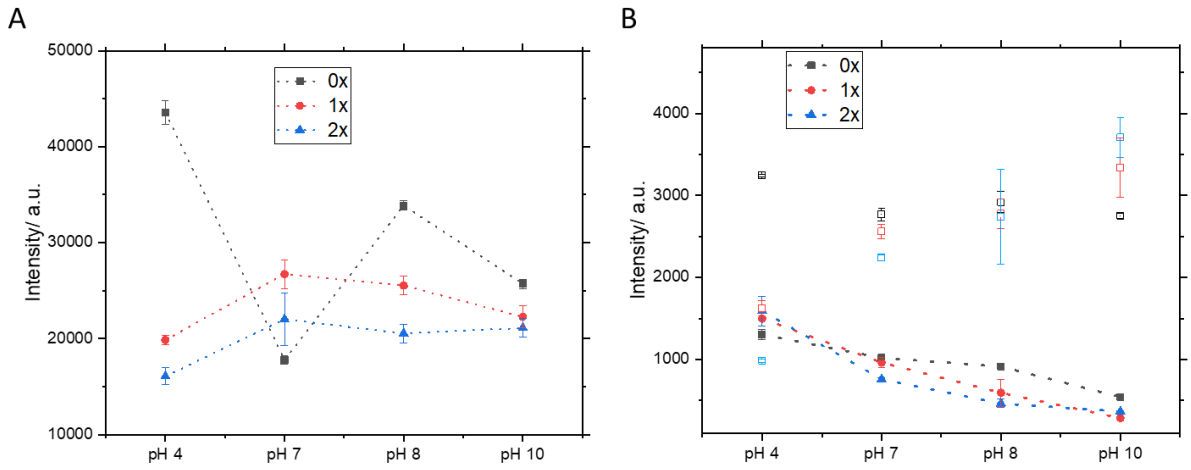

Figure 45: Fluorescence intensity measurements of the DBCO-anthracene azide complex on HES-NCs determined after adjustment of different pH values and after different washing steps (0x, 1x, 2x). **A:** High DBCO concentration (3.3 mg/mL) and **B:** Low DBCO concentration (0.055 mg/mL) added to the NCs. Hollow squares in **B** represent respective supernatants.

No significant changes in fluorescence intensity were observed at pH of 4, 7, 8 and 10 for the high DBCO concentration used (Figure 45 A). Moreover, the number of washing cycles prior to functionalization is not relevant for the binding, as the small decrease in fluorescence intensity is more likely to occur due to material loss during centrifugal washing than due to actual less DBCO attachment. The detected DBCO amount of the non-washed sample (Figure 45 A, black curve), reveals one data point, which shows a drop in DBCO concentration (pH 7), but due to the errors, this change is of no relevance. For low DBCO concentrations added, a slight decrease of fluorescence intensity with increasing pH is detected (Figure 45 B). This suggests that a binding under basic conditions does not perform as well as at neutral or acidic pH. One reason for this trend could be the increased hydrolysis of the NHS ester under alkaline conditions. A too acidic environment might lead to the protonation of amino groups on the capsule surface resulting in a lower binding capacity. However, this is not observed here. In accordance with the decrease of detected DBCO groups at increasing pH value, the DBCO groups found in the supernatant at different pH values for the different washing cycles show the opposite trend, which supports the findings (Figure 45 B, transparent red, blue and black curves). At lower added DBCO concentrations, again, there is no significant difference of detected DBCO groups in dependency of the number of washing cycles observable (Figure 45 B). These findings let conclude, that SDS might not play a significant role for the binding of the DBCO-NHS ester to the HES-NCs.

As already discussed in Section 2.2.1, acidic pH values lower the colloidal stability of the NCs with SDS present in the sample (Figure 23) and might play a role for the detection of the fluorescence intensity of the samples. In the experiments shown in Figure 45, the NCs were purified by washing up to two times. It was therefore also examined how much DBCO is still in the dispersion after an extended washing process and how much enters the supernatant.

Again, different DBCO-NHS ester concentrations were added to a HES-NC dispersion, a high DBCO ester concentration (3.3 mg/mL, Figure 46 A, black curve) a medium DBCO ester concentration (0.55 mg/ml, Figure 46 A, red curve) and a low DBCO ester concentration (0.055 mg/mL, blue curve) and the HES-NCs were washed successively. In each step fluorescence intensity was determined in the dispersion and in the supernatant after addition of the respective amount of **10** (Figure 46 A). The supernatants were collected and also subjected to fluorescence intensity measurements after treatment of azide **10** using the same concentrations as for the respective NC dispersion (Figure 46 B).

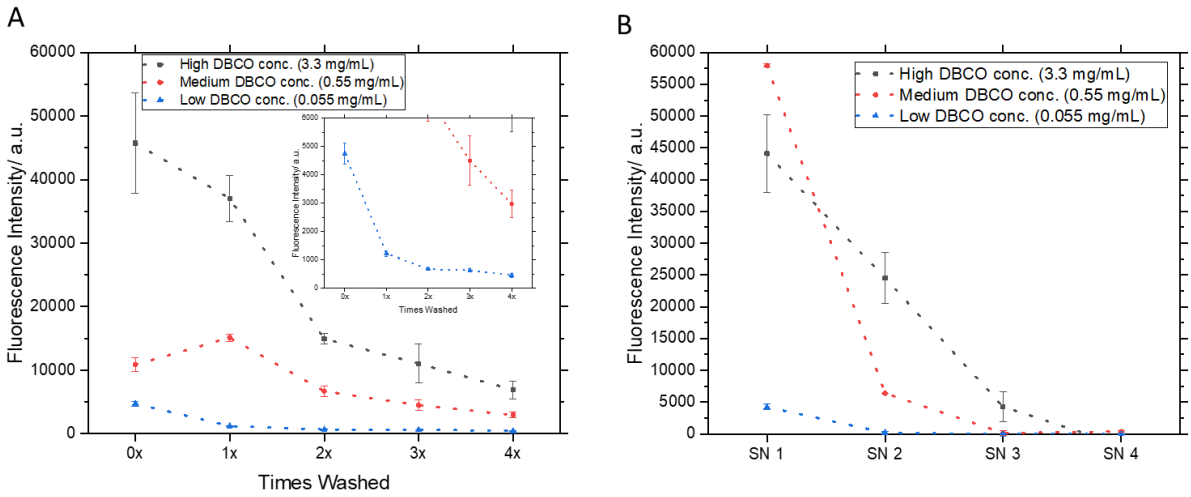

Figure 46: Fluorescence intensity measurements of HES-NCs subjected to different amounts of DBCO-NHS ester **9** and after successive washing cycles. **A:** Measurements of the HES-NCs dispersions. **B:** Measurements of the respective supernatants.

The fluorescence intensity measurements indicate that sufficient DBCO groups were detected in both, dispersion and supernatant (SN) (Figure 46 A and B). If a high DBCO ester concentration (3.3 mg/mL, black curve) is added, significantly more DBCO groups are detected compared to the medium DBCO ester concentration (0.55 mg/mL, red curve) and the lowest concentration (0.055 mg/mL, inlet) (Figure 46 A). After washing steps were performed, detected fluorescence intensities decreased for all samples. Especially for the high added DBCO concentration, washing resulted in a strong decrease after two cycles, while for the other samples, the detected decrease is not as significant. After two washing steps (3x and 4x) only slight reduction of fluorescence intensities of the samples was detected (Figure 46 A), indicating sufficient washing of unbound DBCO groups. The measured intensities of the respective samples of the supernatant reveal a complementary picture (Figure 46 B). A strong drop in fluorescence intensity was detected for the samples with the highest and the medium added DBCO ester concentration (Figure 46 B, black and red curve), revealing a very low intensity for SN3. After 3 washing steps, the measured fluorescence intensity in the supernatant is below those measured in dispersion at high added DBCO ester concentrations. With the addition of the medium DBCO ester concentration (0.55 mg/mL, red curve), this is already visible after 2 washing steps. The fluorescence intensity of SN4 was so low, that it could just be detected in one of the samples (medium DBCO, red curve, Figure 46 B).

This experiment shows that DBCO remains on the capsule being bound to the surface. In most cases, two washing cycles are sufficient to remove large excess amounts of DBCO, as no significant changes are visible in the further washing process.

So far it was demonstrated that different fluorescence intensities were obtained for different additions of DBCO-NHS ester **9** to HES-NCs (1 wt%) and after addition of the respective equimolar amounts of azide **10**. The detected intensities of samples to which a high DBCO ester concentration was added (3.3 mg/mL) and which were washed twice were approx. 20 000 a.u. for all three experiments shown in Figure 44, 45 and 46. For a low DBCO ester concentration (0.055 mg/mL) approx. 1000 a.u. was detected after two washing steps shown in Figure 45 and 46. These results indicate reproducibility of the different samples in the experiments. In the next section it was therefore investigated if the reactivity of the DBCO groups on the NCs was limited in a time-dependent manner.

IV. 3.2.3 Stability of added DBCO groups

To investigate the storage stability of the DBCO groups and to gain insight into how fast the subsequent synthesis steps have to be performed, the fluorescence intensity of the added DBCO ester **9** in aqueous solution is investigated. Therefore, a time-dependent measurement of the fluorescence intensity was performed after addition of azide **10** to DBCO. **9** was constantly stored in an aqueous solution, as it is the case for the DBCO molecules binding to the aqueous HES-NC dispersion and freshly dissolved **10** was added to DBCO samples and the fluorescence intensity checked subsequently. During a time period of 7 h, no change of fluorescence intensity of the triazole derivative **11** could be observed. After 3 days the fluorescence intensity decreased constantly (Figure 47).

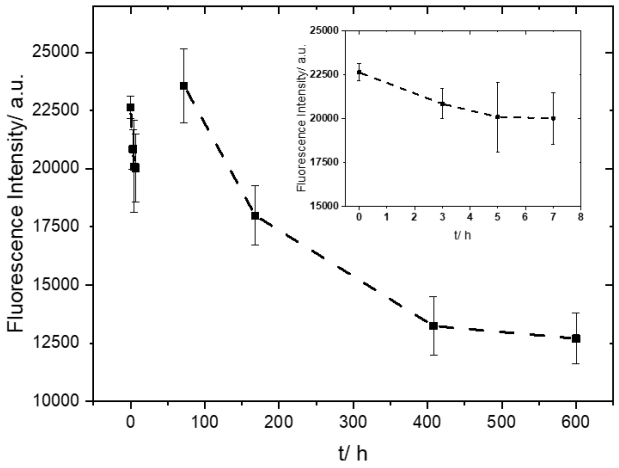

Figure 47: Time dependent decrease of the fluorescence activity of the formed complex of DBCO-PEG-NHS ester **9** with azide **10**.

DBCO ester **9** reveals a stable fluorescence intensity upon reaction with **10** after storing it in aqueous solution for 8 h. A decrease in fluorescence intensity was visible after 3 days, indicating a reduction in reactivity of **9**, which might occur due to the high reactivity of DBCO and its reported sensitivity towards nucleophiles.[244] This shows that after three days, a click reaction can still be efficiently performed using DBCO after it was attached to the HES-NCs. These findings point, that the reproducibility of the click reaction is not affected when this timeframe is complied with.

As well as pure **9**, the fluorescence intensity of the formed triazole **11** decreases over time in aqueous medium as it can be seen in Figure 41 A, in which the fluorescence intensity of **11** is lower after three hours than after two hours.

This decrease in fluorescence intensity of the triazole is attributed to a reduction in the excitation of the fluorophore and not to a chemical instability of the complex, since 1,2,3-triazoles are extremely stable and the 1,3-cycloaddition is irreversible.

In Section 3.2.2 and 3.2.3 it was demonstrated that after two centrifugal washing steps the NCs were sufficiently purified as just a low fluorescence intensity could be detected in the third supernatant. It was also found that a change in pH did not lead to any change in binding. Furthermore, it was shown that the detection of DBCO ester **9** by measuring the fluorescence intensity of triazole **11** depend on added concentrations of **9** on the HES-NCs and on the storage time of **9** in aqueous solution. Therefore, it was analyzed if added concentrations of **9** to the capsules correspond to detected amounts and if the groups can be quantified of the capsule surface in a reproducible manner.

IV. 3.2.4 Reproducibility of detected DBCO on HES-NCs

To determine the reliability of quantification it is recommendable to test the difference in readout of many samples and to determine the limit of detection (LoD).

Therefore, 20 HES-NCs dispersions (1 wt%) which were synthesized in an identical procedure, were modified using 3.3 mg of DBCO-NHS ester per mL dispersion and stirred overnight. After reaction, the HES-NCs were washed twice by centrifugation and the coupling efficiency was determined by a fluorescence intensity measurement using **10**. Illustrated blanks result from the weak fluorescence intensity measured at the same wavelength by pure **10** dissolved in DMSO (Figure 48 A). The resulting size after functionalization was compared to non-functionalized samples and averaged in the graphs (Figure 48 B).

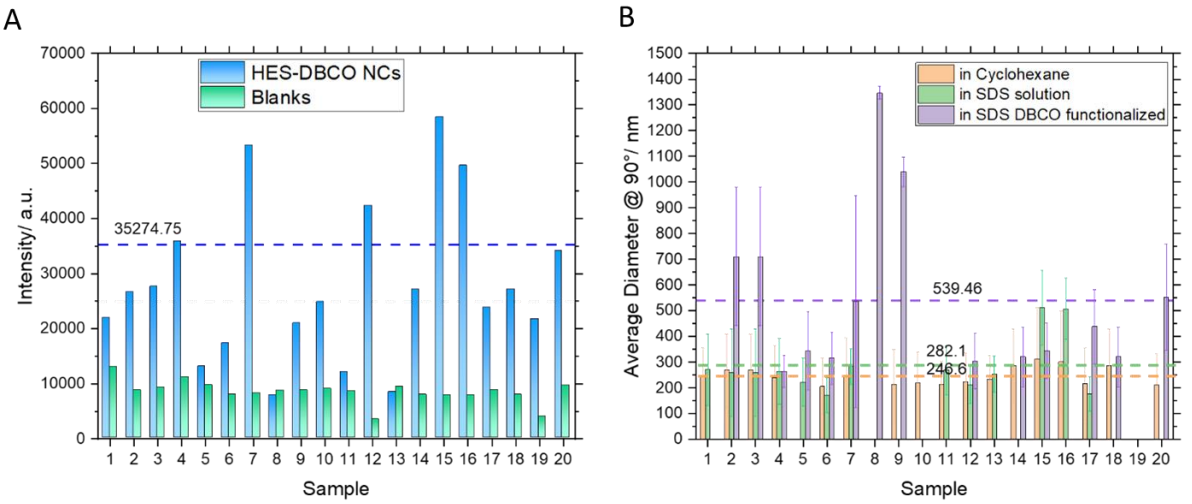

Figure 48: A: Measured fluorescence intensities of different HES-NC dispersions and associated anthracene azide blanks. The blue dashed line reveals the LoD. **B:** Measured average diameters at 90° for the corresponding dispersion in cyclohexane, redispersed in aqueous solution and after functionalization with DBCO ester **9**. The purple dashed line reveals the average diameter of DBCO modified HES-NCs, the green dashed line the average diameter of the HES-NCs after redispersion in SDS solution and the orange dashed line the average diameter in cyclohexane.

Figure 48 A reveals that the fluorescence intensity readout of the samples can alter significantly, while the fluorescence intensity of the measured blanks for each sample stays on a relative constant level and varies around 24% (average fluorescence intensity: 8413.29 ± 2041.49 a.u.).

For the measured HES-DBCO-NCs, the deviation is around 52% (average fluorescence intensity: 27642.43 ± 14287.67 a.u.). The LoD determines the minimum intensity of the sample, to make detection feasible and reliable. The LoD for the 20 HES-NCs samples is given as 35274.75 a.u. and is shown in form of the blue dashed line in the graph (Figure 48 A). In addition, the respective size of the NCs, measured at 90°, were compared to each other in the different synthesis steps (Figure 48 B). It is shown that the diameters obtained in the cyclohexane phase are in average 247 ± 34 nm and therefore do not underly significant variations. The average diameter in SDS solution is 282 ± 107 nm and therefore show a larger variation between the individual samples. This increase of variation can be explained that in every capsule synthesis in cyclohexane, NCs with a specific distribution have been generated which are further varied in the subsequent step, the redispersion. Furthermore, there are minor differences between the individual samples such as the encapsulation of different dyes (SR101 and Cy5 oligo). The majority of the DLS measurements were performed directly after synthesis without removal of SDS. As proof for the reproducibility of the NCs synthesis and since it could already be shown in previous sections that washing steps and the encapsulation of different dyes do not lead to significant changes of the capsule size, some samples were purified by centrifugation and then subjected to DLS measurement. This was for example the case for the SDS phase of sample 16 and therefore all samples were included in the analysis here.

The largest variations can be found for the average diameters after DBCO functionalization of the individual samples. In average a diameter of 540 ± 338 nm was obtained, which represents an increase in size of around 48% in average. According to Figure 48 B, only four samples with average diameters of several hundreds of nanometers are responsible for this enormous increase in size (sample 2, 3, 8 and 9), while the majority of the DBCO functionalized samples are revealing diameters below the mark of 540 nm. None of the samples revealing the large size increase, reached the LoD, sample 8 even shows one of the lowest values, as the fluorescence intensity of the measured HES-DBCO sample and the blank are almost identical. These results could indicate that DBCO addition may cause colloidal instability in some samples, which leads to an increase in size of the NC and prevents active functionalization. If these four samples (2, 3, 8, 9) are excluded, an average diameter of the DBCO-functionalized NC of about 374.42 nm can be obtained, corresponding to a size increase of about 25%. The results of the size analysis, which is illustrated in Figure 48 B, shows clearly that there are similarities between the samples. For all the samples, a significant increase in fluorescence intensity in comparison to the blank was detected, indicating that all samples were modified.

For a few samples (samples 2, 3, 8, 9) the fluorescence intensity measurement as well as size analysis revealed that a sequence of many independently conducted synthesis steps can lead to a considerable variation of generated NCs.

Conclusions can be drawn about the certainty of particular factors, such as the reliable detection of the DBCO groups on the surface as determined exemplarily by the LoD.

It becomes clear that only five samples in the graph cross the blue dotted line and are therefore above the LoD, showing an intensity reliably distinguishable from the blank (sample 4, 7, 12, 15 and 16). Sample 20 is very close to the LoD (fluorescence intensity of 34 055 a.u.).

This result points that the assay gives a reliability of around 25% (sample 20 not included, 30% including sample 20), which means that every fourth sample (every third sample) is reliably detectable with 95% probability. Interestingly, a majority of the samples, which do not exceed the LoD, are found in close proximity of a fluorescence intensity of 25 000 (9 out of 13 samples, grey dashed line). This suggests that these samples may have a similarity in terms of surface coverage of DBCO, although this cannot be confirmed as they are below the LoD.

The evaluation of the reproducibility of the DBCO modification is dependent on the reliability of the detection. With Figure 48 it was shown that the DBCO quantification was performed by fluorescence intensity measurements of triazole **11** revealing reliability of 95% for every fourth (third, including sample 20) sample. Considering the result of the reliability of the DBCO detection by anthracene azide from a chemical point of view, this result is consistent with the experiments on the conversion of the click reaction. It was also shown in the HSQC experiment that the reaction is not quantitative at an equimolar ratio of both reactants leading to two regioisomers and unreacted DBCO. For this reason, the determination of the reproducibility of the detection is an important hint to assess quantification.

IV. 3.2.5 Quantification of DBCO groups on HES-NCs

In our group we have developed an assay that exploits the change of the photochemical properties of **9** using **10** and shows that a quantification on the NCs' surface is possible by adding the appropriate amount of dissolved **10** to DBCO-functionalized NCs and measure the fluorescence emission of the formed complex at 414 nm at an excitation of 370 nm.[225] According to the spectra in Figures 41 and 43, it was referred to only one of the maxima for the quantification of DBCO groups on HES-NCs.

Quantitative analysis of DBCO-functionalization of HES-NCs was performed by the anthracene azide assay[225]. For the determination, it is necessary to know how many capsules are present per mL dispersion and the DBCO concentration per mL dispersion. For the latter, the measured fluorescence intensities were used. The following Eq. 7 demonstrates how the amount of DBCO was calculated.[225]

$$\text{Number of detected DBCO groups per mL} = 400 \times \left(\text{Number of added DBCO groups per well} \times \frac{\frac{\text{Intensity}_{(\text{HES DBCO NC+Anthracene azide})}}{(\text{Intensity}_{(\text{Anthracene azide blank})} - \text{Intensity}_{(\text{HES DBCO Blank})})}}{48}\right) \qquad \text{(Eq. 7)}$$

In Eq. 7, the actually added amount of DBCO-NHS ester per well is multiplied by a factor resulting from the calculation of the respective fluorescence intensities. The value of the intensities is divided by 48, since the quantum yield of the formed triazole complex is 48 times higher than that of the unclicked anthracene azide.[225] Since the fluorescence reaction is only performed with 25 µL NC material and the dispersion is also diluted by 1 to 10, the final multiplication factor is 400 to obtain the amount of DBCO per mL. Exploiting the fluorescent properties and solving Eq. 7 is an easy way to compare DBCO concentrations in different samples and to assess the reproducibility of the DBCO attachment to HES-NCs. The fact that the added amount of DBCO ester is included in the calculation, leads to an inaccuracy of the calculation of the precise value, since not all of the added DBCO ester will be present on the capsule surface, since it was removed by washing steps prior to measurement.

By means of Eq. 7, the DBCO groups per mL dispersion was calculated for 12 samples prepared by the same procedure exhibiting the same solid content (Figure 49).

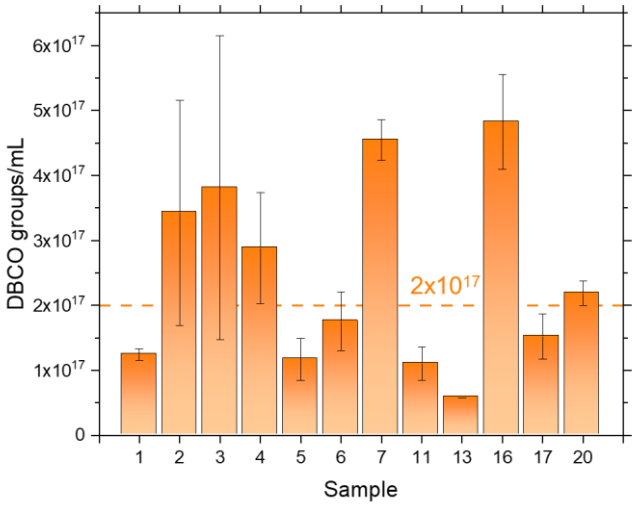

Figure 49: Calculated DBCO groups per mL dispersion using equation 7 for 12 HES-NC dispersions exhibiting the same solid content. The orange dashed line represents the average number of DBCO groups/ mL.

Figure 49 shows the number of DBCO groups found per mL in 12 HES-NC dispersions prepared on different days modified with the same amount of DBCO. The same samples are depicted in Figure 48, in which the fluorescence intensities are illustrated (Figure 48 A) and the averaged diameter in different phases (Figure 48 B). The average number, which is represented by the orange dashed line, is 2.42 x 10^{17} groups per mL (rounded to 2 x 10^{17} groups/mL in the graph). All samples reveal detected DBCO concentrations in the range of 10^{17} groups per mL. Three samples (7, 16 and 19) clearly exceed the average mark and show concentrations which are partially more than double as high as the average amount. Samples 7 and 16 already significantly exceeded the LoD, which was shown in Figure 48 A. However, sample 19 did not exceed the LoD but still reveals a high DBCO concentration. The samples 2 and 3 also clearly exceed the average amount but are revealing high standard deviations. Standard deviations were given by the measurements of two dilutions of each sample (1:10 and 1:100). All the NCs were measured by an anthracene azide assay after they were purified with the same procedure and concentrated to a solid content of 1 wt% to easily compare the samples with each other. However, obtaining the exact solid content for each sample is due to material loss during purification difficult to achieve. Since the detected DBCO amount was correlated with the capsule diameter, the number of DBCO groups per NC was calculated in the next step. Using Eq. 6, the DBCO groups per NC were calculated at a solid content of 1 wt% and an approximate density of 1 g/cm^3 for the samples illustrated in Figure 49. The obtained values for the number of NCs per mL as well as the number of DBCO groups per NC are shown (Table 10).

Table 10: Calculated number of NCs per mL dispersion by means of the average obtained diameter in SDS as well as DBCO groups per NC from 12 different HES-NCs dispersions. Samples with high standard deviations in the determination of DBCO groups/mL are marked in red. Samples which exceeded the LoD are marked in blue.

Sample	Average diameter in SDS solution at 90°/ nm	DBCO-Gr./mL X 10^{17}	Amount of NCs/ mL dispersion (1 wt%)	DBCO/ NC	DBCO/nm^2
1	271	1.24	9.59×10^{11}	129 472	0.56
2	260	3.43	1.09×10^{12}	313 475	1.48
3	260	3.81	1.09×10^{12}	348 477	1.65
4	265	2.89	1.02×10^{12}	282 441	1.28
5	223	1.17	1.73×10^{12}	67 448	0.43
6	172	1.75	3.73×10^{12}	46 922	0.50
7	283	4.55	8.40×10^{11}	541 441	2.15
11	270	1.10	9.68×10^{11}	113 911	0.50
13	254	0.58	1.17×10^{12}	49 486	0.24
16	508	4.82	1.46×10^{11}	3 312 354	4.08
17	177	1.52	3.45×10^{12}	44 060	0.45
20	231	2.19	1.56×10^{12}	140 482	0.84

The amount of material per capsule was kept constant by adjusting the concentration, so the volume of the capsules calculated from the radius has a great influence on the calculated number of capsules per mL. It becomes clear that if the measured capsule diameter is reduced to for instance 172 nm (sample 6), a threefold increase of the capsule quantity per mL dispersion is determined compared to a capsule diameter of 260 nm (sample 2, 3, 4). These findings emphasize that DBCO quantification is strongly dependent on the determined capsule size and is therefore relying on a precise light scattering analysis. In Section 2.1 the capsule diameter of many different HES-NCs was determined. The result was a value of 222 nm ± 69 nm in SDS solution (Figure 22). All measured diameters from Table 10 (except for sample 16) are in this range.

Sample 16 reveals a very high number of DBCO groups per NCs due to the large diameter obtained. Therefore, sample 16 was excluded from the calculation of the average, as were samples 2 and 3, which showed very high standard deviations (values marked in red). The samples marked in blue (4, 7 and 20) were exceeding or were at the LoD showing unambiguous fluorescence intensity from the generated triazole. Including all values of Table 10, except for the ones marked in red, the average amount of DBCO groups found on HES-NCs is 157 295.74 for n = 9 samples.

To calculate the groups independently from the light scattering results, the density of DBCO groups per nm^2 was determined. The results in Table 10 reveal that the number of DBCO groups found per nm^2 was between 0.24 and 2.15. Five samples were found whose DBCO group density was in average 0.49 ± 0.05 DBCO groups/nm^2, demonstrating reproducible group densities with a standard deviation of 10% (samples 1, 5, 6, 11 and 17).

The samples marked in blue (samples 4, 7 and 20), showed higher DBCO densities of 1.42 ± 0.67 DBCO groups/nm^2 revealing a higher standard deviation of 47%. In accordance with the detected DBCO groups per NC, in sample 16 an exceedingly high DBCO density of 4 DBCO groups/nm^2 was detected. The large diameter of more than 500 nm reveals that the NCs aggregated during DBCO modification which resulted in an inefficient purification of residual DBCO from the NCs and is therefore explaining the high detected DBCO concentrations. Sample 13 revealed an exceedingly low surface coverage (0.24 groups/nm^2) which was attributed to insufficient binding. It was found that sample 13 was the only sample which was functionalized with DBCO two months after water transfer was performed. This observation indicates that an alteration of the capsule surface during storage in water phase occurs, leading to a reduced binding when DBCO attachment is performed. Samples 13 and 16 were therefore excluded from further processing. From the 12 samples presented in Table 10, 10 samples were found to be suitable for further processing and analysis since they revealed a suitable surface coverage in a reproducible manner and moreover revealed capsule diameters appropriate for further modification.

To provide a second method for the DBCO determination, an external calibration by preparation of a serial dilution of equimolar amounts of DBCO ester **9** with freshly dissolved azide **10** in DMSO, was performed. The fluorescent triazole **11** shows a concentration-dependent linear correlation with the measured fluorescence intensity (Figure 50).

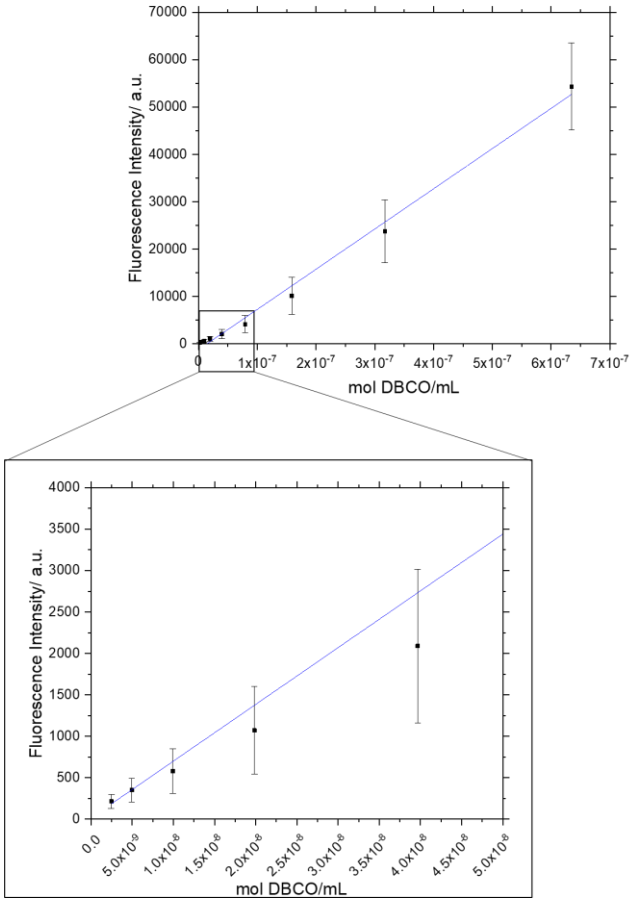

Figure 50: Concentration-dependent average calibration curve of four different calibrations performed of the reaction of DBCO-PEG-NHS ester **9** with anthracene azide **10**.

In order to determine the reproducibility of the concentration to intensity correlation of the formation of triazole **11,** four calibrations were prepared at different days with freshly dissolved **10** which are shown as an averaged calibration curve in Figure 50. The linear correlation of the concentration of complex **11** with the fluorescence intensity illustrated as averaged curve, reveals a high reproducibility, since the serial dilution was performed four times independently of each other. For this reason, an external calibration which has been generated with the help of a dilution series can be used to determine the concentration of DBCO in an unknown sample. The standard deviation of the four measurements reveals a R^2 of 0.95. The total amount of added DBCO ester was recovered in the sum of detected DBCO concentrations in supernatants and in the dispersion using the standard calibration of complex **11** for DBCO quantification (Figure 51 A). Moreover, it was shown that it is possible to bind DBCO in different concentrations to the capsule. With this knowledge, the DBCO density on HES-NCs was determined for the different added DBCO ester concentrations, if the size of the NCs is known (Figure 51 B). Moreover, the two different quantification methods (by calculation or by external calibration) were compared with each other for the different bound DBCO concentrations determined as groups per nm^2 (Figure 51 C).

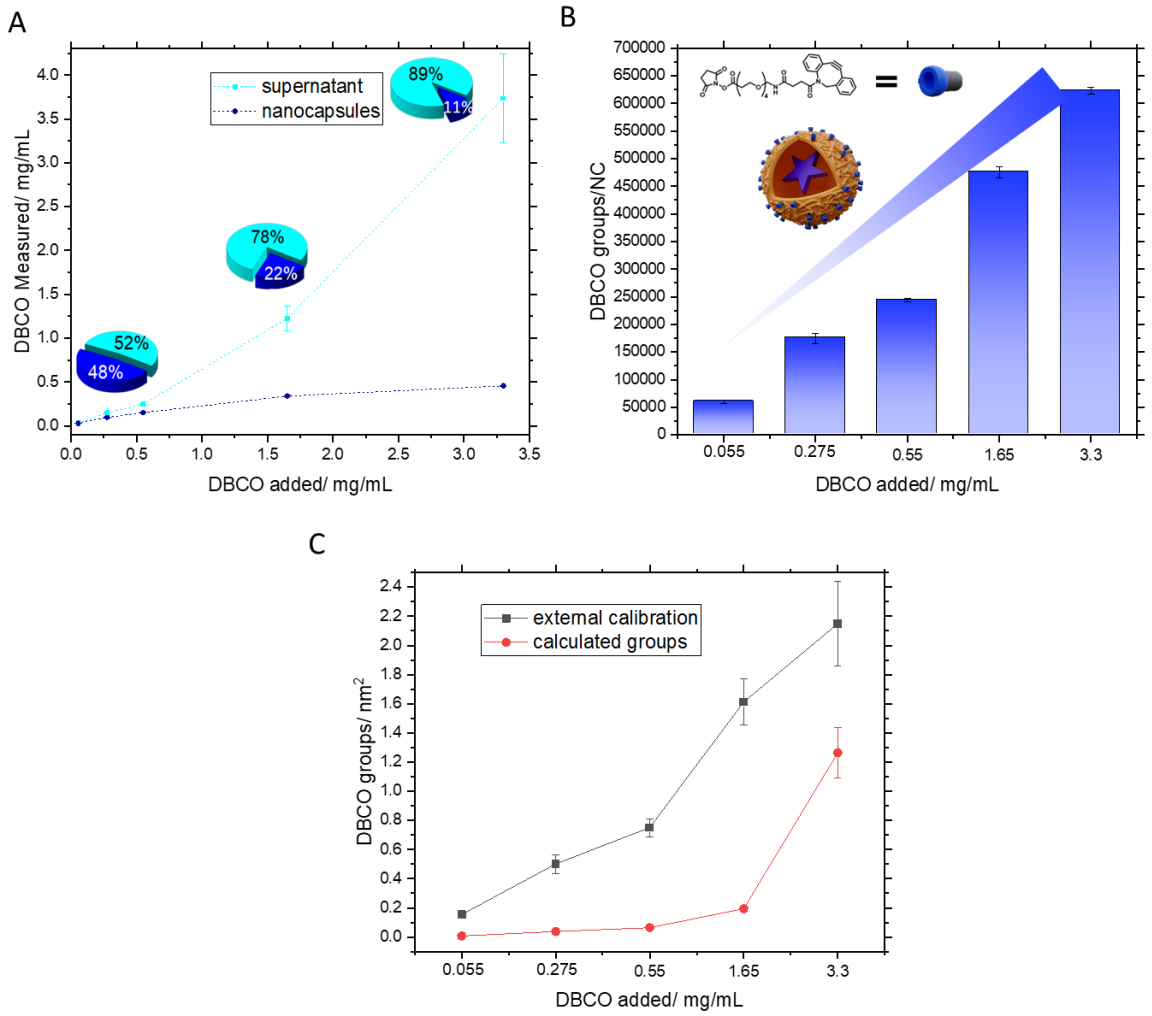

Figure 51: **A:** Comparison of initially added and measured amounts of DBCO to the NC dispersion. The data points/ pie charts in cyan represent the DBCO found in the supernatant, while the data points /pie charts in blue represents the DBCO found in the NC dispersion after addition of different DBCO ester concentrations and subsequent washing. **B:** Total amounts of DBCO on the NC surface in groups/NC. **C:** DBCO groups per nm^2 determined for different bound DBCO concentrations to HES-NCs determined by an external calibration (black curve) and determined by calculation (red curve)

Using a standard calibration of the formed complex, the amount of DBCO on the NC surface in aqueous dispersion was determined. At concentrations starting from around 0.5 mg/mL (4.635 x 10^{17} DBCO groups/ mL) and higher, more DBCO was found in the supernatant than in the NC dispersion, which shows that a surface modification of the HES-NCs with DBCO-NHS ester **9** at such concentrations does not lead to an efficient attachment anymore. The fluorescamine experiments in Section 3.1.2 demonstrated that for sample F1 (Figure 38, blue data points, sample with 6% HES) at a solid content of 1.8 wt% around 1.498 x 10^{17} NH_2 groups /mL were found. Considering the higher solid content (1.8 wt%) and the increased HES concentration used, the number of NH_2 groups/mL for HES-NCs synthesized with 3% HES can be estimated to around 4.161 x 10^{16} NH_2/mL for 1 wt%.

This means that at an added DBCO concentration of 0.55 mg per mL dispersion, an excess of DBCO to amino groups of approximately 10 to 1 was applied. Therefore, as DBCO concentrations higher than 0.55 mg/mL were added, more DBCO was found in the supernatant than in dispersion (Figure 51 A, cyan curve). The linear increase of DBCO in the supernatant between a concentration of 1.6 mg/mL and 0.5 mg/mL is not as steep as at higher concentrations, which could indicate that interactions between DBCO and the dispersion within this concentration window still occur. The curve for the DBCO amounts detected in the NC dispersion reveals a DBCO saturation of the HES-NCs dispersion at around 1.5 mg/mL of DBCO, since a constant level of DBCO is reached (Figure 51 A, blue curve). The less DBCO was added to the dispersions, the more was also found bound on the NCs and not free in the supernatants (Figure 51 A, pie charts), indicating binding of DBCO ester to the HES-NCs. Figure 51 B reveals that there is an increasing number of attached DBCO groups per NCs depending on the addition of DBCO ester, revealing adjustability of the DBCO concentration on the HES-NCs. Up to 600 000 groups were thus detected on the capsule. The error bars refer to measured fluorescence intensities and are comparably low (deviation 1-5%). At an addition of 0.055 mg of DBCO per mL of dispersion, approximately 60 000 groups per NC were detected. According to the calculations mentioned before, 0.055 mg DBCO per mL corresponds approx. to a DBCO to amino ratio of 1 to 1. Between the addition of 1.65 mg DBCO/mL and 0.55 mg/mL a stronger decrease in DBCO groups per capsule were detected than with the other values. This is surprising, because in Figure 51 A, the curve in this area tends to flatten out, and accordingly the curve for the detected amounts of DBCO in the supernatant starts to rise. Since the capsule size changed slightly depending on the degree of modification, this differences in the concentration-dependent evaluations of Figure 51 A and 51 B becomes apparent here. For this reason, the detected DBCO groups per nm^2 were analyzed and revealed as expected a concentration-dependent decrease of detected groups with reduced addition of **9**. The DBCO groups per nm^2 were determined by either detecting the DBCO amount by external calibration (Figure 51 C, black curve) or by using Eq. 7 (Figure 51 C, red curve). Figure 51 C reveals that for the highest DBCO concentration added (3.3 mg/mL) 2.2 ± 0.2 groups/nm^2 were found determined by external calibration while 1.3 ± 0.2 groups/nm^2 were found determined by the calculated method. These detected values are very similar to each other and therefore demonstrate that the range of the surface coverage was reliably detected. At an added concentration of 1.65 mg/mL a significant higher DBCO surface coverage was found by the external calibration than by the calculated method. It is expected that the external calibration provides more accurate values, since the calculated method involves assumptions, which may lead to underrepresentation of detected groups.

Accordingly, for lower added concentrations, lower surface loadings were found and the values of the two methods increasingly converged. Depicted error bars were given as the percentage error of the sum of the error of the fluorescence measurement with the error of the size determination and are in a range between 8-13%. The results demonstrate a high surface coverage of the capsules by DBCO at added DBCO concentrations of 3.3 mg/mL with adjustability to a surface coverage to approx. 0.1 DBCO groups/nm^2.

In summary, in this section the binding of DBCO ester **9** to the HES-NC and detection using anthracene azide **10** was described. It was shown that **10** can be used to quantify DBCO. Using a dilution of the fluorescent triazole **11,** a standard calibration was performed and the number of DBCO groups on the capsule and in the supernatant were compared to each other. It was shown that the number of DBCO groups on the capsule could be adjusted in a range between 2.2 and 0.1 groups per nm^2. It should be noted that only one sample in four is detected with 95% confidence using the assay. This could be due to the fact that the click reaction is not quantitative.

IV. 4. Biofunctionalization of HES-NCs and resulting biological properties

After functionalization of the HES-NCs with DBCO, any azide-modified biomolecule can be bound by a copper-free click reaction.[176] As the strain promoted alkyne azide click reaction (SpAAC) can be performed very efficiently in aqueous solution at room temperature, it is especially convenient for sensitive biomolecules such as proteins, as they can be prone to denaturation or even degradation at elevated temperatures or different pH values.

Since the SpAAC reaction is very reliable, it is a suitable reaction to apply controlled amounts of azide-terminated molecules in a reproducible manner. Especially for immunological processes in the human body, specific amounts of certain messenger molecules or the multiplicity of signaling components are crucial. This section introduces the binding of two molecule classes, which are significantly involved in binding to specific receptors, triggering immunological processes. Both examples of biofunctionalization demonstrate that HES-NCs were reproducibly synthesized and endowed with specific functions to induce biological responses.

IV. 4.1 Binding of defined amounts of interleukin-2 (IL-2) to HES-NCs for the activation of specific T-cell subpopulations

In the first section the attachment of specific amounts of the protein interleukin-2 (IL-2) to HES-NCs was investigated and different parameters were varied in order to analyze the modification (Table 11).

Table 11: Synthesis step and analysis of HES-NCs for the functionalization with azidated IL-2.

Step	Changed parameter	Detection method
Modification of IL-2	Attachment of different linkers	SDS PAGE
	pH	nanoDSF, MALDI-ToF
Surface-functionalization of HES-NCs with IL-2	Binding of different amounts of IL-2	Flow cytometry and secondary antibody, ELISA
	Functionality of bound IL-2	CTLL-2 Assay

IL-2 is a 15 kDa protein which is predominantly secreted by activated T-cells and was one of the first immunotherapeutics used against cancer.[245] IL-2 consists of six α-helices containing 132 amino acids from which 10 amino acids are lysines, which are usually positioned on the exterior of the protein. Figure 52 shows the crystal structure of human IL-2 with highlighted lysines in cyan.

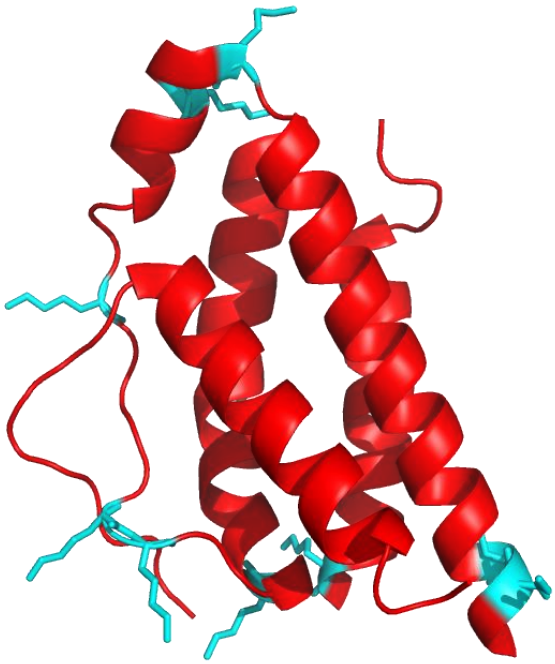

Figure 52: Crystal structure of Interleukin-2 (IL-2) with lysines highlighted in cyan.[246]

The crystal structure shows that the lysines of IL-2 (11 lysines from a protein sequence of 150 amino acids in total), are directed to the exterior and thus offer a suitable possibility to attach linker molecules to the protein. Moreover, there are three cysteines in the central part of the protein, of which at least one can be used for binding. MALDI-ToF is a suitable method to confirm the modification of proteins. It is important to preserve the structure of IL-2 after modification so that the biological activity is not affected. To address the lysines of the protein, NHS esters of azide-containing linkers were reacted with IL-2. In order to analyze the protein conformation after the modification is completed, differential scanning fluorimetry (nanoDSF) measurements were performed.

IV. 4.1.1 Modification of IL-2 with azide-terminated linkers via NHS esters

The modification of the protein is a crucial step for the successful binding on the HES-NCs.

For adding azide groups to IL-2, a commercially available azide linker with flexible PEG spacer was chosen (**12**). Furthermore, a rigid azide linker was synthesized (**13**). These compounds were either used in a threefold excess or in a 1 to 1 molar ratio to the protein. Furthermore, in one sample a subsequent pH adjustment was performed after addition of the linker. Based on the different reaction conditions, the influence of the linker constitution and pH for the attachment of azide-terminated linkers to IL-2 was analyzed (Figure 53).

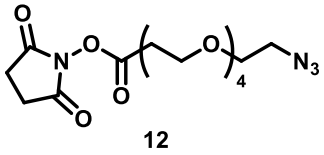

12

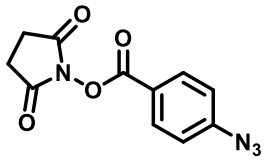

13

Sample	Reaction conditions
IL-2 -1	3-fold molar excess of azide-PEG$_4$-NHS ester **12** in PBS, pH 7.4, w/o pH adjustment
IL-2 -2	3-fold molar excess of azido benzoyl NHS ester **13** in PBS, pH 7.4, w/o pH adjustment
IL-2 -3	1-fold molar excess of azide-PEG$_4$-NHS ester **12** in PBS, pH 7.4, w/o pH adjustment
IL-2 -4	3-fold molar excess of azide-PEG$_4$-NHS ester **12** in PBS, pH 7.4, with pH adjustment to 7.6

Figure 53: Structures of azide-PEG$_4$-NHS ester **12** and azido benzoyl NHS ester **13** used for the modification of IL-2 and used reaction conditions.

In the reaction conditions shown in Figure 53, in three samples there was no pH adjustment of the IL-2 solution after addition of the linker. The addition of the linker which was dissolved in DMSO led to shift to slightly more acidic pH values (~ 7.2). Therefore, in sample IL-2-4, the pH value was adjusted to pH = 7.6 after addition of the linker, since earlier studies proved pH 7.6 to be optimal for the binding of linker molecules by NHS chemistry to IL-2.[123,176] The linkers were reacted with the protein for one hour at room temperature and afterwards dialyzed against deionized water. A quick and convenient test whether one of the reaction conditions resulted in azide-functionalized IL-2, was performed by incubating a DBCO-modified PEG (5 kDa) with the modified protein and qualitatively evaluating it by SDS PAGE after purification (Figure 54).

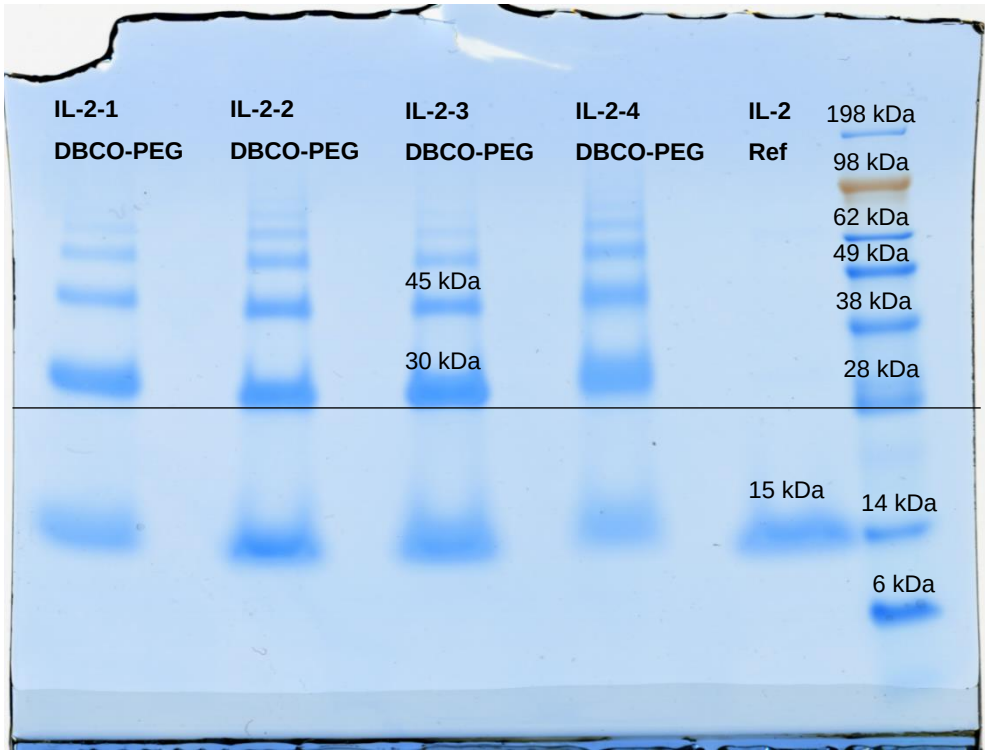

Figure 54: SDS PAGE of azide modified IL-2 using the reaction conditions shown in Figure 53 after reaction of DBCO-PEG (5 kDa).

All samples applied to the gel led to an expected band at 15 kDa, which represents the molecular weight of IL-2. The reference sample (IL-2 Ref) represents the unmodified protein to which no azide linker and no DBCO-PEG was added. Although the sample preparation was identical for all samples and SDS and reducing agent were added to all samples, the modified proteins IL-2-1 – 4 showed dimers and trimers, (30 and 45 kDa). Dimerization and generation of other multimers are common for IL-2 and could be related to the fact that IL-2 has a balanced amount of hydrophilic and hydrophobic helices that prefer certain arrangements.[247] A closer look reveals further differences. The bands of samples IL-2-1 and IL-2-4 have slightly higher molecular weights (ΔM_w ~ 5 kDa) than the bands found for the samples IL-2-2 and IL-2-3 at comparable molecular weights (black line, Figure 54). The same phenomenon can also be observed at 15 kDa and at 45 kDa. The binding of DBCO to the azide linker attached to IL-2 leads to a gain of molecular weight of the proteins as observed by the lift of the bands, indicating a reaction in samples IL-2-1 and IL-2-4 leading to modifications of the IL-2 and therefore qualitatively confirms a successful modification. In conclusion, it was shown that the modification of IL-2 with linker **13** (IL-2-2) and using a 1 to 1 ratio of linker **12** to protein (IL-2-3) did not lead to the same result. In the following, it was clarified whether the modification changes the structure of the protein.

Since a threefold molar excess of the NHS ester **12** (condition 4, Figure 53) proofed to show promising results in the biomodification of IL-2, it was investigated, if the applied modification or the use of different pH, changes the structure of IL-2. For this reason, differential scanning fluorimetry (nanoDSF) measurements of different IL-2 samples were performed by taking the modification and the pH into account and comparing it to unmodified protein (Figure 55).

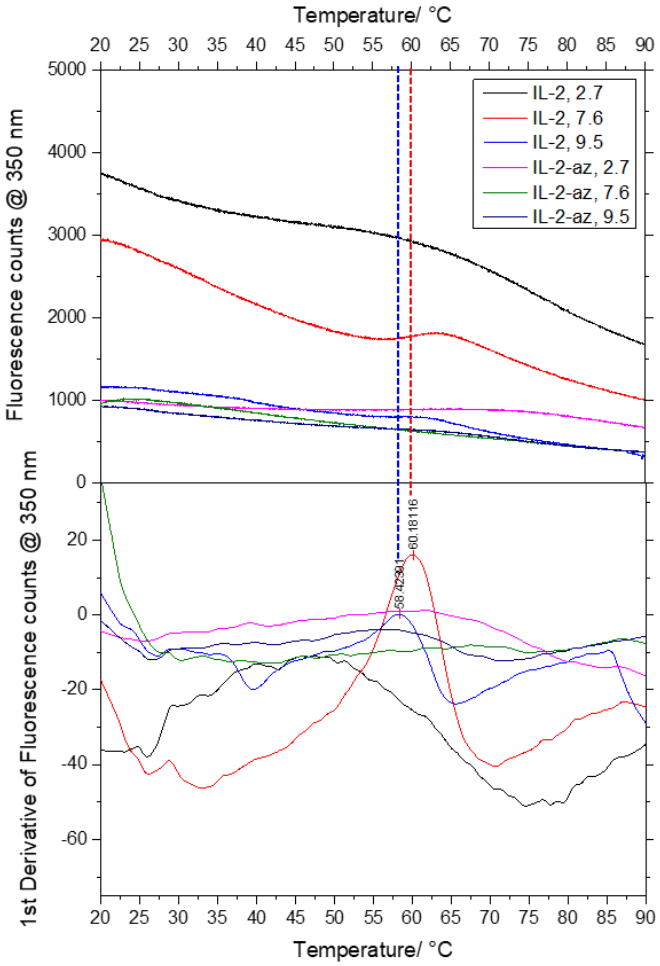

Figure 55: Differential scanning fluorimetry (nanoDSF) measurement of different IL-2 samples at three different pH, modified with azide PEG NHS ester (3-fold excess, IL-2-az) in comparison with unmodified protein.

The melting point of IL-2 was obtained from the first derivative of temperature dependent fluorescence intensity measurement at 350 nm determined by nanoDSF. For native IL-2 in phosphate buffer at pH 7.6 (Figure 55, red curve), the melting point was determined to be around 60.2 °C, while for IL-2 in phosphate buffer at pH 9.5, the melting point shifted to around 58.4 °C (Figure 55, blue curve). At an acidic pH of 2.7 (Figure 55, black curve), IL-2 shows a broad peak in the first derivative of the fluorescence intensity measurement, which is visible between 30 °C and 75 °C. At pH 2.7, changes in fluorescence intensity occured at low temperatures and no specific melting point upon heating was observed, indicating a preliminary change of the protein structure due to the change in pH or ionic strength. However, functionalization with azide-PEG-NHS ester results in irreversible conformational change of the protein since no fluctuations in temperature-depending fluorescence intensites were registered. These observations are independent of the pH value (Figure 55, pink curve, green curve, dark blue curve). Although nanoDSF measurements indicate that covalent functionalization of IL-2 by NHS linkers change the conformation of the protein, it still needs to be proven how many linkers are attached to the protein and if IL-2 is functional despite of the conformational changes it might undergo.

To prove covalent binding of the azide-PEG-NHS ester to IL-2, MALDI-ToF measurements were performed. With the help of MALDI-ToF, a very gentle ionization method was used which is well established within the analysis of biomolecules.[248]

The number of azide groups attached to the protein were confirmed by the corresponding mass patterns in the MALDI-ToF spectra (Figure 56).

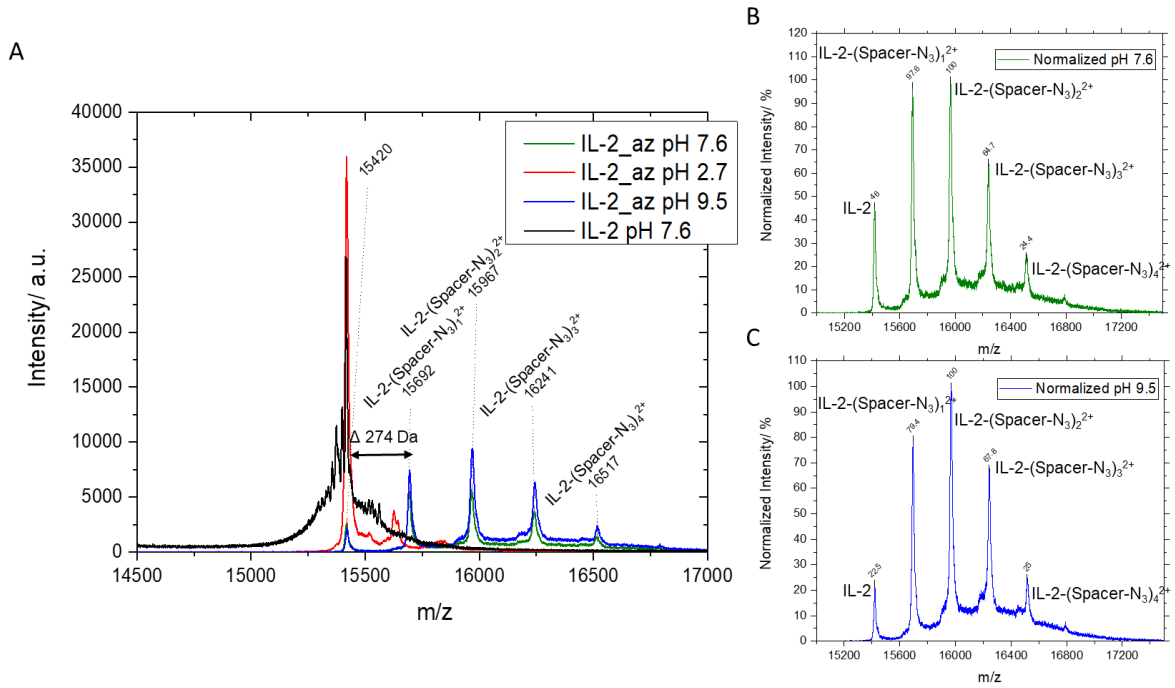

Figure 56: MALDI-TOF spectra of azidated IL-2 by NHS-PEG-azide **12** using different pH values (*α*-cyano-4-hydroxy cinnamic acid was used as matrix). **A:** Mass spectra overlay of different conditions. The black curve shows unmodified IL-2 (15420 Da), while the other curves (green, red and blue) show azidated IL-2 which reacted using three different pH values. The shown mass-to-charge ratios depict the different numbers of linker molecule attached to the protein. **B:** Normalized relative intensity of mass patterns after functionalization of IL-2 at pH 7.6. **C:** Normalized relative intensities of mass patterns after functionalization of IL-2 at pH 9.5.

The mass spectrum highlighted in black was obtained from the IL-2 reference sample prepared in phosphate buffer at pH 7.6 and reveals a mass of 15420 Da which agrees with the values given by the supplier and by literature (15.5 kDa).[249] The observed pattern of 274 Da between the signals (Figure 56 A, blue and green) corresponds to the mass of a single linker molecule **12**. These findings demonstrate that **12** attaches to the protein up to 4 times at neutral (green curve) and basic pH (blue curve). At pH 2.7 (Figure 56 A, red curve) this pattern was not observed, indicating no attachment of **12** to the protein, since at acidic pH the NHS ester **12** did not react with the protein, due to charged lysine groups. Comparing the intensities of the signals of modified IL-2 samples (blue and green) we conclude, that although there is a threefold molar excess of **12** in the reaction mixture, there is unmodified IL-2 present. To compare the obtained signal intensities given for the modified protein in the mass spectra, the detector intensity was normalized to 100% for the most intense signal (Figure 56 B and C). In both mass spectra, the most intense signal corresponded to the IL-2 sample with two bound azide linkers **12**. However, the mass patterns reveal minor differences in the composition of modified IL-2 for the different pH values.

If the relative intensities of the individual signals are considered in the sum of the total intensity, a balanced ratio of about 30% for the mono- and the double-modified IL-2 was obtained for the reaction at pH 7.6 (Figure 56 B). In contrast, a slightly higher proportion of the double-modified protein was obtained at pH 9.5 (Figure 56 C). The proportion of threefold-modified IL-2 also appeared to be slightly higher at pH 9.5 than at pH 7.6, but in return the proportion of unmodified protein was more significant at neutral pH than in the basic range.

For the fourfold modified variant, similarly low percentages were found for both pH values. The MALDI-ToF experiments demonstrate that IL-2 can be modified with linker **12** at pH 7.6 and pH 9.5 leading to a different composition of single and multiple modified protein. Hence, the results indicate that adjustment of the pH value is important for a reproducible attachment of linkers to the protein and consequently also for reproducible binding to the NCs.

IV. 4.1.2 Click and detection of azide-modified IL-2 to DBCO modified HES-NCs

After modification of IL-2, it was used to functionalize HES-NCs by copper free azide alkyne click reaction. The modified IL-2 was added in different ratios to the DBCO-functionalized HES-NCs in dependency to detected DBCO groups on the capsules' surface. The first step was to analyze how the binding of the protein to the NC could be detected. Thereafter, the binding of IL-2 was shown in a quantitative and concentration-dependent manner. Moreover, the influence of different IL-2 preparations on the detected amounts on the capsule were investigated. These findings are important to determine optimal reaction conditions and thus provide reproducible results for subsequently performed cell experiments.

To examine the qualitative binding of IL-2 on the NCs, the protein was detected with a fluorescently labeled secondary anti IL-2 antibody and analyzed by flow cytometry or fluorescence cross correlation spectroscopy (FCCS). Both techniques have particular advantages. For the detection by flow cytometry, excess antibody does not need to be removed, since just the large complex of nanocapsule and antibody is detected. In contrast, when using FCCS, the capsules must be purified after incubation with the antibody, since each species can be observed individually. First, it was determined how much antibody could be added to the modified NCs to visualize them using the flow cytometer. Therefore, 2 µg of HES-NCs which were functionalized with 3.3 mg/mL DBCO and then modified in a 1:1 ratio of IL-2 to DBCO were incubated with different amounts of antibodies. In addition, antibody was also added to HES-NCs which were not functionalized with IL-2 (HES-DBCO NCs). Figure 57 shows normalized fluorescence signals obtained after conjugation of the antibody to HES-NCs with and without IL-2. This experiment was performed by [redacted].

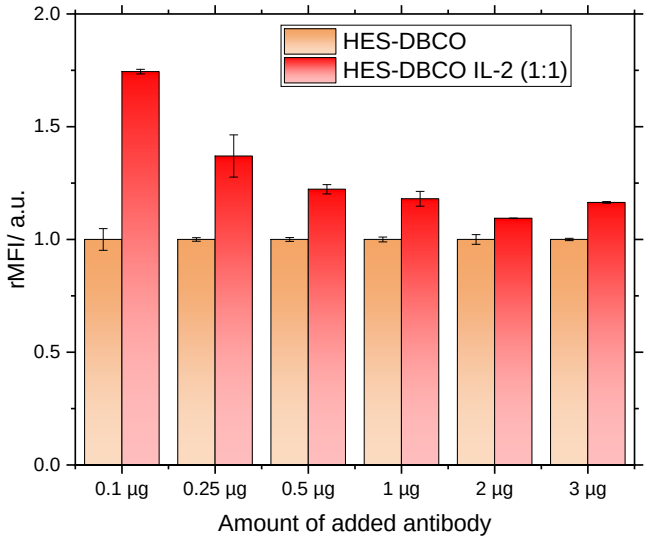

Figure 57: Addition of FITC labeled anti IL-2 antibody to HES-NCs modified with IL-2 (HES-DBCO IL-2 1:1) and without IL-2 (HES-DBCO). Experiment performed by [redacted].

Antibodies are generated to bind to a specific target. However, it is known in literature, that antibodies tend to show unspecific binding affinities.[250] In accordance with these findings, HES-NCs not modified with IL-2 revealed a fluorescence signal originated from FITC-labeled anti IL-2 antibodies (Figure 57, orange bars). By normalizing the signal obtained from HES-DBCO NCs, we observed that in all cases the mean fluorescence intensity was lower than the signal provided by IL-2 modified HES-NCs (Figure 57, red bars), which thus demonstrated higher binding affinities of the anti-IL-2 antibody to IL-2 modified HES-NCs. Furthermore, we found that the lowest amount of antibody (0.1 µg) provided higher MFIs than higher amounts of antibody compared to unmodified capsules. This can be explained by the fact that a higher amount of antibody is more likely to bind non-specifically to the NC. In this context, the amounts of antibodies used for a significant detection of IL-2 on the capsule surface were optimized. This experiment was therefore used as a basis for subsequent flow cytometry experiments in which 0.3 µg of antibody was applied to 2 µg of HES-NC dispersion. In the following flow cytometry experiments, HES-NCs with various DBCO:IL-2 combinations were synthesized and analyzed by using a FITC labeled anti IL-2 antibody. In addition, we evaluated if extended washing had an influence on IL-2 binding to the modified HES-NC. For data analysis, the capsules were gated using a red channel (either RL1 or the orange channel YL3) since Cy5 Oligo was encapsulated into the HES-NCs, which served as a marker to identify them in the flow cytometer. After gating, the MFIs and events were analyzed using the green channel BL-1, which detected the FITC signal (Figure 58). The flow cytometry measurements were performed by [redacted].

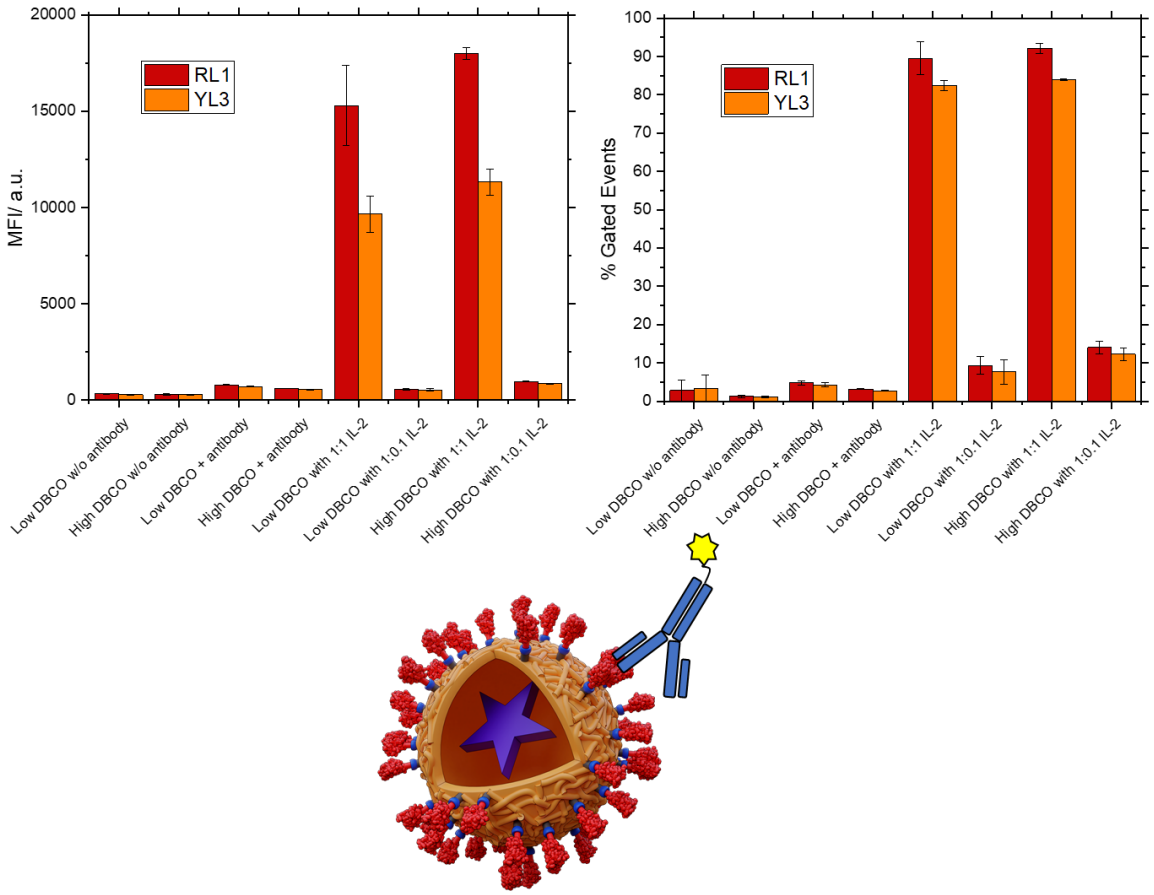

Figure 58: Flow cytometry analysis of the binding of FITC labeled anti IL-2 antibody to IL-2 modified HES-NCs. **A:** MFI and percentage of gated events using the RL1 and YL3 channel of differently modified HES-NCs. High amounts are referring to the use of 3.3 mg DBCO per mL dispersion (approx. 2 DBCO groups/nm^2). Low amounts are referring to the use of 0.55 mg DBCO per mL dispersion (approx. 0.75 DBCO groups/nm^2). 1:1 means a balanced 1:1 ratio of DBCO to IL-2, while 1:0.1 means a 10-fold reduced amount of IL-2 to DBCO was added. Experiment was performed in collaboration with [redacted].

The experiments reveal that it is possible to qualitatively determine different amounts of IL-2 on the surface of HES-NCs using flow cytometry (Figure 58). Samples in which no IL-2 was added (High/ Low DBCO + antibody or w/o antibody) reveal very weak fluorescent signals, while an enormous increase of MFI as well as percentage of gated events was detected when IL-2 was present. In total four different IL-2 loadings were analyzed which were covalently attached to the NC surface and which were washed twice prior to measurements. Azidated IL-2 was added to DBCO modified HES-NCs after DBCO group determination, ensuring addition of the correct IL-2 to DBCO ratios. The amount of DBCO was varied (3.3 mg DBCO per mL dispersion – High DBCO, approx. 2 DBCO groups/nm^2 and 0.55 mg DBCO per mL dispersion – Low DBCO, approx. 0.75 DBCO groups/nm^2) in order to adjust IL-2 binding to the capsule surface. With these different DBCO concentrations, two different IL-2 ratios were generated: the ratios 1:1, which represented a balanced ratio of IL-2 and DBCO groups and 1:0.1 in which a 10-fold reduced IL-2 amount to DBCO amount was added. The experiment reveals that there are no significant differences between high and low DBCO amounts for MFIs and gated events, but a huge decrease in signal for the 10-fold reduced amount of IL-2 (1:0.1) which is observable in both cases, high and low DBCO (Figure 58 A). As expected, high DBCO with 1:0.1 IL-2 shows a slightly higher MFI and gated events, than low DBCO with the same IL-2 ratio, since more IL-2 was added per capsule as the IL-2 addition depends on the calculated DBCO groups.

Extended washing to up to four times did not reduce the fluorescent signals observed in flow cytometry demonstrating that there is no significant decrease of IL-2 and therefore confirms a sufficient purification.

If a FITC-labeled anti-IL-2 antibody is added to non-functionalized HES-NCs to which non-azidated IL-2 was added and washed, comparably low MFIs and percentages of gated events were found (Figure 59). The used IL-2 concentration was based on the theoretically added amount of DBCO and are equal to the amounts used in the previous flow cytometry experiment depicted in Figure 58.

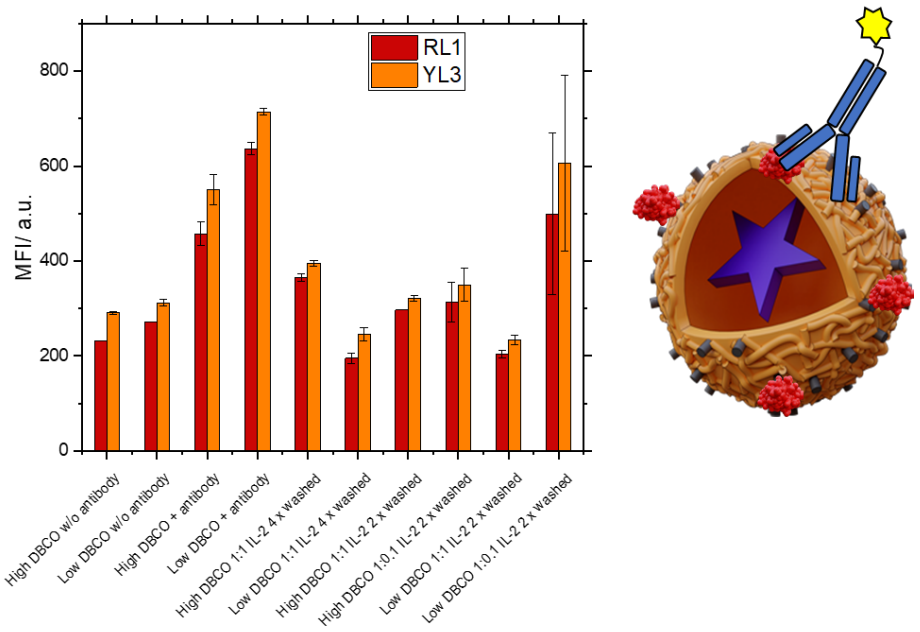

Figure 59: Flow cytometry analysis of the binding of FITC labeled anti IL-2 antibody to non-functionalized HES-NCs with adsorbed IL-2 at pH 7.4. High amounts are referring to the use of 3.3 mg DBCO per mL dispersion (approx. 2 DBCO groups/nm^2). Low amounts are referring to the use of 0.55 mg DBCO per mL dispersion (approx. 0.7 DBCO groups/nm^2). 1:1 means a balanced 1:1 ratio of DBCO to IL-2, while 1:10 means a 10-fold reduced amount of IL-2 to DBCO was added. DBCO was not added to the HES-NCs.

The obtained MFIs of the flow cytometry analysis of HES-NCs with adsorbed IL-2 are very low compared to the result obtained for functionalized samples (Figure 58) and no clear trend of MFI increase towards one sample was detected. The results show that the anti-IL-2 antibody did not interact significantly with pristine HES-NCs. Therefore, it was concluded that IL-2 did not substantially bind to non-functionalized HES-NCs at pH 7.4 (in PBS buffer) and hence no strong interaction between IL-2 and pristine HES-NCs occurred.
The results demonstrate that IL-2 binding is dependent on DBCO modification of the NCs and therefore indicate controlled binding, if DBCO modification is performed in a reproducible manner.

Another method to assess qualitative binding of IL-2 to HES-NCs, was done by fluorescence cross correlation spectroscopy (FCCS) measurement using the same fluorescently labeled anti IL-2 antibody as in the flow cytometry analysis (Figure 58 and 59). This method is very sensitive and must therefore be performed with purified NCs, since the free antibody can also be detected, in contrast to flow cytometry.

Therefore, an excess of anti-IL-2 antibody (10 µg antibody) was added to a diluted and fully with DBCO covered HES-NCs sample (200 µL NCs, 0.1 wt%), which was modified with IL-2 in a 1:1 ratio and washed four times by centrifugation. Since only a very weak FITC signal in FCS was observed in the diluted state, the sample was concentrated, which resulted in a sample concentration of about 0.6 wt%. The result of the FCCS measurement of the concentrated sample is shown in Figure 60 and was performed by [redacted].

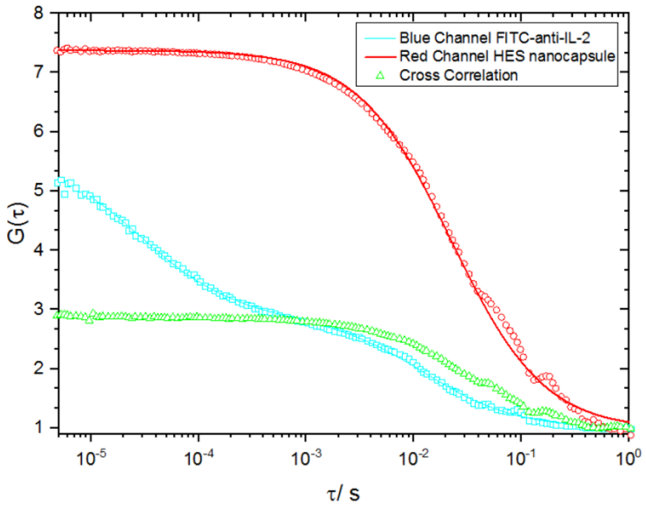

Figure 60: Fluorescence cross correlation spectroscopy (FCCS) experiment of IL-2 decorated HES-NCs, with encapsulated Cy5 Oligo and with high loading IL-2 and full coverage of DBCO (3.3 mg DBCO/ mL dispersion and 1:1 ratio IL-2 to DBCO) with bound anti-IL-2 antibody. The graph shows the fluorescence intensity of encapsulated Cy5 Oligo (red curve), the FITC-labeled anti-IL-2 antibody (cyan curve) and the cross correlation (green curve). Experiment performed in collaboration with [redacted].

In Figure 60, three fluorescent species are depicted. The red curve represents the red fluorescence of the encapsulated Cy5 Oligo inside the HES-NCs and the cyan curve the fluorescence of the bound FITC-labeled anti-IL-2 antibody on the NC surface. The green curve shows the cross correlation of the complex, which represent both fluorescent species moving together, and demonstrating the binding of the components to each other. The curves reveal that there was still free anti-IL-2 antibody available, since the green curve does not lie perfectly between the red and the blue curve, but approximates the red curve starting at lag times from 10^{-2} s. Therefore, it is concluded that some of the anti-IL-2 antibodies bind to the IL-2 decorated HES-NC, while there is still free antibody.

These findings qualitatively prove the presence of IL-2 on the HES-NC surface. The presence of free antibody can be explained by an added excess of antibody to the dispersion, since for the FCCS experiments more antibody was applied than in the flow cytometry experiment to fully cover the NCs and no complete removal of excess antibody was performed. Moreover, a detachment of the antibody is another possible reason. This experiment was also performed with other IL-2 ratios of DBCO modified HES-NCs but binding of the antibody could only be detected in the fully functionalized sample.

By flow cytometry and FCCS experiments, a covalent attachment of IL-2 to the HES-NCs was qualitatively shown and confirmed that binding occurred in a DBCO-dependent manner. To quantify also small amounts of IL-2 other methods were used.

In cooperation with the group of [redacted], a quantification of the IL-2 amount on HES-NCs was performed using sandwich ELISA (enzyme-linked immune-sorbent assay). The IL-2 determined in this way was compared with the added amount and furthermore compared to the amount of DBCO attached to the surface (Figure 61).

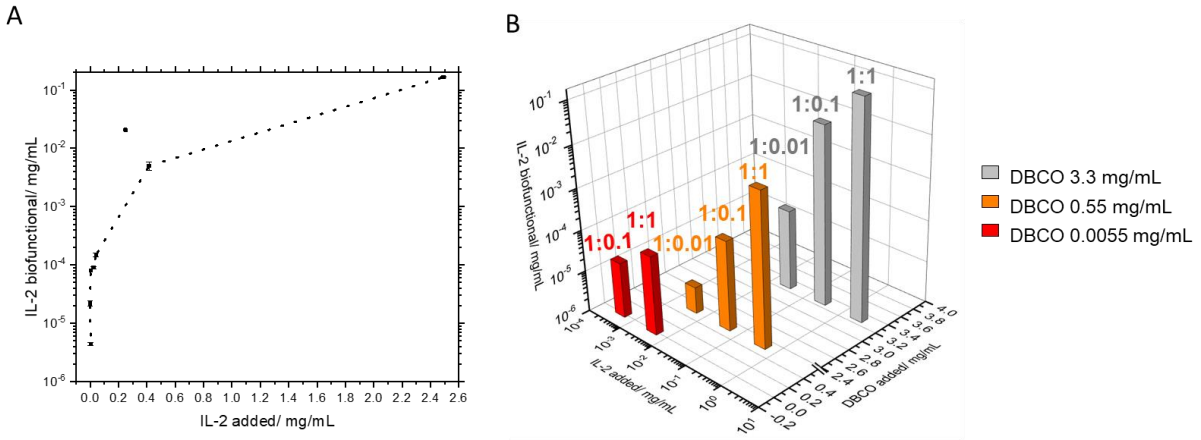

Figure 61: **A**: Correlation between added IL-2 to HES-NCs and biofunctional IL-2 after attachment, analyzed by sandwich ELISA. One data point at an addition of approx 0.25 mg/mL IL-2 is not within the fit and is assumed to be an outlier. **B**: Dependency of the biologically active IL-2 on added DBCO concentrations and added IL-2 concentrations.

Using ELISA, IL-2 (formulated in PBS at pH 7.4) bound to NCs was detected with an anti-IL-2 antibody, which was immobilized on a well-plate. The functionality of IL-2 on the HES-NCs was proven by detectability in ELISA by binding of the anti-IL-2 antibody and therefore was referred to as biofunctional IL-2 in the graphs (Figure 61 A and B). If the added IL-2 concentrations are plotted in ascending order against the biologically active concentrations detected in ELISA, a logarithmic progression is observed. The flattening curve at higher concentrations indicates an approximation to a limit of bound IL-2. The concentrations detected by ELISA are several orders of magnitude lower than the added concentrations. This can be explained by the low accessibility and flexibility of the fixed anti-IL-2 antibody on the decorated NCs (Figure 61 A). The dependency between added IL-2 and biologically active IL-2 is additionally compared with a third dimension, that of the DBCO concentration used (Figure 61 B). The three differently colored columns show three DBCO concentrations, which were incubated with three different IL-2 ratios each. The graph demonstrates that with high DBCO concentrations and correspondingly high IL-2 concentrations, a lot of biologically active IL-2 can be found.

If ten times lower ratios of IL-2 to DBCO (1:0.1) are added to capsules exhibiting different DBCO concentrations (High, 3.3 mg/mL, 2 DBCO/nm^2, low, 0.55 mg/mL, 0.75 DBCO/nm^2 and very low, 0.0055 mg/mL), the biologically active amount is reduced accordingly. However, a constant decrease of the IL-2 concentrations was observed at ratios of 1:1 and 1:0.1 but no longer at 1:0.01, where the amount found is less than expected and corresponds more to the logarithmic course shown in the curve in Figure 61 A. These findings are in contrast to the flow cytometry analyses of the differently modified NCs, which show that an addition of IL-2 which corresponds to a 10-fold reduced IL-2 concentration on the capsule surface (1:0.1), results in a significant decrease of IL-2 bound to HES-NCs (Figure 58). It has to be considered, that flow cytometry detects only large complexes and may not detect smaller objects.

This means that a lower IL-2 addition results in a lower functionalization of HES-NCs with IL-2 and therefore to a reduced attachment of anti-IL-2 antibodies, resulting in smaller antibody-capsule complexes. At the lowest DBCO concentration used (red columns, 0.0055 mg/mL), the 1:100 ratio is no longer detectable in ELISA. Furthermore, the results point that high amounts of DBCO are not necessarily required to obtain HES-NC with sufficient amounts of biologically active IL-2. For example, a DBCO amount of 0.0055 mg/mL (100-times reduced compared to 0.55 mg/mL) with a 1:10 ratio of DBCO and IL-2 (red column, 1:10), shows a higher detected amount of biofunctional IL-2 than the 10-times increased DBCO concentration with a 1:100 ratio of IL-2 (orange column, 1:100) (Figure 61 B).
The results show the attachment of different IL-2 concentrations to the HES-NCs and revealed information about the binding nature and detectability of bound IL-2 using an anti-IL-2 antibody. However, binding to the NCs can be influenced by different protein compositions (formulations) used for the attachment.
Commercially available IL-2 was used which was formulated in PBS at pH 7.4. This IL-2 formulation was bound at the highest surface loading of the capsules with DBCO and IL-2 at a concentration of up to 0.17 mg/mL dispersion. Another formulation of IL-2 was also evaluated, in which the protein was delivered by the supplier lyophilized at acidic conditions. In the following it was analyzed, if different IL-2 formulations resulted in a different amount of IL-2 on the HES-NCs if similar amounts were added to the NCs (Table 12).

Table 12: Detected amounts of IL-2 by ELISA in comparison to detected DBCO groups and added azidated IL-2.

Entry	DBCO content: groups/mL dispersion	Added IL-2-az in mg/mL dispersion	ELISA: Detected IL-2 in mg/mL dispersion	Formulation IL-2
MF-020 (1:1 DBCO:IL-2)	3.8081×10^{17}	2.49	0.17	PBS pH 7.4
MF-020 (1:0.1 DBCO:IL-2)	3.8081×10^{17}	0.249	0.0021	PBS pH 7.4
MF-147 (1:1 DBCO:IL-2)	3.6308×10^{17}	2.49	0.00021	pH 3.5
MF-147 (1:0.1 DBCO:IL-2)	3.6308×10^{17}	0.249	0.0000073	pH 3.5

The data in Table 12 reveal, that the IL-2 formulation plays a significant role for the binding and detection of the protein to the NC. If an acidic formulation is used, an immense decrease of detected IL-2 by ELISA is observed, although similar DBCO concentrations were detected and therefore the same IL-2 concentration was used (MF-147 in comparison to MF-020). The formulation used in entry MF-147 was neutralized with diluted NaOH solution before transfer to the buffer. However, according to the results in Table 12, this did not lead to a significant change in binding detected by ELISA.
As already indicated by the logarithmic curve in Figure 61 A, a tenfold reduction of added IL-2 (1:0.1) leads to a detection of a hundredth of the originally added IL-2 concentration (Table 12, entry MF-020). Moreover, the findings for the loss of binding of acidified IL-2 formulations confirm the nanoDSF (Figure 55, black curve) and MALDI-ToF (Figure 56 A, red curve) findings, which show that acidic conditions do not have a beneficial effect on the protein.

These findings indicate that for a reproducible surface modification of HES-NCs with IL-2, the same protein preparation (formulation) is necessary.

IV. 4.1.3 Concentration-dependent stimulation of CTLL-2 cells using IL-2 decorated HES-NCs

Concentration-dependent attachment of the protein and the associated impact on proliferation of specific cells were analyzed in the last step.

CTLL-2 cells, which are subclones of a murine T-cell line, usually grow in response to offered IL-2 concentration. To evaluate whether the different surface loadings of DBCO and IL-2 have a biological impact, different HES-NCs were incubated with CTLL-2 cells. Figure 62 shows the growth of CTLL-2 cells in dependency of bound IL-2 to the NCs surface, measured and evaluated by [redacted].

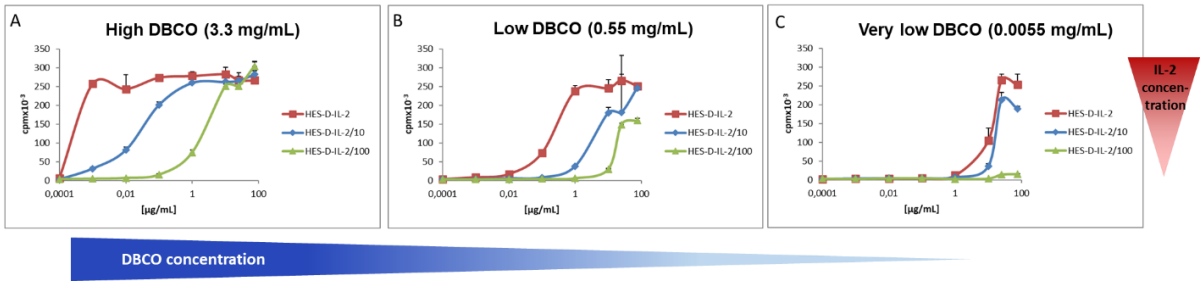

Figure 62: Counted radioactivity (counts per min) of CTLL-2 cell proliferation plotted against added NC concentration in µg/mL. **A:** The cell growth after incubation with NCs with high DBCO loading (3.3 mg/mL, 2 DBCO/nm^2), **B:** with low DBCO loading (0.55 mg/mL, 0.75 DBCO/nm^2) and **C:** with very low DBCO loading (0.0055 mg/mL). All graphs show the curve progression after incubation of CTLL-2 cells with the corresponding DBCO modified NCs with three different IL-2 ratios calculated using the previously obtained DBCO concentration. Experiment performed and evaluated by [redacted].

The proliferation of CTLL-2 cells is depicted by the counted radioactive decay using a ^{3}H-thymidine proliferation assay. The cells were incubated with HES-NCs modified with different surface loadings of DBCO (high – 3.3 mg/mL, low – 0.55 mg/mL and very low 0.0055 mg/mL) and corresponding IL-2 to DBCO ratios (1:1, 1:10 and 1:100, red, blue and green curve in each graph) in different concentrations (Figure 62 A, B and C). CTLL-2 cells proliferate dependently on the presented IL-2 amount on the NCs. The cells which were incubated with NCs exhibiting the highest DBCO amount (3.3 mg/mL), and therefore also the highest IL-2 concentration attached (Figure 62 A – HES-D-IL-2, red curve), show the strongest proliferations at different added NC concentrations. If the DBCO amount on the NCs was kept constant, but the IL-2 amount was reduced, a decrease of the proliferation curve was observed (Figure 62 A,B,C, HES-D-IL-2/10, HES-D-IL-2/100, blue and green curve). To observe a high proliferation effect, as with high IL-2 loadings, more NC dispersion were used, to reach the maximum counts of 250 cpm. This level was reached in all the cases for the highest IL-2 loading (Figure 62 A, B, C, red curves and also with both IL-2 ratios at high DBCO loading (Figure 62 A, blue and green curve), as well as in the medium DBCO loading with the DBCO:IL-2 ratio of 1:10 (Figure 62 B, blue curve). NC concentrations starting from 0.001 µg/mL (Figure 62 A, red curve) up to 100 µg/mL (Figure 62 A, green curve, B, blue curve or C, red curve) were used to achieve a maximum proliferation of the cells.

In addition, the supernatants of the NCs dispersions after washing were analyzed using the ^{3}H-thymidine proliferation assay, which revealed low IL-2 concentrations in the supernatants and thus verified efficient binding of IL-2 to the NCs (Appendix).

These results indicate that a selective stimulation of T-cell like cells in dependence on offered IL-2 was achieved using different combinations of DBCO and DBCO to IL-2 ratios on HES-NCs. A particularly low IL-2 concentration is needed to target regulatory T cells (Tregs). These findings are therefore important, since by adjustment of IL-2 concentrations on the HES-NC surface, different levels of modifications can be achieved resulting in the effective targeting of specific T cell subpopulations such as Tregs.

IV. 4.2 Binding of carbohydrate structures and glycodendrons to HES-NCs for targeted delivery to human dendritic cells via DC-SIGN

In order to deliver drugs to human dendritic cells (hDCs), the surface receptor DC SIGN (dendritic cell-specific intercellular adhesion molecule-3-grabbin non-integrin) was utilized, since it is very characteristic for DCs.[251] DC-SIGN exhibits a C-terminal carbohydrate recognition domain (CRD) which is preferably binding mannose-containing oligosaccharides. Since DC-SIGN comprises four CRDs, it can theoretically bind up to four carbohydrate-containing structures, presented in a multivalent way.[252] Multivalency is a key strategy used by nature to enhance signaling and is employed for both, protein-carbohydrate and protein-protein interactions, using several binding strategies for potential ligands.[55] These include, for example, the clustering of the binding domains by a ligand, chelation or statistical rebinding.[253] For all these possibilities, a ligand with a branched dendron-like structure is needed. For this reason, we investigated in this study the uptake of HES-NCs, whose surface were decorated with different carbohydrate structures, in hDCs via DC-SIGN. We compared a mannose-containing glycodendron structure with unbranched carbohydrate-containing ligands, which are all capable of binding to DC-SIGN according to literature.[56] Figure 63 shows the carbohydrates structures (**14**-**17**) used for the binding onto the HES-NCs surface and were synthesized in the group of [redacted].

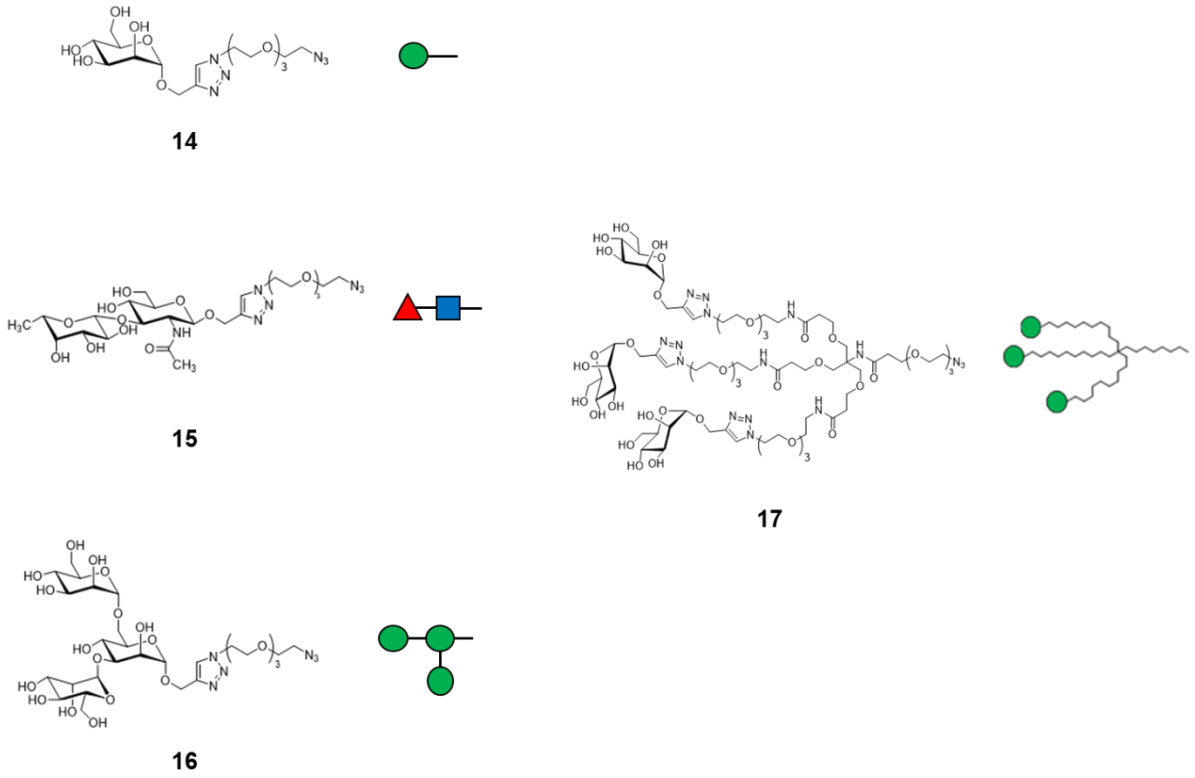

Figure 63: Carbohydrate structures (**14**-**17**) bound to the HES-NCs surface. [redacted].

IV. 4.2.1 Binding and detection of carbohydrates on HES-NCs

The carbohydrate structures were all synthesized with a terminate azide group to enable strain-promoted alkyne-azide click chemistry with DBCO modified HES-NCs. Since a complete coverage of the whole capsule surface was pursued, a high DBCO concentration was added to the HES-NCs (3.3 mg DBCO per mL HES-NC dispersion, 1 wt%). The amount of added carbohydrate resulted from the calculated DBCO groups on the capsule surface, determined by anthracene-azide assay and was always added in a threefold excess, unless stated otherwise. After addition of the carbohydrates and purification of the capsules, again an anthracene-azide assay was performed to determine the remaining DBCO groups after click reaction (Figure 64).

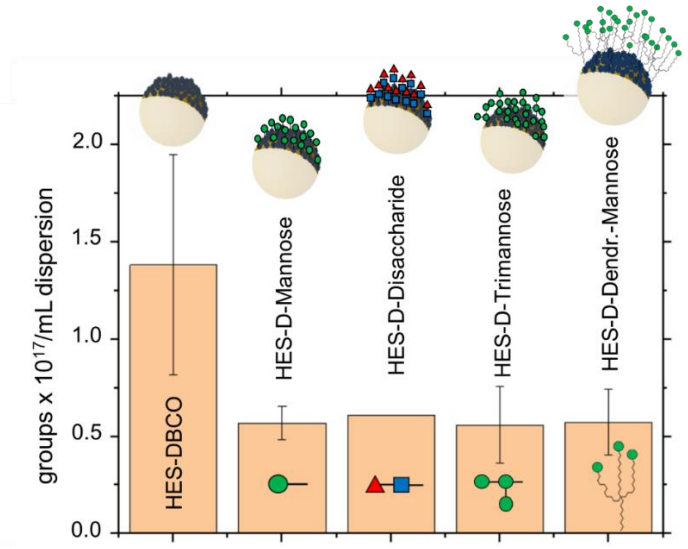

Figure 64: Determined DBCO groups according to the anthracene-azide assay after binding of different carbohydrate derivatives.[215]

After reaction with azide-terminated carbohydrate derivatives, the detectable amount of DBCO on the capsule surface decreased. After three days of reaction, the remaining DBCO groups were quantified. We determined 20% of the initial DBCO groups. The decrease in the DBCO can be attributed to the reaction of the azide, but additionally to the chemical sensitivity of the DBCO molecule to other nucleophiles[244], as a control, a dispersion, which was not reacted with carbohydrates, showed a 36% decrease over time. Therefore, around 42% of the DBCO groups were coupled to carbohydrates, which was independent of the carbohydrate added (Figure 64). The relative size of the nanocapsules with functionalization and the surface charge is shown in Table 13. The surface modification of the NCs caused an increase in the hydrodynamic diameter of the capsule. This is particularly noticeable with the bulky dendron **17**. All samples, after coupling, still showed a negative ζ-potential.

Table 13: Hydrodynamic radii and ζ -potential of carbohydrate modified HES-NCs.[215]

Sample	Average diameter / nm	ζ-Potential/ mV
HES-DBCO	288.87 ± 25.86	-7.87 ± 6.82
HES-DBCO-Mannose	418.0 ± 105.2	-14.94 ± 4.13
HES-DBCO-Disaccharide	391.8 ± 41.15	-11.85 ± 3.21
HES-DBCO-Trimannose	513.7 ± 135.1	-10.13 ± 5.97
HES-DBCO-Dendron-Mannose	543.5 ± 53.53	-13.8 ± 1.13

As already mentioned above, a threefold molar excess of carbohydrates to DBCO groups were added to the particles, for the dendron, in addition a 1:1 ratio was added. For the reduced amount, the diameter decreased to 363.7 nm, while the ζ-potential stayed the same.

In addition to the anthracene azide assay, which indicated the reduced amount of DBCO groups, a HPLC analysis of the supernatant of the modified capsules was performed. Therefore, the supernatant of the modified NCs, was collected after washing and concentrated before injection into HPLC. Beforehand a calibration with DBCO-PEG-NHS ester (**9**) and mannose azide (**14**) was performed to quantify the components in the supernatant. With a mobile phase consisting of 20% water and 80% methanol plus an additive of 0.05% formic acid, the components were successfully separated on a reversed phase C8 column. In the elugrams, the measured components revealed sufficient separation detected at 230 nm and were used for calibration (Figure 65 A). In a longer gradient, more signals were detected at 215 nm in the supernatant of a HES-NC dispersion after modification with **9** and **14,** (Figure 65 B).

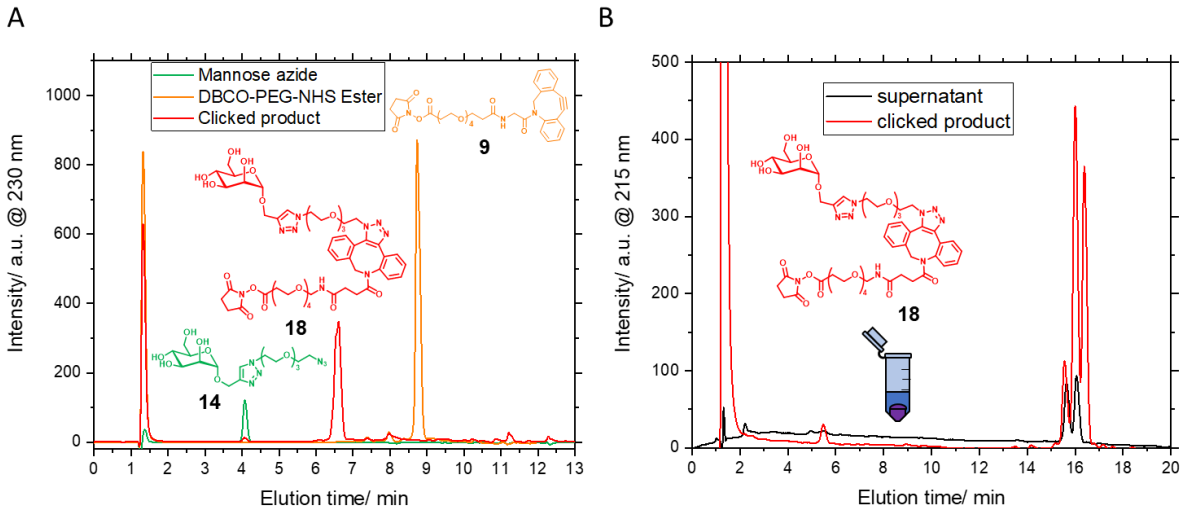

Figure 65: HPLC analysis of the compounds of the click reaction of the HES-NCs surface. **A:** Elugram of mannose azide **14** (green), clicked product **18** (red) and DBCO-PEG-NHS Ester **9** (orange) by HPLC, detected by a UV detector at 230 nm. **B:** Clicked product (red) and signals found in the supernatant (black) after washing of a HES-NCs dispersion, modified with DBCO and mannose azide (3-fold molar excess) using a longer gradient, detected at 215 nm.

Pure mannose azide (**14**) eluted first at 4 min (Figure 65 A, green signals), as it is the most polar component, while the hydrophobic DBCO (**9**, Figure 65 A, orange signals) eluted at around 8.7 min. As the clicked product (**18**) combines the polar mannose group and the apolar DBCO component, it is detected in between the other signals (Figure 65 A, red signals, 6.5 min).

The first signal at 1.4 min is attributed to DMSO which was the solvent used for all components. The area of the integrated signals at defined concentrations were used for a standard calibration to determine residual **14** or **9** and **18** after reaction on the NCs. For calibration, several dilutions of each compound were prepared and measured in HPLC. The signals shown in Figure 65 A represent one of the many dilutions prepared per compound plotted in one graph and demonstrate that all the compounds were easily distinguishable and revealed sharp signals.

When a longer gradient (same mobile phase) was applied, a further separation of the signal given by **18** into three signals was obtained (Figure 65 B). As already observed in NMR, HPLC analysis supports that the clicked product of DBCO and azide was yielded as regioisomers in a balanced ratio, according to the HPLC analysis. Since the NHS ester is very sensitive to hydrolysis, it is likely that during the slightly acidic conditions in HPLC, it hydrolyzed to the respective carboxylic acid. Therefore, it is expected, that the third smaller peak is attributed to the clicked product of **14** and hydrolyzed **9** to the respective carboxylic acid. This product with increased polarity eluted earlier than the non-hydrolyzed ester (Figure 65 B). It was found that the main product in the supernatant of the washed modified HES-NCs, was almost exclusively **18**, since **14** and **9** efficiently reacted also in solution as they were both added in excess to the NCs (Figure 65 B). Surprisingly, only two signals instead of three were found in the supernatant of the washed capsules, which suggested that only one of the regioisomers was generated if modification was performed on the NCs.

Using the short gradient, in which the regioisomers and other by-products were not separated, the amount of washed-off components was determined and compared with the added amount of **9** and **14**. Table 14 shows the results for determining the coupling efficiency via HPLC analysis of HES-NCs which were washed twice by centrifugation after modification.

Table 14: Comparison of found components of the surface functionalization of HES-NCs with mannose azide (**14**) by click chemistry, with added amounts in the supernatant of washed HES-NCs after functionalization.

Entry	Found mannose azide (14) by HPLC	Found clicked product (18) by HPLC	Addition of DBCO ester (9)	Addition of mannose azide (14)	Comparison added to found: added **14**-detected (**14**+**18**)	Coupling efficiency
MF-174	0.027 mg/mL	0.123 mg/mL	3.3 mg/mL	0.231 mg/mL	0.081 mg/mL	35.1%

Next to a large amount of **18** (0.123 mg/mL), a small quantity of **14** was found by HPLC (not visible in Figure 65 B, but observable at 230 nm in the shorter gradient, 0.027 mg/mL). A large excess of **9** was added to the NCs (3.3 mg/mL) but purified prior to addition of **14**, which was added according to the calculated DBCO groups. To obtain the mannose-azide concentration, which was bound to the NCs, the found mannose-containing molecules in the chromatogram (0.15 mg/mL) were subtracted from the added concentration of **14** (0.231 mg/mL). In this way a bound mannose concentration of 0.081 mg/mL was obtained, which corresponded to a coupling efficiency of 35%.

As shown above, using the anthracene azide assay to determine the remaining DBCO groups on the capsule, 42% coupling efficiency was determined. This coupling efficiency was the same for all carbohydrates used and appeared to be very similar to the coupling efficiency obtained by HPLC.

However, since the relative size of the glycodendron (**17**) is significantly larger than that of **14**, it was estimated that there were fewer dendron molecules on the capsules than the less bulky molecules.

IV. 4.2.2 Receptor-mediated uptake of decorated HES-NCs into human dendritic cells (hDCs)

After successful binding of the carbohydrates to the nanocapsules, cell uptake experiments were performed.

Therefore, immature human dendritic cells (hDCs) were incubated with DBCO-modified HES nanocapsules (DBCO), with HES-DBCO nanocapsules surface modified with four different carbohydrates (mannose **14**, disaccharide **15**, trimannose **16** and dendron-mannose **17**) and with pure cell medium as negative control (NC). All nanocapsules were fluorescently labelled with the dye SR101. After incubation and washing, flow cytometry experiments were performed in different experimental setups. First, the cells were incubated with different nanocapsules and the uptake was analyzed (no blocking), in a second experiment the cells were prior to incubation with the nanocapsules, incubated with receptor-specific antibodies (CD 206 – mannose receptor, CD209 – DC SIGN and both together) to block the respective receptor and afterwards the uptake of the nanocapsules was analyzed using flow cytometry (Figure 66). The experiment was performed and evaluated by [redacted].

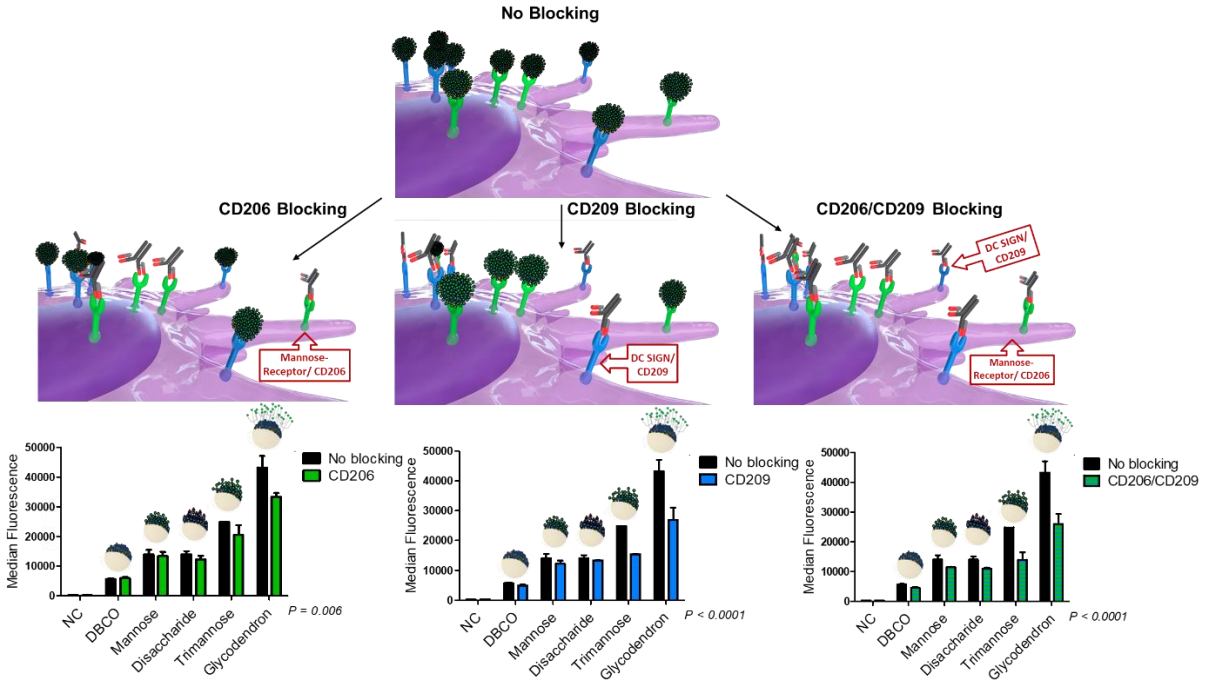

Figure 66: Uptake and blocking experiments of carbohydrate decorated HES-nanocapsules into human dendritic cells (hDCs) in three different experimental setups. The experiments were performed in duplicates using ANOVA for data evaluation with a p-value = 0.006 (**A**), p-value < 0.0001 (**B**) and p-value < 0.0001 (**C**). Experiments performed by [redacted].[215]

In general, we observed that the carbohydrate-modified HES-nanocapsules showed a higher uptake into hDCs compared to pure DBCO-modified HES-nanocapsules. In addition, mannose (**14**) and disaccharide (**15**) modified HES-nanocapsules did not show a significant difference in uptake, while uptake for trimannose (**16**) decorated HES-nanocapsules was slightly preferred. As already mentioned in the last Section, a similar amount of residual DBCO groups was found on the capsule surface, independent on the carbohydrate used. It was expected that the size and steric configuration of the carbohydrate had a significant impact on the binding to the nanocapsules. Therefore, we expected that more of the respective carbohydrate was necessary for a complete coverage of the surface with mannose **14** than for the coverage with dendron **17**. Despite the associated molecular excess of the simpler carbohydrates, dendron **17** proved to be superior in uptake.

When the receptors CD206 or each CD209 were blocked with antibodies, the uptake of mannose (**14**)- and disaccharide (**15**) -modified HES-nanocapsules barely differed from the unblocked scenario, but trimannose (**16**)- or glycodendron (**17**) -modified HES-nanocapsules showed a decrease in uptake. This decrease was even stronger, when a combination of anti-CD206 and anti-CD209 antibodies were used and therefore if both receptors were blocked. In the dual blocked scenario, also a slight decrease in uptake of mannose- and disaccharide modified HES-nanocapsules were observed. These findings suggested that the carbohydrate modified HES-nanocapsules undergo a receptor-mediated uptake.
Since three mannose units are presented in **17**, but the same molar excess was applied for all carbohydrates, an additional sample with a threefold reduced glycodendron concentration was prepared and cell uptake experiments were again performed. In addition, the langerin receptor (CD207) which is very abundant on DCs was blocked with a corresponding antibody (Figure 67).

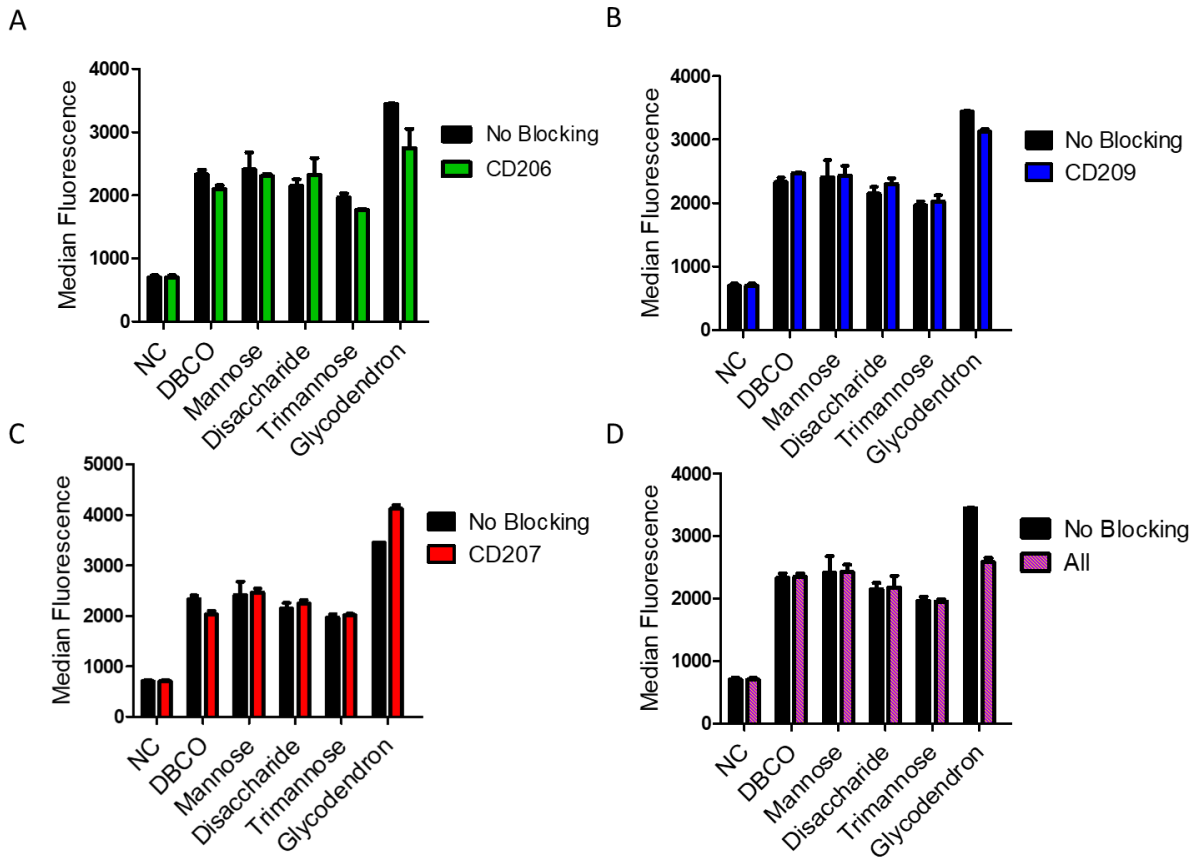

Figure 67: Uptake and blocking experiments of carbohydrate modified HES-nanocapsules into hDCs with one third of the originally used amount of glycodendron (**17**). **A:** Blocking of mannose receptor (CD206). **B:** Blocking of DC SIGN (CD209). **C:** Blocking of langerin receptor (CD207) and **D**: all receptors blocked. The experiments were performed in duplicates using ANOVA for data evaluation with a p-value = 0.0056 (**A**), p-value = 0.0006 (**B**), p-value = 0.0283 (**C**) and p-value = 0.0003 (**D**). Experiments performed by [redacted].[215]

In a second cell uptake series, it was shown that despite a lower modification degree with dendron **17** (a three-fold lower amount was used) was achieved, the capsules modified with **17** again revealed the highest uptake into hDCs. This finding indicates a reproducible cell response, although less dendron was applied, supporting the structural advantage of **17** over the other carbohydrates. However, it was observed from the measured MFIs that generally a lower uptake of the capsules was detected than in the previous experiment.

Next to CD206 and CD209, also CD207 (langerin receptor) was blocked with a specific antibody. For the blocked scenario, only **17** revealed a decrease in uptake (except for blocking of CD207, Figure 67, red bars), while the other samples, did not show a significant reduction. The trend of the trimannose (**16**) modified HES-nanocapsules which showed an increased uptake for the experiment performed in Figure 66, could not be confirmed, but indicated a similar result as mannose (**14**)- or disaccharide (**15**)-modified HES-nanocapsules. As already shown above, the hydrodynamic diameter of the HES-nanocapsules decorated with only one-third of the originally added amount of **17** decreased from 543.5 ± 53.53 to 364 nm.

To prove the potential of a possible receptor-mediated uptake mechanism, a surface expression control of the hDCs and an isotype control were performed (Figure 68). For the isotype control, the cells were incubated with an unspecific IgG antibody and the uptake of the modified HES-nanocapsules was analyzed by flow cytometry.

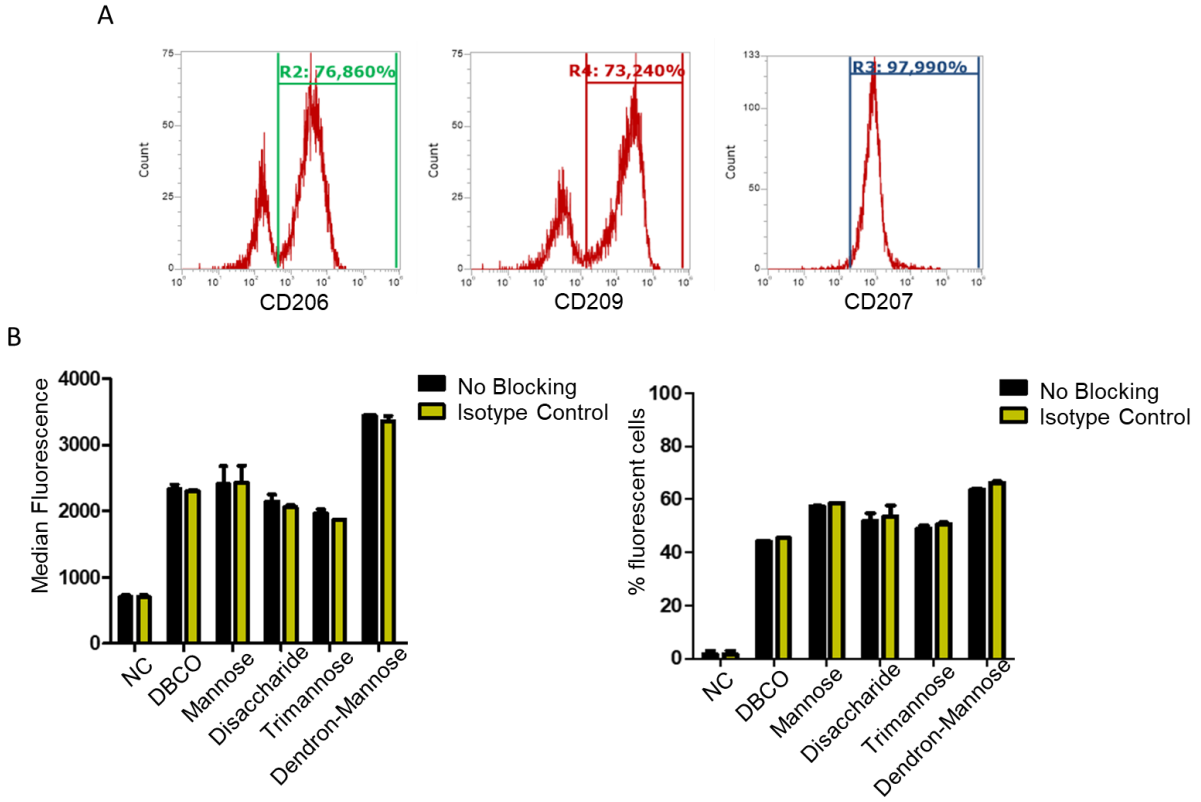

Figure 68: A: Surface expression of CD206, CD207 and CD209 of hDCs. **B:** Uptake experiment with an isotype control. The experiments were performed in duplicates using ANOVA for data evaluation with a p-value = not significant. Experiments performed by [redacted].[215]

Surface expression analysis revealed that the receptors, examined for receptor-mediated uptake of the nanocapsules, were all highly abundant on the analyzed hDCs. CD206 showed an expression of 76.9%, CD209 showed an expression of 73.2% and CD207 showed an expression of 98.0% (Figure 68 A). Furthermore, receptor-mediated uptake of the carbohydrate modified capsules was elucidated by using an isotype control instead of a specific antibody to block receptors of the cells (Figure 68 B). For the isotype control experiment no difference in uptake of the HES-nanocapsules during the blocked scenario in comparison to the non-blocked setup was detected.

These findings supported that the modified capsules were internalized into the hDCs by binding a carbohydrate-binding receptor like CD206, CD209 or CD207.

IV. 5. Conclusion

In this chapter we demonstrated how HES-NCs can be reproducibly synthesized and functionalized to endow them with biological functions. We demonstrated that by splitting up the synthesis into smaller steps, and by controlling them, reproducibility of the synthesis is achieved, since individual changes can be followed more easily.

First of all, it is important to analyze capsule size, dispersity and stabilization, as these are crucial for the reproducible calculation of surface groups. Only with a constant colloidal stability of the dispersion, a systematic surface functionalization can be performed. In extensive studies including many samples which were synthesized independently from each other, it was shown which parameters influence the capsule synthesis regarding hydrodynamic radii, encapsulated dyes, surfactants and solid content.

In the subsequent steps, HES-NCs were then modified with different concentrations of DBCO and biomolecules. In the first part different surface densities of HES-NCs with DBCO could be achieved. We used a fluorescent assay for the quantification of DBCO on the HES-NCs surface. We showed that the modification resulted in HES-NCs exhibiting DBCO groups on the surface detectable in a reproducible concentration range and in a very similar surface coverage determined as groups per nm^2. These results were obtained independently from the method used for determination. However, it was also shown that a precise quantification is complicated since NMR studies revealed that at equimolar amounts no complete conversion and isomer formation of the reagents occurred. Furthermore, we investigated that the DBCO groups lost reactivity in aqueous solution, which could influence the reproducibility of the capsule modification. For this reason, a determination of the actual bound amount of DBCO on the NC surface represents an important quality control for the further procedure of the modification. In this context, it is evident that a variation in the chemical sense triggers a subsequent response in the biological sense.

By complying with this principle, we showed that it is possible to bind defined amounts of the cytokine IL-2 to HES-NCs. These modified NCs in return enabled concentration-dependent growth of T-cell like CTLL-2 cells, displaying a strategy for the targeted drug delivery *via* NCs to different T-cell subpopulations, which is important to adjust particular T-cell dependent immune responses.

In the second part, we demonstrated how a series of mono- and oligosaccharide ligands which are potential binders to DC SIGN were attached to HES-NCs using again the copper-free click strategy. We compared the cell uptake of carbohydrate modified HES -NCs into human dendritic cells, which revealed that a multivalent mannose-terminated glycodendritic structure was superior in cell uptake compared to a single mannose linker, a disaccharide linker and a branched trimannose structure. Moreover, we analyzed a potential receptor-mediated uptake of the modified HES NCs by blocking the receptors CD206 (mannose receptor), CD209 (DC SIGN) and CD207 (langerin receptor) with specific antibodies. Our findings revealed that blocking of these surface receptors led to a significant reduction in cell uptake, especially for the glycodendron-modified HES-NCs. This effect was particularly noticeable when a blockage of DC SIGN or a combination of all the receptors were performed.

These results emphasize the increased influence of multivalent presentation over structural complexity of oligosaccharidic binders for selective DC SIGN targeting.

Using our approach, we showed that by splitting up the synthesis in small steps, a kind of structure-activity relationship was obtained for nanocarriers. With these findings, we believe that detailed protocols for selective binding of biomolecules to HES-NCs, provide higher batch-to-batch consistency of nanocarrier systems and bring them one step closer to clinical application.

Chapter B – Application of multi-step surface modifications on further nanocarrier systems

IV. 1. Introduction

Hydroxylethyl starch nanocapsules (HES-NCs), which are described in Chapter A, are a drug delivery system synthesized using the biocompatible and FDA-approved biopolymer HES.[102] HES-NCs were used to bind specific amounts of biologically relevant molecules on the surface to deliver it to certain cells of the human immune system. Sufficient surface loading of dibenzocyclooctyne (DBCO) for subsequent copper-free click reactions with the desired biomolecules on the HES-NCs surface were achieved. It was shown in Chapter A that the analysis of the surface structure of the HES-NCs is particularly complex. One of the reasons is, that the detection of surface amino groups on the HES-NCs was challenging as their concentration is comparably low and the exact structural constitution is not clear.

For this reason, it was pursued to simplify the nanocarrier system to gain a better insight into the reactivity of the particle surface, leading to a more precisely characterized nanocarrier surface, by using simple polystyrene nanoparticles (PS-NPs) and performing the same reactions as described in Chapter A. This approach should explain in more detail the binding to nanoparticulate surfaces and lead to an easier quantification of groups. Moreover, reaction kinetics of the click reaction on the PS-NP surface was analyzed by isothermal titration calorimetry (ITC).

Next to the analysis of PS-NPs, different protein-NCs were synthesized, which show a higher surface loading of amino groups in comparison to HES-NCs. A big advantage of protein-NCs is their high biodegradability. Protein-NC can be easily degraded using enzymes such as trypsin,[108] whereas the enzyme *α*-amylase, which in nature breaks down glucose polymers such as starch, can only cleave HES to a limited extent depending on the degree of hydroxylethyl branching.[254] This might lead to a poor degradation of HES-NCs in the human body, increasing risks of undesired side effects. For this reasons, physicochemical properties of different protein-NCs were compared to HES-NCs.

IV. 2. Synthesis and binding affinities of surface-functionalized polystyrene nanoparticles (PS-NPs)

The results presented in Chapter A reveal that a sufficient number and an adequate accessibility of surface groups are important to perform a reaction on the capsule surface in a second step.

Especially using biomolecules as nanocarrier material, it is challenging to create an exact number of functional groups on their surface. For this reason, the settings were simplified by using a model system of monodispersed, charged polystyrene nanoparticles (PS-NPs) which are synthesized with adjustable number of amino groups by copolymerization of 2-aminoethyl methacrylate hydrochloride (AEMH, **19**). In the following, the surface charge in dependency of added AEMH **19** by pH-dependent zeta potential measurements is shown (Figure 69).

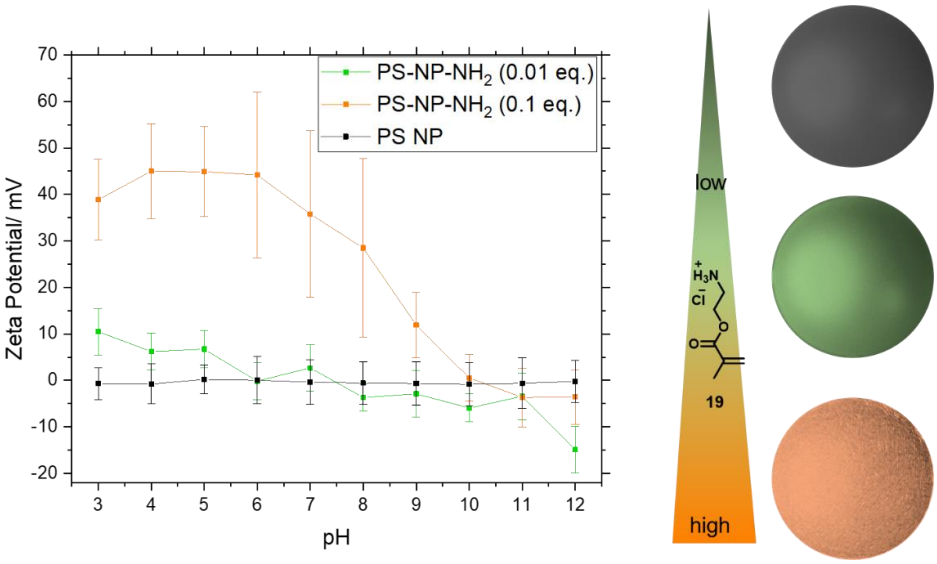

Figure 69: pH dependent zeta potential measurements in dependency of the degree of amino functionalization of PS-NPs.

By pH-dependent zeta potential measurements the degree of amino functionalization of PS-NPs was qualitatively analyzed. Pristine PS-NPs without any surface functionalization reveal nearly a neutral zeta potential after purification at any pH value (Figure 69, black curve), while with increasing amount of **19** inside the emulsion, the more positive is the measured zeta potential of the samples. At a high concentration of **19** (0.1 eq., referred to added styrene), the zeta potential remains in the positive range when the pH value is increased up to pH 10 and only becomes negative in a strongly basic environment (Figure 69, light green curve). Furthermore, at high levels of **19** a plateau at around 45 mV is observable which is dropping at neutral pH. A plateau is not found within the sample with a lower AEMH concentration (0.01 eq., Figure 69, dark green curve) but the sample demonstrates a continuous decrease of the zeta potential upon pH increase.

For a quantitative analysis of amino groups on the surface of PS-NPs, the fluorescamine assay was applied.

IV. 2.1 Synthesis and quantification of surface groups of amino-functionalized PS-NPs

PS-NP were efficiently provided with a specific amino functionality by adding 0.1 eq. of the amino-functionalized methacrylate derivative **19** to the emulsion. Since **19** is soluble in water, it was added into the continuous phase, while all the other components which are necessary for the polymerization reaction, were added in the organic dispersed phase. During the radical polymerization reaction, **19** was actively incorporated into the NP, if the molecules encountered styrene droplets. The copolymerization of **19** leads to the presence of amino groups in the particle and on the particle surface at the water interface.[255] Different added equivalents of **19** with respect to styrene were used to endow the NPs with different degrees of functionalization. After purification by dialysis, the NPs of three independently synthesized batches were compared with each other and the detected amino groups per nm^2 were compared in dependency of added **19** by fluorescamine assay (Figure 70).

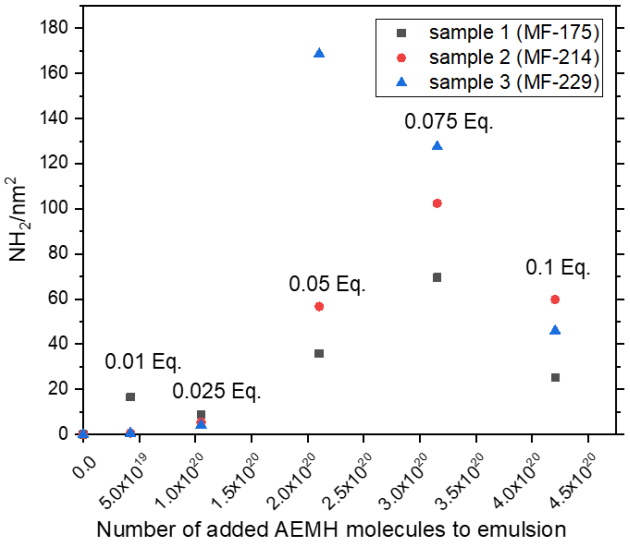

Figure 70: Density of amino groups per nm^2 of three different PS-NP samples (1-3) in dependency of added 2-aminoethyl methacrylate hydrochloride (AEMH, **19**). Equivalents AEMH are given referred to equivalents styrene in the graph.

As expected, with increasing addition of AEMH (**19**) the detected number of amino groups per nm^2 are increasing. At 0.075 equivalents of AEMH referred to styrene, a maximum surface density of in between 70 (sample 1) to 127 (sample 3) NH_2 groups/ nm^2 were obtained. With further addition of **19**, no increase of amino groups on the particle surface was found. With an addition of the lowest amount of 0.01 equivalents AEMH referred to styrene, approx. 0.6 ± 0.03 NH_2 groups/nm^2 were obtained (sample 2 and 3, red and blue data points). All the samples reveal a comparable number of detected amino groups per mL dispersion, indicating a reproducible synthesis of amino-functionalized PS-NPs. Sample 3 reveals one sample deviating from the trend which shows a particularly high amino surface density (sample 3, at an addition of 0.05 eq. AEMH). This sample also revealed a significantly higher amount of amino groups/mg NP and is considered an exception. In Table 15 more characteristics of the functionalized NPs are shown for sample 2 (MF-214 – red data points).

Table 15: Calculated NPs/mL dispersion and amino groups/ mg NP for sample 2.

Equivalents AEMH added to emulsion	NPs/mL	NH_2/mg NP
0	3.05×10^{13}	0
0.01	4.08×10^{13}	$3.36 \times 10^{16} \pm 8.59 \times 10^{15}$
0.025	1.51×10^{13}	$2.20 \times 10^{17} \pm 4.84 \times 10^{16}$
0.05	4.65×10^{11}	$1.07 \times 10^{18} \pm 3.24 \times 10^{16}$
0.075	3.13×10^{11}	$1.86 \times 10^{18} \pm 3.01 \times 10^{17}$
0.1	1.25×10^{12}	$1.63 \times 10^{18} \pm 1.09 \times 10^{17}$

With the known number of amino groups per mL and the solid content, the number of amino groups per mg NPs were calculated and reveal an increasing trend of detected amino groups/ mg NP with increasing AEMH addition, as expected.

It was observed that the number of NPs generated decreases with increasing AEMH content (Table 15). These findings let conclude, that particle formation is affected at increased addition and copolymerization of AEMH. DLS measurements revealed differences in size distributions of the differently functionalized samples (averaged of the three samples MF-175-229) and therefore support the findings (Figure 71).

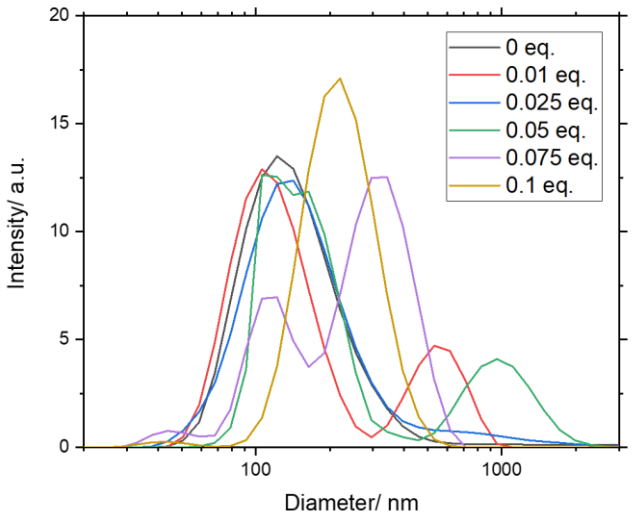

Figure 71: Averaged size distribution of the three samples shown in Figure 70 measured at a scattering angle of 90° after purification.

The averaged size distribution measured at 90° of the three samples (MF-175-229), demonstrates that three samples (0.01 eq., 0.05 eq. and 0.075 eq.) exhibit bimodal distributions after purification of the NPs (Figure 71, red, green and purple curves). As expected, the relative sizes of the NPs become larger the more AEMH was added to the emulsion (compare Figure 71 purple and yellow curve).

These observations demonstrate that the copolymerization of AEMH with styrene plays a crucial role in the dispersity of the formed NPs increasing heterogeneity of the functionalized NP batch and supports earlier reported findings about budding-like processes in the preparation of NP consisting of polyAEMH.[255] For the following experiments, PS-NPs with a high amino loading (0.1 eq.) were selected to achieve the highest possible surface coverage of amino groups on the NPs.

IV. 2.2 Surface functionalization of amino-functionalized PS-NPs with DBCO-PEG-NHS ester and click reaction on the NP's surface

Since the presence of amino groups on PS-NPs were unambiguously confirmed and adjusted, different concentrations of DBCO NHS ester **9** were added to both, functionalized and pristine PS-NPs. According to the determined number of amino groups/mL of the three samples MF-175-229 (Figure 70, 0.1 eq. AEMH) DBCO NHS ester **9** was added to the NPs, stirred overnight and purified by centrifugal filters. The bound DBCO groups were detected using azide **10** by applying an external calibration of the formed complex **11**. The results of the DBCO-functionalization of PS-NP with and without amino groups reveal distinct differences in the degree of functionalization (Figure 72).

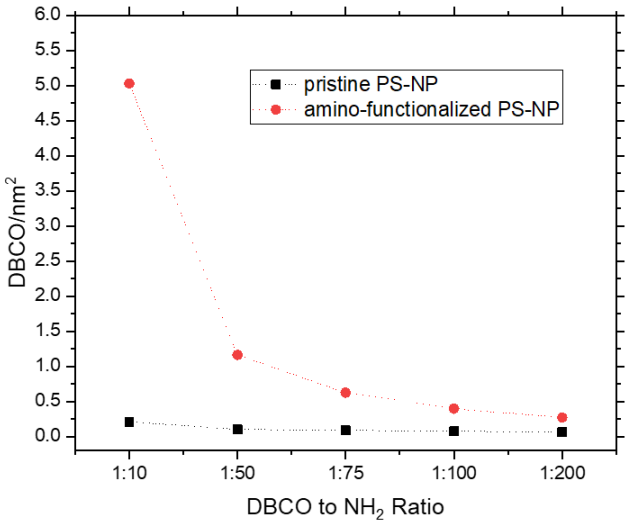

Figure 72: Detected DBCO groups/ nm^2 after reaction of DBCO NHS ester **9** with amino-functionalized PS-NPs (0.1 eq. AEMH) at different DBCO:NH_2 ratios and **9** adsorbed to pristine PS-NPs at the same concentrations.

The detection of DBCO using azide **10** reveals that amino-functionalized PS-NPs have bound significantly more DBCO than non-functionalized PS-NPs after purification, which were used as a control showing the tendency of DBCO adsorption to the NP (Figure 72). Different added concentrations of DBCO NHS ester to pristine PS-NPs did not result in a variation of attached DBCO molecules to the particle but the detected DBCO remained at a contant level, as the free molecules were removed. Approx. 0.11 ± 0.06 DBCO groups/nm^2 were adsorbed to the surface of pristine PS-NPs. For amino-functionalized PS-NPs, DBCO groups in the range of 5.0 (1:10 ratio) to 0.27 (1:200 ratio) DBCO groups/nm^2 were detected. Due to the planar nature of the DBCO molecule, a high surface saturation of the particle with DBCO at a 1:10 ratio DBCO:NH_2 (detected DBCO groups: 5/nm^2) is expected. With the decrease of the DBCO ester addition to the amino-functionalized NPs, the number of detected DBCO groups per nm^2 are continuously decreasing, reaching a DBCO loading of 0.27 groups/nm^2 (1:200 DBCO:NH_2). The lowest surface loading of 1:200 DBCO:NH_2 reveals a 2.5-times higher number of detected DBCO groups as for pristine NPs at the same addition.

These observations point out, that DBCO attachment is underlying two different processes for the different PS-NPs, which is either a covalent reaction for the amino-functionalized NPs or physical adsorption in the case of pristine PS-NPs. Yet, this does not mean that adsorptive attachment of DBCO does not precede covalent attachment to amino-functionalized NPs.

The comparison of expected DBCO groups/nm^2 according to the added DBCO NHS ester:amino ratio with the detected DBCO surface density, reveals, that the number of expected DBCO groups/nm^2 agrees well with the number of detected DBCO groups/nm^2 and are within the error (Table 16).

Table 16: Comparison of expected DBCO groups/nm^2 according to the added DBCO-NHS ester to amino ratio with detected DBCO groups/nm^2 on amino functionalized PS-NPs.

Averaged amino surface density of PS-NPs (0.1 eq. AEMH)	**Expected DBCO surface density according to ratio**	**Found DBCO groups**
44 NH_2/nm^2	4.4 groups/nm^2 (1:10 DBCO:NH_2)	5.03 groups/nm^2 (1:10 DBCO:NH_2)
	0.87 groups/nm^2 (1:50 DBCO:NH_2)	1.16 groups/nm^2 (1:50 DBCO:NH_2)
	0.58 groups/nm^2 (1:75 DBCO:NH_2)	0.62 groups/nm^2 (1:75 DBCO:NH_2)
	0.44 groups/nm^2 (1:100 DBCO:NH_2)	0.40 groups/nm^2 (1:100 DBCO:NH_2)
	0.22 groups/nm^2 (1:200 DBCO:NH_2)	0.27 groups/nm^2 (1:200 DBCO:NH_2)

After successful surface functionalization of the PS-NPs with DBCO, a copper-free click reaction on the particle surface was employed. As a model system, BSA which was modified with the azide-terminated linker **12**, was added to the functionalized NPs. BSA was reacted with **12** in a threefold molar excess, purified by dialysis and freeze-dried to remove residual DMSO and for long-term storage. In order to determine the number of azide linkers attached, MALDI-ToF measurements were performed (Figure 73).

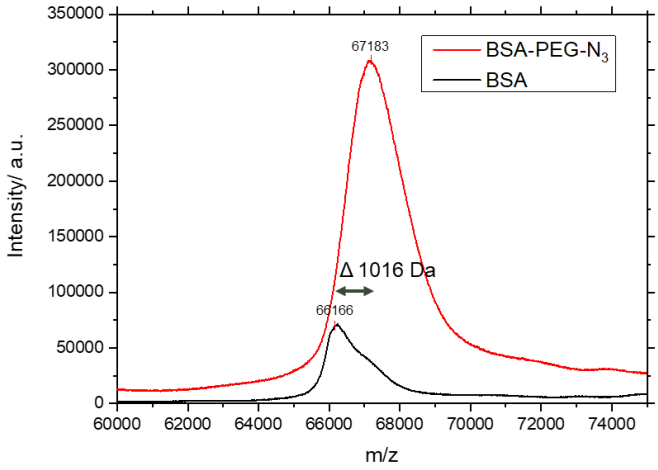

Figure 73: MALDI-ToF measurement of BSA and modified BSA with azide linker **12** measured in MilliQ water. *α*-cyano-4-hydroxy cinnamic acid was used as matrix.

The mass spectrum highlighted in black was obtained from the BSA reference sample and reveals a mass of 66,166 Da which agrees with the values given by the supplier and by literature (66 kDa).

The size increase of 1016 Da illustrated in the MALDI-ToF measurement of modified BSA, reveals an attachment of three linker molecules **12** to the protein (Figure 73, red curve).

In a second step, the binding of BSA-PEG-azide to the different NPs exhibiting different numbers of DBCO molecules on their surface was determined in different ratios. Therefore, three ratios of the samples depicted in Figure 72, were selected (1:10, 1:50 and 1:200), each sample was splitted into two and different ratios of BSA-PEG-azide were added to each batch according to the previously determined DBCO groups per mL dispersion (Figure 74).

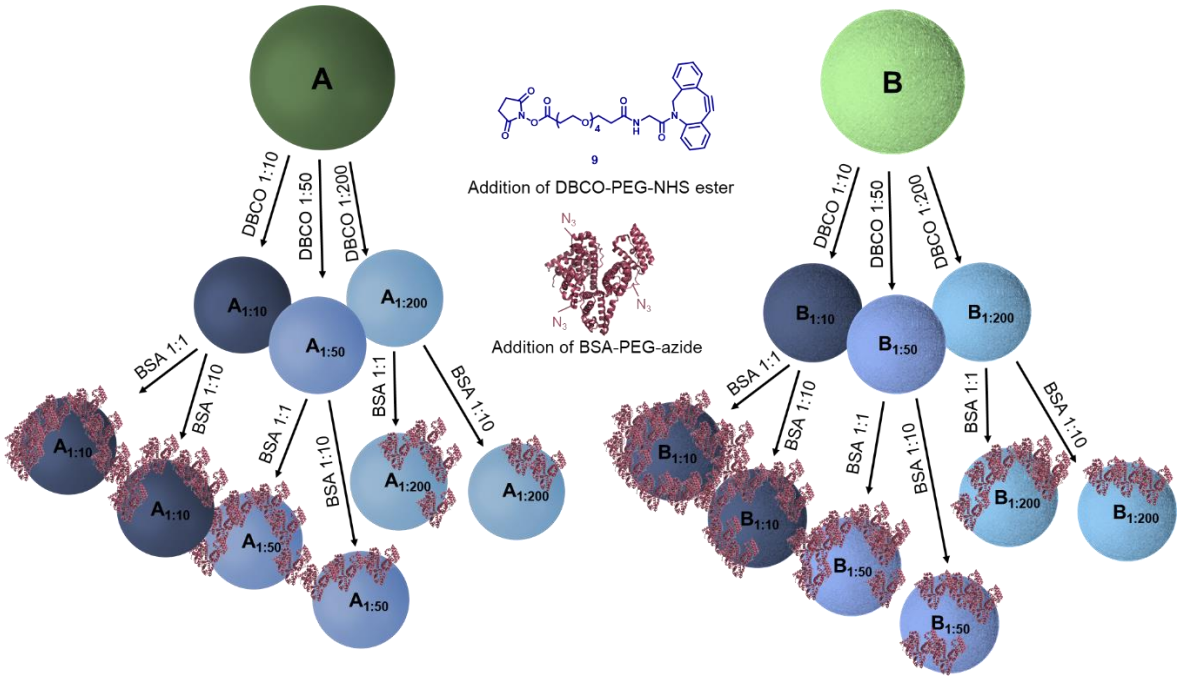

Figure 74: Schematic representation of the stepwise modification of pristine PS-NPs (A) and amino-functionalized PS-NPs (0.1 eq. AEMH, B) with three different ratios of DBCO **9** and with two different ratios of azidated BSA (1:1 and 1:10 according to calculated DBCO groups) Each combination of DBCO/BSA represents a single batch.

With this experimental setup, the binding of azidated BSA molecules *via* copper-free click chemistry was analyzed on 12 different samples after purification and compared to added BSA concentrations (Figure 75). For the determination of the protein concentration, a Pierce™ assay was used with pure BSA as external standard.

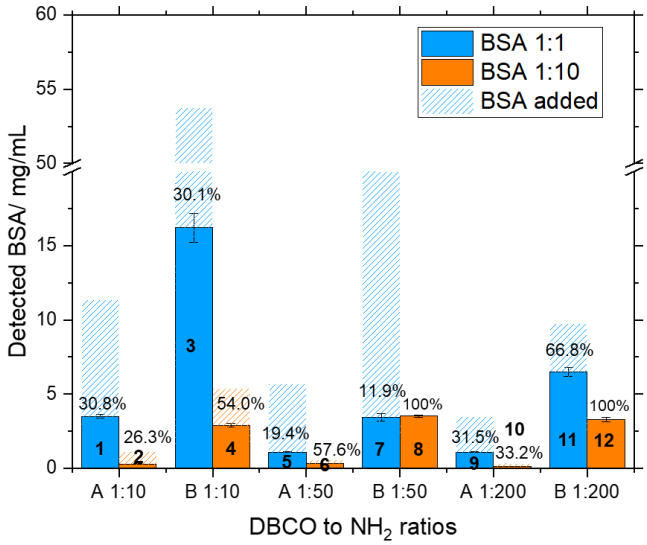

Figure 75: Determination of bound BSA to differently modified PS NPs by Pierce™ Assay. Sample A refers to pristine PS NPs with adsorbed DBCO groups calculated according to Figure 72. Sample B refers to amino-functionalized PS NPs with 0.1 equivalents of AEMH. DBCO to NH_2 ratios correspond to the samples shown in Figure 72. Blue bars refer to a BSA to DBCO ratio of 1:1 and orange bars refer to a BSA to DBCO ratio of 1:10 in dependency to previously determined DBCO groups. Dashed bars refer to BSA concentrations added.

Figure 75 reveals that except for samples 8 and 12, the amount of added BSA was not recovered on the particles, since not every DBCO molecule on the surface can be reacted with BSA due to sterical hindrance.

If the BSA to DBCO ratio is lowered to 1:10, all the added BSA molecules were found on the particles with low DBCO surface density (1:50 and 1:200). These observations reveal that these ratios are necessary to enable a full surface coverage of the BSA on the PS-NPs reaching every DBCO molecule on the NP surface. For the 1:10 ratio of BSA:DBCO, all the NPs onto which DBCO was adsorbed (samples A) revealed a reduced detected BSA amount compared to the same samples on which a covalent reaction was accomplished (samples B).
The found BSA surface density is listed in Table 17 for samples B shown in Figure 75.

Table 17: Determination of surface groups after stepwise modification of amino-functionalized PS-NPs with three different DBCO ratio (1:10, 1:50, 1:200) and two different BSA ratios (1:1 and 1:10).

Sample	NH_2/nm^2 (averaged MF-175-229)	DBCO groups/nm^2	BSA molecules/ nm^2
3	44 (0.1 eq. AEMH)	5.03 (1:10 DBCO:NH_2)	1.52
4			0.272
7	44 (0.1 eq. AEMH)	1.16 (1:50 DBCO:NH_2)	0.139
8			0.142
11	44 (0.1 eq. AEMH)	0.27 (1:200 DBCO:NH_2)	0.180
12			0.0908

It is again important to note here that the addition of the various ratios of BSA was not based on the previously determined surface density of DBCO, as listed in the table, but on determined DBCO amounts per mL dispersion. A maximum BSA density of 1.5 BSA molecules/nm^2 was found for the highest DBCO loading on the particles (1:10 DBCO:NH_2 and 1:1 DBCO:BSA, sample 3). The sample with the same DBCO loading and a one-tenth reduced amount of BSA (sample 4) revealed an expected trend of about one tenth of the detected BSA surface density compared to sample 3. All other samples, show very similar BSA surface densities of 0.14 ± 0.04 BSA molecules/nm^2 regardless of how much DBCO and what DBCO:BSA ratio was used (compare samples 7, 8, 11, 12, Table 17). These results indicate that with sufficiently low added amounts of DBCO and BSA, a complete and uniform BSA surface density of about 0.14 BSA molecules/nm^2 can be achieved. With a high DBCO surface density and a correspondingly high number of added BSA molecules, a ten times higher number of BSA molecules was attached, however given by the hydrodynamic radius of the protein (~ 7 nm)[256] this result may indicate an oversaturation of protein on the particle.
Based on the found results from Table 17 and Figure 75, the lowest possible surface density of DBCO molecules on the surface (1:50 or 1:200) is more advantageous for the binding of BSA to PS-NPs.

Pierce Assay for protein determination is an easy and fast method. In Table 17 it was demonstrated that differences in quantification of bound proteins were observed dependent from the binding of previously added DBCO molecules. However, simple quantification is not sufficient to give an accurate statement about the adsorptive or covalent binding of the molecules on the particle surface, since also the BSA molecule could adsorb to the particle surface. Differences in covalent binding and adsorptive binding are difficult to detect by the assay method, since a high addition of protein to be bound will result in a large amount of protein adsorptively binding onto the particle and probably a comparably small percentage will bind covalently. This has already been proven in earlier studies that with classical, albeit bioorthogonal reactions, only a small percentage of proteins, like BSA was covalently bound to particles.[257] Furthermore, ionic interactions of the protein with charged amino groups on the NP surface could occur. For more accurate thermodynamic assessments regarding the binding affinities of a modified protein to a functionalized particle, more complex methods are therefore required. In the next section, a quantification of DBCO-modified PS-NPs using isothermal titration calorimetry (ITC) is therefore demonstrated and discussed.

IV. 2.3 Analysis of the thermodynamic processes at the modified particle surface using isothermal titration calorimetry (ITC)

In the previous Sections, the amount of DBCO or protein attached to the particles were determined by the assay method. This method is often not sensitive enough to assess differences between the binding constitutions of molecules which tend to adsorb to surfaces such as BSA.[258] For this reason, ITC was employed since thermodynamics of molecule interactions can be analyzed instead of pure concentrations quantified. Therefore, in this section the thermodynamic parameters which govern the interactions between the protein (BSA-PEG-azide) and functionalized PS-NPs were studied. Amino-functionalized PS-NPs (0.1 eq. AEMH) were reacted with DBCO (NH_2:DBCO ratio 1:1) purified and a diluted dispersion was loaded into the measurement cell. The protein BSA-PEG-azide in MilliQ, which was also used for the protein quantification in the section before, was added into the syringe and titrated into the NP dispersion. The same procedure was performed for amino-functionalized NPs (0.1 eq. AEMH) adding a freshly dissolved protein solution. The particle concentrations were calculated using the solid content of the dispersion as well as the hydrodynamic radius measured by DLS. The corresponding heat rates were recorded, and the measurements repeated in triplicates each (Figure 76 A and B).

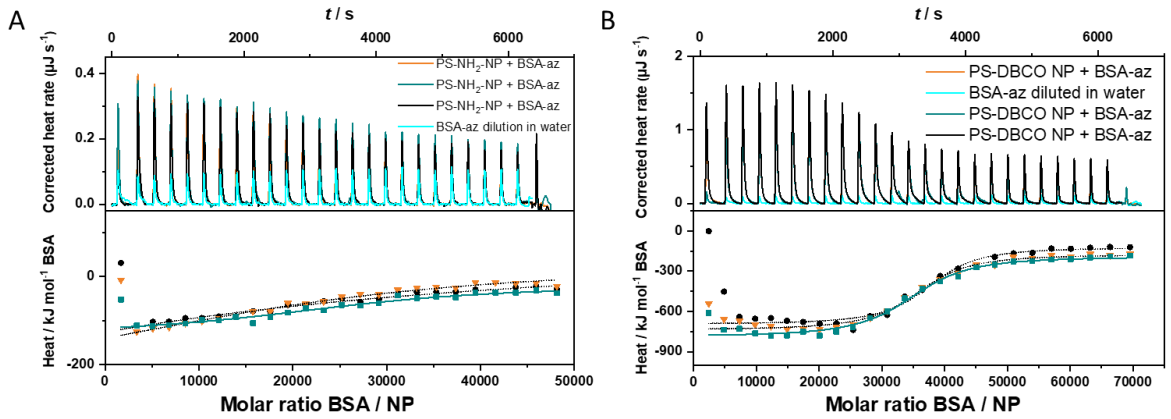

Figure 76: ITC data of the titration of azidated BSA (BSA-PEG-azide, 0.037 mM) to functionalized PS-NPs. Corrected heat rate (upper graph) and adsorption isotherms after corrected heat integration in kJ/mol (bottom graph) for amino-functionalized PS-NPs (**A**) and DBCO-functionalized PS-NPs (**B**). Measurements in triplicates and analysis were performed by [redacted].

In both cases, the protein was titrated to a water solution, and the integrated reference heats were then subtracted from the integrated heats of the adsorption experiments. The comparison of heat rate upon addition of azidated BSA to both particle samples reveal, that for DBCO-functionalized PS-NPs a higher heat was generated than for amino-functionalized PS-NPs in a reproducible manner. These findings suggest that stronger interactions between the protein and the DBCO-functionalized PS-NPs take place than for particles in which no DBCO was used. Furthermore, in the adsorption isotherms, the stoichiometry of protein per particle was derived, which reveal a flat curve for the amino-functionalized particles, but a rising slope with inflection point for the DBCO-functionalized NPs, demonstrating the maximum of binding BSA molecules to the particles, reaching a limit at approximately 50,000 BSA/NP. Using an independent fit model[213,214] the respective thermodynamic parameters as well as the stoichiometry can be calculated when the used particle and protein concentrations are known (Table 18).

Table 18: Parameters obtained from fits of ITC measurements of modified PS-NPs with azidated BSA at 25 °C according to an independent binding model.

Sample	K_a / M^{-1}	ΔH/ kJ/mol	ΔS/ J/molK	ΔG/ kJ/mol	n
PS-NH_2-NPs	(5.5 ± 4.0) x 10^5	-196 ± 115	(-1.76 ± 1.3) x 10^4	-32.2 ± 2.3	(2.6 ± 0.8) x 10^4
PS-DBCO-NPs	(1.2 ± 0.2) x 10^7	-578 ± 14	(-18.0 ± 0.5) x 10^2	-40.4 ± 0.4	(3.5 ± 0.1) x 10^4

The calculated values depicted in Table 18 show that azidated BSA molecules have a higher affinity to DBCO functionalized PS-NPs than to PS-NH_2-NPs which support the finding of a covalent binding. The binding affinity K_a shows an approximately 20-times higher affinity for DBCO modified particles to azidated BSA, however, the error for the amino-functionalized PS-NPs is very high, and for this reason the significance of the binding affinity should not be overrated.

Although the free Gibbs energy of both samples demonstrate an almost identical value, a significant decrease in enthalpy and a significant increase in entropy becomes evident upon DBCO functionalization, indicating a potential change in the thermodynamic processes.
The increase of entropy supports a chemical reaction between the DBCO and the azide-modified protein. It has to be considered, that DBCO hydrophobizes the surface of the particles leading to a disruption of hydrogen bonding, resulting in a reorganization of water molecules in the surrounding. If the freedom of mobility of the water molecules is restricted, due to a limited number of molecules to interact with, the entropy is usually decreased.[259] An entropy increase of DBCO-functionalized NPs in comparison to amino-functionalized NPs is observed, which could be explained by higher resulting mobility of free water molecules. In the case of hydrophobized particles no hydrate shell is formed, in which the surrounding water molecules are in a confined structure. In addition, in a phenomenon similar to a hydrophobic effect, there are compensating contributions of entropy and enthalpy of the same order of magnitude.[260] Since entropy increase and enthalpy decreases with respect to the respective energy contributions of PS-NH_2-NPs, this could be a further hint for a water reorganization upon hydrophobicity increase. Due to the complexity of the thermodynamic processes, it is challenging to limit the evaluation to only one effect and therefore many energy contributions have to be included.

By means of the fit model, more BSA molecules were determined on the surface of PS-DBCO-NPs, revealing an increase of 9000 BSA molecules per particle compared to amino-functionalized NPs, which makes up approx. 35% more BSA (Table 18).
Related to the surface of the particles, the number of BSA molecules were calculated to be 0.171 BSA/nm^2 for the amino-functionalized PS-NPs and 0.293 BSA/nm^2 for DBCO-functionalized PS-NPs. These values are similar to the number of BSA molecules on the NP surface determined by Pierce Assay (compare Table 17) in which approx. 0.14 ± 0.04 BSA molecules/nm^2 were obtained for DBCO-functionalized NPs. If the results from both methods (Pierce Assay and ITC) are considered, a surface density of 0.22 BSA molecules/nm^2 is obtained, which make up 1 BSA molecule for 5 nm^2. Since one BSA molecule has a hydrodynamic diameter of approx. 7 nm,[256] depending on temperature and pH value, this indicates a high density of proteins on the particle surface.
Furthermore, it has to be considered that the hydrophobization of the particle surface due to DBCO functionalization leads to a different adsorption behavior of BSA to the PS-NPs than in the case of a charged surface. Jeyachandran *et al.* found that BSA adsorbs to hydrophilic (GeO_2 crystal) as well as to hydrophobic (PS) surfaces, however, the conformation of the BSA molecule upon adsorption to the respective surface differs. They found a higher surface coverage of BSA molecules to a hydrophilic surface resulting in higher interaction of BSA to the surface.[261] However, for charged surfaces such as in the case of amino-functionalized PS-NPs the interaction of BSA to the particle is dependent from the isoelectric point of the protein, revealing the strongest adsorptive properties at its isoelectric point.[262] This means that upon pH changes of the dispersions, the interaction of BSA to the particles might vary significantly. All experiments were performed without additional pH adjustment in MilliQ at pH 6-7.

According to Figure 69, PS-NH_2-NP are positively charged at pH 6-7, while the isoelectric point of BSA is between 4.5 and 4.9[263] meaning, that sufficient negatively charged surface groups were present on BSA, enabling electrostatic interactions with the particles. However, it should also be considered performing the ITC measurement at the isoelectric point of the protein.

This Section demonstrates that the surface density of reactive groups significantly contributes to subsequent reaction steps on the particle surface. PS-NPs can be specifically provided with functional groups which can be adjusted. In this way, further groups can be selectively attached.

Protein nanocapsules (NCs) also have amino groups on their surface which can be addressed. In the next section, the synthesis and surface modification of different protein-NCs will be discussed.

IV. 3. Reproducible synthesis of different protein nanocapsules (NCs) and surface modification

Protein nanocapsules (NCs) were prepared by inverse miniemulsion by dissolving the protein in the aqueous dispersed phase which reacts at the droplet interface with a suitable crosslinker added to the organic continuous phase. To crosslink the protein at the interface, again toluene diisocyanate (TDI) was used, which reacts in a polyaddition reaction with the protein of choice (see Figure 14, Chapter A).[108]

Bovine serum albumin (BSA) and human serum albumin (HSA), which are considered transport proteins in the body[264,265], are suitable materials for protein-NC synthesis due to their biocompatibility. In addition, they are also available in large quantities at a reasonable price. The protein ovalbumin (OVA) which is found in chicken egg white has a different molecular structure than BSA or HSA, thus indicates a different function[266] and was additionally used for protein-NC synthesis and compared to BSA- and HSA capsules. OVA is moreover interesting as drug delivery material since it is functioning as an adjuvant.[107]

Using FTIR spectroscopy, the chemical stability and conversion of TDI during the miniemulsion procedure were compared, and the functional groups and new bonds were detected (Figure 77).

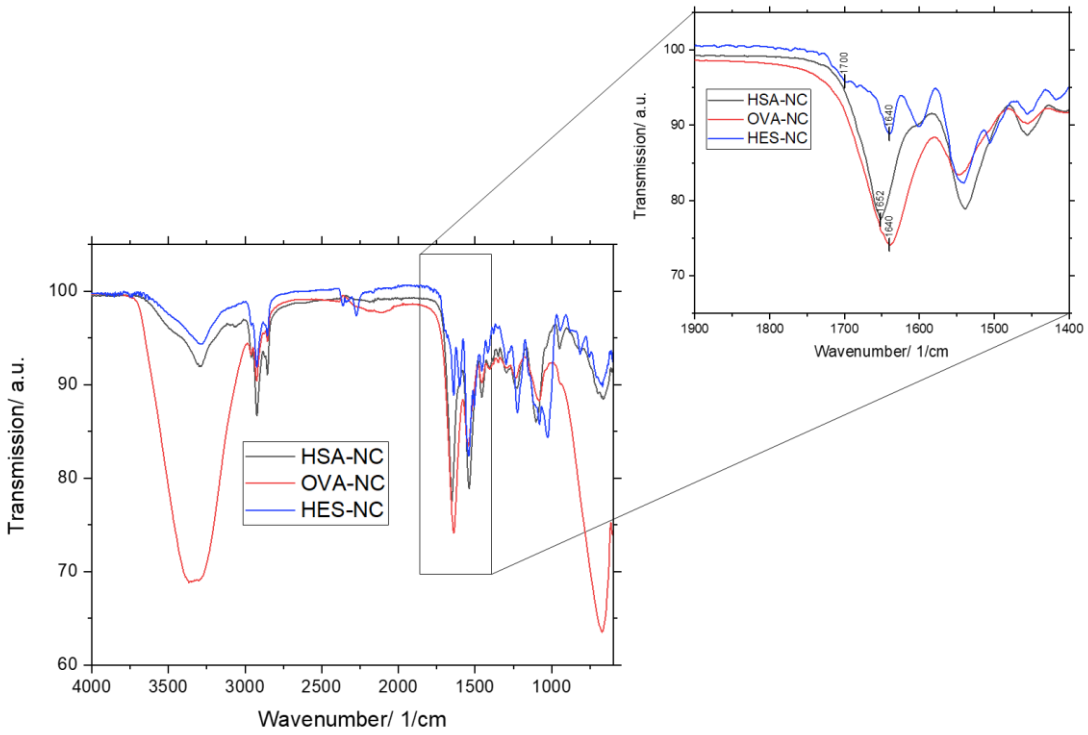

Figure 77: FTIR spectra of dried nanocapsule dispersions in cyclohexane of HSA- OVA- and HES-NCs.

Comparing FTIR spectra of HSA-, OVA- HES NC dispersions which were dried in cyclohexane, a major difference can be identified (Figure 77). In Chapter A it was shown that a HES-NC dispersion reveals bands attributed to polyurea vibrations (1640 cm^{-1}) and bands attributed to polyurethane vibrations (1700 cm^{-1}) (Figure 16). However, in the spectra shown in Figure 77, it is visible that for OVA- and HSA-NCs the vibration at 1700 cm^{-1} is missing, implying the reaction of exclusively amino groups of the proteins with TDI, leading to pure polyurea bonds in the NCs. Furthermore, the bands resulting from the polyurea bonds, 1640 cm^{-1} and 1652 cm^{-1} are slightly shifted to each other, indicating the different structures of the proteins.

Since the conversion of TDI during the protein-NC synthesis was verified by FTIR, the generated capsule sizes are compared to each other.

IV. 3.1 Size distribution of different protein-NCs

The generated protein NCs are compared to HES-NCs by light scattering measurements at 90° (Figure 78 A) and by means of a multiangle light scattering measurement of one representative BSA-NC sample (Figure 78 B). Since the proteins BSA and HSA are structurally very similar, the light scattering results for BSA- and HSA-NCs were combined. For the comparison in cyclohexane, the size distribution of six BSA- and HSA-NCs dispersions, which were synthesized independently from each other in time, were averaged and compared to the averaged size distribution of two OVA-NCs dispersions and 21 HES-NCs dispersions (Figure 78 A).

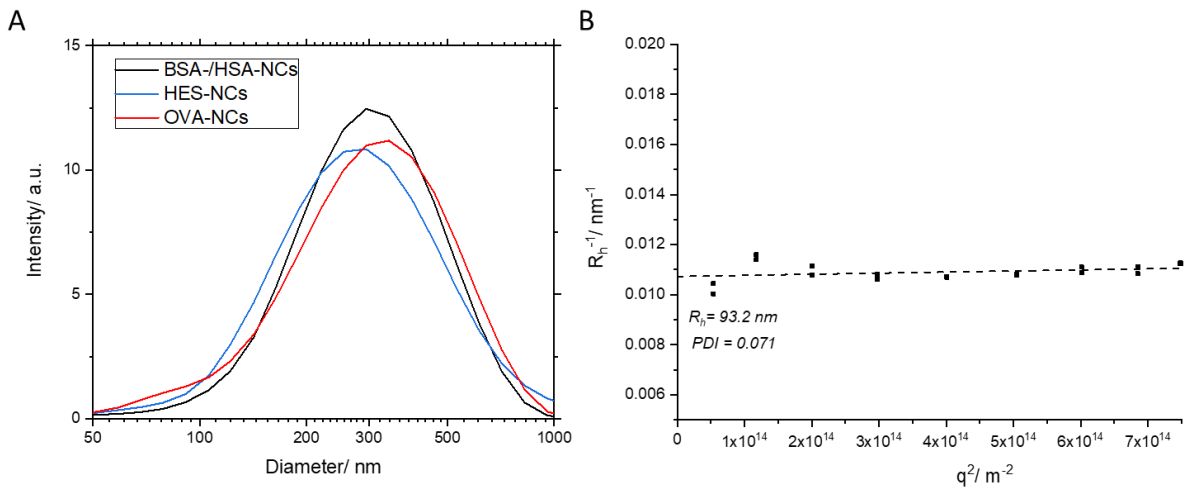

Figure 78: Light scattering experiments of different BSA-/ HSA- and OVA-NCs compared to HES-NCs in cyclohexane. **A:** Averaged size distribution of six different BSA-/HSA-NC dispersions in comparison to the averaged size distribution of two OVA-NC dispersion and 21 HES-NCs dispersion measured at a scattering angle of 90°. **B:** Multiangle light scattering measurement of a representative BSA-NC dispersion in cyclohexane. Filtered through 5 µm LS. Experimental error is 10%.

Light scattering experiments of different protein-NCs reveal that a similar size distribution of BSA/HSA-NCs and OVA-NCs in cyclohexane was obtained. In addition, the averaged size of BSA/HSA (black curve) as well as OVA-NCs (red curve) were almost identical to HES-NCs (blue curve) in the same continuous phase (Figure 78 A). These findings are supported by the multiangle light scattering measurement of BSA-NCs in cyclohexane (Figure 78 B), in which the capsules showed a hydrodynamic radius of 93 nm which is similar to the obtained radius for HES-NCs (compare Chapter A, Figure 17). In addition, the measurement (Figure 78 B) reveals that the obtained hydrodynamic radius was similar at different angles indicating a low polydispersity.

After synthesis in cyclohexane, protein-NCs were redispersed in aqueous phase, which is necessary to use them for biological samples. To sufficiently disperse them in water, the surfactant SDS was added. The same samples shown in Figure 78 were transferred to an aqueous SDS solution (0.1 wt%) and again the averaged size distribution of six BSA-/HSA-NCs and three OVA-NCs in water was determined by light scattering at 90° (Figure 79 A). Furthermore, the size distribution of one individual NC sample per protein-NC was determined by multiangle light scattering after purification and concentration (Figure 79 B).

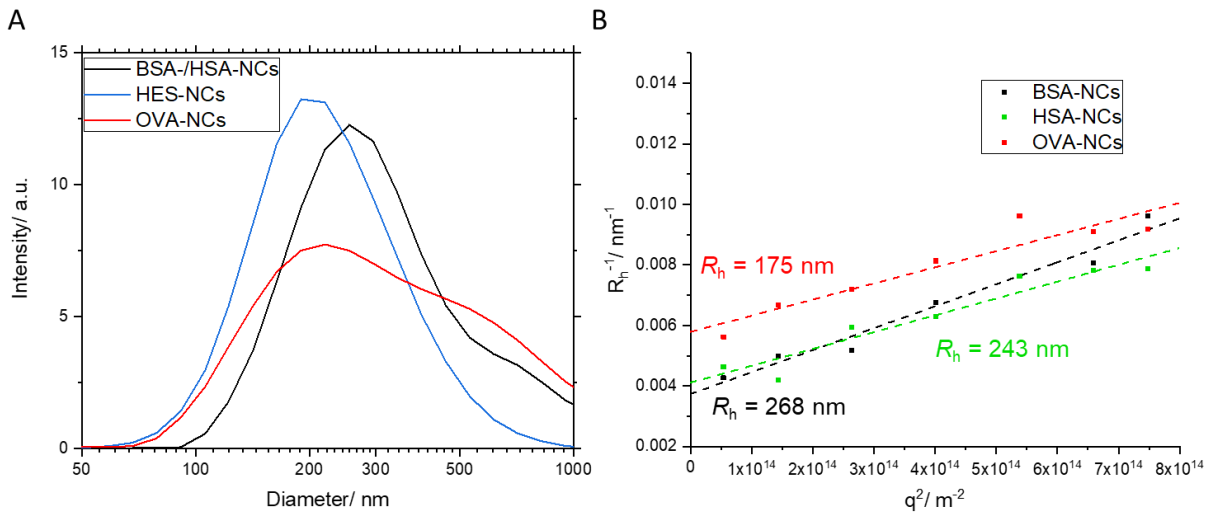

Figure 79: Light scattering experiments of different BSA-/ HSA- and OVA-NCs compared to HES-NCs in water. **A:** Averaged size distribution of six different BSA-/HSA-NC dispersions in comparison to the averaged size distribution of three OVA-NC dispersions and 21 HES-NCs dispersions measured at a scattering angle of 90°. **B:** Multiangle light scattering measurements of individual protein-NCs samples after purification and a tenfold concentration of the dispersion to approx. 1 wt%.

When protein-NCs were transferred to aqueous phase, a change in size distribution in comparison to that one in cyclohexane was detected. This change in size distribution from organic to water phase was more apparent than for HES-NCs (compare Chapter A, Figure 18 and 22). In the 90° light scattering setup, BSA-/HSA-NCs show a moderate shift towards larger diameters with OVA-NCs tending to significantly broader size distributions in comparison to HES-NCs (Figure 79 A, black and red curves). These findings are supported by the multiangle light scattering measurement, which reveal that the hydrodynamic radii and the polydispersity of all the protein-NCs increase significantly when they were transferred to water and purified from SDS. All the tested protein-NCs (one sample per protein) demonstrate an increase of the hydrodynamic radius to up to 268 nm (Figure 79 B, black data points). HSA- and BSA-NCs show similar radii while OVA-NCs reveals a smaller hydrodynamic radius (Figure 79 B, red data points) in the performed experiment. This is interesting, since the proteins HSA and BSA have an almost identical molecular weight, while OVA exhibits a significantly smaller molecular weight. The large increase in size is explained by the fact that proteins, like other biopolymers, can incorporate water molecules and thus swell.[267] Furthermore, it is known that proteins act like surfactants and might compete with added surfactant for the interface.[268] This could mean that after removal of SDS due to purification processes, an adsorption of protein could be favored. This could be achieved either by allowing free protein, which is much more mobile in aqueous solution than in cyclohexane, to accumulate on formed capsules or by allowing the crosslinked capsules to retain their interfacial adsorption property.

IV. 3.2 Surface charge and surface groups of protein-NCs in aqueous medium

The surface charge of protein-NCs was determined by means of zeta potential measurements as a function of pH value. The capsules were compared with dissolved protein and under different conditions such as different crosslinking densities as well as solid contents (Figure 80).

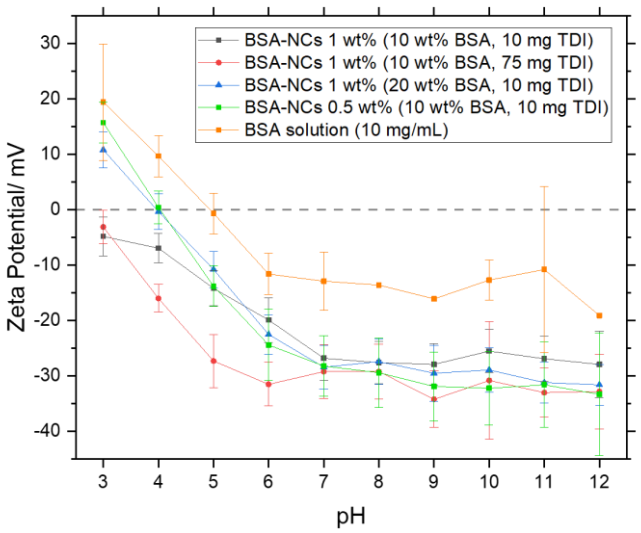

Figure 80: pH dependent zeta potential measurements of BSA-NCs in different concentrations, as well as highly crosslinked BSA-NCs (10 wt% BSA, 75 mg TDI), a higher amount of BSA (20 wt% BSA, 10 mg TDI) and pure BSA protein (10 mg/mL). Error bars resulted from the measurement of technical triplicates.

Since the capsules, like the protein itself, have different groups on the surface, the pH dependent zeta potential measurement shows a similar trend as the pure protein in the case of BSA. In acidic pH up to pH 4 the NCs with higher BSA content (20 wt%, Figure 80, blue curve), capsules with a solid content of 0.5 wt% (Figure 80, green curve) as well as pure protein (Figure 80, orange curve), reveal a positive zeta potential and thus indicate mainly protonated groups on the surface. At more alkaline conditions, the zeta potential decreases rapidly for all the samples and reach an end point of approximately -30 mV for the capsule samples and -20 mV for the pure protein solution. At very basic pH values, the dissolved protein was unstable, which is evident from the high error bar at pH 11 (orange curve). At higher capsule concentrations and at high crosslinking densities (compare Figure 80, red and black curve), the zeta potential is more negative and do not reach positive values at any pH value. The isoelectric point of the samples appears at a zeta potential of 0 mV (grey dotted line). The protein sample shows an isoelectric point at approx. pH 4.9, which corresponds to values from the literature (pH 4.5-4.9)[263]. Interestingly, the BSA-NCs (0.5 wt% and NCs prepared with 20 wt%) show an isoelectric point at a lower pH value (pH 4.0). This shift of the isoelectric point to acidic pH values could be caused by the crosslinking of the protein, which leads to fewer amino groups on the surface being accessible for protonation, since they have been crosslinked to a large extent by TDI. Next to the lower availability of amino groups on the capsule surface in comparison to non-crosslinked protein, it was investigated if the amount of SDS plays a role for the zeta potential determination.

The SDS concentration was determined using a SDS assay (Chapter A, 2.2.1) for protein-NCs and compared to HES-NCs. In addition, the zeta potential after each washing cycle was analyzed (Figure 81 A and B).

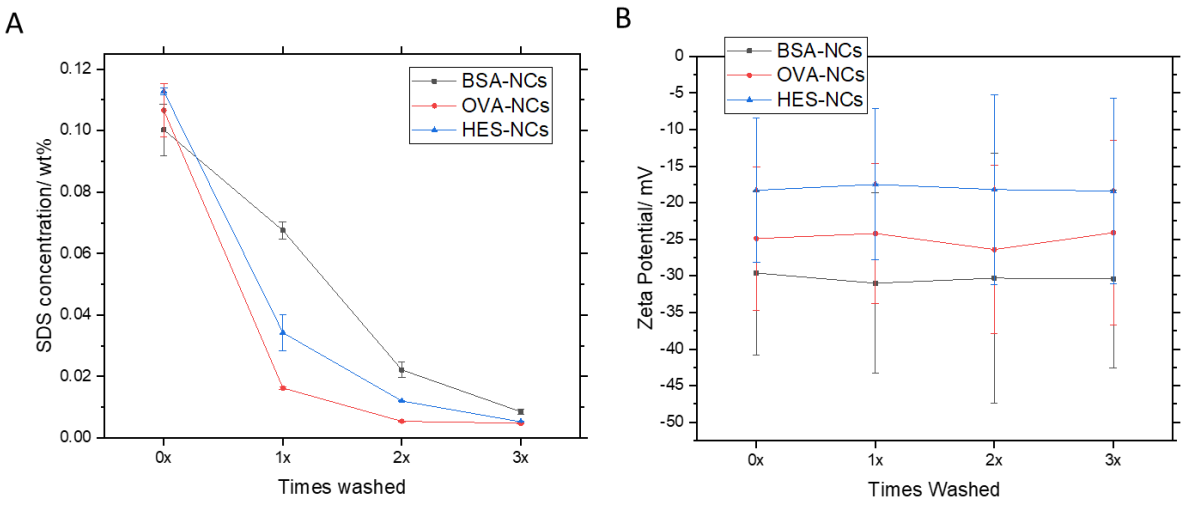

Figure 81: A: SDS concentration in BSA-, OVA and HES-NCs decreases with amount of washing. **B:** Zeta potential measurements of the corresponding capsules after washing cycles at pH 7.

Figure 81 A shows that by successive washing by centrifugation, SDS was removed from the protein-NCs samples, as described before for HES-NCs (Figure 25 A). After three washing cycles, the SDS concentration decreased to under 0.01 wt% for all samples. The zeta potential at pH 7 during successive washing cycles remained constant (Figure 81 B). This was also observed in the same way for the HES NCs (Figure 27). In general, the zeta potential for protein-NCs is slightly more negative than for HES-NCs. The pH-dependent zeta potential measurement supports the assumption that different surface groups are present in the case of protein-NCs. At acidic pH, the amino groups on the NCs are protonated, which results in a more positive zeta potential. The exact number of amino groups was verified with a fluorescamine assay. For the amino content analysis of the different proteins, the assay was calibrated using hexylamine (compare Chapter A), in the case of protein-NCs the obtained molar amount of amino containing material was calculated using the molecular weight of the respective protein, since this leads to more precise results. Again, differences between the proteins used were observed. In addition, the protein batches of different manufacturers were analyzed (Figure 82).

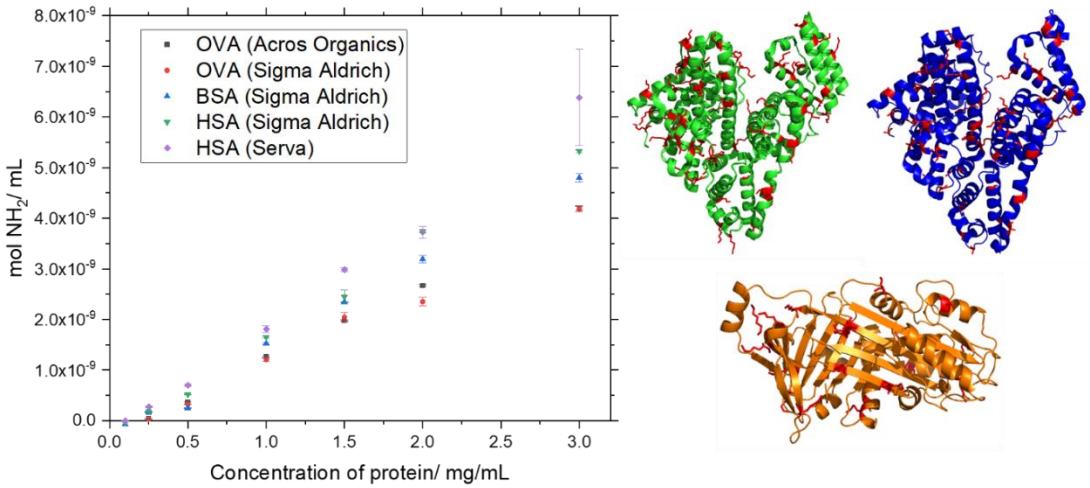

Figure 82: Fluorescamine assay of different proteins dissolved in deionized water from different suppliers. Crystal structures of the corresponding proteins with highlighted lysines in red (green: BSA, blue: HSA and orange: OVA).[269–271]

The amount of detected amino groups is linear with increasing concentration of the respective proteins (Figure 82). HSA seems to have the highest amino content in comparison to all proteins, although the difference in mol NH_2/mL to BSA is just marginal. The molecular weight of BSA and HSA is almost identical at about 66 kDa. OVA exhibits only 2/3 of the molecular weight of the other proteins (43 kDa). Nevertheless, the number of amino groups per mL detected in OVA is only slightly lower than in the other proteins. Compared to the total molar amount of protein, the obtained amino content of the different proteins is in agreement with the expected amount of lysines in the respective protein (10% for BSA and HSA and 5% for OVA). No significant differences in the amino content was found between the manufacturers. The protein crystal structures (Figure 82) reveal a high structural similarity for BSA (protein in green) and HSA (protein in blue), whereas OVA (protein in orange) has a completely different protein structure. The lysines in the proteins, which each represent the highest proportion of detectable amino groups per protein, were highlighted in red in the crystal structures. These amino acids are predominantly visible at the outer surface of the proteins and point to the exterior. They are often responsible for ionic interactions or hydrogen bonds with surrounding water molecules or other ionic amino acids. This structural difference between the proteins is also reflected in the capsule synthesis, which leads to a different size distribution of OVA-NCs compared to BSA- or HSA-NCs, especially after redispersion and water transfer of the formed NCs.

Since the analysis of the amino groups in the proteins correspond to the proportion of lysines in the respective protein, the assay was used to quantifiy the number of amino groups on the NCs. Therefore, the NCs were purified and concentrated and the amino content was determined using three concentrations of the NCs to prove linearity of the fluorescence-based quantification. The respective protein, dissolved in buffer, was used as external standard (Figure 83).

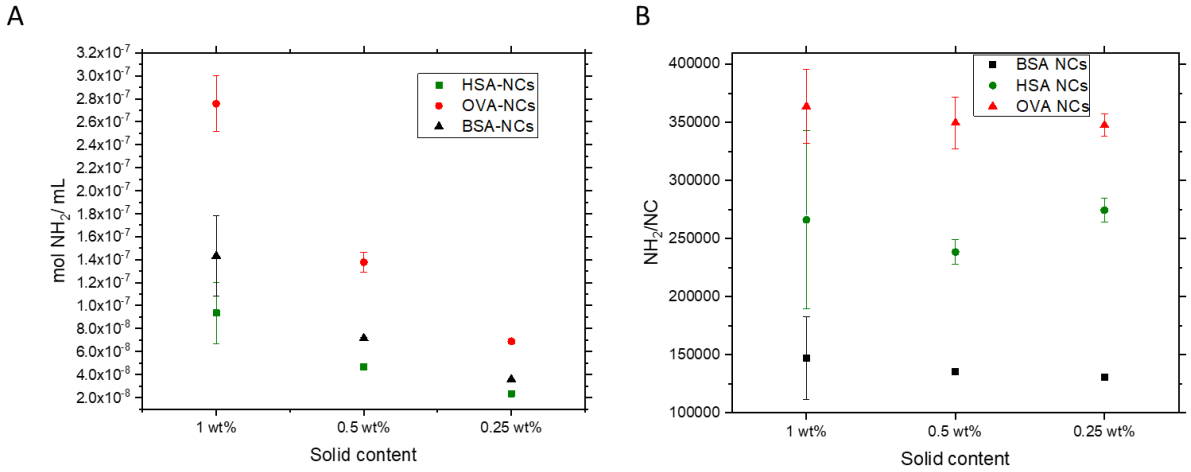

Protein capsule	NH_2/nm^2	R_h
BSA-NC	0.43 ± 0.03	160 nm
HSA-NC	0.41 ± 0.03	224 nm
OVA-NC	0.93 ± 0.02	174 nm

Figure 83: Detected amino groups on different protein-NCs. **A:** mol NH_2 per mL dispersion plotted against solid content. **B:** Determined amino groups/nm^2

The protein-NCs reveal an unambiguous detectability of amino groups on their surface. As expected, the molar amount of detected amino groups per mL dispersion decreases with decreasing solid content of the dispersion (Figure 83 A). Just as expected, the number of amino groups per NC remains constant as the solid content decreases (Figure 83 C). In all the plots shown in Figure 83, a moderate tendency for OVA NCs to have a slightly increased amino content is observed (compare Figure 83 A and B, red data points). If the surface area of the respective capsules was considered, a surface density of amino groups of about 0.4 groups/nm^2 for BSA- and HSA-NCs was obtained, whereas for OVA-NCs 0.9 groups/nm^2 was obtained (Table inlet Figure 83). As expected, BSA- and HSA-NCs revealed a similar number of amino groups/nm^2 which was expected due to the high similarity of both proteins. Equal amounts of proteins were added to each emulsion, however, due to the lower molecular weight of OVA, more OVA molecules were present in the emulsion (35% more OVA molecules than BSA/HSA). Since the lysine share in OVA is only half that in BSA and HSA (5% lysines in OVA and 10% lysines in BSA/HSA), the overall number of amino groups was expected to be lower for OVA-NCs. The higher surface density of amino groups on OVA-NCs compared to BSA- and HSA-NCs can be explained by the smaller molecular weight of OVA and thus more OVA could be crosslinked into one protein-NC. Furthermore, it was demonstrated that the number of amino groups on HES-NCs were influenced by TDI hydrolysis (Chapter A, 3.1.1). OVA could exhibit a different reactivity towards TDI due to the different protein conformation compared to the other proteins.

The results obtained from the pH-dependent zeta potential measurements (Figure 80) indicate that a higher crosslinking density leads to a less positively charged surface (Figure 80, red curve). Therefore, it was examined if the TDI concentration plays a significant role for the quantification of amino groups on protein-NCs by fluorescamine assay. Therefore, the same samples analyzed in Figure 80 exhibiting different crosslinking densities and a different protein concentration (20 wt% instead of 10 wt%) were analyzed and the amino content was compared by fluorescamine assay while the morphology of the corresponding NCs was checked using electron microscopy (Figure 84).

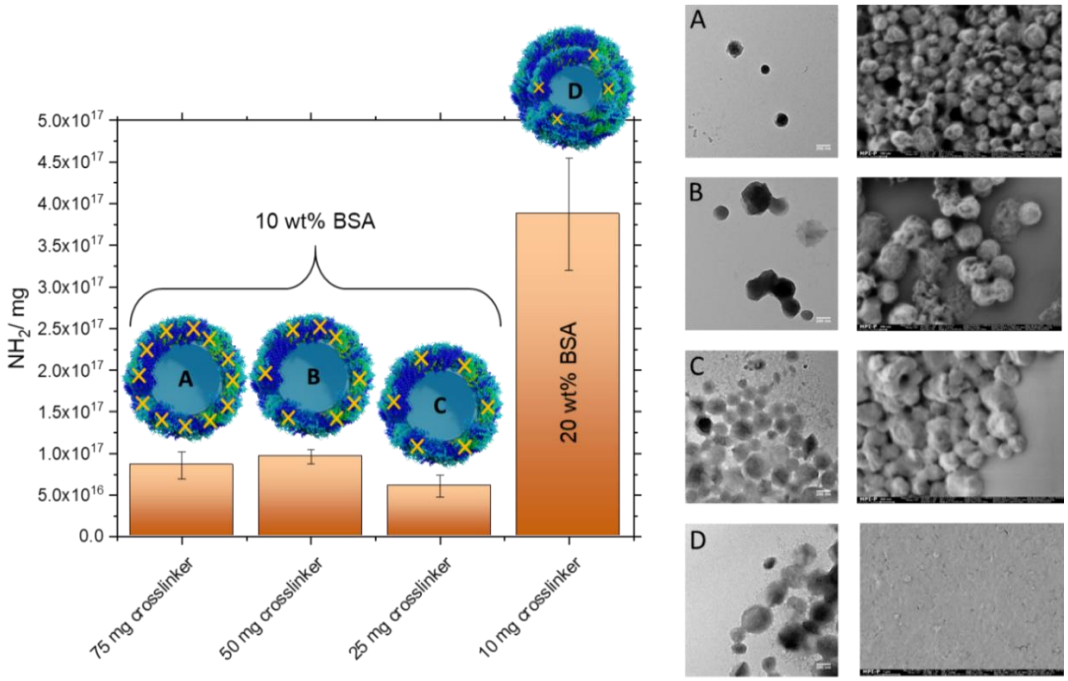

Figure 84: Amino groups per mg of NCs in dependency of added crosslinker concentration and TEM/SEM images of the corresponding capsules generated (A-D).

An increased amount of crosslinker TDI, which was added to the emulsion had no significant influence on the detected amino groups on the capsules, as a constant level of amino groups were observed (Figure 84, A-C). These results indicate that the crosslinker TDI crosslinked the protein generating polyurea groups and does not significantly contribute to the amino content of the capsules.

If the protein concentration in the emulsion was doubled from 10 wt% to 20 wt% (sample D) and the TDI concentration was reduced 1.5-times (10 mg TDI instead of 25 mg), an almost 5 times increase of detected amino groups was observed. This result is surprising since it suggests that the crosslinking influences the amino group detection by fluorescamine assay and indicates that fewer groups might have been detected than are possibly present. TEM and SEM images of the corresponding capsules illustrate the morphology obtained by the varied synthesis (Figure 84, right). Image A demonstrates that the capsules had a dense shell and revealed a much higher contrast than sample C or D. Furthermore, the shape was rounder than for NCs crosslinked with less TDI. The less crosslinker was added, the softer the generated capsules appeared in TEM, which was also verified by SEM images. Since in previously reported studies it was shown that higher crystallinity goes along with a thicker shell[181], the generated capsules formed using more crosslinker could exhibit a thicker polyurea shell and therefore reveal a higher crystallinity. These findings may provide evidence that at higher crystallinity there is reduced detectability of the amino groups, for example caused by a limited accessibility.

IV. 3.3 Surface functionalization of protein-NCs with DBCO-PEG-NHS ester

In order to perform a bioorthogonal copper-free click reaction on protein-NCs, the amino groups accessible on the surface of the NCs were used to attach dibenzocycloocytne (DBCO) *via* an NHS ester reaction. Therefore, DBCO ester **9** was added to an aqueous protein-NCs dispersion of known solid content.

As shown in Chapter A, 3.2, azide **10** was used for detection of the attached DBCO groups and quantified by means of a fluorescent assay using an external calibration. The DBCO amount on the different protein-NCs and a concentration dependency of the added DBCO ester were compared (Figure 85). For the functionalization of the protein-NCs with DBCO ester **9**, the same molar excesses of **9** were used as for HES-NCs (Chapter A, 3.2.1). As already observed in the case of HES-NCs, the addition of 3.3 mg DBCO per mL protein-NC dispersion led to a high concentration of DBCO in the supernatant of the NCs and to colloidal instability resulting in difficulties in recovering the dispersion after the centrifugal washing steps. Reducing the added concentration of **9** to the protein-NCs dispersion led to an improvement of the colloidal stability and enabled reliable quantification by means of a DBCO-anthracene azide assay (external calibration) (Figure 85).

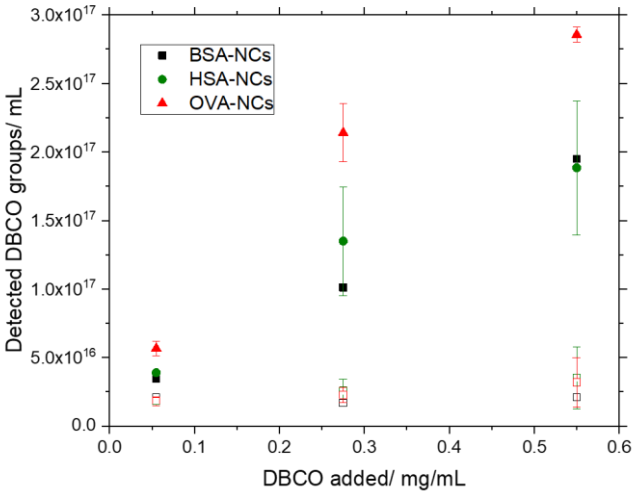

Figure 85: DBCO functionalization of different protein-NC (1 wt%) and detected DBCO concentration inside the supernatant after three centrifugal washing steps (filled data points). Non-filled data points refer to corresponding DBCO concentrations inside the supernatant.

In Figure 85 the averaged DBCO groups per mL of two different HSA- and OVA-NCs and of one BSA-NCs batch are depicted. As expected, with increasing addition of **9** more DBCO was detected on the NCs. In accordance with the results of the amino group quantification by fluorescamine assay (Figure 83), in which a higher amino content for OVA-NCs was demonstrated, also for the attachment of DBCO *via* NHS chemistry slightly higher binding tendencies of OVA-NCs in comparison to HSA-NCs were observed (Figure 85 A red data points). As expected, BSA- and HSA-NCs revealed a similar amount of DBCO groups/ mL. These results indicate that DBCO modification on protein-NCs occurs *via* a chemical bond and is not purely controlled by adsorption. At an addition of 0.55 mg **9** per mL dispersion, almost 3 x 10^{17} DBCO groups were detected on OVA-NCs, which is approx. 60% of the added DBCO. Compared to the detected DBCO groups per mL obtained on HES-NCs (in average 2 x 10^{17} DBCO groups/mL at an addition of 3.3 mg DBCO per mL), the results reveal that the binding efficiency of protein-NCs is higher, since also the DBCO concentrations found in the supernatant are low (non-filled data points. Furthermore, the surface density of DBCO groups/nm^2 for HSA- and OVA-NCs were determined (Table 19).

Table 19: Calculated DBCO groups/nm^2 for HSA- and OVA-NCs at different DBCO NHS ester additions.

	HSA-NCs	**OVA-NCs**
Added DBCO ester mg/mL	**Detected DBCO groups/nm^2**	**Detected DBCO groups/nm^2**
0.55	1.80 ± 0.47	1.31 ± 0.0258
0.275	1.38 ± 0.41	0.970 ± 0.0958
0.055	0.309 ± 0.0143	0.257 ± 0.0235

When the number of DBCO groups per nm^2 capsule is considered, it was observed that the surface densities were very similar and therefore no difference in binding affinities between the proteins was identified. As expected, the number of DBCO groups/nm^2 decreases with decreasing addition of DBCO NHS ester. A high surface density of approx. 1.56 DBCO/nm^2 (average of both capsules) and a low surface density of 0.283 DBCO/nm^2 was achieved.

Next, the chemical modification of dissolved protein with **9** was compared to the respective protein-NC, using MALDI-ToF. When BSA was treated with ten times the molar excess of DBCO NHS ester **9**, the mass increased about 4871 Da. This corresponds to an attachment of around 7.5 DBCO molecules per BSA molecule (Figure 86, blue curve).

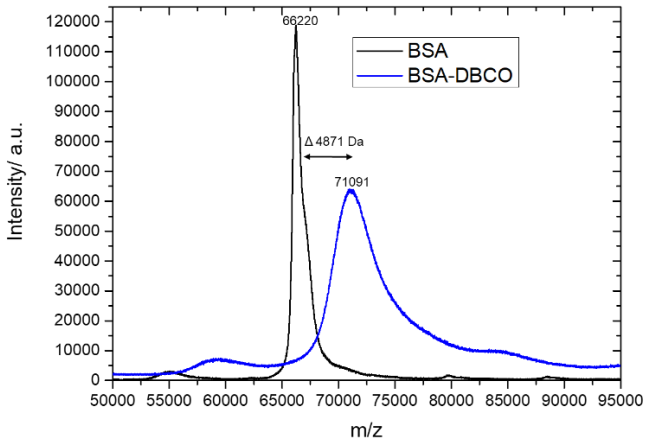

Figure 86: MALDI-ToF measurement of pure BSA protein and after modification of BSA with a tenfold molar excess of DBCO-PEG-NHS ester **9**. Both proteins were dialyzed against MilliQ water. 10 mg/mL. *α*-cyano-4-hydroxy cinnamic acid was used as matrix.

The mass spectrum highlighted in black illustrates the BSA reference sample in MilliQ water and reveals a mass of 66 220 Da which agrees well with the values given by the supplier and by literature of 66 kDa (Figure 86, black curve). The attachment of 7.5 DBCO groups per protein, corresponds to 12.5% of bound lysines, since a BSA molecule exhibits 60 lysines.[272] BSA-NCs with a solid content of 1 wt% revealed about 1 x 10^{-7} mol of amino groups per mL (Figure 85 A, black data point). At an addition of 0.055 mg DBCO/ per mL of dispersion, which corresponds to a DBCO to amino ratio of 0.85:1, 3.46 x 10^{16} DBCO groups per mL could be detected (Figure 85, black data points at 0.055 mg/mL). This corresponds to about 5.746 x 10^{-8} mol of detected DBCO and therefore makes up 57.5% of attached amino groups (with a maximum of 85% to be attached), if it is assumed that all the detected DBCO groups are attached to a lysine *via* NHS linkage.

These findings indicate that, when a linker molecule is bound to a colloid, significantly less material can be used than when the molecules to be reacted are present in solution. Already at 0.275 mg DBCO per mL (ratio of 4.233 to 1 DBCO: NH_2) the amount of detected DBCO groups exceeded the number of amino groups present on the capsule. In the case of the dissolved protein, significantly more DBCO ester was used, as even a tenfold molar excess relative to protein was used and not relative to lysines, however the binding efficiency was much lower compared to the NCs. These findings can be explained that in the case of colloids various physicochemical properties such as surface energy and surface tension play further roles in functionalization.

These results again highlight the importance of precise surface modification of nanocarriers and show that reactions at the interface have to be assessed differently than reactions in solution.

IV. 4. Conclusion

With the help of pH-dependent zeta potential measurements, different nanocarrier systems can be compared with respect to their surface charge and the presence of potential surface groups (Figure 87).

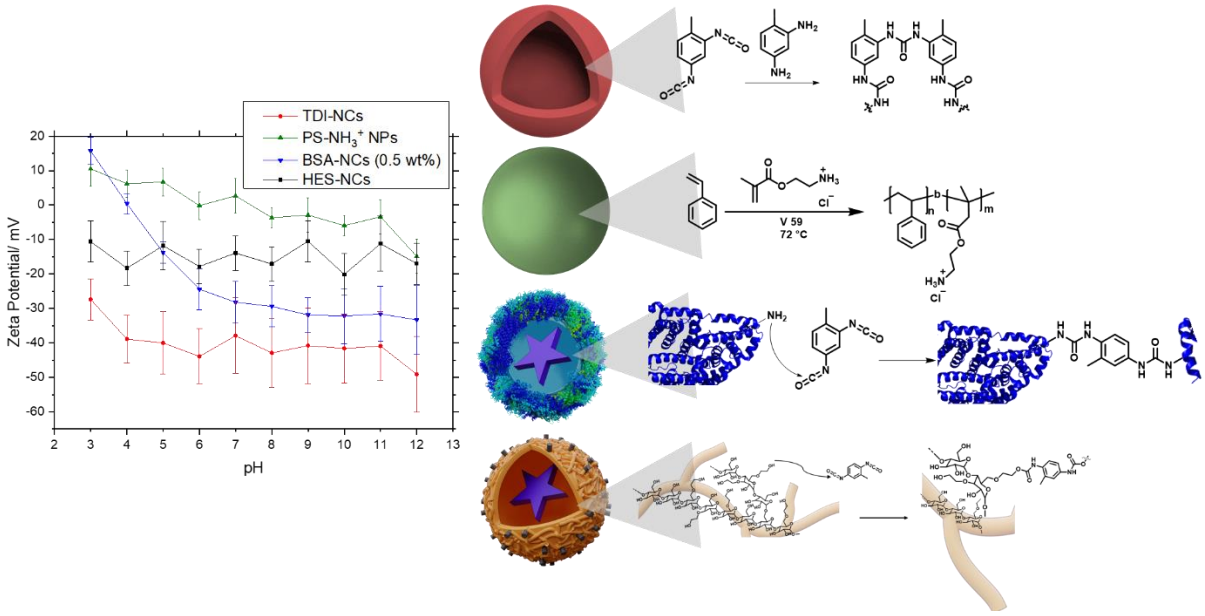

Figure 87: Comparison of pH dependent zeta potential measurements of different particle and capsule systems.

Using pH-dependent zeta potential measurements, the tendency of the surface charge of different particles and capsule systems can be evaluated. For BSA-NCs (Figure 87, blue curve) and amino-functionalized PS-NPs (Figure 87, green curve), it was observed that at acidic pH values (to up to about pH 6 for PS-NP), a positive zeta potential was obtained, whereas the other systems did not show a positive zeta potential at any of the measured pH values. For NCs consisting purely of TDI (Figure 87, red curve) and HES-NCs (Figure 87, black curve), no pH dependent change in zeta potential was observed. The TDI-NCs however, even revealed the most negative values. The physicochemical properties of the nanocarriers shown in Figure 87 are listed in Table 20.

Table 20: Physicochemical properties of the different nanocarrier systems shown in Figure 87.

Entry	Composition	R_h (H_2O, pH 7)	ζ Potential (pH 7)
MF-121	HES-NC	142 ± 34 nm	-13.9 ± 5.30 mV
MF-122	BSA-NC	120 ± 39 nm	-28.2 ± 4.17 mV
MF-131	TDI-NC	195 ± 83 nm	-37.9 ± 7.69 mV
MF-133	PS-NH_3^+-NP	82 ± 41 nm	2.68 ± 4.94 mV

Customized PS-NPs were prepared which were selectively provided with different number of amino groups on the particle surface. It was demonstrated that with increasing concentration of added amino methacrylate precursor (AEMH) lower yields of functionalized particles were obtained. Both, pristine PS-NPs and amino-functionalized PS-NPs, were covered with a different DBCO surface density, but there was a significant increase in detected DBCO groups when amino groups were present on the particle surface, revealing a covalent modification of the particles with DBCO.

Afterwards a copper-free click reaction with azidated BSA on the particle surface was performed revealing a uniform surface density of BSA at particularly low DBCO surface densities. However, a differentiation between adsorbed BSA and covalently bound BSA is complicated when a pure quantification by Pierce Assay is performed.

Hence ITC measurements using amino-functionalized PS-NPs and DBCO functionalized PS-NPs to which azidated BSA was titrated, revealed differences between both particle species. A stronger interaction between the protein and the DBCO functionalized particles were found. Furthermore, increased entropy and reduced enthalpy terms during the reaction of PS-DBCO-NPs with the protein in comparison to the same energetic contributions of PS-NH_2-NPs with the protein were calculated. Nevertheless, these results cannot be clearly attributed to a chemical reaction, since effects such as hydrophobicity, which have a significant influence on the entropy and enthalpy in a system, must also be taken into account.

Thus, in future experiments, particles with different amounts of DBCO should be considered, as well as measurements at different pH values to investigate different charged states of the protein. Furthermore, it would also be useful to first perform the ITC measurement for dissolved molecules instead in dispersion. For this purpose, accurate energy terms of the click reaction for the respective molecules could be determined, however, a water-soluble DBCO derivative would be necessary.

In reference to the obtained results of the PS-NP modification, different protein-NCs were synthesized revealing different number of amino groups on the surface. It was demonstrated that protein-NCs were prepared with similar size distribution as HES-NCs in inverse miniemulsion, the size of the capsules in aqueous SDS solution depended on the respective protein used. For the protein-NCs, BSA, HSA and OVA were exploited for NCs synthesis, from which BSA and HSA have structural similarities, while OVA exhibits a fundamentally different protein structure. The number of amino groups determined by fluorescamine assay in each protein is consistent with the theoretically expected number of lysines. OVA contains a lysine content of about 5% whereas HSA and BSA have twice as many (10%). More amino groups were detected in OVA-NCs than in HSA- or BSA-NCs after capsule preparation, suggesting a profoundly different protein folding during capsule formation.

By comparing the number of attached DBCO molecules to pure dissolved protein, with the number of attached groups to protein-NCs, it was observed that with similar excesses of added DBCO to detected amino groups, significantly more DBCO was found on the colloid after purification than on the dissolved protein, indicating the complex physicochemical properties and the need for a precise addition of linker molecules to the particle.

Chapter C – Bio-orthogonal triazolinedione (TAD) crosslinked protein nanocapsules affect protein adsorption and cell interaction

This chapter is based on the paper published in Polymer Chemistry, 2020, 11, (23), 3821-3830 and is reproduced from Ref.[178] with permission from the Royal Society of Chemistry.

TAD and all capsules were synthesized and characterized by me, Marie-Luise Frey. All cell uptake experiments including analysis by flow cytometry, as well as protein corona analysis by Pierce™ assay, SDS PAGE and LC-MS were performed by [redacted]. Cell uptake experiments for confocal imaging and a cell viability assay were performed by [redacted].

IV. 1. Introduction

In the previous Chapter it has been elucidated that proteins are a suitable material for biocompatible and biodegradable nanocarriers. By specific surface modifications, they can be functionalized leading to receptor-mediated cell uptake or cell-specific proliferation. However, not only the transport of biomolecules attached to the outer surface of the nanocapsule is important for the nanocarrier to reach its destination, but also the encapsulated cargo, as it is the drug which needs to be delivered to a specific location.

As already reported, proteins can easily be crosslinked in an addition reaction by using 2,4-toluene diisocyanate (TDI), which leads to a dense polymeric nanocapsule shell. However, TDI reacts unspecifically with different nucleophilic groups, like amine-, hydroxyl- or thiol-functionalities, which are mostly present in the side chains of the amino acids of the protein.[108,273] In recent studies there have been several approaches to supply more specificity in the composition of the nanomaterial by using bioorthogonal chemistry.[274,275] For example, Piradashvili *et al.* presented a method using a tetrazole-ene cycloaddition to synthesize protein nanocarriers.[276] However, in the reported approach, UV irradiation for interfacial crosslinking is necessary, which may also provoke other photochemical reactions within the protein, destroying its native function.[277] Strain-promoted azide–alkyne cycloadditions (SPAAC) become increasingly popular and provide high selectivity.[278] However, the corresponding groups need to be introduced into the biomolecule before the click reaction, which may not inevitably occur in a bioorthogonal manner. Other bioorthogonal bioconjugation methods like e.g., hydrazone or oxime ligations are strongly dependent on the pH value and can be reversible in aqueous medium.[274,279]

Herein we report the synthesis of protein nanocapsules that were crosslinked with a 4-phenyl-triazolinedione (TAD) derivative, which specifically reacts with amino acids with delocalized π-electron systems.[140,280–282] The ability of TAD to act as a strong dienophile in a Diels–Alder reaction has already been shown almost 60 years ago.[283] Recent studies performed by Du Prez and coworkers again showed its versatility in current applications in polymer science.[141,284,285] We show that particularly TAD's extraordinarily fast and specific reaction behavior leads to a remarkable responsiveness towards proteins in aqueous emulsion, forming nanocapsules with narrow size distribution, in spite of the reported sensitivity of TAD in regards to hydrolysis and reduction to the corresponding urazole derivative.[128,133,134,286]

TAD-crosslinked protein nanocapsules were synthesized with bovine serum albumin (BSA), human serum albumin (HSA) or ovalbumin (OVA) via an inverse miniemulsion procedure. Additionally, nanocapsules using only the amino acid tryptophan instead of full proteins were prepared. In all cases, the protein nanocapsules showed low plasma protein adsorption. The significant differences in the cell uptake of the TAD- crosslinked protein nanocapsules and TDI-crosslinked nanocapsules can be explained by a different protein conformation at the nanocapsule surfaces.

IV. 2. Synthesis and characterization of TAD crosslinked nanocapsules

Protein nanocapsules were synthesized by an interfacial bioorthogonal crosslinking reaction in inverse miniemulsion adding MDI-TAD as difunctional TAD-derivative to the organic continuous phase (see Figure 88). The aqueous droplet phase either consists of the protein BSA (bovine serum albumin) or the amino acid tryptophan (Trp). As control reaction, also no further reactant was added allowing TAD-TAD reactions (see Figure 88 A). Upon reaction, the intensive pink color of the MDI-TAD molecules vanished within a few minutes and the emulsion turned slightly yellow, indicating conversion of MDI-TAD. After reaction, the sizes of the formed nanocapsules as revealed by dynamic light scattering (DLS) are about 120 nm in diameter for Trp-TAD and 240 nm for BSA-TAD, with a narrow size distribution for Trp-TAD nanocapsules (PDI of 0.100, see Table 21). The morphology analyzed via scanning electron microscopy (SEM) showed a well-defined morphology for Trp-TAD nanocapsules as well as for BSA-TAD nanocapsules (Figure 88 B, middle and right panel). Pure TAD crosslinking leads to a more undefined and film-like structure (Figure 88 B, left panel). The collapse of the nanocapsules occurs due to the drying process in the sample preparation and the vacuum used during the measurement.

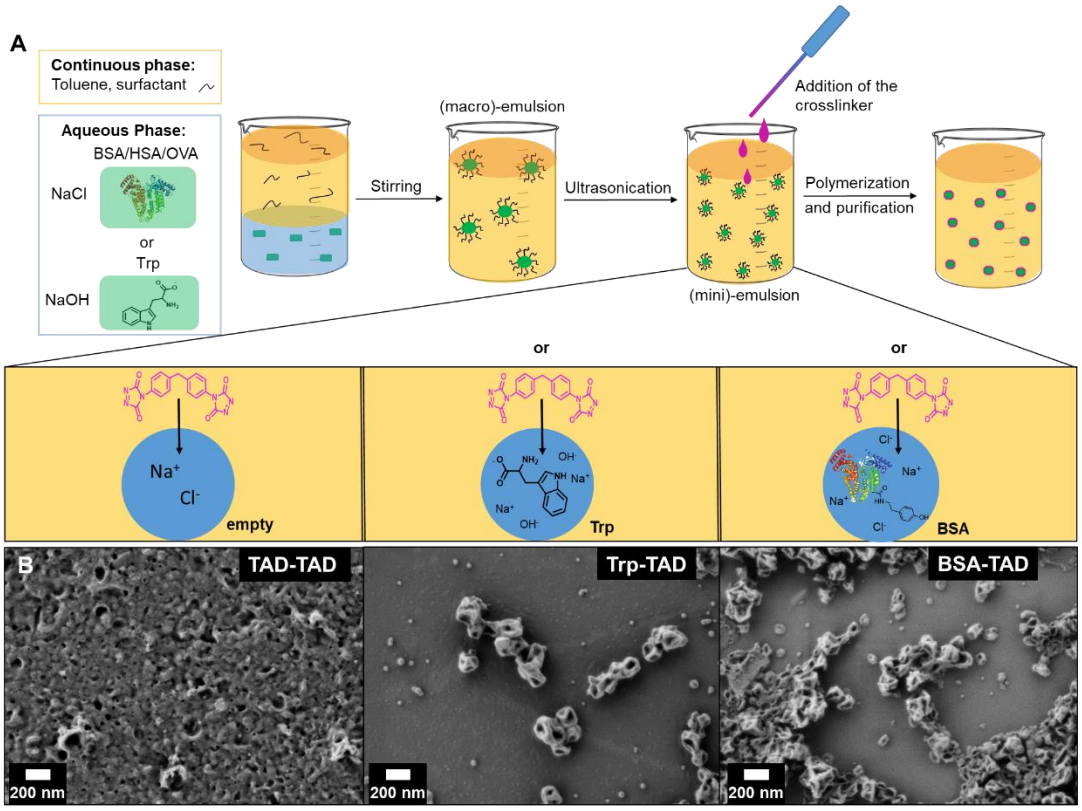

Figure 88: A: Scheme of the protein nanocapsule synthesis by an inverse miniemulsion procedure and MDI-TAD as crosslinker. Trp-TAD (tryptophan) and BSA-TAD nanocapsules, as control pure TAD nanocapsules were used; **B:** Scanning electron microscopy (SEM) images of the TAD nanocapsules.[178]

Consistent with Figure 88, pure TAD nanocapsules appear smaller in size (84 nm) but reveal a significantly higher polydispersity index (PDI of 0.220, see Table 21). After redispersion in water, the sizes increased. This change occurs by the formation of a hydration shell or by swelling of the polymer in water. The measured ζ-potentials were negative in all cases.

Table 21: Physico-chemical characteristics of different synthesized TAD nanocapsules.[178]

NC-sample	Average diameter in toluene*	Average diameter in water*	PDI in toluene (90°)	ζ – potential/ mV
TAD-TAD	84 ± 8 nm	155 ± 16 nm	0.220	-37 ± 5
Trp-TAD	119 ± 12 nm	163 ± 16 nm	0.100	-41 ± 5
BSA-TAD	238 ± 24 nm	350 ± 40 nm	0.171	-

* determined by multiangle DLS (at scattering angles of 30 to 150°).

As analyzed by nuclear magnetic resonance (NMR) spectroscopy, tryptophan and TAD successfully reacted at the interface of the miniemulsion, as indicated by occurrence of the TAD indole reaction (Figure 89).

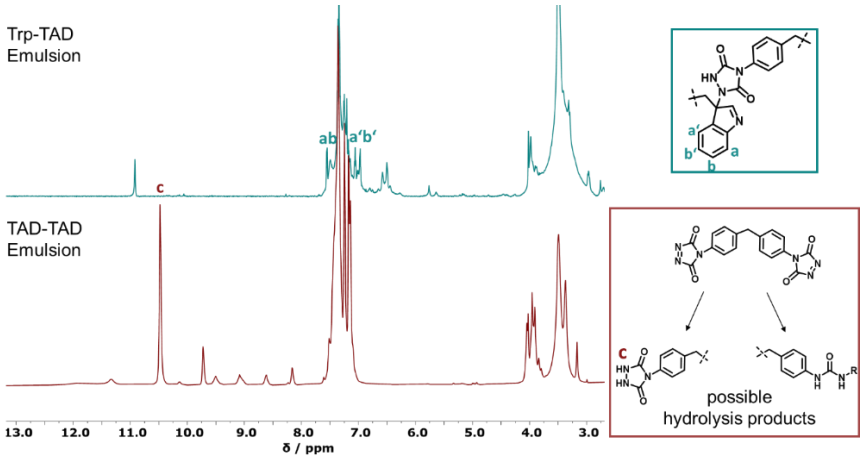

Figure 89: ^{1}H-NMR spectra of a Trp-TAD emulsion (green) in comparison to a TAD-TAD emulsion (red) in DMSO-d6 after reaction. Next to the spectra, possible products formed during the reaction are shown.[178]

The marked signals a, a', b and b' (green box Figure 89) can be attributed to the indole-ring of the added tryptophan as TAD is able to perform an electrophilic aromatic substitution at the indole ring, leading to bioorthogonally formed Trp-TAD adducts.[141,280] In comparison to this specific reaction, the product formed in TAD-TAD emulsion (red spectrum) is less defined as demonstrated by a variety of signals at 8 and 10 ppm visible, indicating hydrolysis products occurring due to the handling of TAD in an aqueous environment. In turn, in the Trp-TAD emulsion these signals were missing. The signal at a chemical shift of 10.5 ppm in the red spectrum (marked with c) is specific for the proton of the NH- group of the urazole pre-species, which forms by means of decomposition of TAD molecules as depicted in the red box (Figure 89). In a TAD-TAD emulsion, the TAD crosslinker is able to hydrolyze in aqueous environment to an amine species, which is then able to react with remaining TAD molecules.[136]

These observations point to the fact that Trp-TAD emulsions undergo a more specific reaction than TAD-TAD emulsions and therefore react with the offered amino acid in a bioorthogonal way.

IV. 3. Encapsulation of magnetite (Fe_3O_4) nanoparticles into TAD-crosslinked BSA and Trp nanocapsules

For imaging purposes, magnetite (Fe_3O_4) nanoparticles were encapsulated into the BSA- and Trp-TAD nanocapsules (Figure 90). These capsules were then again characterized by multiangle dynamic light scattering as well as transmission electron microscopy (TEM) to verify the presence of magnetite. The TEM micrographs in Figure 90 show that the Fe_3O_4 nanoparticles were encapsulated into Trp-TAD nanocapsules (A and B) as well as into BSA-TAD nanocapsules (D and E) with a high number of particles per capsule. They can be separated from empty nanocapsules by using a neodym magnet. The encapsulation proved a high loading capacity of the TAD crosslinked nanocapsules. Both nanocapsule types slightly changed their shape due to encapsulation of magnetite nanoparticles. Light scattering measurements revealed narrow size distributions also for nanocapsules with cargo (Figure 90 and Table 22).

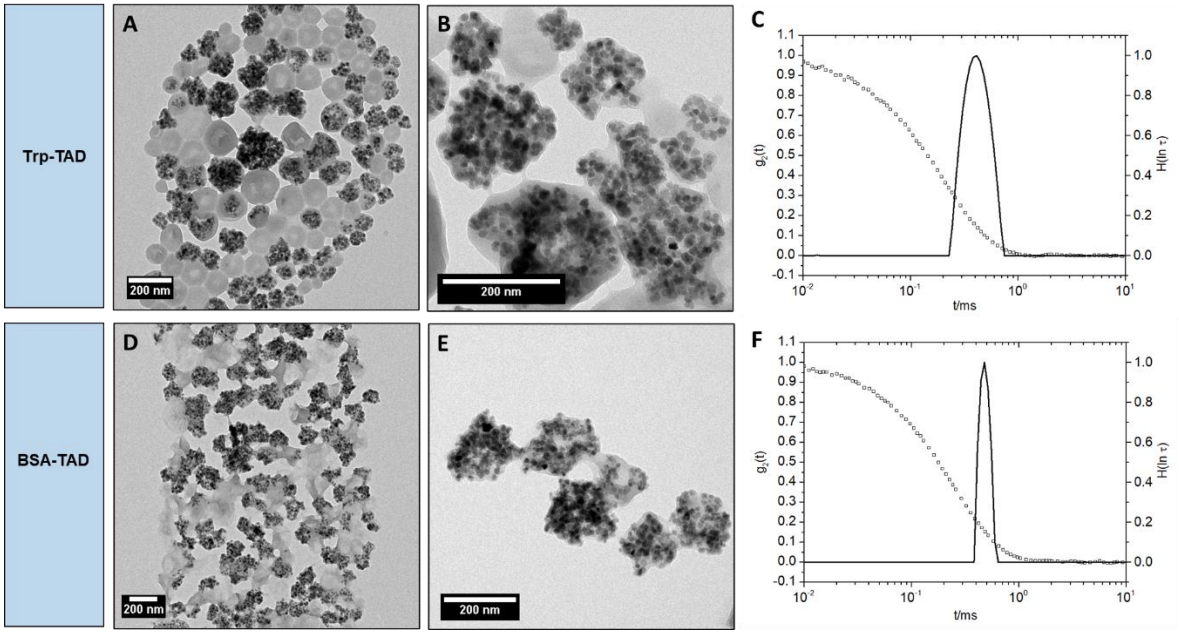

Figure 90: TEM micrographs of Trp-TAD nanocapsules (**A-B**) and BSA-TAD nanocapsules (**D-E**) with encapsulated magnetite nanoparticles in toluene and size distribution of the different nanocapsules at an exemplary scattering angle of 90° in toluene represented by the distribution of relaxation times H (ln τ) (solid lines) together with the respective autocorrelation functions g2(t) (filled squares) (**C, F**).[178]

Table 22: Physicochemical characteristics of Trp- and BSA-TAD nanocapsules with magnetite cargo.[178]

NC-sample	Average diameter in toluene*	Average diameter in water*	PDI in toluene (90°)	ξ – potential/ mV
BSA-TAD + Fe_3O_4 – NPs	167 ± 17 nm	177 ± 18 nm	0.041	-39 ± 5
Trp-TAD + Fe_3O_4 – NPs	146 ± 15 nm	198 ± 20 nm	0.097	-37 ± 5

* determined by multiangle DLS (at scattering angles of 30-150°).

IV. 4. BSA-, HSA-, OVA-TAD nanocapsules

Proteins such as HSA and OVA have been extensively exploited for the use in different nanocarrier preparations and are widely applied in therapeutic materials.[105] We therefore synthesized TAD crosslinked nanocapsules with these proteins and compared them to TDI crosslinked protein nanocapsules. DLS and ξ-potential analysis revealed good consistency in the characteristics of the different nanocapsules (Table 23). However, OVA-TAD nanocapsules had the largest nanocapsule diameters in toluene as well as in water and showed a broader size distribution in comparison to nanocapsules with other proteins. The ζ-potential of all nanocapsules was negative.

Table 23: Comparison of TAD and TDI crosslinked protein nanocapsules regarding size distribution and surface charge.[178]

NC-sample	Average diameter in toluene*	Average diameter in water*	PDI in toluene (90°)	ζ – potential/ mV
BSA-TAD	115 ± 55 nm	193 ± 150 nm	0.182	-34 ± 5
HSA-TAD	145 ± 69 nm	192 ± 91 nm	0.144	-25 ± 5
OVA-TAD	189 ± 82 nm	214 ± 135 nm	0.334	-38 ± 5
BSA-TDI	122 ± 53 nm	199 ± 75 nm	0.144	-27 ± 5
HSA-TDI	152 ± 51 nm	178 ± 46 nm	0.141	-16 ± 5
OVA-TDI	108 ± 45 nm	200 ± 54 nm	0.161	-30 ± 5

* determined by DLS at 90°.

IV. 4.1 Cellular interaction of protein nanocapsules with cancer cells

For cellular experiments, nanocapsules consisting of a shell of BSA, OVA or HSA were crosslinked with TDI or TAD and the fluorescent dye SR101 (sulforhodamine 101, Figure 20, **1**) were prepared. HeLa cells were exposed to protein nanocapsules (75 µg mL^{-1}) for 2 h or 24 h. The amount of fluorescent positive cells was determined via flow cytometry (Figure 91 A and B) and visualized by cLSM (Figure 91 C). In addition, it is known that the behavior of a nanocarrier in a physiological environment (e.g. blood) is strongly dominated by the surface interaction with blood proteins forming a protein corona, which further affects the biodistribution, toxicity and cellular uptake of the nanocarrier.[119,287,288] To explore the effect of protein corona formation for the here presented protein nanocapsules, cellular uptake experiments were either performed under serum free conditions (−HS) or in cell culture medium supplemented with human serum (+HS).

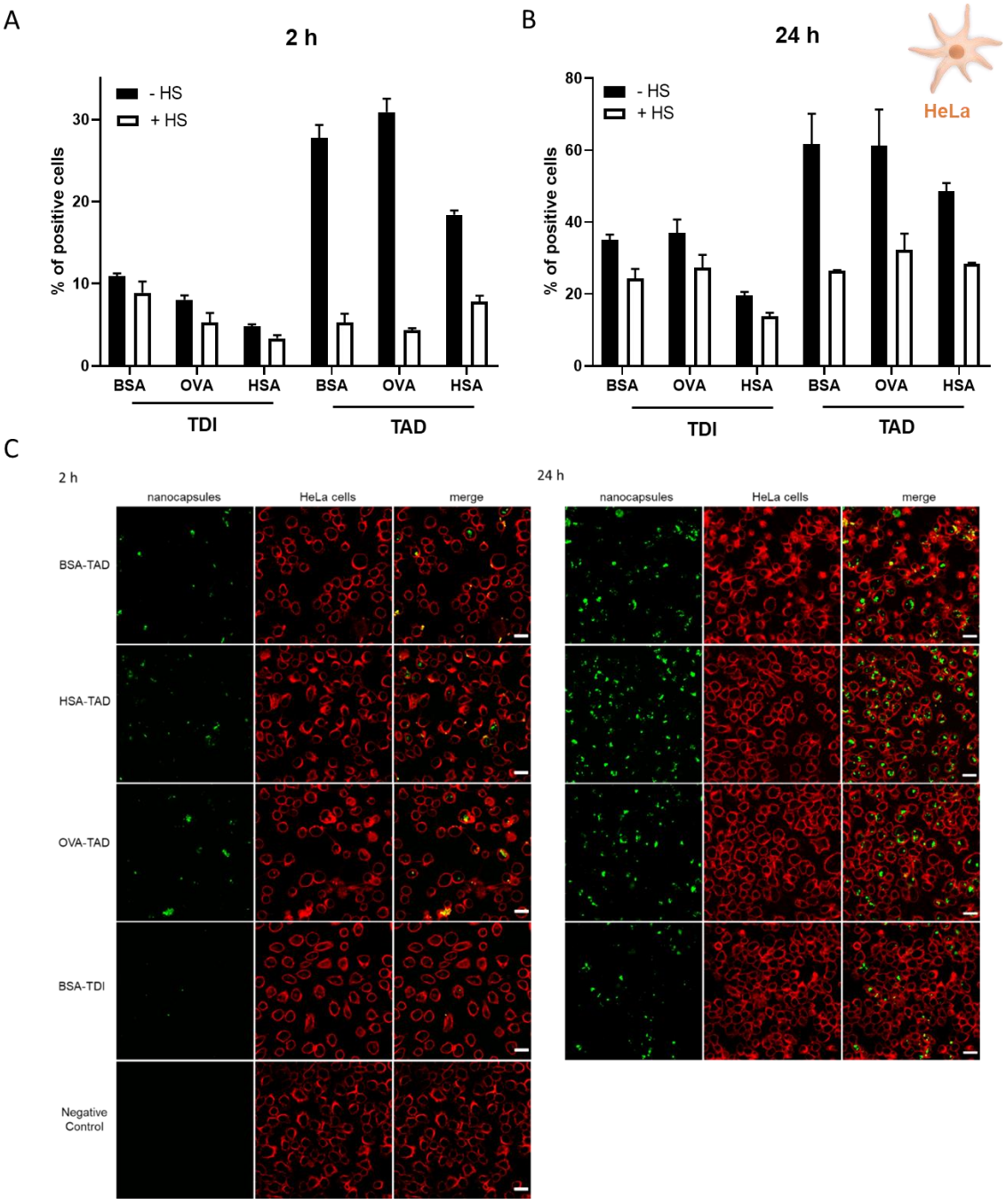

Figure 91: Cellular uptake of protein nanocapsules cross-linked with TDI or TAD. HeLa cells were incubated with BSA, OVA and HSA nanocapsules at 75 µg mL^{-1} for 2 h (**A**) or 24 h (**B**) under serum free conditions (- HS) or in cell culture medium with 10% human serum (+HS). Experiments performed by [redacted]. **C:** Confocal laser scanning microscopy (cLSM) of HeLa cells incubated with differently crosslinked protein nanocapsules. On the left panel, cells incubated with nanocapsules with a concentration of 75 µg mL^{-1} for 2 h are shown, while on the right panel, cells incubated with the same concentration (75 µg mL^{-1}) for 24 h are shown. All experiments were performed in cell culture medium containing 10% FBS. As a negative control, HeLa cells without nanocapsules treatment were stained with CellMask Deep Red only. The cell membrane is pseudo-coloured in red and the nanocapsules are pseudo-coloured in green. All scale bars represent 25 µm. Experiments performed by [redacted].[178]

We found that the cellular interaction of all protein nanocapsules with HeLa cells was strongly influenced by the crosslinker type (TDI vs. TAD). Under serum free conditions, independently of the protein type (BSA vs. OVA vs. HSA), nanocapsules crosslinked with TAD interacted stronger with HeLa cells compared to nanocapsules crosslinked with TDI in a time dependent manner (Figure 91).

After 2 h of incubation, up to only 10% HeLa cells showed significant uptake of TDI-crosslinked protein nanocapsules, while for TAD-crosslinked nanocapsules it was more than twice as much (20–30%). This difference in uptake was again observed when the cells were exposed to the nanocapsules for 24 h. In strong contrast to that, the cellular interaction was strongly reduced in cell culture medium with human serum compared to serum free condition. Here, we detected minor differences between the TDI and TAD crosslinked nanocapsules. Furthermore, the cell viability was analyzed by CellTiter-Glo® Luminescent Cell Viability Assay and was found to be nearly 100% for every sample and both incubation times (Figure 92).

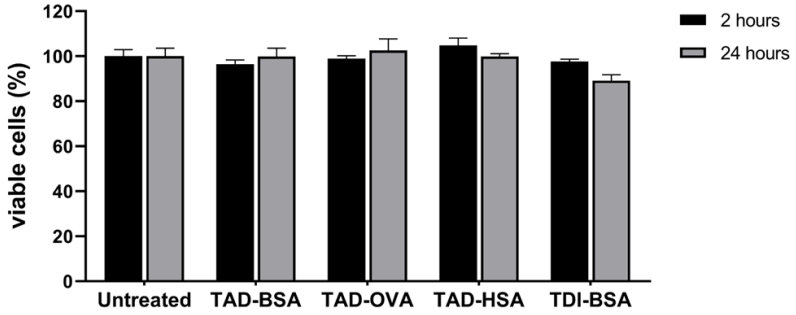

Figure 92: Cell viability of HeLa cells treated with differently crosslinked protein nanocapsules at concentrations of 75 µg mL^{-1} for 2 h and 24 h of incubation. Untreated cells were incubated with the same volume of 10% FBS supplemented DMEM. The percentage of viable cells is proportional to the measured luminescence signal. Experiments performed by [redacted].[178]

IV. 4.2 Impact of protein structure on cellular uptake of TAD and TDI crosslinked nanocapsules

One explanation for the difference in the cellular uptake behavior under serum free conditions could be related to a difference in the protein structure for the nanocapsules crosslinked with TDI vs. TAD. As an example, Fleischer *et al.*[289] studied the cellular interaction of BSA coated polystyrene nanoparticles and showed that the structure of BSA was preserved once it adsorbed onto negatively charged nanoparticles. In contrast, upon adsorption of BSA on positively charged nanoparticles, BSA was denatured. Changes in the secondary structure of BSA eventually had a major impact on cellular binding. Negatively charged nanoparticles coated with native BSA especially bound to albumin receptors present on the cell surface of monkey kidney epithelial cells (BS-C-1), whereas positively charged nanoparticles coated with denatured BSA interacted with the scavenger receptors. This highlights the distinct role of the protein structure and cell surface receptor interaction. Thus, the protein structure of the here presented protein nanocapsules could be different depending on the chosen crosslinker as also different amino acid side chains are involved in the crosslinking process. HSA and BSA are both carrier proteins and have a structural homology of 76%. OVA belongs to the superfamily of the serpins, and has therefore a different structure, size and also a different function.[290,291] The isocyanate containing crosslinker TDI favorably reacts with mostly nucleophilic groups, like amino groups, which are well accessible through the lysine residues of the proteins.

TAD on the other hand reacts with aromatic amino acids like tyrosine and tryptophan residues, which are located more in the interior of the protein. In Figure 93, the crystal structures of BSA, HSA and OVA are compared to each other and the corresponding amino acids, which react with the different crosslinkers are highlighted. In OVA as well as in BSA and HSA many lysine residues are present (Figure 93 labeled in red). These lysine residues are usually located at the exterior of the protein, enabling hydrogen bonding and ionic interactions. The amount of lysines in BSA and HSA is around 10% (59 and 57 lysines respectively), while OVA has about 5% of lysines (20 lysines). The groups are well accessible and, therefore, many reactions are possible. Tyrosine (in blue) and tryptophan residues (in magenta) are usually found buried inside the protein due to their hydrophobicity. BSA, HSA and OVA all have approximately the same amount of tyrosine residues (around 3% – 20 tyrosines in BSA, 18 in HSA and 10 tyrosines in OVA). BSA has two tryptophan residues per unit, while HSA just has one. In contrast to that, in the protein structure of OVA, three tryptophan residues can be found, while OVA has just two-thirds of the size of BSA and HSA. Comparing the locations of the different amino acids in the proteins, TDI and TAD might lead to variable degrees of denaturation of the proteins, exhibiting different structures to the outer surface of the generated nanocapsules, which finally leads to a different cell uptake behavior, depending on the crosslinking type. Changes in the protein structure can usually be analyzed using e.g., CD spectroscopy. However, it is difficult to use this method for dispersions because the absorption measured can be affected by the scattering of the nanocapsules as well as of other components, like e.g., dyes, salts or surfactants present in the dispersion.

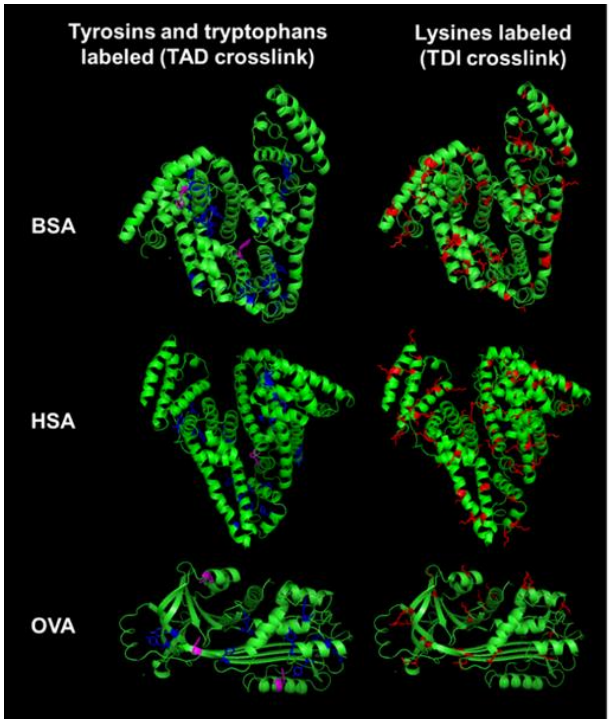

Figure 93: Crystal structures of BSA (PDB ID: 3v03), HSA (PDB ID: 1BM0) and OVA (PDB ID: 1OVA). To visualize the localization of the different amino acids the crystal structures of BSA, HSA and OVA are shown. Lysine residues are labeled in red in the protein structures. Tyrosine residues are labeled in blue and tryptophan residues are labeled in magenta.[269,292,293][178]

IV. 4.3 Adsorption of blood proteins to protein nanocapsules

As shown in Figure 91, protein corona formation had a major impact on the cellular uptake towards HeLa cells. Therefore, we aimed to deeply investigate the interaction of the protein nanocapsules with blood proteins. All nanocapsules were incubated with human serum for 1 h at 37 °C. Protein corona coated nanocapsules were isolated via centrifugation and further analyzed by Pierce Assay (Figure 95 A), SDS-PAGE (Figure 95 B-D) and mass spectrometry (Figure 94).

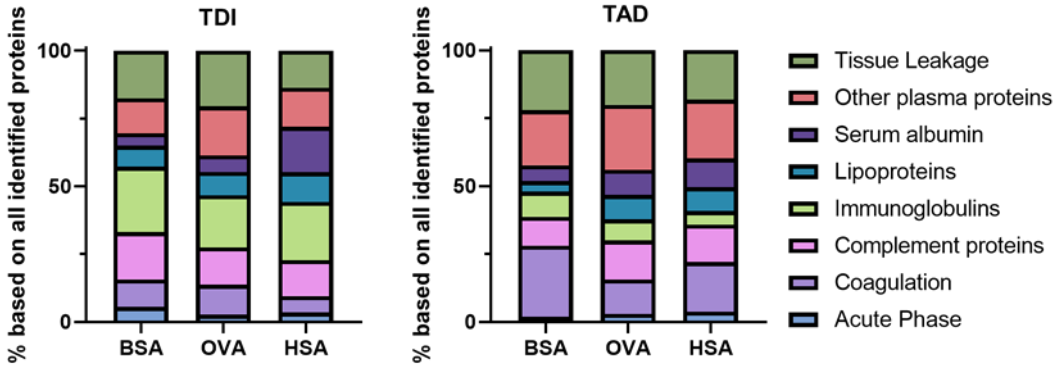

Figure 94: Protein corona profile of TDI and TAD nanocapsules. Protein nanocapsules were incubated with human serum for 1 h at 37 °C and the protein corona was analyzed by LC-MS and classified into eight different groups according to function. The amount of each protein was calculated in % based on the total amount of all identified proteins. The two different crosslinkers TDI or TAD were used for the nanocapsule preparation. Experiments performed by [redacted].[178]

All corona proteins identified by mass spectrometry were classified into eight different protein groups depending on their biological function and are summarized in Figure 94. We found that regardless of the protein type and crosslinker, there was no specific enrichment of one or two major protein classes in the protein corona of all nanocapsules (see also protein corona profiles Figure 95 B-D). This is in strong contrast to other nanocarrier systems such as nanocapsules prepared from hydroxyethyl starch (HES)[121,294] or polystyrene nanoparticles.[113,119] Generally, for those systems, one or two protein groups (e.g. lipoproteins or serum albumin) are the dominant class proteins with an overall amount between 50–70%.

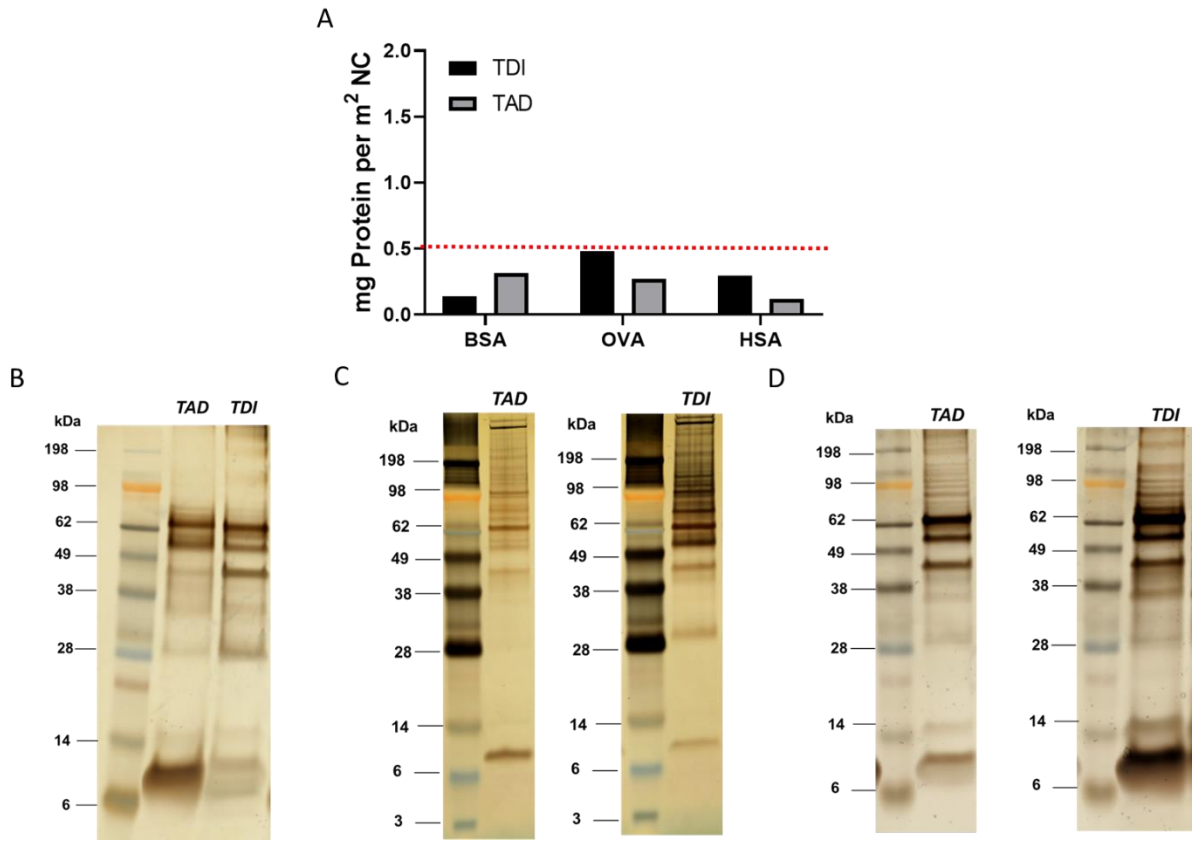

Figure 95: A: Quantification of the protein corona amount. Protein nanocapsules (0.05 m^2) were incubated with human serum (1 mL) for 1 h at 37 °C and the amount of all corona proteins was quantified via Pierce Assay (in mg). The red line indicates the threshold of 0.5 mg m^{-2} protein, below which quantification becomes less sensitive to differences. **B:** Protein corona profile. BSA-nanocapsules were incubated with human serum for 1 h at 37 °C and the protein corona was analyzed SDS-PAGE. **C:** Protein corona profile. OVA-nanocapsules were incubated with human serum for 1 h at 37 °C and the protein corona was analyzed SDS-PAGE. **D:** Protein corona profile. HSA-nanocapsules were incubated with human serum for 1 h at 37 °C and the protein corona was analyzed SDS-PAGE. Experiments performed by [redacted].[178]

Next to this, the absolute amount of corona proteins (Figure 95 A), which bound to all protein nanocapsules was comparable (<500 µg m^{-2} surface area) and significantly lower compared to polystyrene nanoparticles (~2–3 mg m^{-2}) or HES nanocapsules (~1 mg m^{-2}). This could possibly be a result of different hydrophilicities of the materials and the fact that proteins are natural molecules also occurring in the human body. This was already found for other nanocarriers made from “body-similar” components.[113,190,295] However, having a closer look at the individual protein classes, we found that the crosslinker type (TAD vs. TDI) had an influence on the relative amount of specific protein classes. As an example, the amount of immunoglobulins was higher for TDI (~20%) compared to TAD nanocapsules (5–9%). In contrast to that, proteins involved in the coagulation cascade especially interacted with TAD nanocapsules (13–26%) compared to TDI nanocapsules (6–11%). This effect was observed for all protein nanocapsules leading to the conclusion that the crosslinker type and not the base material (BSA vs. OVA vs. HSA) shaped the protein corona profile.

In general, the surface hydrophilicity has a strong influence on protein adsorption. As TDI is more hydrophobic than TAD, this could have an impact on the surface properties the protein nanocapsules and eventually mediate a specific protein interaction. In literature, it was shown that with increasing surface hydrophobicity the amount of immunoglobulins in the protein corona increased.[119]

This goes along with the here presented data as the amount of immunoglobulins was higher for TDI nanocapsules compared to TAD nanocapsules.

The influence of the crosslinker type on the protein interaction effect became very prominent for certain individual proteins, which is shown in Figure 96.

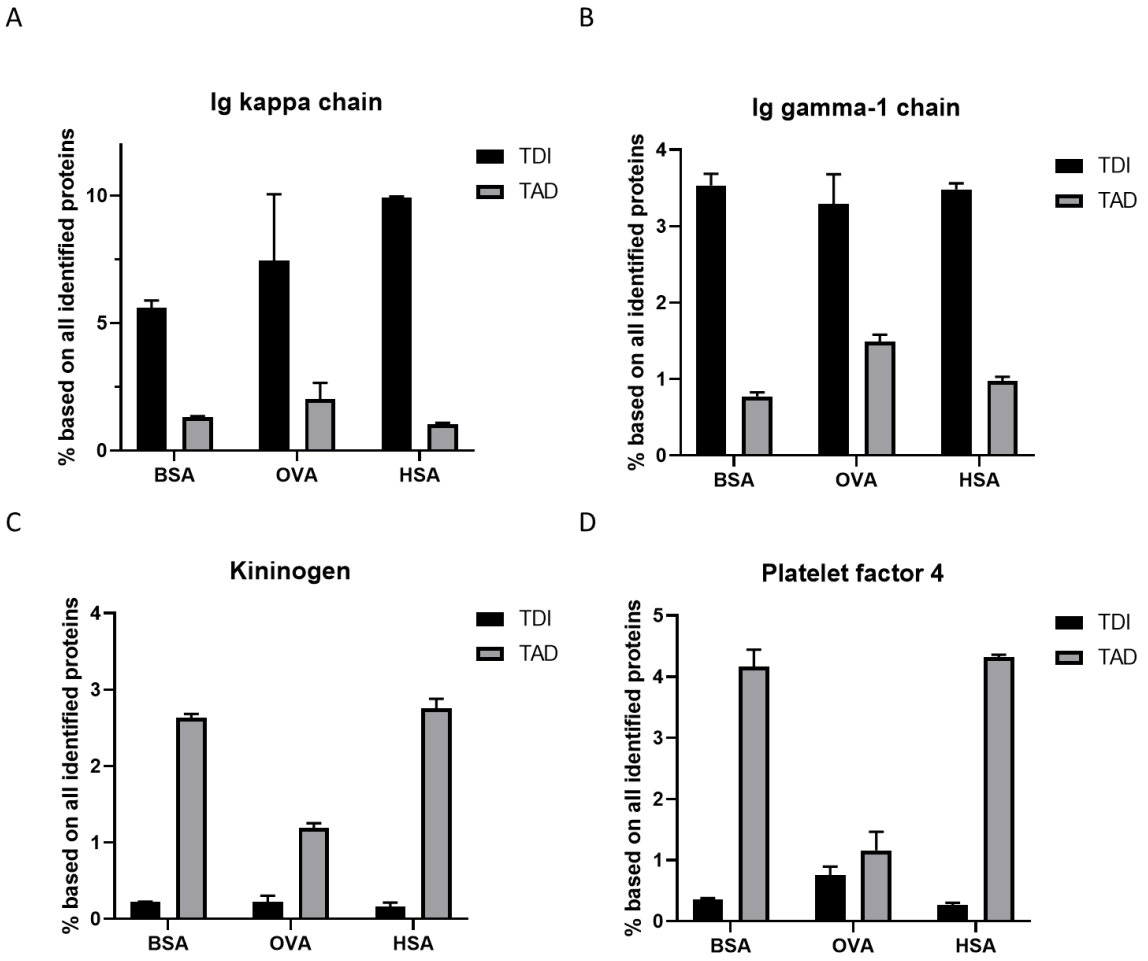

Figure 96: Relative abundance of single proteins in the protein corona of TDI and TAD protein nanocapsules determined by LC-MS given in %. The amount of Ig kappa chain (**A**), Ig gamma-1 chain (**B**), Kininogen-1 (**C**) and platelet factor 4 (**D**) in the protein corona of the different nanocapsules was compared.[178]

For all protein nanocapsules crosslinked with TDI, Ig kappa and Ig gamma-1 (two examples of proteins belonging to the group of immunoglobulins) were enriched on the surface in comparison to TAD cross-linked nanocapsules (Figure 96 A and B). Next to this, for all TAD nanocapsules, the amount of kininogen-1 and platelet factor 4 (two examples of proteins belonging to the group of coagulation) was higher in comparison to all TDI nanocapsules (Figure 96 C and D). Immunoglobulins belong to the protein class of opsonins. These proteins are known to mediate interactions with phagocytic cells.[296,297] Therefore, adsorption of immunoglobulins on the surface of nanocarriers can contribute to a decreased blood circulation time. In the case of TAD nanocapsules, lower amounts of immunoglobulins were detected in the protein corona, which could contribute to a prolonged blood circulation time. However, to answer this question, further *in vivo* biodistribution studies are needed.

IV. 5 Conclusion

We report the synthesis of nanocapsules crosslinked by 4,4'-(4,4'-diphenylmethylene)-bis-(1,2,4-triazoline-3,5-dione) (MDI-TAD) in an inverse miniemulsion process. MDI-TAD reacts with aromatic amino acids and also with full proteins in a bioorthogonal way leading to nanocapsules with narrow size distributions and defined morphologies. Magnetite nanoparticles could be encapsulated into Trp-TAD and BSA-TAD nanocapsules with a high loading capacity. The average diameter and ζ-potential of TAD-crosslinked nanocapsules and TDI-crosslinked nanocapsules consisting of different albumins, were similar. However, in our study we showed that the crosslinker type used for the preparation of protein nanocapsules is a key factor that mediates cell and protein interaction. TAD crosslinked nanocapsules interacted stronger with HeLa cells than TDI nanocapsules under serum free conditions. This could be caused by a change in surface hydrophilicity of the differently crosslinked nanocapsules or due to significant differences in the degree of denaturation of the crosslinked proteins depending on the chosen crosslinker type. Moreover, the protein corona profile was influenced by the crosslinker type. The protein corona of TDI crosslinked nanocapsules was enriched with immunoglobulins, whereas the corona of TAD nanocapsules mainly consisted of proteins involved in the coagulation cascade. Therefore, our study sheds light onto the biological properties of protein based nanocarriers and this knowledge is needed for the successful application of nanocarriers as drug delivery vehicle *in vivo*.

Chapter D – Visualizing the destiny of protein nanocarriers along the endolysosomal pathway – different compartments are involved in processing protein nanocarriers

This chapter is based on the correspondent manuscript in preparation.

[redacted] performed nanoplatelet synthesis, I, Marie-Luise Frey, performed nanocapsule synthesis, characterization and labeling. [redacted] and [redacted] performed CLEM execution and analysis. [redacted] performed cLSM and correlation analysis.

IV. 1. Introduction

The use of nanocarriers for drug delivery is becoming increasingly popular in medical research.[298,299] Besides liposomes and nanoparticles, which already find applications in clinics, also core-shell structures like nanocapsules (NCs) are appropriate candidates for the use as drug delivery platforms.[95,273,300,301] Especially NCs made from proteins have many advantages, such as their biodegradability, high loading capacity and low toxicity.[108,178] Due to their size, nanocarriers can permeate cells easily and therefore it is of great importance to elucidate how the uptake and the further fate of the nanocarrier in the cell occur.[302]

Nanocarriers are usually processed along the endolysosomal pathway.[303] However, polymeric nanocarriers, such as protein-NCs, are hard to track within this pathway since they cannot be clearly identified: they require either fluorescent markers to be observed by light microscopy (LM) or electron-dense markers to be observed by electron microscopy (EM). Correlative light and electron microscopy (CLEM) combine the strengths of both techniques and contributes to a precise localization of the nanocarriers in the cell. Ideally, the CLEM preparation features a fluorophore with a stable inherent fluorescence suitable for cLSM which, in combination, has a contrasting component suitable for TEM. For instance, this can be achieved with inorganic, fluorescent nanoparticles. Current markers to track nanocarriers like quantum dots cannot be visualized readily – they are difficult to distinguish from cellular components, due to their small size (~5 nm) and spherical shape.[304,305] This means additional elemental analysis (e.g. EDX or ESI) must be done to confirm the identity of the quantum dots to ultimately locate the nanocarrier.[306–308]

Here we developed a fluorescent system by using large (20-50 nm), rectangular nanoplatelets (NPLs) as markers for polymeric NCs in LM and EM. We encapsulated these NPLs into biocompatible NCs, a type of drug delivery vehicle, by a polyaddition at the droplet interface in inverse miniemulsion. The key to success of the NPL markers hinged on the protective coating on the NPLs.[309] This coating makes NPLs both easy to disperse in aqueous medium and protects the NPLs' surface from major damage during the encapsulation process, thus leading to high fluorescence after encapsulation. We used NCs made of bovine serum albumin (BSA), crosslinked at the interface with toluene diisocyanate (TDI), forming a dense polymeric shell.[108,273] The NPLs were added to the aqueous dispersed phase during the miniemulsion process, leading to the encapsulation of the NPLs into the NCs.

To follow the intracellular pathway, RAW264.7 macrophages were incubated with these NCs followed by different techniques like flow cytometry, cLSM and electron microscopy.

By employing a combination of incubation and ripening time, the NCs were localized inside cells revealing different terminal destinations along the endolysosomal pathway involving early and late endosomes and endolysosomes.

IV. 2. Synthesis and characterization of BSA-NCs encapsulating nanoplatelets (NPLs)

We used the miniemulsion method to synthesize protein NCs made of BSA,[108] loaded with NPLs. We accomplished the loading of the NPLs into biocompatible NCs by adding water-dispersible NPLs to the aqueous phase of a miniemulsion. The number of NPLs per nanodroplet of the miniemulsion - the precursor for the subsequent NC -is assumed to follow a Poisson distribution. Hence, we employed an excess of NPLs per expected NC to achieve a labeling of all capsules with at least one NPL. In addition, we synthesized a 1:1 ratio (NPLs : NCs) and NCs without NPLs to uncover any changes of the capsule properties due to excess NPLs.

After the NPLs have been evenly dispersed in the aqueous phase, BSA was added followed by emulsification in cyclohexane in presence of the surfactant poly-((ethylene-co-butylene)-b-(ethylene oxide) (P(E/B)-b-EO)).[310] The final step to obtain the BSA-NCs is the addition of a crosslinker toluene diisocyanate (TDI), which reacts in a polyaddition reaction at the droplet interface and leads to a shell made of crosslinked BSA on the water-cyclohexane interphase.

However, in order to use these NCs for biomedical applications, they need to be transferred to an aqueous phase (Figure 97 A) by replacing the cyclohexane with water. This is achieved by redispersing the NCs in aqueous SDS solution followed by evaporation of the cyclohexane.

We then analyzed the size distribution and hydrodynamic radii. Three different NPL:NC ratios and one NC without NPL were synthesized and the size distribution was measured in cyclohexane as well as in aqueous phase after the transfer of the NCs from the organic to the water phase. Furthermore, we analyzed the morphologies of the obtained BSA-NCs in cyclohexane (Figure 97 C) and in water (Figure 97 D) by cryo-TEM. To check the suitability for cLEM measurements, we studied the photoluminescence of the BSA-NCs with different NPLs loadings in cyclohexane (Figure 97 E) and after redispersion to water (Figure 97 F).

A

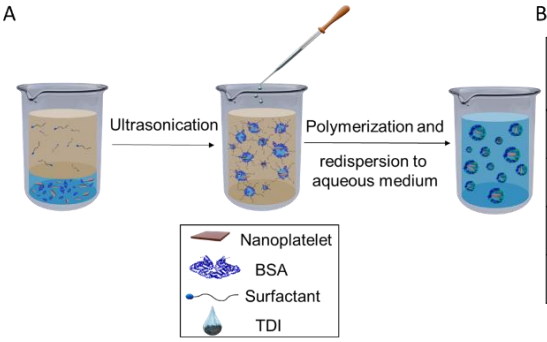

B

Ratio (NPLs:NC)	R_h/ PDI (cyclohexane)*	R_h/ PDI (water)**	Zeta Potential/ mV
10:1	163 ± 88 nm/ PDI: 0.225	202 nm/ PDI: 0.207	-27.8 ± 4.42
5:1	156 ± 73 nm/ PDI: 0.241	192 nm/ PDI: 0.202	-30.0 ± 3.86
1:1	150 ± 63 nm/ PDI: 0.240	218 nm/ PDI: 0.219	-29.3 ± 4.11
0	141 ± 83 nm/ PDI: 0.233	172 nm/ PDI: 0.261	-30.8 ± 3.71

*Measurement at a scattering angle of 90°
** Multi-angle DLS measurement, experimental error is 10%

C D

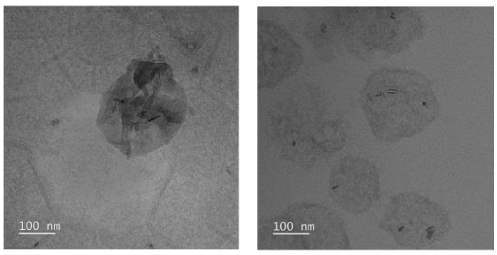

E F

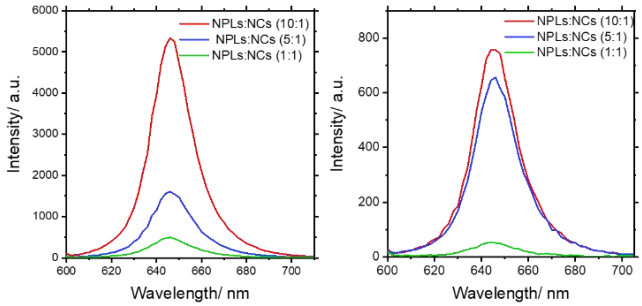

Figure 97: Characterization of BSA nanocapsules (NCs) loaded with different amounts of water-dispersible nanoplatelets (NPLs). **A:** Synthesis scheme for the inverse miniemulsion. **B:** Table with physicochemical properties of BSA-NCs containing different NPLs ratios. **C:** Cryo-TEM image of a BSA-NCs loaded with NPLs (5:1 ratio) in cyclohexane and **D:** in water. **E:** Fluorescence intensity measurements of BSA-NCs encapsulating different NPLs ratios in cyclohexane and **F:** after redispersion in water.

The average hydrodynamic radius (R_h) of the capsules with the different NPL loadings in cyclohexane is 153 ± 9 nm (Figure 97 B), where the NCs without NPLs have the smallest R_h (141 ± 83 nm), while NCs with the 1:10 ratio of NPLs revealed the largest capsule R_h (163 ± 88nm). These results point out, that BSA-NC formation is not significantly influenced by the presence of NPLs. After transfer to the water phase, we observe a moderate increase of the capsule radii ranging from 172 nm (without NPLs) to 218 nm (at a NC:NPL ratio of 1:1). The light scattering results clearly show the similarity of the NCs at the different NPL loadings with regards to size distribution. Zeta potentials were negative for all NCs (Figure 97 B).

Cryo-TEM images confirmed the spherical core-shell morphology of the capsules in both phases (Figure 97 C-D), revealing contrast-rich NPLs encapsulated inside the NCs. Imaging in water phase showed contrast-poor objects indicating the gel-like appearance of the BSA-NCs in water (Figure 97 D). Cryo-TEM confirmed that by encapsulating a 5:1 ratio of NPLs into NCs, every NC contains at least one NPL. We analyzed the fluorescence intensity of the BSA-NCs in cyclohexane (Figure 97 E) and in water (Figure 97 F), revealing the fluorescence emission maximum at 646 nm in both cases. As expected, the measured fluorescence intensity increases with increasing NPL concentration. After transfer to water, the capsules were again subjected to fluorescence intensity measurements, demonstrating similar fluorescence intensities for the 10:1 and the 5:1 ratio and a low fluorescence intensity for the 1:1 ratio. These observations corroborate, that excess NPLs, which were not encapsulated, were removed during the water transfer process. In addition, we confirmed successful loading of the NPLs to the NCs by fluorescence quenching of fluorescein isothiocyanate (FITC) attached to the capsule surface.[311] The fluorescence quenching of the FITC increases with the number of encapsulated NPLs, which suggests Förster resonance energy transfer (FRET) to the NPLs.

Previous studies of FRET with NPLs[312,313] determined Förster radii of just a few nm, indicating close proximity of the NPLs to the FITC attached to the thin capsule shell (Figure 98). This indicates, that the NPLs appear to stay close to the capsule walls, rather than freely disperse outside or inside the capsule, where fluorescence quenching via FRET from the FITC to the NPLs would be less likely.

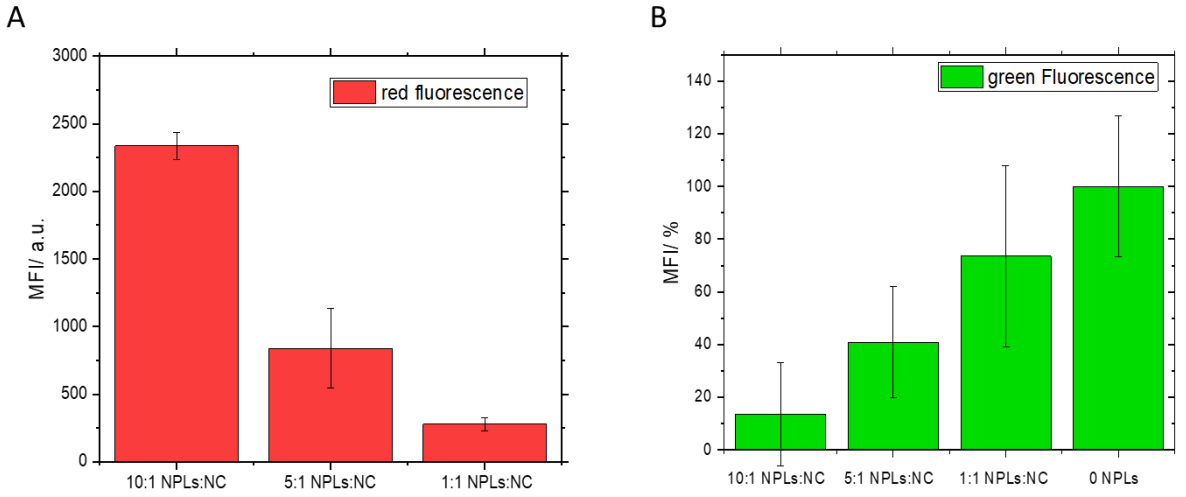

Figure 98: Median Fluorescence Intensity (MFI) of BSA-NC with different ratios of encapsulated NPLs with green fluorescent label on the surface (FITC). The decrease of green fluorescence (**B**) in dependency of the NPLs concentration (**A**) occurs due to a energy transfer to the NPLs and therefore demonstrates close proximity of the encapsulated NPLs to the dye on the surface, which is the result of effective encapsulation of the NPLs into the NC.

In addition, we did not observe NPLs in the supernatant of aqueous capsule dispersions, but the NPLs were always associated within the BSA-NCs. Based on these findings, we continued with cell experiments using BSA NCs prepared at a 5:1 ratio.

IV. 3. Cell uptake and correlation of BSA-NCs encapsulating NPLs

In order to study the uptake behavior of the BSA-NCs, RAW264.7 macrophages were exposed to BSA-NCs for 1 h (Figure 99). We analyzed time-dependent cell uptake by confocal laser scanning microscopy (cLSM). Cells were treated with BSA-NCs (75 µg/mL, + FBS) and identified by means of their fluorescence emission. We visualized lysosomal cell compartments using LysoTracker™ Green (Figure 99 A) and correlated the measured fluorescence intensities to the BSA NCs signal (Figure 99 B-C). The LysoTracker™ Green DND-26 marker stains acidic compartments, thus marking endo-lysosomal membranes.

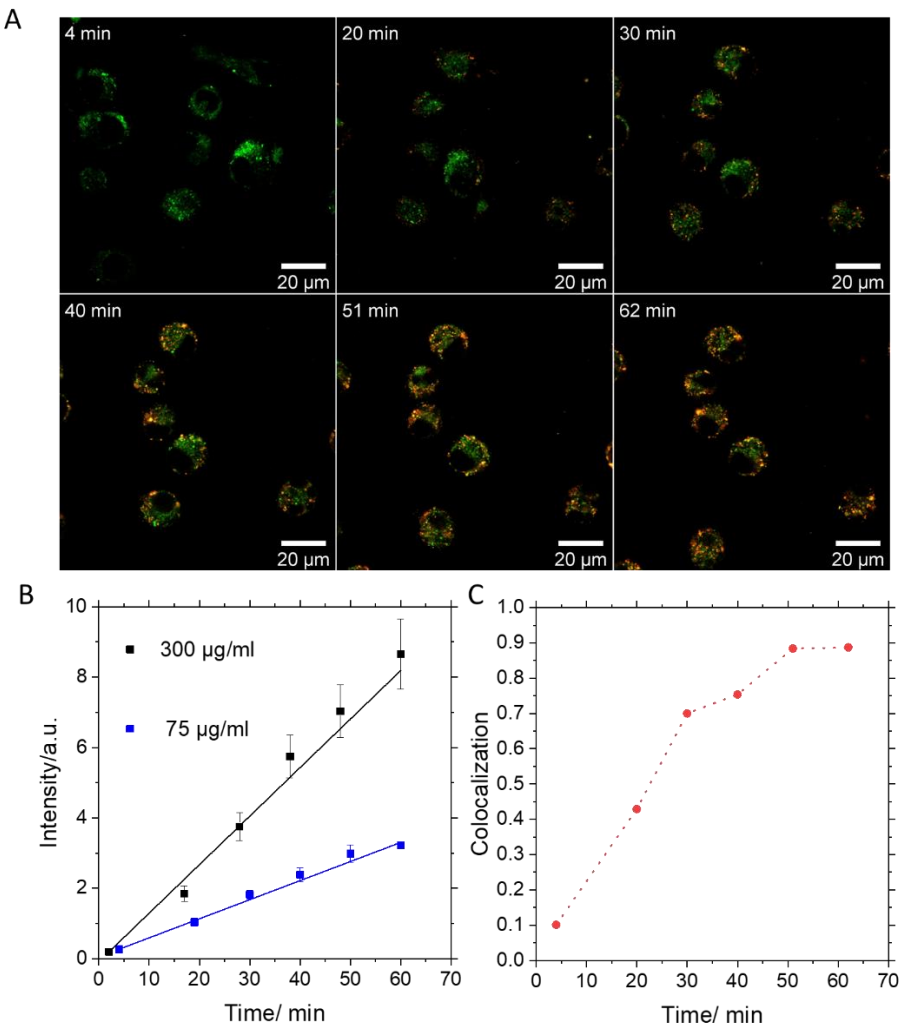

Figure 99: Cell uptake experiments of NPL loaded NCs (5:1) into RAW264.7 macrophages. **A:** Live cell imaging by confocal laser scanning microscopy (cLSM) of macrophages stained with LysoTracker™ Green after the uptake of NCs (NPL displayed in red) at a concentration of 75 µg/mL. **B:** Time-dependent increase of detected fluorescence intensity of NPLs encapsulated in BSA-NCs in RAW264.7 macrophages. **C:** Time-dependent correlation of overlapping fluorescence signals obtained from the cLSM data (A) of the cell uptake of BSA-NCs into macrophages determined by Manders (M2) coefficient. The M2 coefficient shows the fraction of NPLs that colocalize with endosomes/lysosomes. It ranges between 0 and 1.

We observe a low amount of intracellular NPLs after 4 min of incubation time, with almost a linear increase in uptake during the next 62 min for high (300 µg/mL) and low (75 µg/mL) NC loadings (Figure 99 A-B). The NCs were transported during that time from the membrane into the cell where they gradually colocalize with endosomes/lysosomes marked by LysoTracker™ Green.

Shortly after the uptake, there is almost no colocalization of the NPLs with LysoTracker since they were not yet transferred to the acidic compartments like late endosomes/lysosomes. Within the first 30 min, the fraction of NPLs that are found in late endosomes/lysosomes linearly increases. Despite linear uptake of NPLs with time over 60 min, we stopped live cell imaging to avoid phototoxicity having an impact on the uptake process. Anyways, the M2 colocalization coefficient levels off after about 50 min (Figure 99 C).

Considering a continuous uptake of NCs, this leveling off can be interpreted as a reduction of endosome maturation to lysosomes or may indicate endosomal escape as NCs were continuously taken up (Figure 99 B). Moreover, TEM images are used to corroborate this hypothesis.

IV. 4. CLEM and trafficking

In order to analyze NCs trafficking inside the cell, we incubated RAW264.7 macrophages with BSA-NCs loaded with water-dispersible NPLs (5:1) at a concentration of 300 µg/mL. We exposed the macrophages to the NCs for 2 h, to ensure sufficient and continuous uptake, washed them to stop the uptake. Subsequently, they were allowed to ripe for another 24 h to allow processing of the NCs inside the cells (ripening time).

We performed CLEM on 100 nm sections to precisely localize intracellular BSA-NCs in high resolution after incubation of BSA-NCs with RAW264.7 macrophages. Cell integrity was well maintained and the fluorescence from NPLs was clearly detected in cLSM even after the harsh electron microscopy preparation with osmium tetroxide, uranyl acetate and embedding in an epichlorohydrin derived epoxy resin (EPON) (Figure 100).

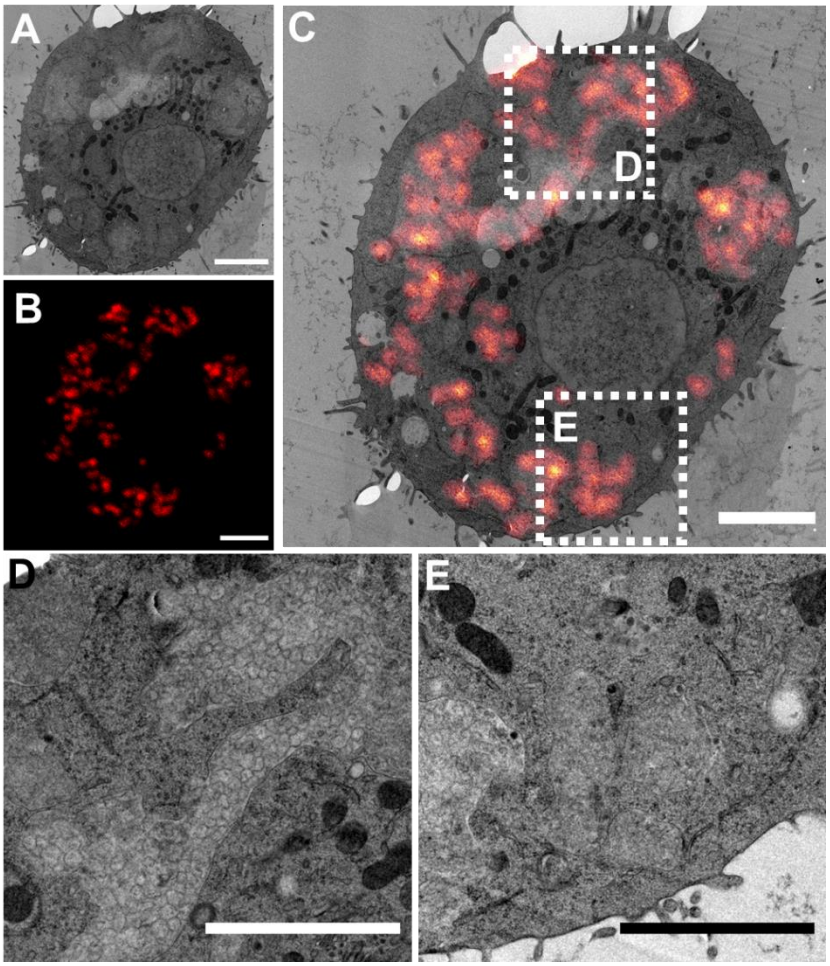

Figure 100: CLEM micrograph of BSA-NCs containing NPLs (5:1) in RAW264.7 macrophages after 2 h uptake + 24 h ripening (300 µg/mL). A: Electron microscopy micrograph of one macrophage with internalized BSA NCs; B: Fluorescence microscopy micrograph of the same macrophage in A; C: CLEM overlay of A and B; D and E: Zoomed in area of C showing BSA-NCs in an enlarged vesicle and a late endosome. Scale bars: 2 µm.

We analyzed the uptake of the nanocapsules into a macrophage in detail by TEM (Figure 100 A) and fluorescence microscopy (Figure 100 B). Superimposing the EM (A) with the fluorescence microscopy micrograph (B) yields the CLEM micrograph (Figure 100 C). The bright fluorescence from the NPLs helps to unambiguously facilitate the localization of BSA-NCs in the cell. The NCs are distributed over the whole cell except for the nucleus. We can clearly localize different parts of the macrophage exhibiting accumulations of BSA-NCs (D and E) showing a high fluorescence intensity. Here, the electron micrographs reveal irregular shaped vesicles wich are packed with BSA-NCs (Figure 100 D) as well as late endosomes, in which the structural identity of the NCs is no longer clearly recognizable (Figure 100 E). These findings indicate, that the NCs are processed by the cell in different manners: On the one hand there was a high accumulation of NCs in irregularly shaped, large vesicles (D) and on the other hand a degradation of the NCs (E). We captured the different processing mechanisms by varying the ripening time of the BSA NCs inside the macrophages at 2 h uptake + 0 h ripening time and 2 h uptake + 24 h ripening time. Based on our findings, we can reconstruct the processing pathway and therefore follow the track of the BSA-NCs inside the cells (Figure 101).

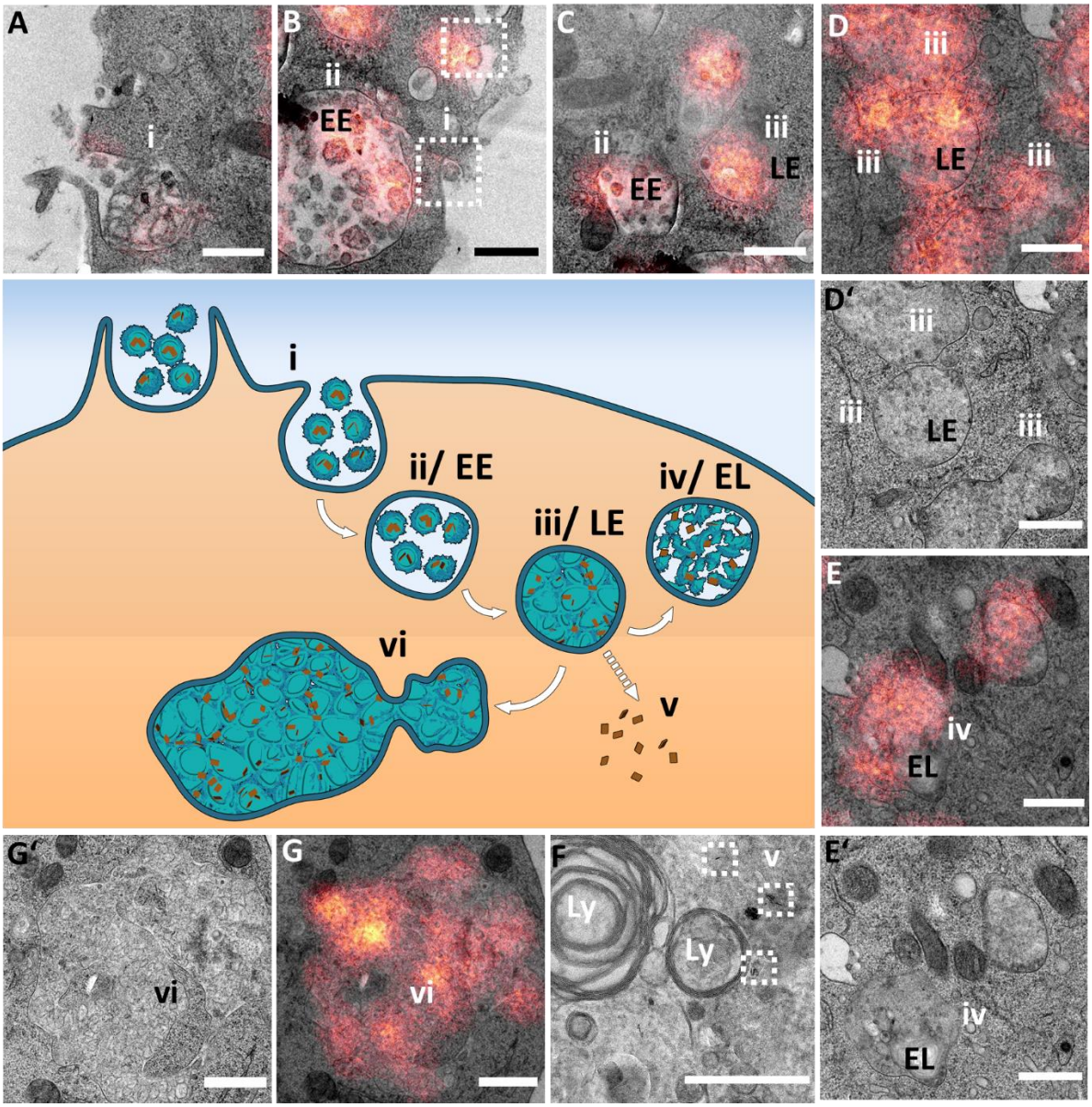

Figure 101: Intracellular fate of BSA-NCs by TEM micrographs. **A**: Uptake event (i) of BSA-NCs in a cell captured after 2 h incubation **B**: Uptake event (i) and early endosome (ii/EE) of BSA-NCs captured after 2 h incubation. **C:** Early endocytosis of BSA-NCs (ii) and a late endosome (LE) with BSA-NCs after 2 h incubation + 24 h ripening. **D:** Late endosomes (LE) with BSA NCs visible after 2 h incubation + 24 h ripening. E: Degradation of BSA NCs in an endolysosome (iv/EL) after 2 h incubation + 24 h ripening **F:** Escaped NPLs (v) captured after 24 h ripening. Ly: lysosome G: Enlarged endosome with BSA-NCs at high concentration (300 µg/mL) after 2 h incubation + 24 h ripening D', E' and G' correspond to the same respective EM images without fluorescence correlation. Scale bars:500 nm.

Within the first 2 h of incubation, we observe the uptake of BSA-NCs into RAW264.7 (Figure 101 A(i)). During this incubation phase, all events which take place during the first 120 min interval of uptake can be observed. During the incubation time we can also observe early endosomes (EE) with NCs (Figure 101 B (ii)). These findings are consistent with the cLSM images revealing that within one hour a colocalization of NPLs with endolysosomal compartments occurred (Figure 99 A). To enable further processing of the NCs in the cells, we performed a ripening phase to complete the observation of the NCs' processing. During the 24 h ripening phase, we found BSA-NCs in EE and also in densely packed late endosomes (LE) (Figure 101 C (ii) and (iii)).

The integrity of the BSA-NCs was maintained at the early stage of endocytosis, while they started to lose their integrity since the acidic environment in endolysosomal compartments enables the conditional degradation of the NCs (Figure 101 D (iii), Figure 102 A).[314] Some LE were found fusing with lysosomes forming endolysosomes (EL) (Figure 101 E (iv)) where the shape integrity of the NCs was not observed anymore. The missing integrity is particularly visible in images Figure 101 D', E'. The respective fluorescence overlays (Figure 101 D and E) confirm that the endosomes contained capsules with NPLs as the endosomes appear highly fluorescent. These results indicate that the shell of the BSA-NCs was impaired within 24 h by enzymatic and acidic conditions in endolysosomal compartments, which are normally revealing a dark contrast, like lysosomes, in TEM micrographs.[315] These findings are supported by previously reported observations of fully degradable protein-NCs enabling cargo release upon enzymatic cleavage leading to CD86 upregulation of bone-marrow derived dendritic cells.[276] Only at high concentrations (300 µg/mL) we found enlarged endosomes filled with NCs (Figure 101 G/G'(vi)) revealing the capsule integrity (Figure 102 B). We conclude from these findings, that at high capsule loadings, endosomal compartments fuse to enlarged endosomes with a big storage capacity of the NCs. The maintained capsule integrity may be explained with the pH value in the large endosomal vesicles. There, the pH is not sufficient to degrade the capsules and NCs are hindered from moving further along the pH gradient with increasing acidity. This observation indicates a kind of blockade of the degradation pathway.

In some cases, we observed NPLs in the cytosol (Figure 101 F (v)). Since no freely diffusing NPLs were found neither in TEM images nor in the performed FRET experiments (Figure 98), this finding is concluded to be an endosomal escape. This result is supported by the observation that the shell of the NCs degraded during endolysosomal processing and therefore releasing NPLs upon ripening.

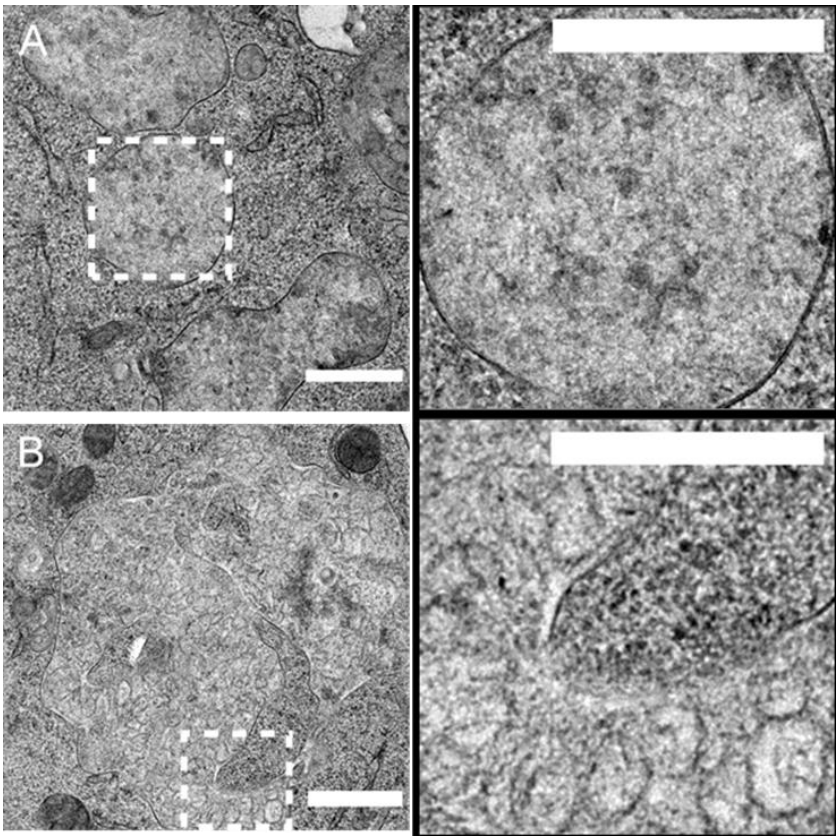

Figure 102: Zoom-in image to show the integrity of the BSA-NCs. **A:** Corresponding image of Figure D'. **B:** Corresponding image of Figure G'. Scale bars: 500 nm.

IV. 5. Conclusion

We demonstrated that NPL containing NCs were detected and unambiguously localized in different endolysosomal compartments by CLEM. The encapsulation of the NPLs into biocompatible NCs was accomplished without disturbing the NC formation and damaging the NPLs' properties, obtaining a stable dispersion with high fluorescence intensity. We were able to adjust different NPL concentrations inside the NCs and obtained reproducible size distributions. The bright fluorescent signal in the cLSM examinations indicated that the NCs were taken up and incorporated into the macrophages used for the uptake experiments. From the CLEM data we could identify the different cell compartments containing the NCs. In this way, we could not only determine the timing of endolysosomal colocalization, but also trace the NCs in each compartment. We show that the NCs are processed at three different locations upon the endolysosomal pathway: The NC shell was impaired in late endosomes, indicating degradation, the NCs were stored in large endosomes at high capsule concentrations revealing an intact shell, and we observed an endolysosomal escape which is crucial for the successful delivery of a potential drug encapsulated inside the BSA-NCs. The findings are very important for future research on cell uptake mechanisms and may reveal the metabolic pathway of an encapsulated drug.

V. Experimental Part

V. 1. Experimental section to Chapter A

V. 1.1 Materials

All chemicals and reagents were purchased from commercial suppliers and used without further purification. Ampuwa® water (sterile and pyrogen-free water, Product No.: 1088813) and hydroxylethyl starch (HES, M_w: 200 kDa, substitution degree 0.5, 3%), dissolved in an isotonic sodium chloride solution, were obtained by Fresenius Kabi (Germany). Sulforhodamine (SR101, Product No.: S7635), 2,4-toluene diisocyanate (TDI, 95% Product No.: T39853), dimethylsulfoxide (DMSO, anhydrous, >99%, Product No.: 276855), sodium dodecyl sulfate (SDS, LiChropur™, ≥99.0% (Art.No.: 71726), Stains-all (Art.No: E9379), 5-carboxyfluorescein (BioReagent, >95%, HPLC), *N*-(3-Dimethylaminopropyl)-*N'*-ethyl-carbodiimide hydrochloride (EDC x HCl, commercial grade powder) and Dulbecco's phosphate-buffered saline (DPBS, without $CaCl_2$ and $MgCl_2$, Art.No.: D8537) were obtained by Sigma Aldrich (USA). Cyclohexane (HPLC grade) was purchased from VWR Chemicals. Cy5 Oligo was obtained by IBA Lifesciences (Germany) dissolved in aqueous solution at a concentration of 0.1 nm/µL, Lutensol AT50 was obtained by BASF (Germany). Fluorescamine was purchased from Alfa Aesar (Lot# 10215046). DBCO-PEG_4-NHS ester (Art.No.: CLK-A134-100, purity >95%) and DBCO-mPEG (5 kDa, Art.No.: CLK-A118N-100, purity > 90%) was purchased from Jena Bioscience GmbH (Germany). Azido benzoic acid (>97%, Lot# SCYTO-NO) and *N*,*N*'-Dicyclohexyl carbodiimide (DCC, >98%) were obtained from TCI Chemicals. *N*-Hydroxy succinimide (>99%) was obtained from Carl Roth GmbH (Karlsruhe, Germany). NHS-PEG_4-azide was obtained by Thermo Fisher Scientific Inc. (USA). Aqua ad iniectabilia (Art.No.: 03710653) was obtained from B. Braun (Germany). IL-2 (Art.No.: CRI100XX) was purchased from cell sciences Inc. (USA). Sodium hydroxide solution, Volumetric, 0.1 M NaOH (0.1N) Honeywell Fluka™ purchased by fisher scientific (USA). FITC-labelled anti-IL-2 antibody (Art.No.: 500305) was purchased from Biolegend (USA). Human IL-2 ELISA Kit was purchased from BD Biosciences (USA) (Product No.: 550611). Anthracene azide and the block copolymer poly((ethylene-*co*-butylene)-*b*-(ethylene oxide) P(E/B)-*b*-EO) used as surfactant were synthesized according to previously published procedures.[225,310]

V. 1.2 Synthesis and procedures

Synthesis of HES nanocapsules (HES-NCs)

The nanocapsules were prepared adopting previously published procedures from Baier *et al.* using an inverse miniemulsion process.[227]

Cyclohexane was dried over molecular sieve (5 Å) before use for at least one day. 1400 mg of an aqueous HES solution (200 kDa, 0.5, 3%) were mixed with 1 mg of sulforhodamine 101 (SR101) or 200 µL Cy5 Oligo (0.1 nmol/µL) and 20 mg of sodium chloride (dispersed phase). The solution was covered with aluminum foil and was stirred for 5 min at room temperature until all components were completely dissolved. 100 mg of the surfactant P(E/B-*b*-EO) were dissolved in 7.5 g of dry cyclohexane under shaking and added at once to the dispersed phase. The mixture was pre-emulsified by vigorous stirring for 1 h at room temperature.

Afterwards, the emulsion was subjected to ultrasound for 3 min (70%, 20 s pulse, 10 s pause) and subsequently placed in an oil bath at 25 °C equipped with a stirrer. Under stirring at 700 rpm, a mixture of 30 mg P(E/B-*b*-EO) and 100 mg TDI in 5.0 g dry cyclohexane was added dropwise with a syringe. The emulsion was stirred at 25 °C for 24 h.

Redispersion of HES-NCs into aqueous SDS solution

5 mL of the nanocapsule dispersion were distributed over three 2 mL Eppendorf tubes, 1.667 mL each and centrifuged for 30 min at 4000 rpm. The supernatant was replaced with the same amount of fresh dry cyclohexane and the procedure was repeated. The pellets were finally redispersed in 500 µL fresh cyclohexane and added dropwise into 5 mL of aqueous SDS solution (0.1 wt%) over a time period of 5 min under constant sonication in an ultrasonic bath. The aqueous dispersions were placed on a stirring plate and the cyclohexane was evaporated at room temperature under vigorous stirring at 1000 rpm.

Labeling of HES with carboxyfluorescein and subsequent nanocapsule preparation for CLSM imaging

200 mg of HES (130 kDa) was dissolved in 2 mL of dry DMSO and dicyclohexyl carbodiimide (DCC, 17.8 mg, 8.621 x 10^{-5} mol) and 4-dimethyl amino pyridine (DMAP, 52.6 mg, 8.621 x 10^{-5} mol) which were dissolved in 500 µL of dry DMSO each, were added. 32.4 mg (8.62 x 10^{-5} mol) carboxyfluorescein was added which was dissolved in 1 mL of dry DMSO was added subsequently after all components were dissolved in the reaction mixture. The addition of carboxyfluorescein was adjusted according to the expected functionalization of every tenth glucose unit on the HES polymer:

$\left(\frac{0.2\ \text{g HES}}{232\ \frac{\text{g}}{\text{mol}}\text{Glucose unit}} = 8.621\ \text{x}\ 10^{-4}\ \text{mol x}\ 0.1\ \text{eq.}\right)$ The reaction mixture was stirred at 40 °C over the weekend in the dark. Afterwards the modified HES was precipitated in isopropanol and further purified by dialysis in MilliQ water.

For the capsule synthesis, 100 mg of fluorescein modified HES was added into the dispersed phase together with 5 µL of an aqueous SR101 solution (1 mg/ 460 µL) and nanocapsule synthesis was conducted as described above.

Functionalization of HES-NCs with DBCO-PEG_4-NHS ester

The aqueous nanocapsule dispersion (solid content of ca. 0.1 wt%) was centrifuged at 4000 rpm for 30 min and the supernatant was replaced once with the same amount of Ampuwa® water (sterile and pyrogen-free water). The dispersion was again centrifuged at 4000 rpm for 30 min and the supernatant was removed. The pellet was then resuspended in one tenth of the original volume. This procedure led to an increase of the solid content from 0.1 wt% to 1.0 wt% 10 mg of DBCO-PEG_4-NHS ester were dissolved in 500 µL dry DMSO. DMSO was dried over molecular sieve (4 Å) before use. In order to compare the degree of functionalization, different amounts of DBCO were added to the dispersion. The amounts added varied between 3.3 mg DBCO per mL dispersion (165 µL of DBCO stock solution in DMSO (10 mg/500µL)) to 0.04 mg/mL dispersion. The mixture was stirred in a 4 mL glass vial over night at room temperature. Afterwards, the dispersion was centrifuged at 8000 rpm for 30 min and the supernatant was replaced with the same amount of fresh Ampuwa water. The procedure was repeated with 5000 rpm centrifugation speed.

After functionalization and purification of the nanocapsules, the attached DBCO groups were quantified by an anthracene azide assay.

Synthesis of 4-azidobenzoyl hydroxysuccinimide

4-azido benzoic acid (500 mg, 3.07 mmol, 1 eq.) was placed in a 25 mL round-bottom flask and dissolved in 9.76 mL of dry DMF under argon atmosphere under cooling at 0 °C. *N*-Ethyl-*N*′-(3-dimethylaminopropyl) carbodiimid hydrochloride (EDC x HCl, 706 mg, 3.68 mmol, 1.2 eq.) and *N*-hydroxy succinimide (424 mg, 3.68 mmol, 1.2 eq.) were added and the whole mixture stirred for 2 h at 0 °C. The reaction mixture was continued stirring overnight at room temperature. On the next day, DMF was removed under reduced pressure, the reaction mixture dissolved in 30 mL of ethyl acetate and transferred into a separation funnel. The organic phase was washed three times with 20 mL of water, dried over $MgSO_4$ and the solvent was removed under reduced pressure.
Yield: 541 mg, 68%
Rf: 0.35 (cyclohexane/ethyl acetate 2:1)
^{1}H NMR (250 MHz, $CDCl_3$) δ: 8.13 (d, *J* = 8.8 Hz, 2 H-aromat.), 7.13 (d, *J* = 8.8 Hz, 2 H-aromat.), 2.92 (s, 4 H).

Functionalization of IL-2 with NHS-PEG_4-azide

Phosphate buffer was prepared by dissolving 1.78 g Na_2HPO_4 x 2 H_2O and 1.38 g NaH_2PO_4 x H_2O in 100 mL of Ampuwa® water each. For pH 7.6, 13.0 mL NaH_2PO_4 x H_2O solution was mixed with 87.0 mL of the Na_2HPO_4 x 2 H_2O solution. By addition of 90 mL sterile water and addition of 5 mL of each of the phosphate solutions, a phosphate buffer with a concentration of 50 mM and pH of 7.6 was obtained.
1 mg ($6.67 \cdot 10^{-8}$ mol) of IL-2 was dissolved in 1 mL freshly prepared phosphate buffer (50 mM, pH 7.6). The buffer was directly added to the IL-2 vial, which was vortexed and transferred to an Eppendorf tube (1.5 mL). 107 µL NaOH (0.1 M) was added to this mixture to re-adjust the pH of the mixture. 100 mg of NHS-PEG_4-azide were dissolved in 1 mL of dry DMSO and a threefold molar excess ($2 \cdot 10^{-7}$ mol, 7.77 µL (1:10 dilution)) was added to 1 mL of IL-2 solution. The mixture was stirred at room temperature for 2 h. To prepare the IL-2 functionalized nanocapsules as described here, usually 2 mg of IL-2 needs to be functionalized. Therefore, the same procedure can be repeated for another 1 mg of IL-2 in a separate Eppendorf tube. In the end, both IL-2 mixtures can be combined for purification. For purification, the mixture was dialyzed against phosphate buffer for two days at 4 °C to remove residual azide linker. After purification, the functionalized IL-2 was concentrated with a centrifugal filter (Amicon® centrifugal filters 3 kDa, Merck Millipore) to 2 mL and the final concentration was determined by a Pierce™ 660 nm Assay (Thermo Fisher Scientific) according to manufacturer's instructions.

Reaction of DBCO-mPEG with azidated IL-2 and subsequent analysis via sodium dodecyl sulfate polyacrylamide gel electrophoresis (SDS PAGE)

After reaction with NHS-PEG_4-azide, the azidated IL-2 was reacted with DBCO-mPEG (5 kDa) in a threefold molar excess. Therefore, a stock solution of DBCO-mPEG (5 kDa) was prepared in DMSO and added to the IL-2 sample in phosphate buffer. The samples were reacted at room temperature for two days in the dark and purified by dialysis.

Afterwards 32.5 µL of protein sample (~12 µg protein) were mixed with 12.5 µL of a SDS solution and 5 µL reducing agent. The total volume was loaded onto a NuPAGE® Novex® 10% Bis-Tris Gel (Thermo Fisher Scientific) and run at 100 V for 60 min.
As a marker SeeBlue™ Plus2 Pre-Stained (Thermo Fisher Scientific) was run in parallel. Staining was employed by Coomassie Brilliant Blue for 22 h.

Clicking of azide-functionalized IL-2 to DBCO modified HES-NCs

In order to compare the relationship between biological function and IL-2 concentration, different amounts of IL-2 were added to the DBCO-functionalized nanocapsules. The IL-2 was added according to the calculated number of DBCO groups per nanocapsule in three different ratios (1:1, 1:10 and 1:100). Therefore, to fully functionalized DBCO-HES nanocapsules (functionalized with 3.3 mg/mL DBCO-PEG_4-NHS ester), 1538 µL IL-2 (1:1), 153.8 µL IL-2 (1:10) and 15.38 µL IL-2 (1:100) were added to 350 µL nanocapsule dispersion each. The dispersions were then stirred at 4 °C for three days. Afterwards, they were dialyzed against Ampuwa water (Visking Cellulose dialysis tube, Carl Roth, MWCO 14 kDa) and centrifuged twice at 6000 rpm for 30 min to remove residual IL-2, to concentrate the dispersion and to maintain the sterility of the water.

Labeling of IL-2 modified HES-NCs with FITC-anti-IL-2 antibody for flow cytometry experiments

According to initially performed experiments in which different amounts of FITC-anti-IL-2 antibody were added to IL-2 functionalized HES-NCs, and MFIs determined by employing flow cytometry, 0.3 µg of FITC-anti-IL-2 antibody was added to 2 µg of HES-NCs in 20 µL total volume in PBS. In parallel another sample without antibody was prepared in the same volume of PBS. The samples were incubated at 4 °C for 40 min in the dark. After incubation, additionally 1 mL of PBS was added to each sample, vortexed and analyzed by flow cytometry.

Labeling of IL-2 modified HES-NCs with FITC-anti-IL-2 antibody for FCCS experiments

20 µL of IL-2 modified HES-NCs (1 wt%) were diluted with 180 µL of PBS buffer and 20 µL of FITC-anti-IL-2 antibody (0.5 mg/mL) was added. The sample was vortexed and incubated for 30 min in the dark. Afterwards, the dispersion was centrifuged 4 times at 20000 g for 15 min each and the supernatant was replaced with the same amount of fresh PBS. In the end, the dispersion was concentrated to 30 µL by removal of the supernatant in the last centrifugation step and resuspension of the pellet in 30 µL of PBS buffer. The modified nanocapsules were subjected to FCCS measurements.

V. 1.3 Cell experiments to Chapter A

All cell experiments and related procedures were performed by [redacted].

Generation of immature or mature dendritic cells

Buffy coats were obtained from human donors and peripheral blood mononuclear cells (PBMCs) were isolated. Donor blood was obtained according to the declaration of Helsinki. Dendritic cells were generated from monocytes using plastic adherence. PBMC were seeded at a density of 5 x 10^6 cells per well of a 24-well plate.

Cells were allowed to adhere in a humidified environment at 37 °C with 5% CO_2 for 1 h in 1 mL per well of DC-medium (RMPI with 2% heat-inactivated pooled human serum (HS), 100 U/ mL penicillin (Gibco), and 100 mg/mL streptomycin (Gibco). By multiple washing with phosphate buffered saline (PBS, Invitrogen) non-adhering cells were removed. Monocytes were kept in DC-medium containing 100 ng/mL granulocyte-macrophage-colony stimulating factor (GM-CSF, PeproTech) and 100 ng/mL interleukin-4 (IL-4, PeproTech) at 37 °C/ 5% CO_2 for two days. On day 3, immature dendritic cells (iDC) were harvested by washing once with PBS and incubating cells with PBS/ EDTA (2 mM) at 4 °C for 10 min. Prior to experiments, cells were examined for the expression of CD11c and CD86 by employing flow cytometry.

Loading of DC with nanocapsules

$1 \cdot 10^5$ DCs were incubated with NC at 37 °C/ 5% CO_2 in DC medium supplemented with 1600 U/mL GM-CSF and 500 U/mL IL-4. Two different nanocapsule concentrations (37.5 or 75 µg/mL) were analyzed after an incubation period of 2 h. Afterwards cells were collected using multiple washing steps with cold PBS. The nanocapsule containing supernatant was removed by centrifugation for 5 min at 470 g.

Flow cytometry analysis of NC-loaded DC

Pelleted DC were stained with CD11c-FITC (Miltenyi), CD45-APC-Cy7 (BD) and CD45-V450 (BD). Cells were allowed to incubate with the various antibodies for 15 min at 4 °C. After a washing step with PBS/ 0.1 % BSA, the cells were centrifuged and resuspended in 300 µL PBS/ 0.1% BSA. NC uptake by DC was detected using an Attune NxT flow cytometer (Thermo Fisher, USA), selecting the cells with an FSC/SSC plot, thereby excluding cell debris. Fluorescence of the NC dye sulforhodamine (SR101) was detected using a 586/15 nm bandpass filter with excitation by a 100 mW/ 561 nm laser.

Statistical methods

For the cell uptake experiments the program GraphPad Prism 5 (GraphPad Software, San Diego, USA) was used. Data analysis was conducted using two-way analysis of variance (ANOVA). The cell uptake experiments were performed in duplicates. Two different nanocapsule batches were used.

V. 2. Experimental section to Chapter B

V. 2.1 Materials

All chemicals and reagents were purchased from commercial suppliers and used without further purification except for styrene which was distilled prior to use. Bovine serum albumin (>98%, Lot# 120M1922V), human serum albumin (>96%, Lot# SLBL6442V) and ovalbumin (>90%, Lot# SLBB4341V) were obtained as lyophilized powders from Sigma Aldrich. Furthermore, another batch of human serum albumin was obtained from Serva (>97.0% purity, Lot# 130189) and another ovalbumin batch was obtained from Acros Organics. For the capsule syntheses just proteins obtained from Sigma Aldrich were used unless stated otherwise. Styrene (stabilized with 4-tert-butylcatechol, >99%) was obtained from Sigma Aldrich, V59 was a gift from Wako Chemicals, 2-Aminoethyl methacrylate

hydrochloride (AEMH, >90%, Lot# J2218) was purchased from Santa Cruz Biotechnology (Dallas, USA). In this Chapter again toluene diisocyanate (TDI), sodium dodecyl sulfate (SDS), Lutensol AT50, sulforhodamine (SR101), stains-all, dimethyl sulfoxide (DMSO), cyclohexane, fluorescamine, DBCO-PEG_4-NHS ester, NHS-PEG_4-azide, Aqua ad iniectabilia and Ampuwa® were used, which can also be found in the material section of Chapter A (V. 1.1).

V. 2.2 Syntheses and procedures

Synthesis of protein nanocapsules (NCs) and capsules consisting purely of TDI

The nanocapsules were prepared adopting previously published procedures from Piradashvili *et al.* using an inverse miniemulsion process.[108]

Cyclohexane was dried over molecular sieve (5 Å) before use for at least one day. 50 mg of protein was dissolved in 500 µL of sterile water. If Cy5 Oligo was added, the water volume was adjusted to a total volume of 500 µL. Furthermore, 8 mg of sodium chloride was added into the dispersed phase. The solution was covered with aluminum foil and was stirred for 5 min at room temperature until all components were completely dissolved. 35 mg of the surfactant P(E/B-*b*-EO) were dissolved in 7.5 g of dry cyclohexane under shaking and added at once to the dispersed phase. The mixture was pre-emulsified by vigorous stirring for 1 h at room temperature. Afterwards, the emulsion was subjected to ultrasound for 3 min (70%, 20 s pulse, 10 s pause) and subsequently placed in an oil bath at 25 °C equipped with a stirrer. Under stirring at 700 rpm, a mixture of 11 mg P(E/B-*b*-EO) and 10 mg TDI (approx. 9 µL) in 5.0 g dry cyclohexane was added dropwise with a syringe. For protein NCs with different degrees of crosslinking, either 25 mg, 50 mg, or 75 mg of TDI was added. For the NC synthesis using more BSA, the amount of BSA in the dispersed phase was doubled (100 mg), while the amount of the other components stayed the same.

For NCs consisting purely of TDI, 50 µL of TDI in 5.0 g cyclohexane and 12 mg of P(E/B-*b*-EO) were added to the emulsion, consisting of only sodium chloride (8 mg) in water and 31 mg of P(E/B-*b*-EO) in 7.5 g cyclohexane. All the emulsions were stirred at 25 °C for 24 h. For redispersion into aqueous SDS solution and DBCO functionalization the same procedure was performed as described in V.1.2.

Synthesis of pristine and amino-functionalized polystyrene nanoparticles (PS-NPs)

Styrene (862 µL, 1 eq.) is placed in a glass vial (20 mL) and hexadecane (43.1 µL, 0.5 eq.) and V59 (14 mg, 0.01 eq.) are added. The styrene phase is shaken gently to dissolve and homogenize all components. In another glass vial 80 mg of Lutensol AT-50 is added and dissolved in 3.2 mL MilliQ water. Furthermore, depending on the degree of functionalization, different amounts of 2-aminoethyl methacrylate hydrochloride (AEMH) are added, starting from 0.01 eq. (12.8 mg), 0.025 eq. (35.8 mg), 0.05 eq. (61.7 mg), 0.075 eq. (95.7 mg) and 0.1 eq. (128.1 mg). For pristine PS-NPs no AEMH was added. The aqueous continuous phase was stirred slowly and placed in a ultrasonic bath for a few minutes to dissolve all components. When all compounds were dissolved, the aqueous phase was added at once to the dispersed phase and preemulsified by vigorously stirring for one hour. Afterwards, the emulsion was further homogenized by ultrasonication at 70% for 2 min without pause (1/2’ tip). The emulsion was reacted at 72 °C under stirring overnight.

Purification and functionalization of PS-NPs

After the particles have reacted overnight, the dispersion was filtered through a low-linting wiper removing big aggregates and purified by dialysis (Carl Roth, regenerated cellulose, MWCO: 6-8 kDa) against MilliQ for three days. Then the solid content of the NPs was determined by drying and weighing a particular volume of dispersion and the amino groups were quantified by fluorescamine assay. According to quantified amino groups per mL dispersion, the amount of DBCO was calculated and the respective volume of DBCO-PEG-NHS ester (in DMSO) was added to the PS-NPs and reacted overnight. On the next day the PS-NPs modified with DBCO were purified with a centrifugal filter (Amicon® Ultra 2 mL, regenerated cellulose, MWCO: 100 kDa) by replacing the supernatant with fresh MilliQ water for four times. The functionalized PS-NPs were subjected to anthracene azide assay to quantify the attached DBCO groups. According to the found DBCO groups per mL the added concentration of BSA-PEG-azide was adjusted. BSA-PEG-azide which was readily dissolved in borate buffer (0.1 M, pH 8.3) was added to the PS-DBCO NPs (either 1:1 DBCO/BSA or 1:10 BSA/DBCO) and the mixture stirred for 4 days. Afterwards the NPs were purified by centrifugal filters (Amicon® Ultra 2 mL, regenerated cellulose, MWCO: 100 kDa) by replacing the supernatant for 3 times. Afterwards, the protein content was determined by Pierce™ Assay.

Modification of BSA with NHS-PEG_4-azide

280 mg of BSA (4.264×10^{-6} mol, 1 eq.) was dissolved in 2 mL of borate buffer (0.1 M, pH 8.3) and 50 µL of NHS-PEG_4-azide (5 mg, 1.279×10^{-5} mol, 3 eq.) dissolved at a concentration of 100 mg/mL dry DMSO, was added. The mixture was stirred for 2 h and subsequently dialyzed against MilliQ until the next day. After determination of the protein concentration of the solution, the modified BSA was directly used for PS NPs functionalization or freeze-dried for storage. For the ITC measurements, the modified BSA was dissolved in MilliQ after freeze-drying and again freeze-dried for several days to remove residual DMSO in the sample.

Modification of BSA with NHS-PEG_4-DBCO

To 8 mg of BSA (dissolved in 333 µL borate buffer, 0.1 M, pH 8.3) 39.4 µL of DBCO-PEG-NHS ester (0.7875 mg, 1.212×10^{-6} mol, 10 eq.) dissolved in dry DMSO was added. The reaction mixture was stirred overnight at room temperature. On the next day, the protein was dialyzed against borate buffer for the rest of the day, following by dialysis against MilliQ for another day. Afterwards, the protein was freeze-dried.

Isothermal titration calorimetry (ITC) with modified PS-NPs and azidated BSA

The experiments were performed and evaluated by [redacted]. 10 µL of PS-DBCO-NPs (solid content: 1.28 wt%, R_h = 98 nm) were diluted to 300 µL in MilliQ water resulting in a total particle concentration of 1.8×10^{-7} mM were loaded into the measurement cell. Lyophilized BSA-PEG-azide was dissolved in MilliQ to a concentration of 0.037 mM and loaded into the syringe. The protein solution was titrated to the NPs in the measurement cell until the endpoint was reached.

For PS-NH_2-NPs, 30 µL of dispersion (solid content: 0.706 wt%, R_h = 110 nm) was diluted to 300 µL with MilliQ water resulting in a total particle concentration of 2.6 x 10^{-7} mM were added to the measurement cell and freshly dissolved BSA solution (0.037 mM) were titrated. The experimental temperature was kept constant at 25 °C. Additionally the same amount of BSA solution was titrated into pure water to determine the heat of dilution for reference. The number and injected volume of the titration steps were the same for all measurements. The spacing between injections was set to 200 s. The integrated reference heats were then subtracted from the integrated heats of the adsorption experiments. An independent binding model was employed to fit the adsorption isotherms and obtain the association constant, (Ka), the reaction enthalpy (ΔH), the entropy (ΔS), the Gibbs free energy (ΔG) and reaction stoichiometry (n). The measurements were carried out by triplicate, showing the mean value together with the standard deviation for each parameter. Nano Analyze Data Analysis software from TA Instruments was used for the data evaluation of the ITC measurements (Software version 2.5.0).

V. 3. Experimental section to Chapter C

V. 3.1 Materials

All chemicals were used without further purification. Bovine serum albumin (BSA), human serum albumin (HSA) and ovalbumin (OVA) were purchased from Sigma Aldrich, as well as 2,4-toluene diisocyanate (TDI, Mw = 174.16 g mol^{-1}, 95% Product No.: T39853), 4,4'- methylenebis-(phenylisocyanate) (Mw = 250.25 g mol^{-1}, 98%), polyvinylalcohol (PVA - Mowiol® 4-88, product# 81381), *L*-tryptophan (Mw = 204.23 g mol^{-1}, HPLC grade), dry toluene, dimethylsulfoxide (DMSO, anhydrous, >99%, Product No.: 276855) and sodium dodecyl sulfate (SDS, LiChropur™, ≥99.0% (Art.No.: 71726). Ethyl carbazate (Mw = 104.11 g mol-1), dichloromethane (HPLC grade, stabilized) and NaCl were purchased from VWR. Tetramethylammoniumhydroxid (TMAOH - 1.0 M, aqueous solution) was purchased from Alfa Aesar. The block copolymer poly((ethylene-co-butylene)-b-(ethylene oxide) P(E/B)-*b*-EO) used as surfactant was synthesized according to previously published procedures from Schlaad *et al.*[310]

Human blood serum was collected from ten healthy donors at the Transfusion Center of the University Clinic of Mainz, Germany, according to standard guidelines. All serum batches were pooled and stored at -20 °C.

HeLa cells (obtained from ATCC® CCL-2™) were cultured in Dulbecco Modified Eagle Medium (DMEM, Gibco, USA) supplemented with 10% fetal bovine serum (FBS), 100 U mL^{-1} penicillin, 100 mg mL^{-1} streptomycin and 2 mM glutamine (all Thermo Fisher, Germany). Cells were split about two times a week at 80-90% confluency. For cell uptake analysis, cells were detached with 2.5% trypsin (Gibco, Germany) and seeded out in 24-well plates (100 000 cells/well) in cell culture medium with 10% FBS. After overnight incubation, the medium was changed to serum-free medium.

V. 3.2 Syntheses and procedures

Synthesis of 4,4'-(4,4'-diphenylmethylene)-bis-urazol

This procedure was adopted from a previously published procedure from Du Prez and coworkers.[133]
20 g of ethyl carbazate (Scheme 1, compound 1) (0.192 mol, 2 eq.) were dissolved in a three-neck flask in 150 mL of dry toluene with a mechanical stirrer. In a dropping funnel, 4,4'-methylenebis(phenylisocyanate) (Scheme 1, compound 2) (0.096 mol, 1 eq.), dissolved in 100 mL of dry toluene, was placed and added to the ethyl carbazate under vigorous stirring and N_2 atmosphere. The mixture was stirred at room temperature for 2 h and afterwards 2 h at 90 °C. After the mixture cooled down, the semi carbazide (Scheme 1, compound 3) could be filtered off and washed with toluene.
44.4 g of the semi carbazide 3 was then dissolved in 200 mL of a 4 M KOH-solution and heated to 100 °C for 1.5 h. The hot yellowish solution was filtered off and 200 mL of concentrated HCl was added stepwise until a colorless solid precipitated. The solid was filtered and dried under reduced pressure. Yield: 15.94 g (0.0435 mol, 45%) colorless solid. ^{1}H-NMR (250 MHz, d6-DMSO): δ (ppm) = 10.46 (s, 4H), 7.36 (m, 8H), 4.02 (s, 2H).

Synthesis of 1,4-diazabicyclo(2,2,2)octane bromide salt (DABCO-Br)

3.36 g DABCO was placed in a 250 mL round-bottom flask and dissolved in 50 mL chloroform. 10.0 g bromine in 50 mL chloroform was slowly added to DABCO under stirring using a dropping funnel. The mixture was stirred under N_2 atmosphere for 2 h. DABCO-Br precipitated as a yellow solid and was filtered using a Büchner funnel and dried at 40 °C over night.
Yield: 12.23 g (7.78 mmol, 65%) yellow solid.

Synthesis of 4,4'-(4,4'-diphenylmethylene)-triazolinedione

1.002 g of 4,4'-(4,4'-diphenylmethylene)-bis-urazol (Scheme 8, compound 4) (2.74 mmol, 1 eq.) and DABCO-Br (2.68 g, 1.66 mmol, 0.60 eq.) were placed in a 50 mL flask and 25 mL dichloromethane were added. The suspension was stirred at room temperature for 2.5 h.
The yellow solid was filtered off and the filtrate was washed with 200 mL dichloromethane. The dichloromethane was removed under reduced pressure and the product was dried and stored at 4 °C.
Yield: 750.5 mg (2.071 mmol, 76%) pink solid. ^{1}H-NMR (250 MHz, d6-DMSO): δ (ppm) = 7.47 (d, 4H), 7.36 (d, 4H), 4.10 (s, 2H).

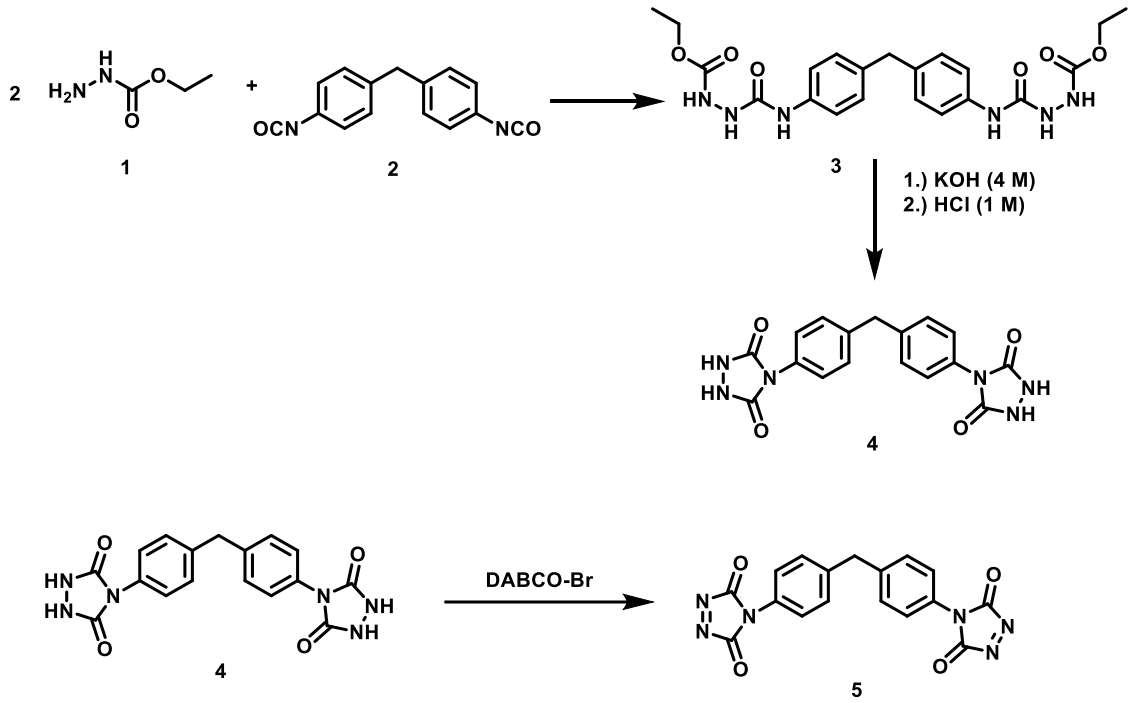

Scheme 8*:* Synthesis scheme of 4,4'-(4,4'-diphenylmethylene)-bis-(1,2,4-triazoline-3,5-dione) MDI-TAD.

TAD-nanocapsule synthesis

The nanocapsules were prepared adopting to previously published procedures from Piradashvili *et al.* using an inverse miniemulsion process.[108]

50 mg of protein or *L*-tryptophan was dissolved in 500 µL of demineralized water and 8.0 mg of NaCl was added to the mixture. In the case of *L*-tryptophan the pH was adjusted to pH 11 with NaOH. In the case of TAD-TAD nanocapsules just NaCl was added into the aqueous phase. 35.0 mg of P((E/B)-*b*-EO) were dissolved in 7.5 g of toluene and the mixture was added at once to the stirring aqueous solution. This mixture was pre-emulsified by vigorously stirring for approx. 30 min. Afterwards, the pre-emulsion was subjected to ultrasound for 3 min (70%, 20 s pulse, 10 s pause) and stirred shortly after at 700 rpm at room temperature. A solution of 10.0 mg P((E/B)-b-EO) in 5.0 g of toluene was prepared and 100 mg of MDI-TAD was added to the solution. To improve the solubility of MDI-TAD in the mixture, it was homogenized in an ultrasound bath at 40 °C for 5 min. The MDI-TAD solution was then added dropwise over a period of one minute to the stirring miniemulsion and the mixture stirred for another 24 h at room temperature.

Transfer of TAD nanocapsules into aqueous medium

5 mL of nanocapsule dispersion were split in three Eppendorf tubes (1.667 mL each) and centrifuged at 4000 rpm for 30 min. The supernatant was replaced against the same volume of toluene and the pellet was redispersed in the fresh solvent. This process was repeated one more time. The first supernatant was distributed into fresh Eppendorf tubes and also centrifuged once more. The pellets generated from the centrifugation steps were concentrated together with 500 µL of fresh toluene and redispersed in 5 mL of aqueous SDS solution (0.1 wt%) by shaking in a sonication bath while the nanocapsule dispersion was added in 100 µL steps.

The sonication process was performed for 5 min and afterwards the dispersion was placed in a cooling bath and additionally sonified (Branson Digital Sonifier W-450-D) for 30 s, 10%, 10 s pulse, 10 s pause. Afterwards the dispersion was placed on a stirring plate and the vial was stirred open over night at 1000 rpm to evaporate the solvent.

Tryptophan-TAD nanocapsules with encapsulated magnetite-nanoparticles

50 mg of *L*-tryptophan were dissolved in 350 µL of demineralized water and 50 µL of conc. NaOH-solution (pH 11) and 8.0 mg of NaCl as well as 100 µL of an aqueous magnetite-nanoparticle solution (5 wt%) was added to the mixture. 35.0 mg of P((E/B)-b-EO) were dissolved in 7.5 g of toluene and the mixture was added at once to the stirring aqueous solution. This mixture was pre-emulsified by vigorous stirring for about 30 min. Afterwards, the pre-emulsion was subjected to ultrasound for 3 min (70%, 20 s pulse, 10 s pause) and stirred shortly after at 700 rpm at room temperature. A solution of 10.0 mg P((E/B)-b-EO) in 5.0 g of toluene was prepared and 100 mg of MDI-TAD was added to the solution. To improve the solubility of MDI-TAD in the mixture, it was homogenized in an ultrasound bath at 40 °C for 5 min. The MDI-TAD solution was then added dropwise over a period of one minute to the stirring miniemulsion and the mixture stirred for another 24 h at room temperature.

Transfer of magnetite (Fe_3O_4) nanoparticles into aqueous medium

This procedure was adopted from a previously published procedure from Bannwarth *et al.*[316]

50 mg of magnetite nanoparticles (stabilized with oleic acid) were placed in a screwcap vial and 5 mL of a TMAOH solution (1 M) was added. The mixture was placed in an ultrasound bath for one hour. Afterwards, the nanoparticles were centrifuged at 20 000 rpm for 40 min and the supernatant was removed. The pellet was resuspended in a small amount of a 0.1 wt% TMAOH solution and afterwards the whole dispersion was added to 50 mL of a 0.1 wt% TMAOH solution while placing the whole solution into an ultrasound bath. 50 mg of carboxymethylated PVA (CPVA) were dissolved in 50 mL of hot water and slowly added to the redispersed nanoparticles. The whole mixture was homogenized in an ultrasound bath for 5 min and stirred overnight. On the next day, the nanoparticles were centrifuged at 14 000 rpm for 30 min, the supernatant was removed, and the pellet was redispersed in 1 mL of demineralized water.

V. 3.3 Cell experiments to Chapter C

All cell experiments and related procedures were performed by [redacted].

Cellular uptake and protein corona analysis

For cellular uptake experiments, the nanocapsules were washed several times by centrifugation to remove excess SDS. The SDS concentration in the dispersion was checked by a colorimetric assay. Then protein nanocapsules (75 µg mL^{-1}) were added to cells in serum-free cell culture medium (-HS) or cell culture medium containing 10% human serum (+HS) for 2 h or 24 h at 37 °C.

Purification of protein corona

Nanocapsules (0.05 m^2) were incubated with 1 mL of human serum at 37 °C for 1 h. Protein coated nanocapsules were centrifuged (20 000 g, 30 min, 4 °C), the supernatant was removed and the pellet was washed with 1 mL PBS solution. To fully remove all loosely bound proteins, this step was repeated three times. Finally, the strongly attached corona proteins were desorbed from the nanocapsules´ surface with an aqueous solution containing 2 wt% SDS supplemented with 62.5 mM Tris-HCL. The sample was incubated for 5 min at 95 °C. In a last step, the dispersion was centrifuged and the supernatant containing the corona proteins was isolated. The protein concentration was analyzed using a Pierce 660 nm Protein Assay (Thermo Fisher, Germany) according to manufacturer's instructions.

SDS-PAGE of the protein corona

Corona proteins (2 µg in 26 µL) were incubated with sample buffer (10 µL) and reducing agent (4 µL) for 10 min at 70 °C and applied onto a 10% NuPAGE Bis-Tris Gel. The SDS-PAGE was run at 120 mV for 1 h. The protein bands were visualized by the SilverQuest Silver Staining Kit according to the manufacturer's instructions. All components were obtained from Thermo Fisher, Germany.

In solution digestion

In a first step, SDS was removed via Pierce detergent removal columns (Thermo Fisher, Germany) according to the manufactures' instruction. Tryptic in solution digestion was carried out according to former reports.[113,123] Proteins were precipitated using a ProteoExtract protein precipitation kit (Merck Millipore, Germany) for at least 2 h. After centrifugation, the protein pellet was resuspended in RapiGest SF (Waters, USA) dissolved in 50 mM ammonium bicarbonate (Sigma Aldrich, Germany). The samples were incubated at 80 °C for 15 min. For reduction, dithiothreitol (5 mM, Sigma Aldrich, Germany) was added to the solution for 45 min at 56 °C and for alkylation iodoacetoamide (15 mM, Sigma Aldrich, Germany) was added for 1 h in the dark. Finally, a protein:trypsin ratio of 50:1 was used for tryptic digestion (incubation time 16 h at 37 °C). The digestion was stopped with hydrochloric acid (Sigma Aldrich, Germany) and the resulting peptide sample was centrifuged (14 000 g, 15 min, 4 °C) to remove degradation products of RapiGest SF.

Liquid chromatography-mass spectrometry (LC-MS)

Peptide samples were diluted with 0.1% formic acid and 50 fmol of Hi3 EColi Standard (Waters, USA) was added for absolute protein quantification. LC-MS measurements were performed with a nanoACQUITY UPLC system coupled to a Synapt G2-Si mass spectrometer (Waters, USA). A nanoLockSpray source was used for electrospray ionization (ESI) in positive ion mode and the mass spectrometer was operated in resolution mode performing data-independent experiments (MSE). Data was processed with MassLynx 4.1 and all proteins were identified with Progenesis QI. A reviewed human data base was downloaded from Uniprot.

The absolute amount of each protein was calculated based on the TOP3/Hi3 approach.

Visualization of intracellular localization by cLSM

To visualize the cellular uptake behavior of the protein nanocapsules in HeLa cells, confocal laser scanning microscopy (cLSM) images were taken. Nanocapsules containing the dye SR101 were excited with a 561 nm laser and detected with an emission filter at 569 – 624 nm. The cell membrane was stained with CellMask DeepRed (stock solution: 5 mg mL^{-1}, Thermo Fisher), excited with a 633 nm laser and detected with an emission filter at 680 – 695 nm. For the visualization of intracellular localization, 5 x 104 cells in 200 µL DMEM with 10% FBS were seeded out into 8-well µ-slides with a glass bottom (ibidi). After an overnight incubation at 37 °C and 5% CO2 in the incubator, the cells were treated with the respective sample in medium with 10% FBS. After the 2 h and 24 h incubation with a nanocapsule concentration of 75 µg mL^{-1}, the wells were washed with PBS to remove unbound nanocapsules. Afterwards, the cells were directly imaged. Cell membrane staining was conducted shortly before the cLSM analysis for 5 min in the dark using CellMask Deep Red (Dilution of stock solution: 1:1000 in PBS).

Cell viability assay

HeLa cells were seeded out into 96-well plates (Greiner Bio-One, Austria) with a cell number of 10 x 103 cells per well in 100 µL DMEM with 10% FBS. After overnight incubation at 37 °C and 5% CO_2, the medium was removed. The respective protein nanocapsules were prepared in 10% FBS supplemented DMEM and added in a volume of 100 µL to the cells (75 µg mL^{-1} final concentration). Water (Ampuwa®) was used as positive control. All samples were handled in triplicates. HeLa cells were incubated at 37 °C and 5% CO_2 for 2 and 24 h before conducting the viability assay. A CellTiter-Glo® Luminescent Cell Viability Assay (Promega, Germany) was performed according to the manufacturer´s instructions. The luminescence signal was measured with an Infinite M1000 plate reader (Tecan, Switzerland).

V. 4. Experimental section to Chapter D

V. 4.1 Materials

All chemicals were purchased from commercial suppliers and used without further purification. Bovine Serum Albumin (BSA, lyophilized powder), 2,4-toluene diisocyanate (TDI, M_w = 174.16 g/mol), sodium dodecyl sulfate (SDS, LiChropur™, ≥99.0%, Art.No.: 71726), FITC Isomer I (≥95%), 1-Octadecene (technical grade 90%), oleic acid (technical grade 90%), cadmium nitrate tetrahydrate ($CdNO_3(H_2O)_4$, 98%), zinc nitrate hydrate ($ZnNO_3(H_2O)$, 99.999%), poly(isobutylene-alt-maleic anhydride) (85%, average Mw ~6000, 12-200 mesh) were obtained from Sigma Aldrich. Cyclohexane (HPLC grade), n-hexane (analytical reagent grade 95%) were obtained from Fisher Chemical. Aqua ad iniectabilia (sterile water, Art.No.: 03710653) was obtained from B.Braun (Germany). Chloroform, stabilized with amylene (100%), absolute ethanol and sodium hydroxide (NaOH, 1 mol/L 1N) were purchased from VWR Chemicals. 1-dodecylamine (>97%) was purchased from TCI. Boric acid (>99.8%) was purchased from Carl Roth GmbH. Gibco Dulbecco's modified eagle medium (DMEM), fetal bovine serum (FBS) and trypsin-EDTA (0.25% + phenol red) were purchased from Thermo Fisher Scientific. Phosphate buffered saline (PBS) was purchased from Sigma Aldrich. The block copolymer poly((ethylene-co-butylene)-b-(ethylene oxide) P(E/B)-b-EO) used as surfactant was synthesized according to previously published procedures from Schlaad *et al.*[310]

V. 4.2 Syntheses and procedures

[redacted] performed the nanoplatelet synthesis and characterization. I, Marie-Luise Frey performed the nanocapsule synthesis, characterization and labeling.

Synthesis of 4 monolayer (4ML) thick CdSe nanoplatelets (NPLs)

4ML thick CdSe NPLs were synthesized by a modified procedure published by Mahler *et al.*[317] Briefly, 60 mL of 1-octadecene, 320 mg (1.20 mmol) of $Cd(OAc)_2(H_2O)_2$, and 879 µL (787 mg, 2.79 mmol) of oleic acid were combined inside a 100 mL three-necked flask attached to a water-cooled condenser. The mixture was stirred and degassed under vacuum at 110 °C for 90 min. After stopping the vacuum line, the flask was filled with argon and 48 mg (0.607 mmol) of Se powder was swiftly added into the flask. Then the temperature of the heating mantle was set to 240 °C. When the temperature in the flask reached 205 °C, 160 mg (0.600 mmol) of $Cd(OAc)_2(H_2O)_2$ was added into the mixture and the reaction proceeded for 15 min at 240 °C. Afterwards the flask was then cooled to room temperature using a water bath and 6.7 mL of oleic acid was injected. The mixture was centrifuged for 10 min at 5000 rpm (2599 g), the supernatant was discarded. Finally, the precipitated NPLs were re-dispersed in 12 mL hexane.

Synthesis of $Cd_{0.33}Zn_{0.67}S$ Shell

The CdZnS shell was synthesized using a one-pot method, modified from an existing procedure.[317] Briefly, 6 mL of the as-synthesized 4ML NPLs (with optical density at 510 nm = 30) were added into a 50 mL round bottom flask containing a stir bar. In a separate flask, 300 mg (3.99 mmol) of TAA, 3 mL (18.2 mmol) of octylamine and 9 mL of chloroform were gently mixed and then sonicated in an ultrasound bath until all the TAA dissolved. The TAA solution was added to the NPL solution while stirring. After a couple of minutes, 500 µL of $CdNO_3$ solution (0.2 M in ethanol) and 1000 µL of $ZnNO_3$ solution (0.2 M in ethanol) were added into the mixture. The flask was sealed with a glass stopper and left to stir for 24 hours in ambient conditions.

To precipitate the NPLs, the mixture was concentrated by evaporating a portion of the solvent using a rotatory evaporator at approximately 280 mbar, 40°C for a couple of minutes. Then the concentrated mixture (volume approx. 15 mL) was centrifuged for 10 min at 8000 rpm (6654 g), the supernatant was discarded, and the precipitated NPLs were re-suspended in 15 mL chloroform. To stabilize the NPLs, 300 µL of $ZnNO_3$ solution (0.2 M in ethanol) and 600 µL of oleic acid were added into the NPL dispersion while stirring and the mixture was kept at ambient conditions for a couple of days for PL recovery.

To remove the excess oleic acid introduced in this step, methyl acetate was added to the chloroform dispersion of core/shell NPLs (in the ratio of chloroform:methyl acetate = 1:1 v/v). The NPLs were precipitated by centrifugation and re-dispersed in chloroform.

Synthesis of dodecyl-grafted-poly(isobutylene-*alt*-maleic acid) (polymer coating for NPLs)

The amphiphilic polymer was synthesized according to the method described by Riedinger *et al*.[318] Briefly, 105.3 mg (0.662 mmol monomer units /1.10×10^{-5}mmol polymer) of poly(isobutylene-alt-maleic anhydride), 92.0 mg (0.497 mmol, equivalent to 75% of monomer units) of 1-dodecylamine and 25 mL of THF were combined in a 50 mL round bottom flask containing a magnetic stir bar.

Then a reflux condenser was attached and the mixture was heated to reflux using an oil bath. After approximately 10 minutes, the solution turned clear and it was kept refluxing for 18 hours. Then the solution was brought back to room temperature and the THF was removed using a rotatory evaporator. 13.24 mL of chloroform was then added to the solid polymer film to make a 0.05 M solution (based on monomer concentration).

Phase transfer of NPLs by polymer coating for water-dispersed NPLs

The NPLs were coated with the amphiphilic polymer and subsequently transferred to water using a method developed by Halim *et al.*[309] To coat the NPLs with the polymer, 7.5 mL of the core/shell NPLs (optical density = 2.574 at lowest-energy exciton peak) was added into a 2.125 mL polymer solution in a 50 mL round bottom flask. The flask was gently shaken for a few seconds and the mixture was then evaporated gently using a rotatory evaporator until all the solvent is removed (approx. 10 minutes, 40°C water bath). The remains were re-dispersed in chloroform, re-evaporated again for a total of three times to ensure an even coating. Then 30 mL of boric acid buffer (pH 12) was added to open the remaining anhydride rings of the polymer in the dried polymer and NPLs mixture. The flask was gently shaken for 10 minutes for complete dispersion in water.
The excess polymer was removed by sucrose gradient centrifugation and the sucrose was washed away by rinsing the NPLs with water while they were trapped in an Amicon filter (Mw cutoff = 100k). The molar and weight concentration of the core/shell NPLs were determined from their relationship with the sample absorbance calculated in the previous study.[309]

Synthesis of BSA nanocapsules (NCs) with encapsulated water-dispersed NPLs

The NCs were prepared adopting previously published procedures from Piradashvili *et al.* using an inverse miniemulsion process.[108] Cyclohexane was dried over molecular sieve (5 Å) before use.
To a total volume of 500 µL, 50 mg BSA and 8 mg NaCl were dissolved in sterile water and NPL dispersions in a 10:1, 5:1 and 1:1 ratio to expected NCs were added. Expected NCs were calculated using the hydrodynamic radius and solid content. 35 mg of the surfactant P(E/B-*b*-EO) were dissolved in 7.5 g of dry cyclohexane under shaking and added at once to the aqueous phase. The mixture was pre-emulsified by vigorous stirring for 1 h at room temperature. Then, the mixture was subjected to ultrasound for 3 min (70%, 20 s pulse, 10 s pause, ½’ tip). The emulsion was placed in an oil bath at 25°C equipped with a magnetic stirrer and under stirring at 700 rpm, a mixture of 12 mg P(E/B-*b*-EO) and 10 mg TDI in 5.0 g dry cyclohexane was added dropwise with a syringe. The emulsion was stirred at 25°C for 24 h.

Redispersion of NCs into aqueous SDS solution

5 mL of NCs dispersion were distributed over three Eppendorf tubes, 1.667 mL each and centrifuged for 30 min at 4000 rpm. The supernatant was replaced with the same amount of fresh cyclohexane and the procedure was repeated. The NCs were redispersed in 500 µL fresh cyclohexane and added into 5 mL of aqueous SDS solution (0.1 wt%) over a time period of 5 min under constant sonication in an ultrasonic bath.

The aqueous dispersions were placed on a stirring plate and the cyclohexane was evaporated under vigorous stirring at 1000 rpm overnight. For cell uptake experiments, the aqueous dispersions were washed by a centrifugal filter (Merck Millipore Amicon™ Ultra-2.0, MWCO: 100 kDa) for at least three times with sterile water to remove residual surfactant and concentrated to one tenth of the volume.

Labeling of BSA NCs encapsulating NPLs with fluorescein isothiocyanate (FITC)

Prior to labeling, protein concentration of the BSA NCs was determined using a Pierce™ Assay conducted according to instructions. According to the obtained protein concentration, a tenfold excess of FITC was added to the dispersion. Therefore, to 300 µL of BSA NCs (1.7 wt%) 86 µL of FITC solution in DMSO (1 mg/mL) was added. The dispersion was stirred at room temperature over three days in the dark. Afterwards, the labeled NCs were purified using Amicon® ultra centrifugal filters (100 kDa) centrifuging the NCs at 6000 rpm for 15 min each washing the NCs for 8 times with 2 mL of sterile water each cycle.

V. 4.3 Confocal laser scanning microscopy (cLSM)

cLSM was performed by [redacted].

For the cLSM data the cells were seeded in an Ibidi 6x3 well chamber, stained with Lysotracker and mounted on an inverted Leica TCS SP5 microsope that was heated to 37°. After placing the sample on the stage, medium in the wells was exchanged to NCs solutions at a concentration of 75 µg/mL and 300 µg/mL containing FBS. Images in the wells were recorded at a time lapse of approximately 10 minutes. During the experiment, the sample was flushed with an atmosphere of 5% CO_2. NPL and Lysotracker channels were recorded linewise sequentially, NPL emission was excited at 561 nm and detected at 599 nm – 669 nm, Lysotracker was excited at 488 nm and detected at 505 nm – 588 nm. Colocalization/correlation was evaluated for the images (75 µg/mL) using the ImageJ Colocalization Analysis Plugin (Coloc 2). For Pearson correlation coefficient the R-value above threshold was chosen, threshold being automatically determined by the program.

V. 4.4 TEM sample preparation and correlative light and electron microscopy (CLEM) imaging

CLEM was performed by [redacted].

For preparation, RAW 264.7 cells were seeded out with a concentration of 50.000 cells/mL in a 24-well plate (Greiner, Germany) containing three C-coated sapphire disks, and adhered for 24 h on the sapphire discs. BSA NCs with NPLs were added at concentrations of 75 µg/mL and 300 µg/mL to the cell medium and incubated for 2 h and 24 h.

After incubation, the sapphire discs were removed from the wells and dipped into 1-hexadecane to remove the remaining medium. The discs were placed between two aluminum plates to create a ‘sandwich’ and afterwards were mounted into a holder (Engineering Office, M. Wohlwend) and placed into a Wohlwend HPF Compact 01 high-pressure freezer (Engineering Office, M. Wohlwend) and were pressure-frozen with 2100 bar. The frozen sandwich was stored in liquid nitrogen.

After high-pressure freezing, sapphire discs were removed from the sandwich and place into 1.5 mL Eppendorf tubes filled with precooled 1 mL freeze substitution solution with 0.2% (w/v) osmium tetroxide, 0.1% (w/v) uranyl acetate, 5% (v/v) distilled water in acetone.
The samples were slowly warmed up to 0 °C, over a period of 18–20 h. After being warmed up, the freeze-substituted samples were brought to room temperature, then the substitution medium was removed and the discs were washed 3 times with acetone at half an hour intervals. Then the discs were incubated sequentially in 1:1 EPON®-Acetone, in 1:2 EPON®-Acetone and in 2:1 EPON®-Acetone for 1 h. Samples were then infiltrated in 100% epoxy resin overnight. Finally, each sample was transferred into a new Eppendorf tube containing fresh epoxy resin for polymerization at 60 °C for 24 h.
After polymerization, sample blocks were trimmed and sectioned into 100 nm sections by by a 45° diamond knife (Diatome) in EM UC6 ultramicrotome and afterwards carefully placed onto H6 copper finder grids.
Ultrathin section was first imaged in cLSM (Leica SP5, Germany) to obtain fluorescence image of ROIs. Then the same sections was observed using a FEI Tecnai F20 transmission electron microscope operated at an acceleration voltage of 200 kV. Micrographs were taken on a Gatan US1000 2k slow scan CCD camera. The images from cLSM and TEM of the same ROI were then registered and overlaid by Icy software (ec-CLEM).

V. 5. Instrumentation and methods

Differential scanning fluorimetry (nanoDSF) measurements

Nano DSF measurements were performed on a Prometheus NT.48 nanoDSF device from NanoTemper Technologies (Munich, Germany). Standard glass capillaries (NanoTemper Technologies GmbH) were filled with 10 µL sample applying a temperature ramp from 20 – 95 °C with a heat rate of 1 °C min^{-1}.

Flow Cytometry and confocal laser scanning microscopy

For flow cytometry analysis, cells were detached, or nanocapsules were diluted in PBS and measurements were performed on an Attune NxT flow cytometer (Thermo Fisher, USA).
Confocal laser scanning microscopy (cLSM) was conducted on the LSM SP5 STED Leica Laser Scanning Confocal Microscope (Leica, Germany), composed of an inverse fluorescence microscope DMI 6000CS equipped with a multi-laser combination using a HCX PL APO CS 63 x 1.4 oil objective.

Fluorescence correlation spectroscopy (FCS) and fluorescence cross-correlation spectroscopy (FCCS)

FCS and FCCS measurements were performed using a commercial setup LSM 880 microscope (Carl Zeiss, Jena, Germany). For excitation of FITC and Cy5-Oligo an argon ion laser (488 nm) and a He/Ne-laser (633 nm) were used. The excitation light was focused into the sample by a C-Apochromat 40x/1.2 W (Carl, Zeiss, Jena, Germany) water immersion objective. The fluorescence light was collected with the same objective and after passing through a confocal pinhole, directed to a spectral detection unit (Quasar, Carl Zeiss). The detected emission range was in the spectral range 500-553 nm for FITC and int the range 642-696 nm for Cy5-Oligo. For calibration of the detection volumes Alexa Fluor488® and Atto Fluor643® were used.

The measurements were performed in an eight-well polystyrene-chambered coverglass (Laboratory-Tek, Nalge Nunc Internation, Penfield, NY, USA). For all solutions, a series of twenty measurements with a total duration of 3 min were performed. Beside the measurement of the HES nanocapsules, HES capsules were incubated with Cy5-Oligo to exclude an adsorption of the dye on the surface of the nanocapsules. For FCCS measurements IL-2 modified HES nanocapsules were incubated with FITC-labeled anti IL-2 antibodies. All measurements were performed in cooperation with [redacted].

Fluorescence intensity measurements

Fluorescence intensity measurements were operated in 96-well plates on the Infinite M1000 plate reader from Tecan, Austria.

High-performance liquid chromatography (HPLC)

HPLC measurements were performed on an Agilent Technologies Series 1200 setup equipped with a UV detector and an ELSD detector 385-LC (both Agilent Technologies, USA) by [redacted]. The mannose-linker quantification was performed using a reversed phase C8 column with an eluent consisting of 20% water and 80% methanol plus an additive of 0.05% formic acid.

Infrared spectra (FTIR)

Infrared spectra measurements were performed on a SpectrumBX FTIR spectrometer from Perkin Elmer equipped with a diamond ATR unit.

Isothermal titration calorimetry (ITC) measurements

ITC measurements were performed using a NanoITC Low Volume (TA Instruments, Eschborn, Germany) with an effective cell volume of 170 µL performed by [redacted]. In an experiment 50 µL of BSA solution with a concentration 0.037 mM were titrated to a suspension of two different NPs. First, amino functionalized NPs (2.6×10^{-7} mM) and NPs fully functionalized with DBCO groups (1.8×10^{-7} mM). The experimental temperature was kept constant at 25 °C. Additionally the same amount of BSA solution was titrated into pure water to determine the heat of dilution for reference. The number and injected volume of the titration steps were the same for all measurements (25 x 2 µL). The spacing between injections was set to 200 s. The integrated reference heats were then subtracted from the integrated heats of the adsorption experiments. An independent binding model[213,214] was employed to fit the adsorption isotherms and obtain the association constant, (K_a), the reaction enthalpy (ΔH), the entropy (ΔS), the Gibbs free energy (ΔG) and reaction stoichiometry (n). The measurements were carried out by triplicate, showing the mean value together the standard deviation for each parameter. Nano Analyze Data Analysis software from TA Instruments was used for the data evaluation of the ITC measurements (Software version 2.5.0) from TA Instruments.

Light Scattering

Average sizes and size distributions at multiple angles were measured by dynamic light scattering (DLS) at 20 °C using an instrument from ALV GmbH consisting of a goniometer and an ALV-5000 multiple-tau full digital correlator with 320 channels. As a light source a helium-neon laser (JDS Uniphase with a single mode intensity of 25 mW operating at a laser wavelength of 632.8 nm) was used. Measurements were performed in quartz light scattering cuvettes (inner diameter 18 mm, Hellma, Müllheim) and dispersions were filtered dust-free with a 0.45 µm LCR filter prior to the measurements by [redacted]

DLS measurements at a fixed angle of 90° were performed in triplicates on a Malvern Zetasizer Nano S90 (Malvern Panalytical GmbH, Kassel, Germany).

Matrix-assisted laser desorption and ionization time of flight (MALDI-ToF)

MALDI-TOF measurements were performed on a Bruker Reflex II MALDI-ToF mass spectrometer (Bremen, Germany) equipped with a N_2-laser (λ = 337 nm). α-Cyano-4-hydroxycinnamic acid was used as matrix dissolved in water/acetonitrile with trifluoro acetic acid as cationizing agent. All MALDI-ToF experiments were performed by the core facility mass spectrometry.

Nuclear magnetic resonance (NMR) spectroscopy

NMR measurements were performed on a Bruker Avance III either at 250 MHz, 300 MHz or 700 MHz (Billerica, MA, USA). All spectra were measured either in d_6-DMSO, $CDCl_3$ or D_2O and spectra were analyzed using MestReNova 14 (Mestrelab Research S.L., Santiago de Compostela, Spain).

Purifications and concentration by centrifugation

Purification of nanocapsules with or without centrifuge filters (Amicon® centrifuge filters 2 mL or 15 mL, 100 kDa, regenerated cellulose, Merck Millipore) were performed on a Sigma 3K30 centrifuge by Sigma, Germany in a speed range from 4000 – 6000 rpm (1446 x g – 3254 x g).

Scanning electron microscopy (SEM)

Scanning electron microscopy (SEM) was performed by placing a drop of diluted nanocapsule dispersion onto a silica wafer and drying under ambient conditions. SEM measurements were operated on a 1530 Gemini LEO (Zeiss) field emission microscope by [redacted].

Sonication and Homogenization

Ultrasonication was performed with a Branson Sonifier W-450-Digital with a 1/2' tip or in an ultrasonic bath Bandelin Sonorex RK52H from Bandelin electronic Berlin, 160 W, 0.6 L. Homogenization by microfluidics was performed on a high-shear LV1 Low Volume Microfluidizer® Homogenizer by Microfluidics Corp. (Westwood, MA, USA).

Time of Flight secondary ion mass spectrometry (ToF-SIMS)

ToF SIMS measurements were performed on a IONTOF TOF.SIMS5 NCS (IONTOF GmbH, Münster, Germany) with Bi3@30 keV primary ion pulses, 0.11 pA, on a field of view of 200 x 200 µm². Cycle time: 150 µs (Mass Range: 1-2070 u). Measurement and analysis were performed by [redacted].

Transmission electron microscopy (TEM)

TEM was performed by placing a drop of diluted nanocapsule dispersion onto a 300 mesh carbon-coated copper grid and drying under ambient conditions. TEM measurements were operated on a Jeol 1400 transmission electron microscope by [redacted].

Zeta Potential

Zeta potential was measured using a Malvern Zetasizer NanoZ (Malvern Panalytical GmbH, Kassel, Germany). Nanocapsule dispersions were diluted (1:9) in a potassium chloride solution (1 mM, 25 °C, pH 6.8) prior to measurement and measured in triplicates.

V. 6. Assays

Anthracene azide assay

Anthracene azide was freshly dissolved in DMSO (1.7 mg/mL) and corresponding molar amounts were added to of the DBCO-functionalized HES NCs The following amounts of anthracene azide were added to 25 µL of functionalized nanocapsules: A)(3.3 mg/mL DBCO): 17.1 µL anthracene azide, B) (1.65 mg/mL DBCO) 5.68 µL anthracene azide, C) (0.55 mg/mL DBCO): 2.84 µL anthracene azide, D) (0.275 mg/mL DBCO): 1.42 µL anthracene azide and E) (0.055 mg/mL DBCO): 2.84 µL anthracene azide (1:10 dilution of stock solution). Furthermore, blank samples were prepared by mixing the corresponding amount of anthracene azide (A-E) with 25 µL of water each and without nanocapsules. The total volume was adjusted with DMSO to 50 µL for each sample. The same procedure was followed with supernatants. The calibration was performed, mixing 16.5 µL of DBCO-PEG_4-NHS ester (10 mg/500 µL DMSO) with 68.1 µL anthracene azide (1.70 mg/mL DMSO) ($5.079 \cdot 10^{-7}$ mol) and adding 15.4 µL DMSO to obtain a total volume of 100 µL. This first concentration was diluted 1:1 with DMSO, to obtain a calibration in concentrations from 3.3 mg/mL to $1.61 \cdot 10^{-3}$ mg/mL. All samples were subjected to reaction for one hour on a shaker at room temperature in the dark. After incubation, the samples were vortexed and a 1:10 dilution (90 µL DMSO + 10 µL sample) and a 1:100 dilution (99 µL DMSO + 1 µL sample) were pipetted in duplicates into the wells of a 96-well plate (Greiner Bio-one GmbH, Germany) and the fluorescence was measured on the Infinite M1000 plate reader (Ex.: 370 nm, Em.: 414 nm). For the data calculation, the average concentration of all replicates and dilutions was determined.

CTLL-2 proliferation assay

CTLL-2 proliferation assessed by means of ^{3}H-Thymidine assay upon HES-IL-2 NCs addition was performed and evaluated by previously published procedures by [redacted].[319] Briefly CTLL-2 cells were cultured together with HES-IL-2 NCs in different concentrations.

As a reference, Proleukin® was added to another group of CTLL-2 cells. The plates were pulsed with ^{3}H-Thymidine and proliferation analyzed by radioactivity measurements.

Fluorescamine Assay

A fluorescamine stock solution of 0.5 mg/mL in DMSO was freshly prepared. 25 µL of sample or standard was mixed with 725 µL of borate buffer (0.1 M, pH 8.3) and vortexed. Right before fluorescence intensity measurements, 250 µL of fluorescamine solution was pipetted to the mixture and subsequently 100 µL was pipetted into 96-wells in triplicates (excitation: 410 nm, emission: 470 nm). The standard was prepared either with hexylamine in the case of HES NCs and polystyrene NPs or the respective protein for protein NCs. Therefore, hexylamine in concentrations starting from 40 µg/mL to 19 µg/mL (sometimes also from 0.8 mg/mL) in borate buffer or a protein standard in concentrations starting from 10 mg/mL to 0.00391 mg/mL in borate buffer were prepared.

Pierce™ Assay

Pierce™ Assay was conducted according to manufacturer's specifications. 10 µL of a protein solution or protein containing sample was mixed with 150 µL Pierce Reagent™ and subsequently 100 µL was transferred to a 96-well plate and the absorbance was measured at 660 nm in triplicates. A BSA solution at dilutions starting from 2 mg/mL to 0.1 mg/mL was used as a standard calibration.

SDS quantification on nanocapsule samples

This procedure was adopted from previously published procedures.[320] Briefly, 1 mg of stains-all dye was dissolved in 1 mL of isopropanol/water (1:1). 1 mL of the dye solution was mixed with 1 mL of formamide and 18 mL water. Then 200 µL of the mixed dye solution was mixed with 1-2 µL of nanocapsule sample or SDS standard. The absorbance was measured at 438 nm or 510 nm or an absorbance scan was performed in 96-well plates.

Sandwich-ELISA

ELISA was conducted according to protocols of BD Biosciences OptEIA™ (USA) and after previously published procedures.[319] The IL-2 capture antibody was incubated on 96 well microplates at 4 °C overnight. After a washing step with washing buffer (1xPBS supplemented with 0.05% Tween-20) to remove residual capture antibody, unspecific epitopes were saturated by incubation of blocking buffer (1xPBS supplemented with 10% fetal calf serum (FCS)) for 1 h. Afterwards, the nanocapsules with different IL-2 modifications were incubated on the prepared microplates at dilutions ranging from 1:1000 to 1:10 000 000 for 2 h at room temperature. After washing the microplates again with washing buffer, an enzyme-linked detection antibody (1:250) and the streptavidin horseradish peroxidase reagent (Streptavidin-HRP conjugate 1:250) were added and the mixture was incubated for again 1 h at room temperature. Then, plates were washed again with washing buffer to remove residual reagents and the substrate 3,3',5,5'-tetramethylbenzidin was added. After 20-30 min, enzymatic activity was stopped by addition of stop solution (1 M H_3PO_4 and 1 N H_2SO_4) and extinction was detected with a photometer (Medel 450, Bio-Rad Laboratories, München, Germany Software: KC Junior Bio-Tek Instruments GmbH, Bad Friedrichshall, Germany) at 450 nm.

VI. Summary and conclusion

In this thesis aqueous core NCs were illuminated from various perspectives.

The first perspective elucidates the reproducibility of the NCs synthesis on HES-NCs. HES-NCs were synthesized by inverse miniemulsion using an ultrasonic tip or microfluidics for homogenization. It has to be considered using the same equipment and to make sure that there are no quality variations for the used reactants and detergents. Toluene diisocyanate (TDI) was used as crosslinker in order to generate a dense polymeric shell exhibiting a mixture of polyurethane and polyurea bonds. The size distribution of 21 different HES-NCs after reaction in cyclohexane and 28 different redispersed HES-NCs in SDS solution obtained at a scattering angle of 90° were averaged and revealed a hydrodynamic diameter of 292 ± 67 nm for capsules in cyclohexane and 222 ± 69 nm for aqueous dispersions. These values were comparable with sizes obtained by multiangle light scattering measurements, pointing that 90° DLS measurements are suitable as a quality control of capsules prepared by the same procedure and redispersed from the same batch. Using a colorimetric assay, residual SDS on the capsules was detected and removal of SDS to concentrations lower than 0.01 wt% by washing was assured. Next to the determination of the size, light scattering can also be utilized to determine the solid content of NCs of the same batch. It was verified that the dyes SR101 and Cy5 Oligo stay inside the capsules when encapsulated. Using ToF-SIMS and the fluorescent fluorescamine assay, amino-containing species on the NCs shell were confirmed and quantified for capsules containing a shell with a particular thickness by using an increased crosslinker concentration.

HES-NCs were then surface modified using DBCO-PEG-NHS ester to enable copper-free click reaction on the capsule surface. It was shown that fluorescence intensity of DBCO modified capsules increased upon addition of anthracene azide in a time-dependent manner, indicating functionalization of the HES-NCs with DBCO and subsequent click reaction. In addition, limit of detection and limit of blank were determined for 20 samples functionalized in the same manner and DBCO groups per mL dispersion, per NCs and per nm^2 were identified and compared with each other. It was demonstrated, that HES-NCs were functionalized with DBCO in a concentration-dependent manner. The pH value did not play a significant role during binding, however, it was shown that fluorescence intensity of the DBCO-anthracene conjugate decreases in a time-dependent manner.

In the further synthesis course, the DBCO modified NCs were reacted with azide functionalized biomolecules. The modification of interleukin-2 (IL-2) using an azide-terminating NHS ester could be verified by MALDI-ToF and the protein structure was examined by nanoDSF. The amount of IL-2 on the capsule surface was qualitatively determined by flow cytometry and FCCS, while it was quantified by ELISA. A concentration-dependent uptake into CTLL-2 cells in dependency on the IL-2 loading on the NCs was achieved. Enabling a controlled uptake of IL-2 modified HES-NCs in dependency of the IL-2 loading on the surface is important to target specific subpopulations of T cells revealing a specific sensitivity towards IL-2 such as regulatory T cells (Tregs).

Using the same synthesis setup, different azide-modified carbohydrates were bound to the NCs surface and the binding efficiency was verified by determination of residual DBCO groups on the capsules' surface and by HPLC analysis of the supernatant after washing. HES-NCs which were functionalized with a glycodendron structure and trimannose were taken up by immature dendritic cells (DCs) to a higher extent than NCs functionalized with mannose or a disaccharide derivative.

Furthermore, different blocking experiments using specific antibodies against DC-SIGN and CD206, revealed that the capsules underwent receptor-mediated uptake.

After demonstrating that HES-NCs were reproducibly endowed with different biological functions, in the second Chapter the focus was set on protein NCs. Therefore, the size distribution, chemical constitutions, as well as surface charge and SDS content of different protein and HES-NCs were compared with each other. It was shown, that protein NCs revealed a broader size distribution after redispersion into aqueous phase than HES-NCs, while in organic phase the distribution was comparable. Furthermore, FTIR experiments revealed predominantly polyurea groups for protein NCs while the HES-NCs shell indicated a mixture of polyurethane and polyurea groups. It was shown that the isoelectric point for protein NCs at specific concentrations were comparable with the isoelectric point determined for the pure protein. By means of a fluorescamine assay the amino content of BSA, HSA and OVA proteins were determined and compared to the amino content found for the corresponding protein capsules. The results indicated that OVA-NCs exhibit an increased number of amino groups detectable on the NCs although showing a reduced percentage of detectable lysines in the corresponding protein solution. These findings suggested different protein constitutions within capsules for different proteins. Similar as HES-NCs, the protein NCs could be further modified with DBCO NHS ester. In further experiments, polystyrene nanoparticles (PS-NPs) were endowed with specific numbers of amino groups which could be demonstrated by enhanced detection of amino groups by fluorescamine assay with increased addition of precursor. In subsequent experiments showing DBCO binding to the functionalized and non-functionalized PS-NPs, it was clearly demonstrated that DBCO NHS ester binds significantly more to amino-functionalized NPs than to pristine PS-NPs. However, in a subsequent binding of azide-functionalized BSA by copper-free click reaction to the DBCO modified PS-NPs it was not verified that binding happens predominantly at PS-NPs which were unambiguously modified with DBCO, but also pristine PS-NPs onto which DBCO was just adsorbed revealed similar concentrations of bound BSA. Nevertheless, ITC experiments revealed enthalpy and entropy differences for the reaction of azidated BSA on DBCO modified PS-NPs in comparison to PS-NPs without DBCO groups on the surface, indicating a higher calculated number of bound BSA molecules to the PS-DBCO NPs than to PS-NH_2 NPs.
The results from Chapter A and B underline that size, charge, adsorbed molecules, the amount of surface groups as well as the binding constitution plays a significant role for understanding targeted delivery of NCs with a particularly designed surface.

Chapter C reveals that not only specific surface groups have an impact on cells, but also the capsule shell itself can bear particular properties influencing cellular uptake. Using a bioorthogonal crosslinking strategy by employing reactions on aromatic amino acids on BSA, HSA and OVA by the use of a triazolinedione (TAD) crosslinker, NCs with low polydispersity were synthesized. Encapsulation of magnetite NPs demonstrated high loading capacity of the corresponding capsules. Comparison to protein NCs crosslinked with TDI, revealed no significant differences in physicochemical properties such as size, PDI and zeta potential.

Interestingly, cell uptake experiments with and without human serum (HS) incubation of the corresponding capsules revealed slight differences in uptake behavior of HeLa cells towards the capsules. Without HS incubation a higher uptake of TAD crosslinked NCs in a time-dependent manner was observed, while no particular difference in uptake behavior was confirmed when both capsule types were incubated with HS prior to incubation with the cells. The different uptake behavior is caused by different surface constitutions of the different protein capsules. On the one hand they are based on the exhibition of different protein structures on the capsule surface since TAD reacts with aromatic amino acids present in the interior of the proteins, while TDI mostly reacts with lysines, pointing to the exterior of the proteins. On the other hand, the properties are furthermore based on different polarities of the used crosslinkers. In the protein corona profile of all capsules just slight differences between TAD and TDI crosslinked NCs were observed. TAD crosslinked NCs showed increased shares of proteins of the coagulation cascade, while at the same time the percentage for immunoglobulins was reduced in comparison to TDI crosslinked NCs. These marginal differences were not reflected in the NC's uptake behavior after HS incubation. These findings underline that cell uptake can also be influenced by the NCs shell itself without the selective binding of targeting moieties.

The last perspective is taken from the inside of the NCs in Chapter D. It could be shown that nanoplatelets (NPLs) exhibiting high brightness in aqueous medium, due to an amphiphilic polymer coating, were encapsulated in different concentrations into BSA-NCs, without disturbing the capsule formation. It was shown that the NPLs enabled quenching of a dye bound to the NCs surface, indicating close proximity of the NPLs to the NCs shell and therefore confirmed encapsulation. The NCs which were labeled with the NPLs in a ratio of up to five NPLs per NCs were taken up by macrophages in a concentration- and time-dependent manner. CLEM (correlative light and electron microscopy) revealed unambiguous localization of the BSA-NCs in endolysosomal pathways inside the macrophages, enabling visualization of trafficking routes of nanocarriers inside cells. In this way three different terminal destinations of the nanomaterial inside macrophages were determined. The findings are important to understand future work on metabolic pathways and successful delivery of drugs to its destinations.

The Chapters presented in this work highlight different important aspects of nanocarriers for drug delivery. They illustrate the use of different biocompatible materials and analyze the reproducibility of individual steps. Moreover, this work demonstrates that targeting is not only necessarily achieved by selective binding of targeting moieties but also by different surface constitutions obtained by different protein crosslinking. In the last part a possibility to analyze the fate of the nanocarrier inside a biological surrounding was presented. All these findings are important to further develop and understand the synthesis and impact nanocarriers have as drug delivery vehicles.

VII. Appendix

VII. 1. List of abbreviations

a.u.	arbitrary unit
AEMH	aminoethyl methacrylate hydrochloride
AIBN	2,2’-azobisisobutyronitrile
APC	antigen-presenting cell
approx.	approximately
APTMS	(3-aminopropyl) trimethoxysilane
BSA	bovine serum albumin
CD	cluster of differentiation
CD spectroscopy	circular dichroism spectroscopy
CLEM	correlative light and electron microscopy
CLSM	confocal laser scanning microscopy
CMC	critical micelle concentration
CRD	carbohydrate recognition domain
DBCO	dibenzocyclooctyne
DCC	dicyclohexyl carbodiimide
DC-SIGN	dendritic cell-specific intercellular adhesion molecule-3-grabbin non-integrin
DMEM	Dulbecco’s modified eagle’s medium
DLS	dynamic light scattering
DMF	dimethyl formamide
DMSO	dimethyl sulfoxide
DPBS	Dulbecco’s phosphate-buffered saline
EAS	electrophilic aromatic substitution
EDG	electron-donating group
EDTA	ethylenediaminetetraacetic acid
EE	early endosome
EL	endolysosome
ELISA	enzyme-linked immunosorbent assay
Eq.	equivalents
FACS	fluorescence activated cell sorting
FBS	fetal bovine serum
FCS	fluorescence correlation spectroscopy
FCCS	fluorescence cross correlation spectroscopy

FITC	fluorescein isothiocyanate
FTIR	fourier-transform infrared spectroscopy
G	Gibbs-Energy
H	enthalpy
h	hour
hDC	human dendritic cell
HES	hydroxylethyl starch
HPLC	high-performance liquid chromatography
HS	human serum
HSA	human serum albumin
HSQC	heteronuclear single quantum correlation
IL	interleukin
ITC	isothermal titration calorimetry
JAK	janus kinase
K_a	binding affinity
kDa	kilodalton
LC-MS	liquid-chromatography mass spectrometry
LE	late endosome
LoB	limit of blank
LoD	limit of detection
NC	nanocapsule
MALDI-ToF	matrix-assisted laser desorption ionization time-of-flight
MFI	median fluorescence intensity
MHC	major histocompatibility complex
M_w	molecular weight
MWCO	molecular weight cut-off
n	stoichiometric ratio
nano-DSF	nano differential scanning fluorimetry
NHS	*N*-hydroxysuccinimid
nm	nanometer
NMR	nuclear magnetic resonance
NP	nanoparticle
NPL	nanoplatelet
OVA	ovalbumin
o/w	oil in water

PDI	polydispersity index
P(E/B-*b*-EO)	poly((ethylene-*co*-butylene)-*b*-(ethylene oxide)
PEG	polyethylene glycol
PS	polystyrene
R	gas constant
R_f	retarding-front
R_h	hydrodynamic radius
S	entropy
SDS	sodium dodecyl sulfate
SDS-PAGE	sodium dodecyl sulfate polyacrylamide gel electrophoresis
SEM	scanning electron microscopy
SN	supernatant
SpAAC	strain-promoted azide-alkyne cycloaddition
SR101	sulforhodamine 101
STAT	signal transducers and activators of transcription
STD	standard deviation
t	time
TCR	T cell receptor
T_m	melting point
TAD	1,2,4-triazoline-3,5-dione
TDI	toluene-2,4-diisocyanate
TEM	transmission electron microscopy
TFA	trifluoro acetic acid
TLR	toll-like receptor
TMS	tetramethyl silane
ToF-SIMS	time-of-flight secondary ion mass spectrometry
Treg	regulatory T cell
Trp	tryptophan
w/o	water in oil

VII. 2. Additional data and spectra

VII. 2.1 Optical images of covered glass substrates measured by ToF-SIMS

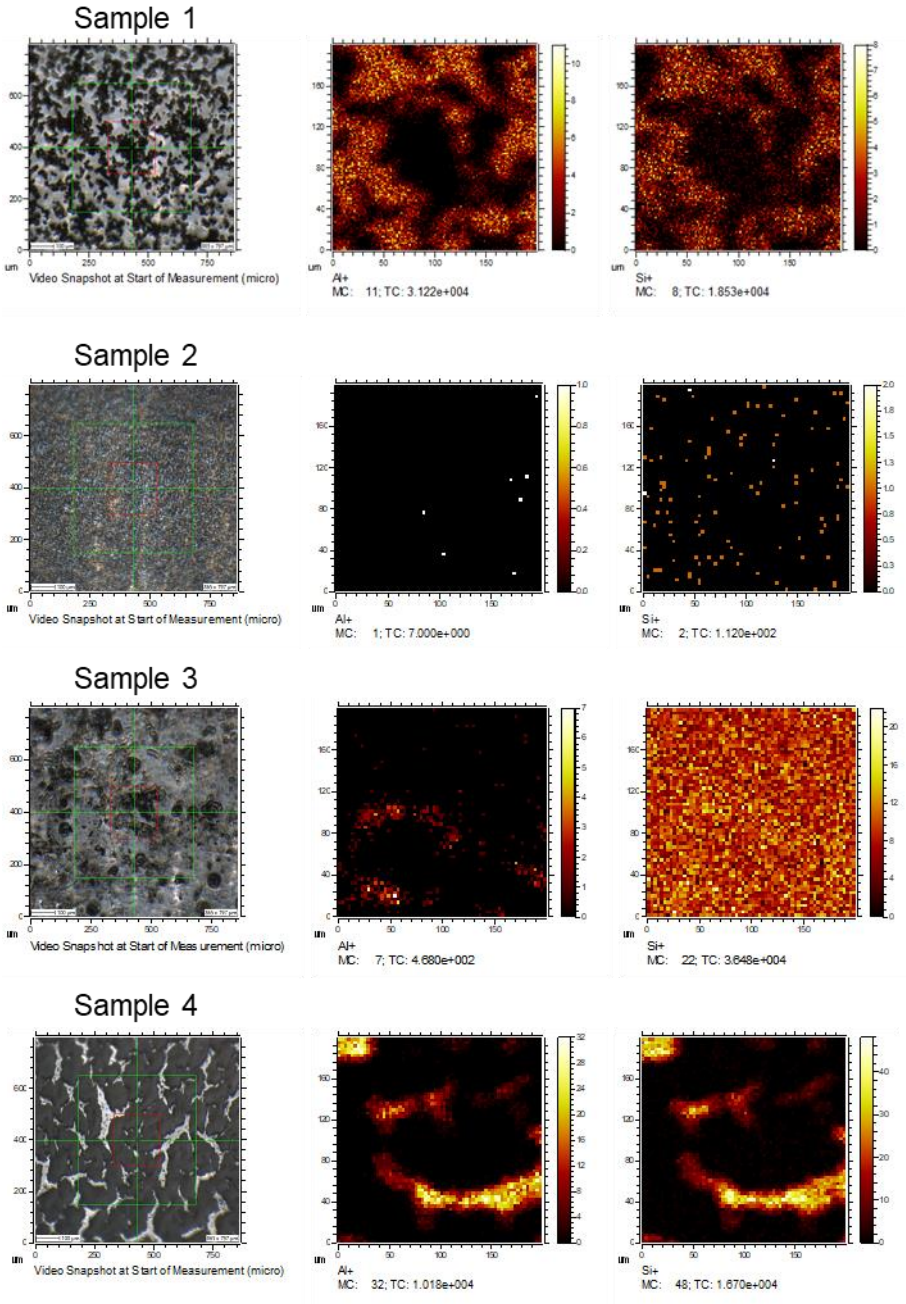

Figure 103: Optical images ("Video Snapshots") of the glass substrates with the samples 1-4 and the corresponding chemical surface images revealing the signal distributions for Al^+ and Si^+ (positive ion mode) measured and evaluated by [redacted]. Red squares in the optical images indicate the position of the ToF-SIMS imaging analyses. TC: total counts in image, MC: Maximum counts in pixel.

VII. 2.2 CTLL-2 assay of HES-NCs modified with different IL-2 ratios

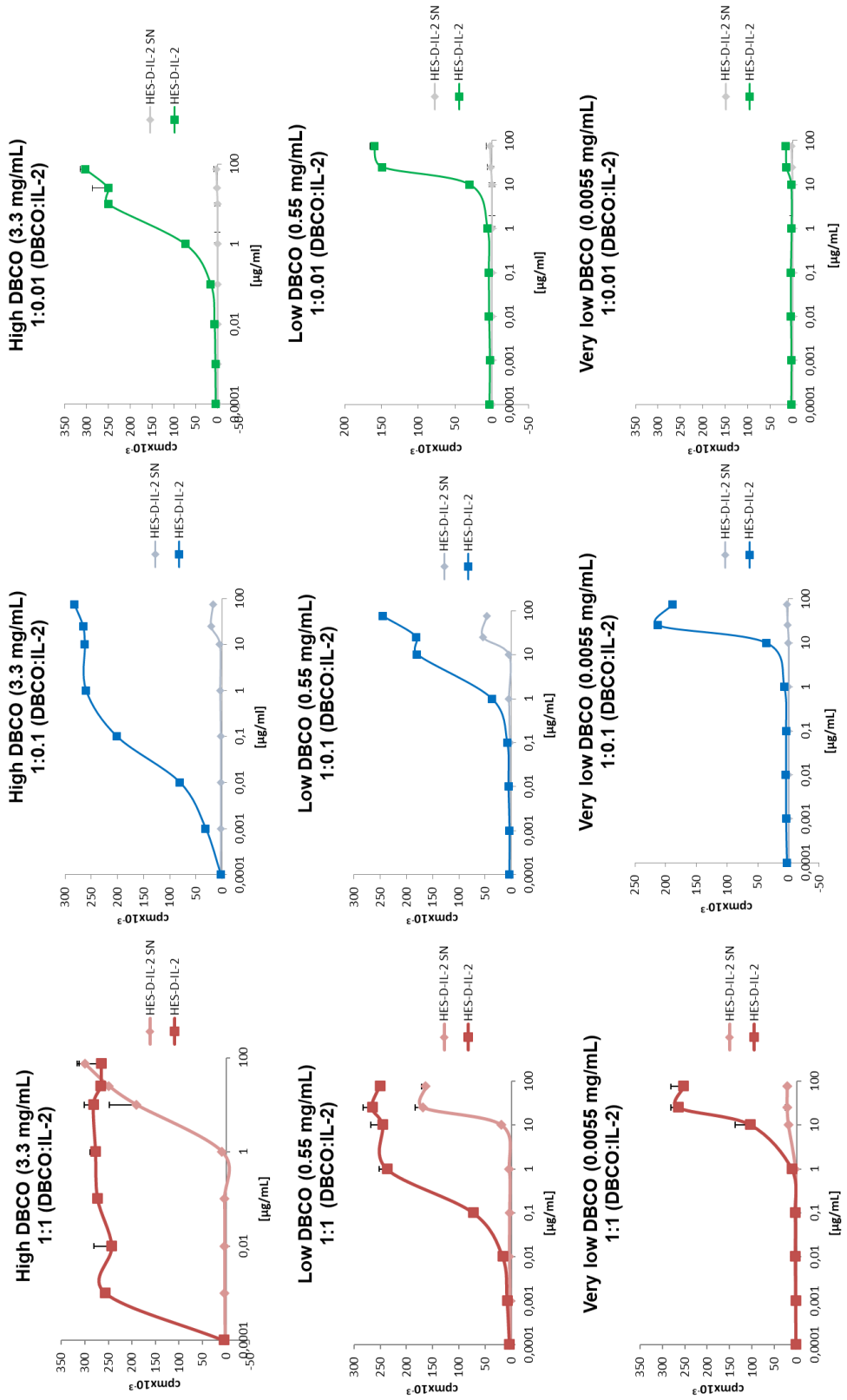

Figure 104: Counted radioactivity (counts per min) of CTLL-2 cell proliferation plotted against added NC concentration in µg/mL. The NC samples are compared to the respective supernatants (SN) after washing, demonstrating low IL-2 concentrations in the supernatant. Experiment performed and evaluated by [redacted]

VII. 2.3 NMR spectra

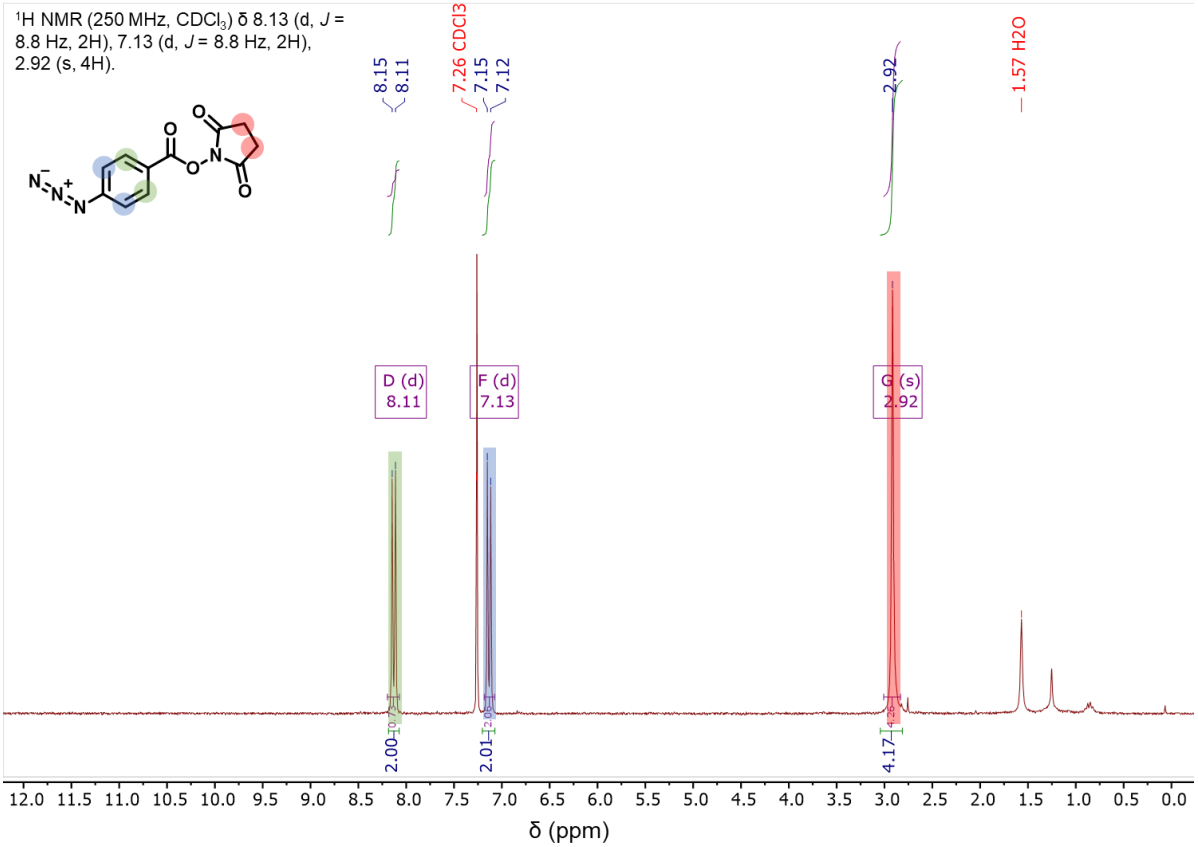

Figure 105: ^{1}H NMR of 4-Azidobenzoyl-*N*-hydroxysuccinimide (250 MHz, 298 K, $CDCl_3$).

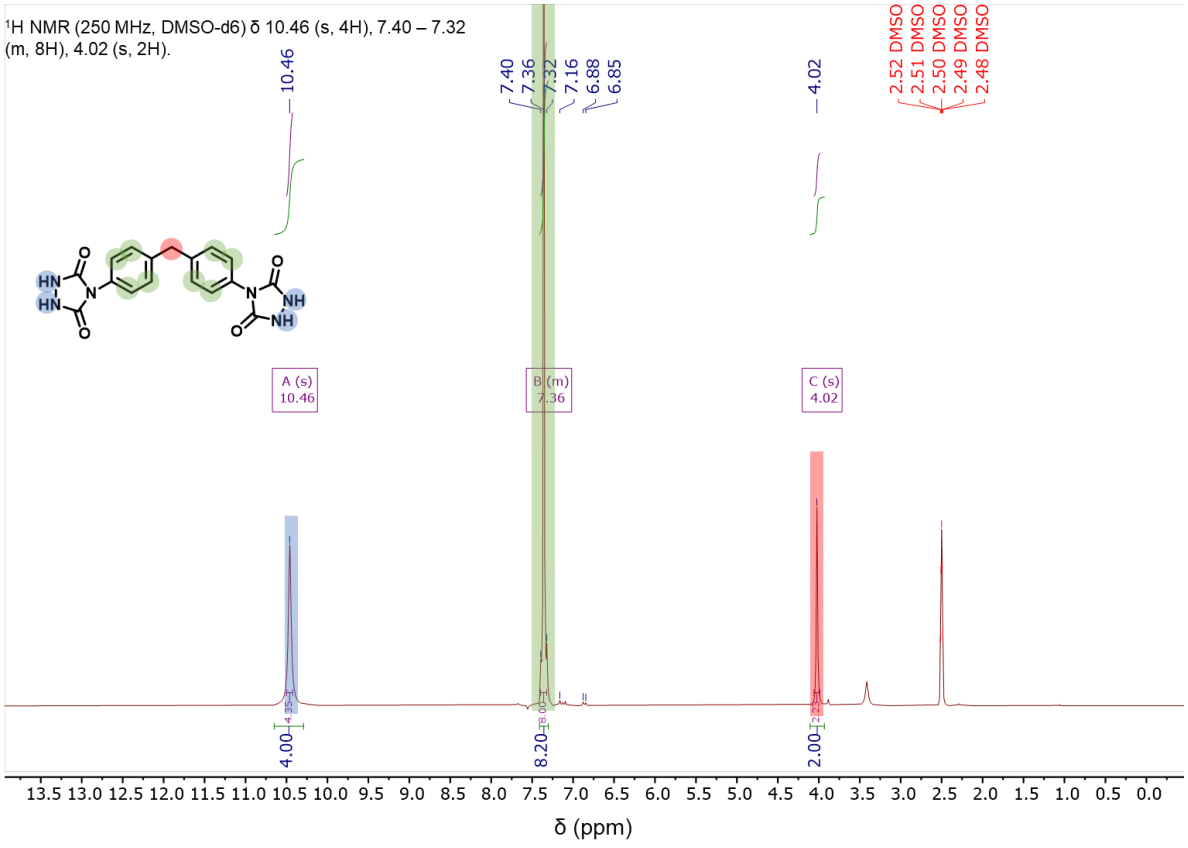

Figure 106: ^{1}H NMR of 4,4'-(4,4'-diphenylmethylene)-bis-urazol (250 MHz,298 K, DMSO-d6).

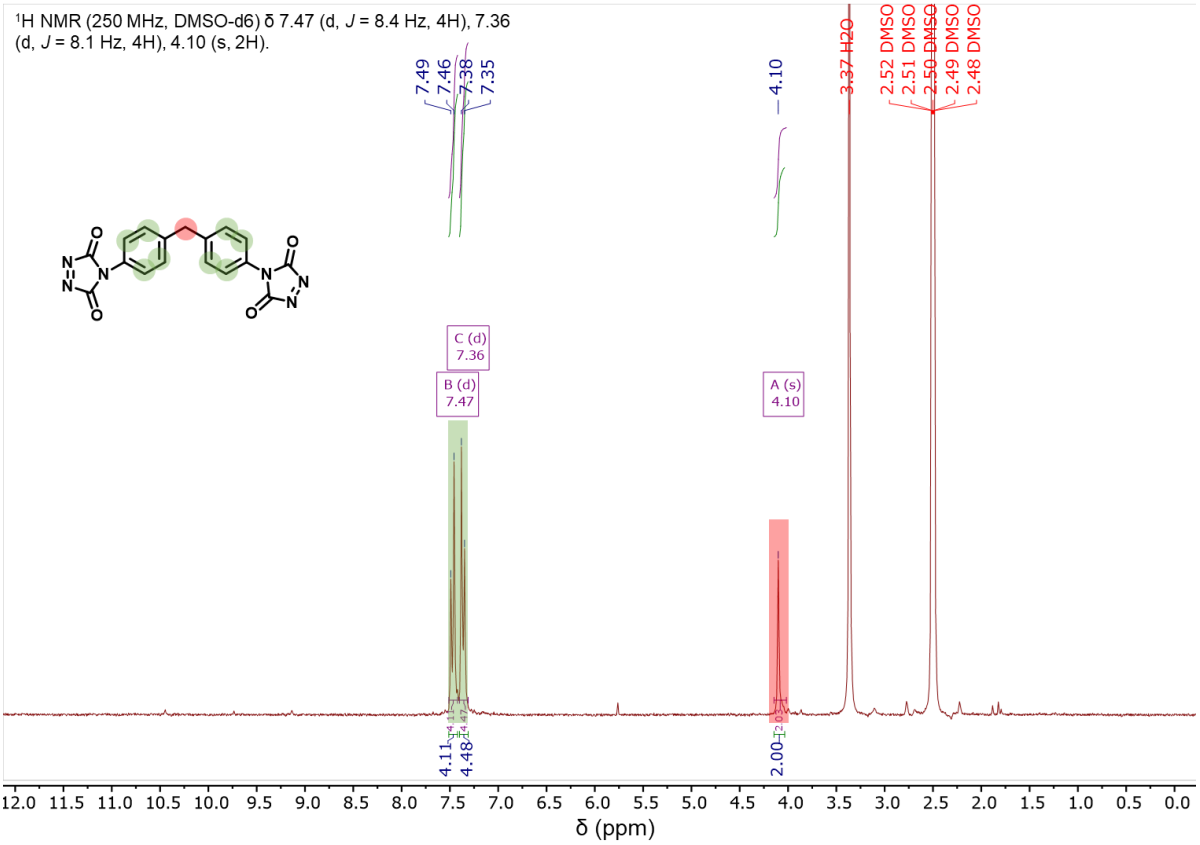

Figure 107: [1]H NMR of 4,4'-(4,4'-diphenylmethylene)-triazolinedione (250 MHz,298 K, DMSO-d6).

Danksagung

Lebenslauf

VIII. Bibliography

[1] "The top 10 causes of death - World Health Organization (WHO)," can be found under https://www.who.int/news-room/fact-sheets/detail/the-top-10-causes-of-death#:~:text=The top global causes of,birth asphyxia and birth trauma%2C, 2020, date accessed: 21.01.21.

[2] H. Ritchie, "Causes of Death," can be found under https://ourworldindata.org/causes-of-death, 2018, date accessed: 21.01.21.

[3] J. S. Rana, S. S. Khan, D. M. Lloyd-Jones, S. Sidney, *J. Gen. Intern. Med.* **2020**, *23*, 1–2.

[4] R. L. Siegel, K. D. Miller, A. Jemal, *CA. Cancer J. Clin.* **2020**, *70*, 7–30.

[5] S. Riedel, *Baylor Univ. Med. Cent. Proc.* **2005**, *18*, 21–25.

[6] W. K. Decker, R. F. da Silva, M. H. Sanabria, L. S. Angelo, F. Guimarães, B. M. Burt, F. Kheradmand, S. Paust, *Front. Immunol.* **2017**, *8*, 829.

[7] P. Dobosz, T. Dzieciątkowski, *Front. Immunol.* **2019**, *10*, 2965.

[8] G. Edgue, R. M. Twyman, V. Beiss, R. Fischer, M. Sack, *WIREs Nanomedicine and Nanobiotechnology* **2017**, *9*, e1462.

[9] A. J. Grillo-López, C. A. White, C. Varns, D. Shen, A. Wei, A. McClure, B. K. Dallaire, *Semin. Oncol.* **1999**, *26*, 66–73.

[10] D. Pardoll, J. Allison, *Nat. Med.* **2004**, *10*, 887–892.

[11] K. Tsumoto, Y. Isozaki, H. Yagami, M. Tomita, *Immunotherapy* **2019**, *11*, 119–127.

[12] I. Mellman, G. Coukos, G. Dranoff, *Nature* **2011**, *480*, 480–489.

[13] R. N. Amaria, A. Reuben, Z. A. Cooper, J. A. Wargo, *ImmunoTargets Ther.* **2015**, *4*, 79–89.

[14] J. M. Wrangle, A. Patterson, C. B. Johnson, D. J. Neitzke, S. Mehrotra, C. E. Denlinger, C. M. Paulos, Z. Li, D. J. Cole, M. P. Rubinstein, *J. Interf. Cytokine Res.* **2018**, *38*, 45–68.

[15] S. A. Rosenberg, B. S. Packard, P. M. Aebersold, D. Solomon, S. L. Topalian, S. T. Toy, P. Simon, M. T. Lotze, J. C. Yang, C. A. Seipp, C. Simpson, C. Carter, S. Bock, D. Schwartzentruber, J. P. Wei, D. E. White, *N. Engl. J. Med.* **1988**, *319*, 1676–1680.

[16] "Milestones in cancer," can be found under https://www.nature.com/immersive/d42859-020-00083-8/index.html, 2020, date accessed: 13.01.21.

[17] S. Joshi, D. L. Durden, *J. Oncol.* **2019**, *2019*, 5245034.

[18] B. Seliger, *Front. Immunol.* **2019**, *10*, 999.

[19] Z. Li, S. Tan, S. Li, Q. Shen, K. Wang, *Oncol Rep* **2017**, *38*, 611–624.

[20] A. D. Bangham, M. M. Standish, J. C. Watkins, *J. Mol. Biol.* **1965**, *13*, 238-IN27.

[21] A. Torang, P. Gupta, D. J. Klinke, *BMC Bioinformatics* **2019**, *20*, 433.

[22] D. D. Chaplin, *J. Allergy Clin. Immunol.* **2010**, *125*, S3–S23.

[23] B. Alberts, A. Johnson, J. Lewis, E. Al., in Molecular Biology of the Cell, 4th Ed., New York: Garland Science, **2002**.

[24] J. K. Actor, in Introductory Immunology Basic Concepts for Interdisciplinary Applications (Ed.: J.K. Actor), Academic Press, Amsterdam, **2014**, pp. 1–15.

[25] E. J. Moticka, in A Historical Perspective on Evidence-Based Immunology (Ed.: E. Moticka), Elsevier, Amsterdam, **2016**, pp. 235–242.

[26] A. J. Filiano, S. P. Gadani, J. Kipnis, *Nat. Rev. Neurosci.* **2017**, *18*, 375–384.

[27] D. I. Godfrey, A. P. Uldrich, J. Mccluskey, J. Rossjohn, D. B. Moody, *Nat Immunol* **2015**, *16*, 1114–1123.

[28] J. O'Keeffe, A. P. Moran, *Helicobacter* **2008**, *13*, 1–19.

[29] T. R. Malek, A. L. Bayer, *Nat. Rev. Immunol.* **2004**, *4*, 665–674.

[30] W. Liao, J.-X. Lin, W. J. Leonard, *Immunity* **2013**, *38*, 13–25.

[31] M. C. Mingari, F. Gerosa, G. Carra, R. S. Accolla, A. Moretta, R. H. Zubler, T. A. Waldmann, L. Moretta, *Nature* **1984**, *312*, 641–643.

[32] S. C. McKarns, R. H. Schwartz, *J. Immunol.* **2008**, *181*, 1272–1281.

[33] G. C. Sim, L. Radvanyi, *Cytokine Growth Factor Rev.* **2014**, *25*, 377–390.

[34] H. P. Kim, J. Imbert, W. J. Leonard, *Cytokine Growth Factor Rev.* **2006**, *17*, 349–366.

[35] X. Zhang, S. Sun, I. Hwang, D. F. Tough, J. Sprent, *Immunity* **1998**, *8*, 591–599.

[36] L. Bani, D. David, J. L. Moreau, A. Cayota, T. Nakarai, J. Ritz, J. Thèze, *Int. Immunol.* **1997**, *9*, 573–580.

[37] G. L. Beatty, W. L. Gladney, *Clin. Cancer Res.* **2015**, *21*, 687 LP – 692.

[38] K. Oleinika, R. J. Nibbs, G. J. Graham, A. R. Fraser, *Clin. Exp. Immunol.* **2013**, *171*, 36–45.

[39] W. Zou, *Nat. Rev. Immunol.* **2006**, *6*, 295–307.

[40] C. Ménétrier-Caux, T. Curiel, J. Faget, M. Manuel, C. Caux, W. Zou, *Target. Oncol.* **2012**, *7*, 15–28.

[41] H. Yu, D. Pardoll, R. Jove, *Nat. Rev. Cancer* **2009**, *9*, 798–809.

[42] M. Kortylewski, M. Kujawski, T. Wang, S. Wei, S. Zhang, S. Pilon-Thomas, G. Niu, H. Kay, J. Mulé, W. G. Kerr, R. Jove, D. Pardoll, H. Yua, *Nat. Med.* **2005**, *11*, 1314–1321.

[43] Y. Matsumura, T. Kobayashi, K. Ichiyama, R. Yoshida, M. Hashimoto, T. Takimoto, K. Tanaka, T. Chinen, T. Shichita, T. Wyss-Coray, K. Sato, A. Yoshimura, *J. Immunol.* **2007**, *179*, 2170 LP – 2179.

[44] H. Yu, M. Kortylewski, D. Pardoll, *Nat. Rev. Immunol.* **2007**, *7*, 41–51.

[45] R. Garcia, T. L. Bowman, G. Niu, H. Yu, S. Minton, C. A. Muro-Cacho, C. E. Cox, R. Falcone, R. Fairclough, S. Parsons, A. Laudano, A.Gazit, A. Levitzki, A. Kraker, R. Jove, *Oncogene* **2001**, *20*, 2499–2513.

[46] R. Fagard, V. Metelev, I. Souissi, F. Baran-Marszak, *JAK-STAT* **2013**, *2*, e22882–e22882.

[47] R. Buettner, L. B. Mora, R. Jove, *Clin. Cancer Res.* **2002**, *8*, 945 LP – 954.

[48] T. A. Patente, M. P. Pinho, A. A. Oliveira, G. C. M. Evangelista, P. C. Bergami-Santos, J. A. M. Barbuto, *Front. Immunol.* **2019**, *9*, 3176.

[49] D. Alvarez, E. H. Vollmann, U. H. von Andrian, *Immunity* **2008**, *29*, 325–342.

[50] C. Reis e Sousa, *Nat. Rev. Immunol.* **2006**, *6*, 476–483.

[51] H. Hemmi, O. Takeuchi, T. Kawai, T. Kaisho, S. Sato, H. Sanjo, M. Matsumoto, K. Hoshino, H. Wagner, K. Takeda, S. Akira, *Nature* **2000**, *408*, 740–745.

[52] S. Akira, H. Hemmi, *Immunol. Lett.* **2003**, *85*, 85–95.

[53] Y. Van Kooyk, T. B. H. Geijtenbeek, *Nat. Rev. Immunol.* **2003**, *3*, 697–709.

[54] U. Švajger, M. Anderluh, M. Jeras, N. Obermajer, *Cell. Signal.* **2010**, *22*, 1397–1405.

[55] M. Mammen, S. K. Choi, G. M. Whitesides, *Angew. Chemie - Int. Ed.* **1998**, *37*, 2754–2794.

[56] A. Holla, A. Skerra, *Protein Eng. Des. Sel.* **2011**, *24*, 659–669.

[57] T. R. Mosmann, L. Li, S. Sad, *Semin. Immunol.* **1997**, *9*, 87–92.

[58] S. Halle, O. Halle, R. Förster, *Trends Immunol.* **2017**, *38*, 432–443.

[59] Y. D. Mahnke, T. M. Brodie, F. Sallusto, M. Roederer, E. Lugli, *Eur. J. Immunol.* **2013**, *43*, 2797–2809.

[60] J. Borst, T. Ahrends, N. Bąbała, C. J. M. Melief, W. Kastenmüller, *Nat. Rev. Immunol.* **2018**, *18*, 635–647.

[61] J. Peng, Z. Yu, L. Xue, J. Wang, J. Li, D. Liu, Q. Yang, Y. Lin, *Mol. Med. Rep.* **2018**, *17*, 5860–5868.

[62] J. Copier, A. G. Dalgleish, C. M. Britten, L. H. Finke, G. Gaudernack, S. Gnjatic, K. Kallen, R. Kiessling, M. Schuessler-Lenz, H. Singh, J. Talmadge, H. Zwierzina, L. Håkansson, *Eur. J. Cancer* **2009**, *45*, 1424–1431.

[63] L. Gravitz, *Nature* **2013**, *504*, S1–S1.

[64] C. Robert, *Nat. Commun.* **2020**, *11*, 10–12.

[65] S. J. Oiseth, M. S. Aziz, *J Cancer Metastasis Treat* **2017**, *3*, 250–261.

[66] P. Darvin, S. M. Toor, V. Sasidharan Nair, E. Elkord, *Exp. Mol. Med.* **2018**, *50*, 1–11.

[67] L. Labanieh, R. G. Majzner, C. L. Mackall, *Nat. Biomed. Eng.* **2018**, *2*, 377–391.

[68] A. P. Rapoport, E. A. Stadtmauer, G. K. Binder-Scholl, O. Goloubeva, D. T. Vogl, S. F. Lacey, A. Z. Badros, A. Garfall, B. Weiss, J. Finklestein, I. Kulikovskaya, S. K. Sinha, S. Kronsberg, M. Gupta, S. Bond, L. Melchiori, J. E. Brewer, A. D. Bennett, A. B. Gerry, N. J. Pumphrey, D. Williams, H. K. Tayton-Martin, L. Ribeiro, T. Holdich, S. Yanovich, N. Hardy, J. Yared, N. Kerr, S. Philip, S. Westphal, D. L. Siegel, B. L. Levine, B. K. Jakobsen, M. Kalos, C. H. June , *Nat. Med.* **2015**, *21*, 914–921.

[69] P. F. Robbins, R. A. Morgan, S. A. Feldman, J. C. Yang, R. M. Sherry, M. E. Dudley, J. R. Wunderlich, A. V Nahvi, L. J. Helman, C. L. Mackall, U. S. Kammula, M. S. Hughes, N. P. Restifo, M. Raffeld, C.-C. R. Lee, C. L. Levy, Y. F. Li, M. El-Gamil, S. L. Schwarz, C. Laurencot, S. A. Rosenberg, *J. Clin. Oncol.* **2011**, *29*, 917–924.

[70] M. Kalos, *J. Transl. Med.* **2011**, *9*, 138.

[71] K. Palucka, J. Banchereau, *Nat. Rev. Cancer* **2012**, *12*, 265–277.

[72] M. S. Diamond, M. Kinder, H. Matsushita, M. Mashayekhi, G. P. Dunn, J. M. Archambault, H. Lee, C. D. Arthur, J. M. White, U. Kalinke, K. M. Murphy, R. D. Schreiber, *J. Exp. Med.* **2011**, *208*, 1989–2003.

[73] K. Palucka, J. Banchereau, *Immunity* **2013**, *39*, 38–48.

[74] N. Leffers, A. J. A. Lambeck, M. J. M. Gooden, B.-N. Hoogeboom, R. Wolf, I. E. Hamming, B. G. Hepkema, P. H. B. Willemse, B. H. W. Molmans, H. Hollema, J. W. Drijfhout, W. J. Sluiter, A. R. P. M. Valentijn, L. M. Fathers, J. Oostendorp, A. G. J. van der Zee, C. J. Melief, S. J. van der Burg, T. Daemen, H. W. Nijman, *Int. J. Cancer* **2009**, *125*, 2104–2113.

[75] T. W. Dubensky, S. G. Reed, *Semin. Immunol.* **2010**, *22*, 155–161.

[76] R. L. Coffman, A. Sher, R. A. Seder, *Immunity* **2010**, *33*, 492–503.

[77] L. Bonifaz, D. Bonnyay, K. Mahnke, M. Rivera, M. C. Nussenzweig, R. M. Steinman, *J. Exp. Med.* **2002**, *196*, 1627–1638.

[78] A. Kretz-Rommel, F. Qin, N. Dakappagari, R. Torensma, S. Faas, D. Wu, K. S. Bowdish, *J. Immunother.* **2007**, *30*, 715–726.

[79] Y. Gu, X. Zhao, X. Song, *Acta Pharmacol. Sin.* **2020**, *41*, 959–969.

[80] R. A. Madan, E. S. Antonarakis, C. G. Drake, L. Fong, E. Y. Yu, D. G. McNeel, D. W. Lin, N. N. Chang, N. A. Sheikh, J. L. Gulley, *JNCI J. Natl. Cancer Inst.* **2020**, *112*, 562–573.

[81] A. S. Cheung, D. J. Mooney, *Nano Today* **2015**, *10*, 511–531.

[82] D. S. Chen, I. Mellman, *Immunity* **2013**, *39*, 1–10.

[83] D. E. Owens, N. A. Peppas, *Int. J. Pharm.* **2006**, *307*, 93–102.

[84] C. H. Kim, S. G. Lee, M. J. Kang, S. Lee, Y. W. Choi, *J. Pharm. Investig.* **2017**, *47*, 203–227.

[85] "Polymer Properties Database," can be found under https://polymerdatabase.com/polymer chemistry/Dendrimers.html, date accessed: 13.01.21.

[86] K. Madaan, S. Kumar, N. Poonia, V. Lather, D. Pandita, *J. Pharm. Bioallied Sci.* **2014**, *6*, 139–150.

[87] D. L. Patton, Y. T. Cosgrove Sweeney, T. D. McCarthy, S. L. Hillier, *Antimicrob. Agents Chemother.* **2006**, *50*, 1696–1700.

[88] A. Janaszewska, J. Lazniewska, P. Trzepiński, M. Marcinkowska, B. Klajnert-Maculewicz, *Biomolecules* **2019**, *9*, 330.

[89] R. Jenjob, T. Phakkeeree, F. Seidi, M. Theerasilp, D. Crespy, *Macromol. Biosci.* **2019**, *19*, e1900063.

[90] S. Hornig, T. Heinze, C. R. Becer, U. S. Schubert, *J. Mater. Chem.* **2009**, *19*, 3838–3840.

[91] C. He, H. Yue, L. Xu, Y. Liu, Y. Song, C. Tang, C. Yin, *Acta Biomater.* **2020**, *103*, 213–222.

[92] M. J. Mitchell, M. M. Billingsley, R. M. Haley, M. E. Wechsler, N. A. Peppas, R. Langer, *Nat. Rev. Drug Discov.* **2020**, *20*, 101-124.

[93] S. Abalde-Cela, P. Taladriz-Blanco, M. G. de Oliveira, C. Abell, *Sci. Rep.* **2018**, *8*, 2440.

[94] S. M. Dadfar, K. Roemhild, N. I. Drude, S. von Stillfried, R. Knüchel, F. Kiessling, T. Lammers, *Adv. Drug Deliv. Rev.* **2019**, *138*, 302–325.

[95] A. C. Anselmo, S. Mitragotri, *Bioeng. Transl. Med.* **2019**, *4*, 1–16.

[96] A. Hatefi, B. Amsden, *Pharm. Res.* **2002**, *19*, 1389–1399.

[97] L. Zhang, F. X. Gu, J. M. Chan, A. Z. Wang, R. S. Langer, O. C. Farokhzad, *Clin. Pharmacol. Ther.* **2008**, *83*, 761–769.

[98] E. Nance, C. Zhang, T.-Y. Shih, Q. Xu, B. S. Schuster, J. Hanes, *ACS Nano* **2014**, *8*, 10655–10664.

[99] O. Pillai, R. Panchagnula, *Curr. Opin. Chem. Biol.* **2001**, *5*, 447–451.

[100] N. Angelova, D. Hunkeler, *Trends Biotechnol.* **1999**, *17*, 409–421.

[101] C. J. Wiedermann, K. Eisendle, *J. Pharm. policy Pract.* **2017**, *10*, 12.

[102] C. M. Paleos, Z. Sideratou, D. Tsiourvas, *Bioconjug. Chem.* **2017**, *28*, 1611–1624.

[103] G. Baier, D. Baumann, J. M. Siebert, A. Musyanovych, V. Mailänder, K. Landfester, *Biomacromolecules* **2012**, *13*, 2704–2715.

[104] A. D. A. Schwoerer, S. Harling, K. Scheibe, H. Menzel, R. Daniels, *Eur. J. Pharm. Biopharm.* **2009**, *73*, 351–356.

[105] A. O. Elzoghby, W. M. Samy, N. A. Elgindy, *J. Control. Release* **2012**, *161*, 38–49.

[106] Y. Chen, M. Su, Y. Li, J. Gao, C. Zhang, Z. Cao, J. Zhou, J. Liu, Z. Jiang, *ACS Appl. Mater. Interfaces* **2017**, *9*, 30519–30535.

[107] D. Paßlick, K. Piradashvili, D. Bamberger, M. Li, S. Jiang, D. Strand, P. R. Wich, K. Landfester, M. Bros, S. Grabbe, V. Mailänder, *J. Control. Release* **2018**, *289*, 23–34.

[108] K. Piradashvili, M. Fichter, K. Mohr, S. Gehring, F. R. Wurm, K. Landfester, *Biomacromolecules* **2015**, *16*, 815–821.

[109] S. Hou, J. Wang, C. R. Martin, *Nano Lett.* **2005**, *5*, 231–234.

[110] X. Jia, K. Minami, K. Uto, A. C. Chang, J. P. Hill, J. Nakanishi, K. Ariga, *Adv. Mater.* **2020**, *32*, 1905942.

[111] R. L. DiMarco, S. C. Heilshorn, *Adv. Mater.* **2012**, *24*, 3923–3940.

[112] J. Nicolas, S. Mura, D. Brambilla, N. Mackiewicz, P. Couvreur, *Chem. Soc. Rev.* **2013**, *42*, 1147–1235.

[113] S. Schöttler, G. Becker, S. Winzen, T. Steinbach, K. Mohr, K. Landfester, V. Mailänder, F. R. Wurm, *Nat. Nanotechnol.* **2016**, *11*, 372–377.

[114] V. Torchilin, *Adv. Drug Deliv. Rev.* **2011**, *63*, 131–135.

[115] H. Maeda, J. Wu, T. Sawa, Y. Matsumura, K. Hori, *J. Control. Release* **2000**, *65*, 271–284.

[116] A. Abuchowski, J. R. McCoy, N. C. Palczuk, T. van Es, F. F. Davis, *J. Biol. Chem.* **1977**, *252*, 3582–3586.

[117] Q. Yang, S. K. Lai, *WIREs Nanomedicine and Nanobiotechnology* **2015**, *7*, 655–677.

[118] K. N. Bauer, J. Simon, V. Mailänder, K. Landfester, F. R. Wurm, *Acta Biomater.* **2020**, *116*, 318–328.

[119] J. Simon, T. Wolf, K. Klein, K. Landfester, F. R. Wurm, V. Mailänder, *Angew. Chemie Int. Ed.* **2018**, *57*, 5548–5553.

[120] L. Tauhardt, D. Pretzel, K. Kempe, M. Gottschaldt, D. Pohlers, U. S. Schubert, *Polym. Chem.* **2014**, *5*, 5751–5764.

[121] B. Kang, P. Okwieka, S. Schöttler, S. Winzen, J. Langhanki, K. Mohr, T. Opatz, V. Mailänder, K. Landfester, F. R. Wurm, *Angew. Chemie Int. Ed.* **2015**, *54*, 7436–7440.

[122] F. Seidi, R. Jenjob, T. Phakkeeree, D. Crespy, *J. Control. Release* **2018**, *284*, 188–212.

[123] M. Tonigold, J. Simon, D. Estupiñán, M. Kokkinopoulou, J. Reinholz, U. Kintzel, A. Kaltbeitzel, P. Renz, M. P. Domogalla, K. Steinbrink, I. Lieberwirth, D. Crespy, K. Landfester, V. Mailänder, *Nat. Nanotechnol.* **2018**, *13*, 862–869.

[124] M. Mahmoudi, *Nat. Nanotechnol.* **2018**, *13*, 775–776.

[125] E. M. Sletten, C. R. Bertozzi, *Acc. Chem. Res.* **2011**, *44*, 666–676.

[126] R. C. Cookson, S. S. H. Gilani, I. D. R. Stevens, *Tetrahedron Lett.* **1962**, *3*, 615–618.

[127] O. Diels, *Zeitschrift für Angew. Chemie* **1929**, *42*, 911–918.

[128] K. De Bruycker, S. Billiet, H. A. Houck, S. Chattopadhyay, J. M. Winne, F. E. Du Prez, *Chem. Rev.* **2016**, *116*, 3919–3974.

[129] S. Chattopadhyay, F. Du Prez, *Eur. Polym. J.* **2016**, *81*, 77–85.

[130] T. Kunde, W. Meesorn, C. Weder, H. G. Börner, *Macromol. Rapid Commun.* **2019**, *40*, 1–6.

[131] M. Squillacote, M. Mooney, J. De Felippis, *J. Am. Chem. Soc.* **1990**, *112*, 5364–5365.

[132] P. S. Baran, C. A. Guerrero, E. J. Corey, *Org. Lett.* **2003**, *5*, 1999–2001.

[133] S. Billiet, K. De Bruycker, F. Driessen, H. Goossens, V. Van Speybroeck, J. M. Winne, F. E. Du Prez, *Nat. Chem.* **2014**, *6*, 815–821.

[134] R. C. Cookson, I. D. R. Stevens, C. T. Watts, *Chem. Commun.* **1966**, 744.

[135] D. W. Borhani, F. D. Greene, *J. Org. Chem.* **1986**, *51*, 1563–1570.

[136] L. Vlaminck, K. De Bruycker, O. Türünç, F. E. Du Prez, *Polym. Chem.* **2016**, *7*, 5655–5663.

[137] H. Ban, J. Gavrilyuk, C. F. Barbas, *J. Am. Chem. Soc.* **2010**, *132*, 1523–1525.

[138] H. Ban, M. Nagano, J. Gavrilyuk, W. Hakamata, T. Inokuma, C. F. Barbas, *Bioconjug. Chem.* **2013**, *24*, 520–532.

[139] D. M. Bauer, I. Ahmed, A. Vigovskaya, L. Fruk, *Bioconjug. Chem.* **2013**, *24*, 1094–1101.

[140] S. Vandewalle, R. De Coen, B. G. De Geest, F. E. Du Prez, *ACS Macro Lett.* **2017**, *6*, 1368–1372.

[141] N. Van Herck, F. E. Du Prez, *Macromolecules* **2018**, *51*, 3405–3414.

[142] M. Breugst, H.-U. Reissig, *Angew. Chemie Int. Ed.* **2020**, *59*, 12293–12307.

[143] A. Michael, *J. für Prakt. Chemie* **1893**, *48*, 94–95.

[144] H. C. Kolb, M. G. Finn, K. B. Sharpless, *Angew. Chemie Int. Ed.* **2001**, *40*, 2004–2021.

[145] V. V. Rostovtsev, L. G. Green, V. V. Fokin, K. B. Sharpless, *Angew. Chemie - Int. Ed.* **2002**, *41*, 2596–2599.

[146] N. J. Agard, J. A. Prescher, C. R. Bertozzi, *J. Am. Chem. Soc.* **2004**, *126*, 15046–15047.

[147] J. M. Baskin, J. A. Prescher, S. T. Laughlin, N. J. Agard, P. V. Chang, I. A. Miller, A. Lo, J. A. Codelli, C. R. Bertozzi, *Proc. Natl. Acad. Sci. U. S. A.* **2007**, *104*, 16793–16797.

[148] X. Ning, J. Guo, M. A. Wolfert, G.-J. Boons, *Angew. Chemie Int. Ed.* **2008**, *47*, 2253–2255.

[149] M. F. Debets, S. S. Van Berkel, S. Schoffelen, F. P. J. T. Rutjes, J. C. M. Van Hest, F. L. Van Delft, *Chem. Commun.* **2010**, *46*, 97–99.

[150] J. C. Jewett, C. R. Bertozzi, *Chem. Soc. Rev.* **2010**, *39*, 1272–1279.

[151] K. Lang, J. W. Chin, *ACS Chem. Biol.* **2014**, *9*, 16–20.

[152] J. Dommerholt, O. van Rooijen, A. Borrmann, C. F. Guerra, F. M. Bickelhaupt, F. L. van Delft, *Nat. Commun.* **2014**, *5*, 5378.

[153] X. Ning, R. P. Temming, J. Dommerholt, J. Guo, D. B. Ania, M. F. Debets, M. A. Wolfert, G.-J. Boons, F. L. van Delft, *Angew. Chemie Int. Ed.* **2010**, *49*, 3065–3068.

[154] H. Hillaireau, P. Couvreur, *Cell. Mol. Life Sci.* **2009**, *66*, 2873–2896.

[155] Y. Tabata, Y. Ikada, *Biomaterials* **1988**, *9*, 356–362.

[156] E. D. Korn, R. A. Weisman, *J. Cell Biol.* **1967**, *34*, 219–227.

[157] T. D. Heath, N. G. Lopez, D. Papahadjopoulos, *Biochim. Biophys. Acta* **1985**, *820*, 74–84.

[158] D. A. Kuhn, D. Vanhecke, B. Michen, F. Blank, P. Gehr, A. Petri-Fink, B. Rothen-Rutishauser, *Beilstein J. Nanotechnol.* **2014**, *5*, 1625–1636.

[159] L. C. Nelemans, L. Gurevich, *Mater.* **2020**, *13*, 366.

[160] P. Sandin, L. W. Fitzpatrick, J. C. Simpson, K. A. Dawson, *ACS Nano* **2012**, *6*, 1513–1521.

[161] S. K. Lai, K. Hida, S. T. Man, C. Chen, C. Machamer, T. A. Schroer, J. Hanes, *Biomaterials* **2007**, *28*, 2876–2884.

[162] G. Sahay, W. Querbes, C. Alabi, A. Eltoukhy, S. Sarkar, C. Zurenko, E. Karagiannis, K. Love, D. Chen, R. Zoncu, Y. Buganim, A. Schroeder, R. Langer, D. G. Anderson, *Nat. Biotechnol.* **2013**, *31*, 653–658.

[163] J. Gilleron, W. Querbes, A. Zeigerer, A. Borodovsky, G. Marsico, U. Schubert, K. Manygoats, S. Seifert, C. Andree, M. Stöter, H. Epstein-Barash, L. Zhang, V. Koteliansky, K. Fitzgerald, E. Fava, M. Bickle, Y. Kalaidzidis, A. Akinc, M. Maier, M. Zerial, *Nat. Biotechnol.* **2013**, *31*, 638–646.

[164] J. Reinholz, C. Diesler, S. Schöttler, M. Kokkinopoulou, S. Ritz, K. Landfester, V. Mailänder, *Acta Biomater.* **2018**, *71*, 432–443.

[165] K. Landfester, *Angew. Chemie Int. Ed.* **2009**, *48*, 4488–4507.

[166] K. Landfester, *Annu. Rev. Mater. Res.* **2006**, *36*, 231–279.

[167] A. J. Webster, M. E. Cates, *Langmuir* **1998**, *14*, 2068–2079.

[168] K. Landfester, *Macromol. Symp.* **2000**, *150*, 171–178.

[169] K. Katta, D. Busko, Y. Avlasevich, R. Muñoz-Espí, S. Baluschev, K. Landfester, *Macromol. Rapid Commun.* **2015**, *36*, 1084–1088.

[170] I. Hofmeister, K. Landfester, A. Taden, *Macromolecules* **2014**, *47*, 5768–5773.

[171] L. Torini, J. F. Argillier, N. Zydowicz, *Macromolecules* **2005**, *38*, 3225–3236.

[172] K. Bouchemal, S. Briançon, H. Fessi, Y. Chevalier, I. Bonnet, E. Perrier, *Mater. Sci. Eng. C* **2006**, *26*, 472–480.

[173] R. Roux, L. Sallet, P. Alcouffe, S. Chambert, N. Sintes-Zydowicz, E. Fleury, J. Bernard, *ACS Macro Lett.* **2012**, *1*, 1074–1078.

[174] R. H. Utama, Y. Jiang, P. B. Zetterlund, M. H. Stenzel, *Biomacromolecules* **2015**, *16*, 2144–2156.

[175] Z. Cao, U. Ziener, K. Landfester, *Macromolecules* **2010**, *43*, 6353–6360.

[176] S. U. Frick, M. P. Domogalla, G. Baier, F. R. Wurm, V. Mailänder, K. Landfester, K. Steinbrink, *ACS Nano* **2016**, *10*, 9216–9226.

[177] S.-M. Jo, S. Jiang, R. Graf, F. R. Wurm, K. Landfester, *Nanoscale* **2020**, *12*, 24266–24272.

[178] M.-L. Frey, J. Simon, M. Brückner, V. Mailänder, S. Morsbach, K. Landfester, *Polym. Chem.* **2020**, *11*, 3821–3830.

[179] G. Baier, M. Fichter, A. Kreyes, K. Klein, V. Mailänder, S. Gehring, K. Landfester, *Biomacromolecules* **2016**, *17*, 148–153.

[180] A. Musyanovych, K. Landfester, in *Prog. Colloid Polym. Sci.* (Eds.: G.K. Auernhammer, H.-J. Butt, D. Vollmer), Springer Berlin Heidelberg, **2008**, pp. 120–127.

[181] I. Schlegel, R. Muñoz-Espí, P. Renz, I. Lieberwirth, G. Floudas, Y. Suzuki, D. Crespy, K. Landfester, *Macromolecules* **2017**, *50*, 4725–4732.

[182] N. Jagielski, S. Sharma, V. Hombach, V. Mailänder, V. Rasche, K. Landfester, *Macromol. Chem. Phys.* **2007**, *208*, 2229–2241.

[183] A. A. Khorasani, J. L. Weaver, C. Salvador-Morales, *Int. J. Nanomedicine* **2014**, *9*, 5729–5751.

[184] M. Danaei, M. Dehghankhold, S. Ataei, F. Hasanzadeh Davarani, R. Javanmard, A. Dokhani, S. Khorasani, M. R. Mozafari, *Pharmaceutics* **2018**, *10*, 1–17.

[185] A. Sen Gupta, *WIREs Nanomedicine and Nanobiotechnology* **2016**, *8*, 255–270.

[186] M. Fregnaux, J. J. Gaumet, S. Dalmasso, J. P. Laurenti, R. Schneider, *Microelectron. Eng.* **2013**, *108*, 187–191.

[187] J. W. Shreffler, J. E. Pullan, K. M. Dailey, S. Mallik, A. E. Brooks, *Int. J. Mol. Sci.* **2019**, *20*, 1–25.

[188] N. Bertrand, P. Grenier, M. Mahmoudi, E. M. Lima, E. A. Appel, F. Dormont, J.-M. Lim, R. Karnik, R. Langer, O. C. Farokhzad, *Nat. Commun.* **2017**, *8*, 777.

[189] C. Sacchetti, K. Motamedchaboki, A. Magrini, G. Palmieri, M. Mattei, S. Bernardini, N. Rosato, N. Bottini, M. Bottini, *ACS Nano* **2013**, *7*, 1974–1989.

[190] C. Weber, M. Voigt, J. Simon, A.-K. Danner, H. Frey, V. Mailänder, M. Helm, S. Morsbach, K. Landfester, *Biomacromolecules* **2019**, *20*, 2989–2999.

[191] M. Lundqvist, J. Stigler, T. Cedervall, T. Berggård, M. B. Flanagan, I. Lynch, G. Elia, K. Dawson, *ACS Nano* **2011**, *5*, 7503–7509.

[192] M. Lundqvist, J. Stigler, G. Elia, I. Lynch, T. Cedervall, K. A. Dawson, *Proc. Natl. Acad. Sci.* **2008**, *105*, 14265 LP – 14270.

[193] S. Schöttler, K. Landfester, V. Mailänder, *Angew. Chemie Int. Ed.* **2016**, *55*, 8806–8815.

[194] "Nanomaterials definition matters", Editorial, *Nat. Nanotechnol.* **2019**, *14*, 193.

[195] D. R. Boverhof, C. M. Bramante, J. H. Butala, S. F. Clancy, M. Lafranconi, J. West, S. C. Gordon, *Regul. Toxicol. Pharmacol.* **2015**, *73*, 137–150.

[196] C. D. Engeman, L. Baumgartner, B. M. Carr, A. M. Fish, J. D. Meyerhofer, T. A. Satterfield, P. A. Holden, B. H. Harthorn, *J. Nanoparticle Res.* **2012**, *14*, 749.

[197] C. L. Haynes, *Anal. Bioanal. Chem.* **2010**, *398*, 587–588.

[198] G. Oberdörster, *J. Intern. Med.* **2010**, *267*, 89–105.

[199] M. Hofmann-Amtenbrink, D. W. Grainger, H. Hofmann, *Nanomedicine Nanotechnology, Biol. Med.* **2015**, *11*, 1689–1694.

[200] W. Schärtl, *Light Scattering from Polymer Solutions and Nanoparticle Dispersions*, Springer Berlin Heidelberg, **2007**.

[201] R. J. Hunter, *Zeta Potential in Colloid Science - Principles and Applications*, Academic Press London, San Diego, New York, Berkely, Boston, Sydney, Tokyo, Toronto, **1981**.

[202] O. Stern, *Zeitschrift für Elektrochemie und Angew. Phys. Chemie* **1924**, *30*, 508–516.

[203] D. A. Armbruster, T. Pry, *Clin. Biochem. Rev.* **2008**, *29 Suppl 1*, S49–S52.

[204] B. W. Whitcomb, E. F. Schisterman, *Paediatr. Perinat. Epidemiol.* **2008**, *22*, 597–602.

[205] EP17-A Protocols for Determination of Limits of Detection and Limits of Quantitation; Approved Guideline Global Consensus Standardization for Health Technologies, CLSI/NCCLS, **2004**.

[206] H. Yang, W. Xu, X. Liang, Y. Yang, Y. Zhou, *Microchim. Acta* **2020**, *187*, 206.

[207] T. Porstmann, S. T. Kiessig, *J. Immunol. Methods* **1992**, *150*, 5–21.

[208] S. J. Goldsmith, *Semin. Nucl. Med.* **1975**, *5*, 125–152.

[209] K. M. Mayer, S. Lee, H. Liao, B. C. Rostro, A. Fuentes, P. T. Scully, C. L. Nehl, J. H. Hafner, *ACS Nano* **2008**, *2*, 687–692.

[210] M.-L. Zhang, C.-Q. Yi, X. Fan, K.-Q. Peng, N.-B. Wong, M.-S. Yang, R.-Q. Zhang, S.-T. Lee, *Appl. Phys. Lett.* **2008**, *92*, 43116.

[211] E. Engvall, P. Perlmann, *Immunochemistry* **1971**, *8*, 871–874.

[212] J. P. Hofmann, M. Rohnke, B. M. Weckhuysen, *Phys. Chem. Chem. Phys.* **2014**, *16*, 5465–5474.

[213] E. A. Lewis, K. P. Murphy, in Protein-Ligand Interactions: Methods and Applications (Ed.: G. Ulrich Nienhaus), Humana Press, Totowa, NJ, **2005**, pp. 1–15.

[214] E. Freire, O. L. Mayorga, M. Straume, *Anal. Chem.* **1990**, *62*, 950A-959A.

[215] M. Krumb, M.-L. Frey, J. Langhanki, R. Forster, D. Kowalczyk, V. Mailänder, K. Landfester, T. Opatz, *Cells* **2020**, *9*, 2087.

[216] D. R. Janero, *Expert Opin. Drug Discov.* **2016**, *11*, 835–842.

[217] K. Manghani, *Perspect. Clin. Res.* **2011**, *2*, 34–37.

[218] R. Sajdak, L. A. Trembath, K. S. Thomas, *J. Nucl. Med. Technol.* **2013**, *41*, 231–233.

[219] D. Liu, F. Yang, F. Xiong, N. Gu, *Theranostics* **2016**, *6*, 1306–1323.

[220] K. W. Witwer, E. I. Buzás, L. T. Bemis, A. Bora, C. Lässer, J. Lötvall, E. N. Nolte-'t Hoen, M. G. Piper, S. Sivaraman, J. Skog, C. Théry, M. H. Wauben, F. Hochberg, *J. Extracell. Vesicles* **2013**, *2*, 20360.

[221] S. Mülhopt, S. Diabaté, M. Dilger, C. Adelhelm, C. Anderlohr, T. Bergfeldt, J. G. de la Torre, Y. Jiang, E. Valsami-Jones, D. Langevin, I. Lynch, E. Mahon, I. Nelissen, J. Piella, V. Puntes, S. Ray, R. Schneider, T. Wilkins, C. Weiss, H. R. Paur, *Nanomaterials* **2018**, *8*, 311.

[222] F. Caruso, *Adv. Mater.* **2001**, *13*, 11–22.

[223] M. Elsabahy, K. L. Wooley, *Chem. Soc. Rev.* **2012**, *41*, 2545–2561.

[224] M. P. Monopoli, C. Åberg, A. Salvati, K. A. Dawson, *Nat. Nanotechnol.* **2012**, *7*, 779–786.

[225] G. Baier, J. M. Siebert, K. Landfester, A. Musyanovych, *Macromolecules* **2012**, *45*, 3419–3427.

[226] C. S. Schollenberger, F. D. Stewart, *J. Elastoplast.* **1971**, *3*, 28–56.

[227] G. Baier, A. Musyanovych, M. Dass, S. Theisinger, K. Landfester, *Biomacromolecules* **2010**, *11*, 960–968.

[228] P. K. Hari, S. Garg, S. K. Garg, *Starch - Stärke* **1989**, *41*, 88–91.

[229] M. S. Alkanawati, F. R. Wurm, H. Thérien-Aubin, K. Landfester, *Macromol. Mater. Eng.* **2018**, *303*, 1700505.

[230] B. Ozel, S. S. Uguz, M. Kilercioglu, L. Grunin, M. H. Oztop, *J. Food Process Eng.* **2017**, *40*, e12465.

[231] J. M. Siebert, G. Baier, A. Musyanovych, K. Landfester, *Chem. Commun.* **2012**, *48*, 5470–5472.

[232] J. P. Marcolongo, M. Mirenda, *J. Chem. Educ.* **2011**, *88*, 629–633.

[233] L. L. Hecht, C. Wagner, Ö. Özcan, F. Eisenbart, K. Köhler, K. Landfester, H. P. Schuchmann, *Macromol. Chem. Phys.* **2012**, *213*, 2165–2173.

[234] V. Castelvetro, C. De Vita, G. Giannini, S. Giaiacopi, *J. Appl. Polym. Sci.* **2006**, *102*, 3083–3094.

[235] I. Capek, *Adv. Colloid Interface Sci.* **2002**, *99*, 77–162.

[236] M. S. Khan, S. A. Bhat, M. T. Rehman, I. Hassan, S. Tabrez, M. F. AlAjmi, A. Hussain, F. M. Husain, S. F. Alamery, *Int. J. Biol. Macromol.* **2018**, *120*, 45–58.

[237] F. Rusconi, É. Valton, R. Nguyen, E. Dufourc, *Anal. Biochem.* **2001**, *295*, 31–37.

[238] H. Nagatani, S. Suzuki, D. J. Fermín, H. H. Girault, K. Nakatani, *Anal. Bioanal. Chem.* **2006**, *386*, 633–638.

[239] G. Raspoet, M. T. Nguyen, M. McGarraghy, A. F. Hegarty, *J. Org. Chem.* **1998**, *63*, 6867–6877.

[240] X. Hou, C. Ke, J. F. Stoddart, *Chem. Soc. Rev.* **2016**, *45*, 3766–3780.

[241] S. Udenfriend, S. Stein, P. Böhlen, W. Dairman, W. Leimgruber, M. Weigele, *Science* **1972**, *178*, 871 LP – 872.

[242] F. Xie, K. Sivakumar, Q. Zeng, M. A. Bruckman, B. Hodges, Q. Wang, *Tetrahedron* **2008**, *64*, 2906–2914.

[243] S. Mädler, C. Bich, D. Touboul, R. Zenobi, *J. Mass Spectrom.* **2009**, *44*, 694–706.

[244] R. Van Geel, G. J. M. Pruijn, F. L. Van Delft, W. C. Boelens, *Bioconjug. Chem.* **2012**, *23*, 392–398.

[245] S. A. Rosenberg, *J. Immunol.* **2014**, *192*, 5451–5458.

[246] M. R. Arkin, M. Randal, W. L. DeLano, J. Hyde, T. N. Luong, J. D. Oslob, D. R. Raphael, L. Taylor, J. Wang, R. S. McDowell, J. A. Wells, A. C. Braisted, *Proc. Natl. Acad. Sci.* **2003**, *100*, 1603 LP – 1608.

[247] C. A. Bergmann, B. J. Landmeier, D. R. Kaplan, *Mol. Immunol.* **1991**, *28*, 99–105.

[248] T. Bonk, A. Humeny, *Neuroscientist* **2001**, *7*, 6–12.

[249] S. D. Emerson, R. Palermo, C.-M. Liu, J. W. Tilley, L. Chen, W. Danho, V. S. Madison, D. N. Greeley, G. Ju, D. C. Fry, *Protein Sci.* **2003**, *12*, 811–822.

[250] I. Buchwalow, V. Samoilova, W. Boecker, M. Tiemann, *Sci. Rep.* **2011**, *1*, 28.

[251] T. B. H. Geijtenbeek, R. Torensma, S. J. van Vliet, G. C. F. van Duijnhoven, G. J. Adema, Y. van Kooyk, C. G. Figdor, *Cell* **2000**, *100*, 575–585.

[252] D. A. Mitchell, A. J. Fadden, K. Drickamer, *J. Biol. Chem.* **2001**, *276*, 28939–28945.

[253] S. Ordanini, N. Varga, V. Porkolab, M. Thépaut, L. Belvisi, A. Bertaglia, A. Palmioli, A. Berzi, D. Trabattoni, M. Clerici, F. Fieschi, A. Bernardi, *Chem. Commun.* **2015**, *51*, 3816–3819.

[254] X. Zhang, S. Caner, E. Kwan, C. Li, G. D. Brayer, S. G. Withers, *Biochemistry* **2016**, *55*, 6000–6009.

[255] A. Musyanovych, R. Rossmanith, C. Tontsch, K. Landfester, *Langmuir* **2007**, *23*, 5367–5376.

[256] G. Yohannes, S. K. Wiedmer, M. Elomaa, M. Jussila, V. Aseyev, M.-L. Riekkola, *Anal. Chim. Acta* **2010**, *675*, 191–198.

[257] C. Guindani, M.-L. Frey, J. Simon, K. Koynov, J. Schultze, S. R. S. Ferreira, P. H. H. Araújo, D. de Oliveira, F. R. Wurm, V. Mailänder, K. Landfester, *Macromol. Biosci.* **2019**, *19*, 1900145.

[258] A. V Elgersma, R. L. J. Zsom, W. Norde, J. Lyklema, *J. Colloid Interface Sci.* **1990**, *138*, 145–156.

[259] I. Rayment, in Encyclopedia of Physical Science and Technology (Third Ed.) (Editor.: R. A. Meyers) Elsevier, New York, **2003**, pp. 191–218.

[260] B. Kronberg, *Curr. Opin. Colloid Interface Sci.* **2016**, *22*, 14–22.

[261] Y. L. Jeyachandran, E. Mielczarski, B. Rai, J. A. Mielczarski, *Langmuir* **2009**, *25*, 11614–11620.

[262] S. H. Lee, E. Ruckenstein, *J. Colloid Interface Sci.* **1988**, *125*, 365–379.

[263] A. Ravindran, A. Singh, A. M. Raichur, N. Chandrasekaran, A. Mukherjee, *Colloids Surfaces B Biointerfaces* **2010**, *76*, 32–37.

[264] X. M. He, D. C. Carter, *Nature* **1992**, *358*, 209–215.

[265] A. A. Spector, K. John, J. E. Fletcher, *J. Lipid Res.* **1969**, *10*, 56–67.

[266] E. Remold-O'Donnell, *FEBS Lett.* **1993**, *315*, 105–108.

[267] D. H. Chou, C. V Morr, *J. Am. Oil Chem. Soc.* **1979**, *56*, A53–A62.

[268] R. Miller, V. B. Fainerman, M. E. Leser, M. Michel, *Curr. Opin. Colloid Interface Sci.* **2004**, *9*, 350–356.

[269] P. E. Stein, A. G. W. Leslie, J. T. Finch, R. W. Carrell, *J. Mol. Biol.* **1991**, *221*, 941–959.

[270] A. Kawai, V. T. G. Chuang, Y. Kouno, K. Yamasaki, S. Miyamoto, M. Anraku, M. Otagiri, *Biochim. Biophys. Acta - Proteins Proteomics* **2017**, *1865*, 979–984.

[271] A. Bujacz, *Acta Crystallogr. Sect. D* **2012**, *68*, 1278–1289.

[272] B. X. Huang, H.-Y. Kim, C. Dass, *J. Am. Soc. Mass Spectrom.* **2004**, *15*, 1237–1247.

[273] K. Landfester, V. Mailänder, *Expert Opin. Drug Deliv.* **2013**, *10*, 593–609.

[274] W. R. Algar, D. E. Prasuhn, M. H. Stewart, T. L. Jennings, J. B. Blanco-Canosa, P. E. Dawson, I. L. Medintz, *Bioconjug. Chem.* **2011**, *22*, 825–858.

[275] E. M. Sletten, C. R. Bertozzi, *Angew. Chemie Int. Ed.* **2009**, *48*, 6974–6998.

[276] K. Piradashvili, J. Simon, D. Paßlick, J. R. Höhner, V. Mailänder, F. R. Wurm, K. Landfester, *Nanoscale Horizons* **2017**, *2*, 297–302.

[277] M. Neves-Petersen, S. Petersen, G. Prakash Gajula, in Molecular Photochemistry - Various Aspects (Ed.: S. Saha), InTech, **2012**, pp. 125–158.

[278] C. M. Madl, S. C. Heilshorn, *Adv. Funct. Mater.* **2018**, *28*, 1–21.

[279] D. K. Kölmel, E. T. Kool, *Chem. Rev.* **2017**, *117*, 10358–10376.

[280] S. B. Hanay, D. F. Brougham, A. A. Dias, A. Heise, *Polym. Chem.* **2017**, *8*, 6594–6597.

[281] S. B. Hanay, B. Ritzen, D. Brougham, A. A. Dias, A. Heise, *Macromol. Biosci.* **2017**, *17*, 1–7.

[282] D. Kaiser, J. M. Winne, M. E. Ortiz-Soto, J. Seibel, T. A. Le, B. Engels, *J. Org. Chem.* **2018**, *83*, 10248–10260.

[283] R. C. Cookson, S. S. H. Gilani, I. D. R. Stevens, *J. Chem. Soc. C Org.* **1967**, 1905–1909.

[284] H. A. Houck, K. De Bruycker, C. Barner-Kowollik, J. M. Winne, F. E. Du Prez, *Macromolecules* **2018**, *51*, 3156–3164.

[285] H. A. Houck, K. De Bruycker, S. Billiet, B. Dhanis, H. Goossens, S. Catak, V. Van Speybroeck, J. M. Winne, F. E. Du Prez, *Chem. Sci.* **2017**, *8*, 3098–3108.

[286] M. J. Bausch, B. David, *J. Org. Chem.* **1992**, *57*, 1118–1124.

[287] I. Lynch, A. Salvati, K. A. Dawson, *Nat. Nanotechnol.* **2009**, *4*, 546–547.

[288] M. Mahmoudi, F. Quinlan-Pluck, M. P. Monopoli, S. Sheibani, H. Vali, K. A. Dawson, I. Lynch, *ACS Chem. Neurosci.* **2013**, *4*, 475–485.

[289] C. C. Fleischer, C. K. Payne, *J. Phys. Chem. B* **2014**, *118*, 14017–14026.

[290] P. G. W. Gettins, *Chem. Rev.* **2002**, *102*, 4751–4804.

[291] E. L. Gelamo, M. Tabak, *Spectrochim. Acta Part A Mol. Biomol. Spectrosc.* **2000**, *56*, 2255–2271.

[292] S. Sugio, A. Kashima, S. Mochizuki, M. Noda, K. Kobayashi, *Protein Eng. Des. Sel.* **1999**, *12*, 439–446.

[293] K. A. Majorek, P. J. Porebski, A. Dayal, M. D. Zimmerman, K. Jablonska, A. J. Stewart, M. Chruszcz, W. Minor, *Mol. Immunol.* **2012**, *52*, 174–182.

[294] J. Simon, S. Christmann, V. Mailänder, F. R. Wurm, K. Landfester, *Isr. J. Chem.* **2018**, *58*, 1363–1372.

[295] B. Kang, P. Okwieka, S. Schöttler, O. Seifert, R. E. Kontermann, K. Pfizenmaier, A. Musyanovych, R. Meyer, M. Diken, U. Sahin, V. Mailänder, F. R. Wurm, K. Landfester, *Biomaterials* **2015**, *49*, 125–134.

[296] H. H. Gustafson, D. Holt-Casper, D. W. Grainger, H. Ghandehari, *Nano Today* **2015**, *10*, 487–510.

[297] P. Aggarwal, J. B. Hall, C. B. McLeland, M. A. Dobrovolskaia, S. E. McNeil, *Adv. Drug Deliv. Rev.* **2009**, *61*, 428–437.

[298] M. Ferrari, *Nat. Rev. Cancer* **2005**, *5*, 161–171.

[299] C. L. Ventola, *P T* **2017**, *42*, 742–755.

[300] E. Beltrán-Gracia, A. López-Camacho, I. Higuera-Ciapara, J. B. Velázquez-Fernández, A. A. Vallejo-Cardona, *Nanomedicine Review: Clinical Developments in Liposomal Applications*, Springer Vienna, **2019**.

[301] K. Landfester, A. Musyanovych, V. Mailänder, *J. Polym. Sci. Part A Polym. Chem.* **2010**, *48*, 493–515.

[302] P. Foroozandeh, A. A. Aziz, *Nanoscale Res. Lett.* **2018**, *13*, 339.

[303] J. Reinholz, K. Landfester, V. Mailänder, *Drug Deliv.* **2018**, *25*, 1694–1705.

[304] B. Dubertret, P. Skourides, D. J. Norris, V. Noireaux, A. H. Brivanlou, A. Libchaber, *Science* **2002**, *298*, 1759–1762.

[305] M. Seleci, D. Ag Seleci, T. Scheper, F. Stahl, *Int. J. Mol. Sci.* **2017**, *18*, 1415.

[306] C. Mi, Y. Wang, J. Zhang, H. Huang, L. Xu, S. Wang, X. Fang, J. Fang, C. Mao, S. Xu, *J. Biotechnol.* **2011**, *153*, 125–132.

[307] K. V. Pavan Kumar, O. S. Nirmal Ghosh, G. Balakrishnan, P. Thirugnanasambantham, S. K.

Raghavan, A. K. Viswanath, *RSC Adv.* **2015**, *5*, 16815–16820.

[308] M. J. D. Clift, C. Brandenberger, B. Rothen-Rutishauser, D. M. Brown, V. Stone, *Toxicology* **2011**, *286*, 58–68.

[309] H. Halim, J. Simon, I. Lieberwirth, V. Mailänder, K. Koynov, A. Riedinger, *J. Mater. Chem. B* **2020**, *8*, 146–154.

[310] H. Schlaad, H. Kukula, J. Rudloff, I. Below, *Macromolecules* **2001**, *34*, 4302–4304.

[311] H. Xu, L. Shen, L. Xu, Y. Yang, *Biomed. Microdevices* **2015**, *17*, 8.

[312] H. Halim, D. Trieb, N. Huber, M. Martínez-Negro, L.-A. Meyer, T. Basché, S. Morsbach, K. A. I. Zhang, A. Riedinger, *J. Phys. Chem. C* **2020**, *124*, 25028–25037.

[313] O. Erdem, K. Gungor, B. Guzelturk, I. Tanriover, M. Sak, M. Olutas, D. Dede, Y. Kelestemur, H. V. Demir, *Nano Lett.* **2019**, *19*, 4297–4305.

[314] N. A. Bright, L. J. Davis, J. P. Luzio, *Curr. Biol.* **2016**, *26*, 2233–2245.

[315] D. Aston, R. A. Capel, K. L. Ford, H. C. Christian, G. R. Mirams, E. A. Rog-Zielinska, P. Kohl, A. Galione, R. A. B. Burton, D. A. Terrar, *Sci. Rep.* **2017**, *7*, 40620.

[316] M. B. Bannwarth, S. Ebert, M. Lauck, U. Ziener, S. Tomcin, G. Jakob, K. Münnemann, V. Mailänder, A. Musyanovych, K. Landfester, *Macromol. Biosci.* **2014**, *14*, 1205–1214.

[317] B. Mahler, B. Nadal, C. Bouet, G. Patriarche, B. Dubertret, *J. Am. Chem. Soc.* **2012**, *134*, 18591–18598.

[318] A. Riedinger, F. Zhang, F. Dommershausen, C. Röcker, S. Brandholt, G. U. Nienhaus, U. Koert, W. J. Parak, *Small* **2010**, *6*, 2590–2597.

[319] M. P. Domogalla, Nanocapsule-Based Vaccination for Inhibition of Tumor Escape Mechanisms, Dissertation, Johannes Gutenberg-Universität Mainz, **2017**.

[320] S. Winzen, Influence of Different Factors on the Interaction between Polymeric Nanomaterials and Blood Plasma Proteins, Dissertation, Johannes Gutenberg-Universität Mainz, **2015**.

IX. List of Figures

X. List of Tables